Electrostatic images and T-matrices for simple geometries

Matt Majic

Primary supervisor: Eric C. Le Ru,

Secondary supervisor: Baptiste Auguié

PhD thesis

Victoria University of Wellington
2020

Abstract

This thesis is concerned with electrostatic boundary problems and how their solutions behave depending on the chosen basis of harmonic functions and the location of the fundamental singularities of the potential. The first part deals with the method of images for simple geometries where the exact nature of the image/fundamental singularity is unknown; essentially a study of analytic continuation for Laplace's equation in 3 dimensions. For the sphere, spheroid and cylinder, new deductions are made on the location of the images of point charges and their linear or surface charge densities, by using different harmonic series solutions that reveal the image. The second part looks for analytic expressions for the T-matrix for electromagnetic scattering of simple objects in the low frequency limit. In this formalism the incident and scattered fields are expanded on an orthogonal basis such as spherical harmonics, and the T-matrix is the transformation between the coefficients of these series, providing the general solution of any electromagnetic scattering problem by a given particle at a given wavelength. For the spheroid, bispherical system and torus, the natural basis of harmonic functions for the geometry of the scatterer are used to determine T-matrix expressed in that basis, which is then transformed onto a basis of canonical spherical harmonics via the linear relationships between different bases of harmonic functions.

Acknowledgements

Thanks to Eric and Baptiste for being cool supervisors, and thanks to Sci-hub and Lib-gen for letting me access the papers and text-books I needed.

Contents

Chapter 1

Introduction

Laplace's equation $\nabla^2 V = 0$ appears in many areas of physics, often as a basic approximation to some more exact differential equation. In electromagnetism, Laplace's equation appears as the static limit of Maxwell's equations, in acoustics as the long wave limit of the wave equation, in thermodynamics as the static limit of the heat equation, in gravity for low mass, and in fluid dynamics when the flow is irrotational. A common question in these areas is "what is the field of a point source in the presence of some boundary?" This field is called the Green function for that particular boundary. For the more complex differential equations, Green functions are only analytically solvable for very simple boundaries such as spheres and planes, but for Laplace's equation, analytic solutions are found for all kinds of geometries.

Laplace's equation is well studied and there are a broad range of basis solutions, "harmonics" which suit different geometries. In two dimensions Laplace's equation coincides with the Cauchy Riemann equations, the condition for a function to be analytic on the complex plane, so there is a huge range of tools to deal with solutions to Laplace's equation, but not all these generalize to more complex equations. By studying new approaches and solutions to known problems, there is hope that these ideas may be generalized to more complex equations where analytic numeric and approximate approaches are more in need.

Two of the approaches we will focus on are the method of images and the T-matrix method, both of which apply also to the time harmonic wave equation, the Helmholtz equation. Common to these are basis transformations of series' of harmonic functions from one geometry to another, which we will also study in detail. Image theory and the T-matrix method apply particularly to problems involving point sources and conducting or dielectric particles, excited by electromagnetic radiation, where the particles are small compared to the wavelength. This is relevant for example to surface enhanced Raman spectroscopy, a way of detecting the Raman spectrum scattered by molecules by using the field enhancement near a particle's surface [1]. Each molecule has unique Raman spectral profile, so Raman spectroscopy can be used to detect the presence of a particular molecule. But the signal is very weak, and a powerful technique to enhance this signal is to attract them to nano-sized metallic particles which have strong electric fields near the surface. Two hot spots for this are near tips of pointy particles such as spheroids, and in gaps between two particles (a "dimer"), where the surface field enhancement is powerful enough to detect even single molecules [2]. To study field enhancements mathematically can be computationally intensive for molecules close to the surface, especially when one wants to model the effects of hundreds of these even around a simple particle such as a sphere [3].

The method of images is one way of alleviating this computational difficulty, which involves the placement of simple electromagnetic image sources inside the particle, that act as the mirror image of the molecule and solve the electromagnetic problem without the need for determining and evaluating fields of complex surface charges and currents. It has been known since Kelvin in the 19th century [4], with the simple example of a point charge near a conducting sphere. In previous work, my supervisor Eric Le Ru and I studied the field of a point source near a dielectric sphere, where for a close source the standard solution as a series of spherical harmonics converges slowly. We investigated spheroidal harmonics [5] and "logopoles" [6] that both mimic the singularity of the analytic continuation of the scattered potential through the sphere – a radial line segment lying inside. These functions can be used to construct series solutions that converge much faster than the standard series solution of spherical harmonics.

The T-matrix method is a more modern solution established in the 1960s [7] where the electric and magnetic fields are expanded on a basis of functions, usually spherical wave functions, and the T-matrix itself provides the series coefficients which are used to expand the field scattered by the particle(s). The problem is shifted to computing the T-matrix which can be done in many ways. The advantage of the T-matrix is that there is one T-matrix for any given object, independent of what the external field is. This is ideal for computing the properties of clusters of particles for example in solution or the atmosphere [8]. Computing a T-matrix can be computationally intensive, so simple approximations, for example for small particle sizes are welcome. T-matrices may even be ill-conditioned, because the fields have different singularities depending on the geometry of the scatterer, while spherical wave functions or any other basis have their own convergence domains and singularities. Considering the nature of the singularity of the potential function is crucial to constructing a well behaved solution, both in the context of image theory or the T-matrix, since it is the interplay between the geometry of the basis functions and the location of the singularity that determines the boundary of convergence. Much of this PhD to investigating the singularities of potentials in electrostatic problems, towards finding new solutions which converge quickly.

1.1 Mathematical concepts

Here we briefly cover the main concepts used throughout the thesis.

1.1.1 Maxwell's equations for static and time harmonic fields

Any electromagnetic problem obeys Maxwell's equations, and if the electromagnetic fields are time-harmonic (changing sinusoidally with time t and frequency ω as $e^{-i\omega t}$) as is the case for a monochromatic light source, then Maxwell's equations reduce to the vector Helmholtz equation $(\nabla^2 + k^2)\mathbf{E} = 0$ for the electric field $\mathbf{E}$ and wavenumber k. The magnetic field also obeys the Helmholtz equation and is proportional to the electric field. If the geometry of the scatterer is very small compared to the wavelength, as is the case for nano particles excited by visible light, and is an approximation used frequently in this thesis, then the Helmholtz equation may be approximated by taking $k \to 0$, where it reduces to Laplace's equation $\nabla^2 V = 0$ for the electric potential V where $\mathbf{E} = -\nabla V$. This is called the quasi-static approximation; it differs from electrostatics in that the fields are to be post multiplied by the factor $e^{-i\omega t}$, and the dielectric permittivity of the particle is given by its value corresponding to that particular frequency, not its static value.

1.1.2 Green functions

We will be dealing with Green functions [1] in every chapter. In general, the Green function for a particular inhomogeneous partial differential equation is the particular solution of the equation when the inhomogeneous part is a delta function of one of the coordinates. In electrostatics, which is governed by the Laplace equation, the Green function is the potential of a point charge. The concept of Green functions may also be generalized to include boundary conditions, for example the potential of a point charge in the presence of a dielectric sphere is sometimes called "the Green function for a sphere".

1.1.3 Method of images/ Image theory

The method of images is an approach to a physical problem comprised of a source potential and surface boundary. It may provide a simple expression for the reflected potential when other methods involving series, integrals or charges on the conductor surface are not practical. In most cases the term "method" of images is misleading since there is no general method of finding the location of the image; usually a guess is made. The term "method" may refer to an algorithm that places image point charges successively, determining the strength of each charge iteratively. Smythe [9] describes the method of images as solving a problem via an ansatz of a discrete sum of point charges, if possible. "Image theory" may then be defined as the more general concept of placing image point, line and surface sources to solve boundary problems, without specifying a method of determining their strength and location.

Image theory is related to the equivalence principle of electromagnetics, which states that different charge and current distributions may produce the same electric and magnetic fields in some region. These source distributions are then said to be equivalent. For example a point charge is equivalent to a concentric spherical

---

[1] Or "Green's functions", but using this phrase is problematic as it creates a tendency to write "the Green's function".

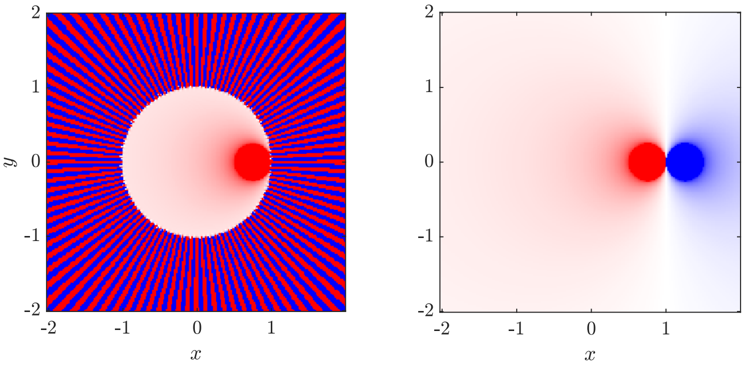

Figure 1.1: Analytic continuation of the real part of the function $f(z)$. Red represents positive values, blue negative. On the left, f is computed by the series $\sum_{n=0}^{\infty} z^n$ with 100 terms. The radial stripes are an artifact due to the series diverging for $|z| > 1$. On the right, f is computed by an equivalent function $\bar{f}(z) = 1/(1-z)$, which reveals f across the whole complex plane.

surface with a uniform surface charge, when one considers just the region outside the sphere. So for the problem of an isolated charge conducting sphere, the potential *outside* the sphere may be modeled as the potential of a point charge at the center. The point charge is the image of the sphere for this problem (well actually one possible image – technically any smaller concentric spherical surface with the same charge is an equivalent source and some may claim that this is also an image, so there is some ambiguity over the definition of an image, which we will get to soon).

Another basic example of an image is that of a point charge next to an infinite conducting plane, where the image is another negative point charge located opposite the plane, just like an optical mirror image but with the additional consideration of sign of charge. The analogy to optical images arises because these two cases are the long- and short-wavelength limits of light scattering governed by the Helmholtz equation $(\nabla^2 + k^2)V = 0$, where the same image solution applies regardless of wavelength. In very few cases are scattering problems for the Helmholtz equation solvable with images, but for Laplace's equation there are many known examples; here is a non-exhaustive list:

- The image of a point charge in multiple parallel planes can be constructed recursively from the solution for a single plane, resulting in an infinite series of point images [10]. The method of images can be used for many boundaries defined by intersecting planes [11].
- The image of a point charge in a conducting sphere is a negative point charge located at the "inversion point" of the sphere; this is known as the Kelvin point charge [9, 12, 13].
- The potential of two charged conducting spheres can be solved using an infinite series of image point charges on the axis of the spheres [9, 12].
- For a point charge near a circular disk, naively there is no volume to put images, but an image can be constructed by considering a second copy of the entire space attached at the disk, where the potential of the point charge in this double space is a different function. The image is then another one of these modified point charges located opposite the disk but in the second space [14]. This is known as the Sommerfeld image method.
- For materials with finite permittivity, images may be stretched relative to the conducting case, for example the image of a point charge in a dielectric sphere is a line extending radially from the center [15, 16].

1.1.4 Analytic continuation, uniqueness and existence

Image theory uses the concept of analytic continuation, which is best illustrated with a basic example. Consider the power series $f(z) = \sum_{n=0}^{\infty} z^n$, the complex plane where $z = x + iy$. This series converges only inside the circle $|z| < 1$, but one can derive an equivalent expression $\bar{f}(z) = 1/(1-z)$, which is equal to $f(z)$ for $|z| < 1$, but also converges for $|z| > 1$, and is smooth for all derivatives across the boundary $|z| = 1$, except for one singular

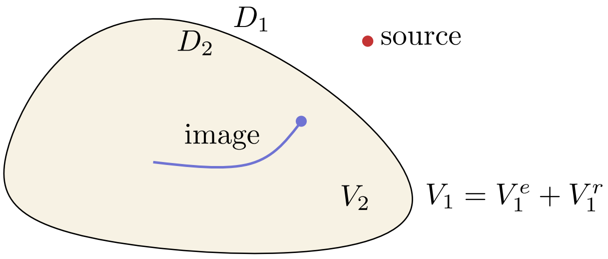

Figure 1.2: Schematic of the types of problems encountered in this thesis.

point at $z = 1$. This is illustrated in Figure 1.1. Because $\bar{f}$ is analytic everywhere except its singular point and equal to f in a sub-domain, we say that $\bar{f}$ is the analytic continuation of f. The word "continuation" can be interpreted as continuing f and all its derivatives through the boundary of divergence. The concept of analytic continuation applies in any number of dimensions.

Two theorems will underly our investigation into image theory and throughout the thesis.

- The *identity theorem* basically states that any analytic function defined in some open domain in any dimension of complex space has a unique analytic continuation defined in all space except for singular points. An analytic function of one or more complex variables is infinitely differentiable in a neighborhood of every point of its domain. All potential that solve Laplace's equation or the Helmholtz equation are analytic.
- *Liouville's theorem* basically states that any non-constant, bounded analytic function is singular (infinite) at least at some point. In electrostatics, these singularities may be thought of as the charge distribution that generates the potential function.

Many of the problems in this thesis have a boundary which divides the space $\mathbb{R}^3$ into two volume domains D_1 and D_2 as illustrated in Figure 1.2, where the domains have different material properties which forces the potential $V(\mathbf{r})$ to be discontinuous in some way across the boundary. For the solution in D_1 we write $V = V_1 = V_1^e + V_1^r$ where V_1^e is the known excitation potential (for example a point charge or a uniform field) and V_1^r is the potential reflected by the boundary which one must solve for. The solution in D_2 is $V = V_2$. The complete solution is $V = V_1(\mathbf{r} \in D_1) + V_2(\mathbf{r} \in D_2)$, i.e. V_1 and V_2 sewed together with a discontinuity at the boundary. V_1^e is harmonic except at the locations of the sources in D_1, while V_1^r is harmonic everywhere in D_1 and V_2 is harmonic everywhere in D_2. Now say we are particularly interested in the properties of V_1^r. By the identity theorem, V_1^r has a unique analytic continuation through the boundary to D_2. This analytic continuation is non-physical; ultimately we do not need to know V_1 in D_2, but D_2 is crucial to image theory as it contains the singularity (or singularities) of V_1^r, guaranteed by Liouville's theorem. D_2 is often termed the "image domain" of V_1^r. With these considerations, we should consider uniqueness and the definition of an image in electrostatics. In general there may be an infinite number of equivalent sources one could place in D_2 which reproduce V_1^r in D_1. These may be point sources, line sources, surface sources, or even volume sources (although these are never practical). Take again the charged conducting sphere – the field outside is equivalent to that created by any concentric conducting sphere with the same charge and smaller radius. These may all be viewed as possible images. In this thesis we will define the *reduced image* as the image which encompasses the smallest domain. In general, any image must spatially encompass the fundamental singularity(s) due to the identity theorem because if the potential created by an image is not identical to the analytic continuation of V everywhere outside its source domain, then it cannot be equal V in *any* open region. For the conducting sphere, the reduced image is the point charge at the center. The reduced image may contain point, line or surface charges, but it must lie on the fundamental singularity(s) of the analytic continuation of the potential V_1.

1.1.5 Complex images

Sometimes the singularity of the potential will not lie at a point or a line in real space. For example an exact solution for an oscillating electric or magnetic dipole near a dielectric plane is to place a semi-infinite image line current in complex space [17, 18, 19]. In electrostatics the problem of a point charge near a wedge may be solved with a complex image [20]. In Section 3.5 we will consider the simple problem of a charged oblate spheroid where the potential is actually equivalent to a charged disk, which is actually finite everywhere. Is this the smallest image that solves the problem? In fact this problem can also be solved by placing a line of charge in complex space, of length equal to the image disk diameter. In some sense this is a more reduced image, since it encompasses less space. This illustrates that the concept of a reduced image depends on whether we restrict ourselves to real space or not. But the potential of any point charge located at (x_0, y_0, z_0) in real or complex space is actually singular on a complex cone, which can be seen from the condition $1/\sqrt{(x-x_0)^2+(y-y_0)^2+(z-z_0)^2}=0$. So if we are to consider multiple complex variables, the picture of charge distributions gets complicated. In this thesis we will mostly restrict ourselves to real space.

1.1.6 Contributions to image theory

Part one of the thesis investigates boundary problems in electrostatics and acoustics to uncover new analytic results for reduced images. Chapter 2 starts with the seemingly simple problem of a point charge located at the center of an infinite conducting cylinder, which is arguably the simplest geometry for which the reduced image system is unknown. For this problem we find an analytic expression for the reduced image location and charge density. The image system is a complicated system of hollow disks which makes an exact image solution impractical, but with knowledge of the reduced image distribution, we derive a simple approximate image solution.

The reduced image for a point charge near a conducting spheroid is another unsolved problem, for which we derive new image solutions in Chapter 3. The standard series solution contains spheroidal harmonics which are singular on the focal segment of the spheroid, but this is not necessarily the nature of the image singularity. For a distant enough source, the image lies exactly on this line segment, while for a source near the surface, the image extends somewhat off the focus, but how exactly is unknown. For the point charge on the spheroid axis, we find that the exact reduced image is a line segment extending somewhat outside the spheroid's focal segment. We also endeavor to find the reduced image of a point charge placed at the center of the spheroid, and find that the image lies on a disk much like the image for the cylinder, being the limit of a long spheroid.

In Chapter 4 we consider a point charge near a dielectric sphere. The known expression for the reduced image is an integral over a radial line segment, but this integral diverges if the sphere's permittivity is less than -1. To reconcile this problem we regularize the integral by adding image multipoles of infinite magnitude.

Then in Chapter 5 we attempt to find the image of an oscillating spherical wave (a point source that changes sign harmonically with time) near a sphere. We derive the low frequency expansion of the image which requires similar regularizations used in the previous chapter, and for a general frequency we apply the Watson series transformation to provide evidence that the reduced image lies on a radial line segment.

1.1.7 Contributions to the T-matrix formalism

Part two of this thesis concerns the T-matrix approach to solving scattering problems for bounded objects. The T-matrix approach for time harmonic scattering usually expresses the incident and scattered fields in terms of spherical wave functions, and the T-matrix itself is the linear transformation that outputs the scattered field series coefficients in terms of the incident coefficients [7, 8]. Normally the T-matrix for a non-spherical scatterer is calculated numerically using the "null field" surface integral equations, but these may be numerically unstable for example in the case of spheroids [21]. In Chapter 6 we derive computationally efficient analytic approximations to the T-matrix for spheroids, that apply in the small-particle limit, relevant to nano-photonics.

The convergence and even existence of the T-matrix depends on both the relationship between the geometry of the scatterer and the geometry of the harmonic basis functions. The T-matrix can be expressed on any basis of harmonic functions, e.g. spherical, cylindrical, spheroidal... and each basis representation has its own properties of existence and convergence. By investigating the T-matrix for different geometries in the electrostatics limit we can obtain analytic expressions which can be used to learn about the convergence problems encountered in full-wave electromagnetic scenarios. One main criteria is the Rayleigh hypothesis that the series for the scattered field converges everywhere outside the particle and on its surface, which is often not true but even in this case the T-matrix may work anyway [22]. There is uncertainty in the field of the exact conditions for the T-matrix to converge or be computable by a particular method – does it converge for non-convex or multiply-connected particles? Image theory is related to this concept in that the field for any scattering problem has intrinsic singularities lying inside the scatterer which can prohibit convergence of a series for the field outside the scatterer. So in Chapters 7 and 8 we investigate the T-matrix for scatterers with interesting topologies: the torus and two sphere system. T-matrices are found in their respective bases of toroidal harmonics and bispherical harmonics. Also for the torus, the T-matrix on a *spherical* harmonic basis is found, and is shown to converge outside the torus, but cannot be used to express the field inside the torus. We also find that for the torus there are four types of T-matrices depending on the source location and region of interest of the scattered field.

1.2 Published works

Most of the work in this thesis has been published or submitted for publication, and there are other papers that I worked on in during the PhD that aren't included in the thesis due a difference of scope.

1.2.1 Works from this thesis

- Chapter 3: Matt Majic, "Image theory for a sphere with negative permittivity", *Journal of Mathematical Physics*, 2019 [23].
- Chapter 5: Matt Majic, Eric C. Le Ru, "Quasistatic limit of the electric-magnetic coupling blocks of the T-matrix for spheroids", *Journal of Quantitative Spectroscopy & Radiative Transfer*, 2018 [24].
- Chapter 7: Matt Majic, "Electrostatic T-matrix for a torus on bases of toroidal and spherical harmonics", *Journal of Quantitative Spectroscopy & Radiative Transfer*, 2019 [25].

1.2.2 Other works from this PhD

- Matt Majic, Baptiste Auguié and Eric C. Le Ru., "Laplace's equation for a point source near a sphere: improved internal solution using spheroidal harmonics" *IMA Journal of Applied Mathematics*, 2018 [26].
  This is an extension of another paper dealing with the external solution - here the image singularity extends out to infinity, and so the spheroidal harmonics are transformed through radial inversion to match this.
- Matt Majic, Luke Pratley, Dmitri Schebarchov, Walter R. C. Somerville, Baptiste Auguié and Eric C. Le Ru, "Approximate T-matrix and optical properties of spheroidal particles to third order in size parameter" *Physical Review A*, 2019 [27].
  This analysed the general scattering problem for a spheroid in the small size limit, Taylor expanding the T-matrix and extending the 'radiative correction' up to third order size parameter.
- Matt Majic, Eric C. Le Ru, "New class of solutions to Laplace equation: Regularized multipoles of negative orders" *Physical Review Research*, 2019 [6].
  The new class of functions dubbed "logopoles" have close links with both spherical and spheroidal harmonics. They were initially studied during my masters, and since then we have redefined them and refined the main concepts.
- Matt Majic, Eric C. Le Ru, "Numerically stable formulation of Mie theory for an emitter close to a sphere" *Applied Optics*, 2020 [28].
  "Normalized Bessel functions" are applied to normalize the Mie coefficients in a way suitable for calculating the series for scattering properties of dipole emitters near the surface of a sphere.
- Matt Majic, "A surface integral approach to Poisson's equation and analytic expressions for the gravitational field of toroidal mass distributions", *Applied Numerical Mathematics*, 2020 [29].
  This work presents an extension of the null-field boundary integral equations for evaluating fields of volume distributions, and derives the gravitational field of a solid torus.

1.3 Notation

Required definitions will be given in each chapter; here is an overview of the commonly used coordinates and functions. The basic orthogonal coordinate systems are:

- Cartesian: x, y, z
- Cylindrical: $\rho = \sqrt{x^2+y^2},\ z,\ \phi = \mathrm{atan2}(y,x)$
- Spherical: $r = \sqrt{x^2+y^2+z^2},\ \theta = \mathrm{acos}\frac{z}{r},\ \phi,$

where atan2 is the arctangent but corrects for different quadrants in the x, y plane so that ϕ increases steadily from 0 to 2π going around the z-axis.
The associated Legendre functions of the first and second kinds appear as solutions to Laplace's equation. They may be defined by the recurrence

$$\begin{aligned}(n-m+1)P_{n+1}^m(u) &= (2n+1)uP_n^m(u) - (n+m)P_{n-1}^m(u)\\ (n-m+1)Q_{n+1}^m(u) &= (2n+1)uQ_n^m(u) - (n+m)Q_{n-1}^m(u)\end{aligned} \tag{1.1}$$

with the initial values for $m = 0$:

$$\begin{aligned}P_0(u) &= 1; \qquad & Q_0(u) &= \frac{1}{2}\ln\left|\frac{u+1}{u-1}\right|\\ P_1(u) &= u; \qquad & Q_1(u) &= uQ_0(u) - 1.\end{aligned}$$

And the functions of any integer order $m \geq 0$ can be defined via

$$P_n^m(u) = |1-u^2|^{m/2}\frac{\mathrm{d}^m P_n(u)}{\mathrm{d}u^m} \tag{1.2}$$

$$Q_n^m(u) = |1-u^2|^{m/2}\frac{\mathrm{d}^m Q_n(u)}{\mathrm{d}u^m} \tag{1.3}$$

for all $u \neq \pm 1$. Some authors multiply by both P_n^m and Q_n^m by $(-)^m$ for $|u| < 1$.

And the external and internal solid spherical harmonics are defined as

$$\begin{aligned}S_n^m &= \left(\frac{a}{r}\right)^{n+1} P_n^m(\cos\theta)e^{im\phi}\\ \hat{S}_n^m &= \left(\frac{r}{a}\right)^{n} P_n^m(\cos\theta)e^{im\phi},\end{aligned} \tag{1.4}$$

where a is some arbitrary length which can be set depending on the geometry of the problem.

Part I

Method of images

Chapter 2

Infinite conducting cylinder

The image of a point charge near an infinite conducting plane is a point charge located exactly opposite, with equal and opposite charge. The image of a point charge inside or near a conducting sphere is again another point charge located at the Kelvin inversion point, with somewhat less charge. But the image of a point charge near or inside an infinite conducting cylinder is previously unknown, and we derive its properties here. The simplest case which we will deal with is for the charge to be placed exactly on the cylinder axis - then there are no variable parameters other than scaling factors. Even in this case we will find that the image is surprisingly complex, consisting of an infinite number of rings on a disk with a complicated surface charge distribution. In particular we manage to prove that the image disk is singular at evenly spaced concentric rings, derive a series expression for the image charge density and find some simple and accurate approximate image solutions. The analysis here will be useful for studying the image of a point charge in a spheroid in the next chapter, since the cylinder is essentially an infinitely long spheroid.

2.1 Problem and series solution

Consider a point charge on the axis of a conducting infinite cylindrical tube radius 1[1], where the total electrostatic potential inside is V. The solution of V is derived in [30], [31], expressed as a series of Bessel functions:

$$V = 2\sum_{n=1}^{\infty} \frac{J_0(k_n\rho)e^{-k_n|z|}}{k_n J_1(k_n)^2} \tag{2.1}$$

where J_0 and J_1 are Bessel functions of the first kind and k_n is the n^{th} zero of J_0. This series accounts for both the point charge and the potential reflected by the cylinder. Physically the solution is only needed inside the

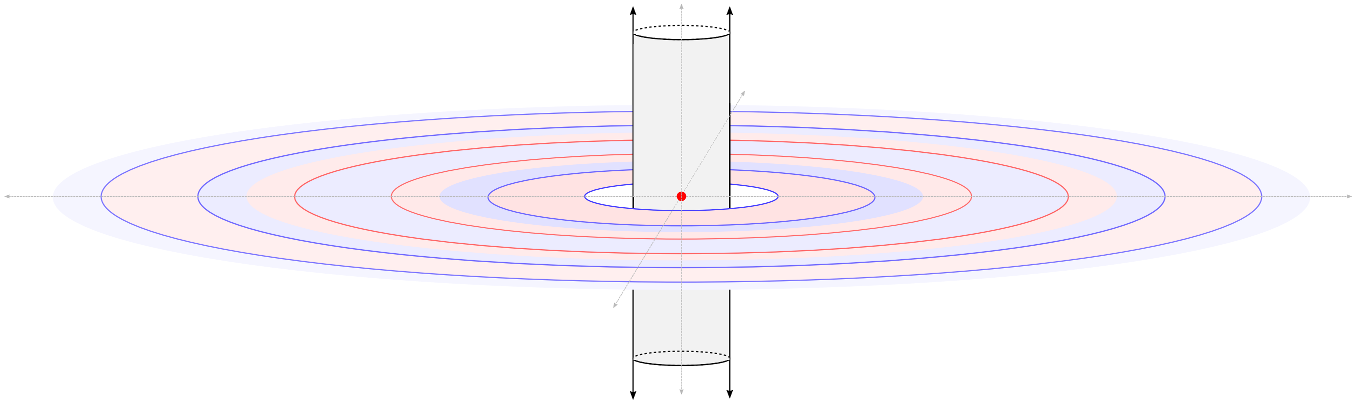

Figure 2.1: Schematic of the source point charge, cylinder and a rough illustration of the image disk, with positive charge in red and negative in blue. The image extends to infinity and has a near-alternating pattern with evenly spaced singular rings.

---

[1] In this chapter we use dimensionless coordinates, but in future chapters the coordinates have dimension.

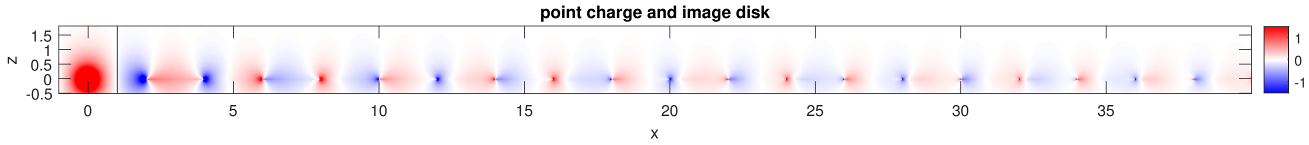

Figure 2.2: A cross section of the potential V showing the source charge and image disk, calculated via series (2.1) with 500 terms, more than necessary to converge to visual accuracy. The black line at $x = 1$ is the cylinder.

cylinder and one simply ignores V outside, but mathematically (2.1) can be evaluated outside for any $z \neq 0$ to reveal the virtual "image" of the point charge. So (2.1) provides the complete analytic continuation of V. A schematic of the cylinder and the general structure of the image is shown in Figure 2.1, and V is plotted more accurately in Figure 2.2 on a cut of the xz plane. The plot required many terms (500) to evaluate due to the series being slowly convergent for small z and conditionally convergent for $z = 0$, meaning the sum of absolute values diverges. The image lies on the disk $\rho \geq 2,\ z = 0$, and also diverges on rings at $\rho = 2, 4, 6, 8\ \ldots$. The singular rings diverge to both positive and negative values on either side, in a different way for each ring. The types of singularity roughly repeat every 4 rings - negative on the inside, negative on the outside, positive on the inside, positive on the outside, repeat. And the charge appears to decay gradually as $\rho \to \infty$.

2.2 Comparison to the two planes problem

The image disk shares a similarity with the image solution for the problem of a point charge at the center of two parallel conducting planes, lying at $z = \pm 1$. For this problem the image is made of point charges located at $z = \pm 2$ with charge -1, $z = \pm 4$ with charge +1, $z = \pm 6$ with charge -1, out to infinity [10]:

$$V_{\text{planes}} = \sum_{k=-\infty}^{\infty} \frac{(-)^k}{\sqrt{\rho^2 + (z - 2k)^2}}. \tag{2.2}$$

These images are shown schematically in Figure 2.3. An alternate approach using cylindrical harmonics was employed in [30] to obtain

$$V_{\text{planes}} = \frac{\pi}{2} \sum_{n=1,\text{ odd}}^{\infty} \cos\left(\frac{n\pi z}{2}\right) K_0\left(\frac{n\pi\rho}{2}\right). \tag{2.3}$$

where K_0 is the modified Bessel function of the second kind. This result can also be obtained from the Watson transformation [32]. This is of a similar form to (2.1), but with different Bessel functions, and the function arguments increasing in integer intervals instead of the zeros k_n – this is to make $V(z = \pm 1) = 0$ on the boundary, where $\cos(\pm n\pi/2) = 0$.

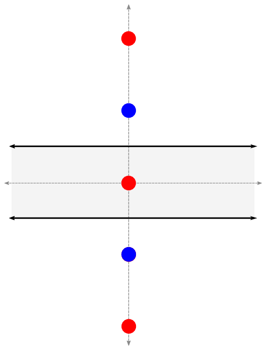

Figure 2.3: Images of a point charge between two planes.

Later we will show that the first order approximation to the cylinder's image rings are actually point charges located at $z = \pm 2i, \pm 4i, \pm 6i\ldots$. So the image disk shares this regular pattern of singularities, but the pattern of ring charges repeats every 4 rings, not every 2, and there is also surface charge between the rings.

In the two planes problem, the image charges can be explained intuitively by considering them two at a time moving outwards. Each image charge induces another image of opposite sign reflected about the plane furthest from it. But this concept does not adapt to the cylinder since there is only one surface.

2.3 Approximation of the series (2.1)

A similar series to (2.1) was encountered in Ref. [33], in computing the velocity field of an axisymmetric jet flow confined to a semi-infinite cylinder. The authors applied Kummer's method of series acceleration - subtracting a similar analytic series whose terms behave the same way as the summation index goes to infinity, so that the remaining series converges faster. We will briefly cover this paper and its technique. They considered a jet confined to $0 \leq \rho \leq 1$ and $z > 0$, and wished to compute for example the axial component of the fluid velocity, which is proportional to the series

$$S_z = 2\sum_{n=1}^{\infty} \frac{J_0(k_n\rho)\cos(k_n z)}{k_n J_1(k_n)}. \tag{2.4}$$

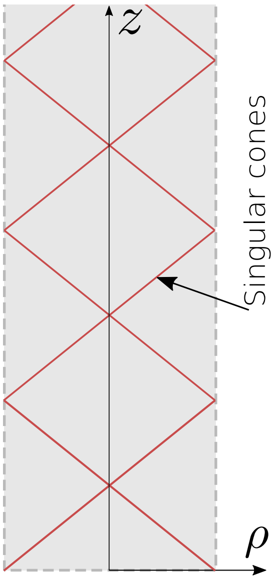

Figure 2.4: Locations of the singularities for a jet flow confined to a semi infinite cylinder.

The terms decrease slowly as $1/n$ so convergence is conditional and nonuniform across both ρ and z, *everywhere* inside the jet - which necessitates a series acceleration technique for practical computation. In fact, the singularities of (2.4) lie in real space - on evenly spaced cone shaped surfaces running along the jet as shown in Figure 2.4. This series differs to our (2.1) by one factor of $J_1(k_n)$ and $e^{-k_n z} \to \cos(k_n z)$, and both series have similar singularities, but in their case they were interested in singularities at integer spaced values of z, not ρ.

The authors of [33] used the following asymptotic formulas for $n \to \infty$:

$$k_n = \left(n - \frac{1}{4}\right)\pi + \frac{1}{8\pi n} + \mathscr{O}(n^{-2}), \tag{2.5}$$

$$J_1(k_n) = \frac{(-)^{n+1}}{\pi}\sqrt{\frac{2}{n-1/4}} + \mathscr{O}(n^{-7/2}), \tag{2.6}$$

$$\begin{aligned} J_0(k_n\rho) = \frac{(-)^n}{\pi}\sqrt{\frac{2}{(n-1/4)\rho}}\Big\{ & \sin[(n-1/4)\pi(\rho-1)] \\ & - \frac{\rho - 1/\rho}{8(n-1/4)\pi}\cos[((n-1/4)\pi(\rho-1)]\Big\} + \mathscr{O}(n^{-5/2}). \end{aligned} \tag{2.7}$$

The series S_z could then be approximated by a simpler trigonometric series related to the Lerch transcendent which could be evaluated analytically. The remainder series converges much faster and is bounded.

We now follow the same approach for our problem to extract the singularities of V. To first order in n the series coefficients behave as

$$2\frac{J_0(k_n\rho)}{k_n J_1(k_n)^2} = (-)^n\sqrt{\frac{2}{(n-1/4)\rho}}\sin[(n-1/4)\pi(\rho-1)] + \mathscr{O}(n^{-3/2}). \tag{2.8}$$

The divergent part of V is then entirely contained within the order $n^{-1/2}$ part, since the remaining series converges as $n^{-3/2}$ which is absolutely convergent (although it still contains discontinuities in the derivative at $\rho = 2,4,6...$ which can be dealt with by considering the next order in the asymptotic expansion). So the poles of V coincide with the poles of a function $\tilde{V}$

$$\tilde{V} = \sum_{n=1}^{\infty}(-)^n\sqrt{\frac{2}{n\rho}}\sin[(n-1/4)\pi(\rho-1)]e^{-(n-1/4)\pi z} \tag{2.9}$$

for $z > 0$. While $\tilde{V}$ does not solve Laplace's equation, it can still be used to determine properties of V. It is clear that $\sqrt{\rho}\tilde{V}$ is periodic in ρ with period 8, and diverges for $\rho = 2,4,6...$ - these are the stationary points where $\sqrt{2}(-)^n\sin[(\rho-1)(n-1/4)\pi] = 1$, which results in the divergent series $\sum_{n\geq 1} n^{-1/2}$. This proves that the singularities of V also lie on $\rho = 2,4,6...$ and follow a repeating pattern every 4 singularities, and decrease in magnitude moving out from the origin as $1/\sqrt{\rho}$ which agrees with the plot in Figure 2.2. To make further deductions, we will rewrite $\tilde{V}$ using an addition formula for the sine function and the polylogarithm of index $\frac{1}{2}$,

$$L_{\frac{1}{2}}(e^{\pi\mu}) = \sum_{n=1}^{\infty}\frac{e^{n\pi\mu}}{\sqrt{n}}, \tag{2.10}$$

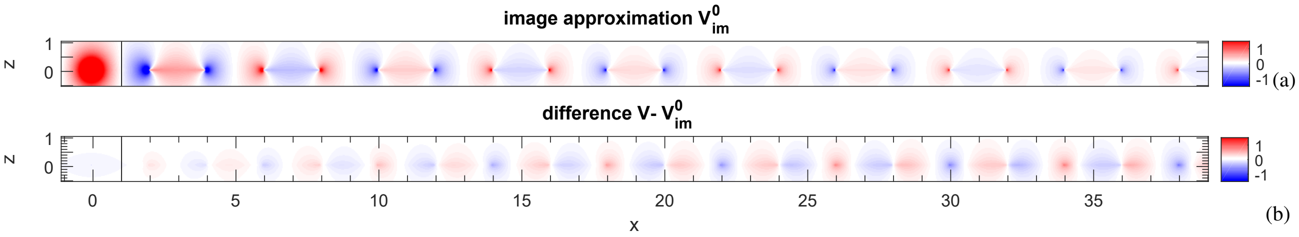

Figure 2.5: (a): the image approximation potential V^0_{im} computed up to $k = 160$ images showing a similar structure to that for V. (b): the difference $V - V^0_{\text{im}}$. The black line at $x = 1$ is the cylinder. The same color scale is used in both plots.

to obtain

$$\tilde{V} = \frac{ie^{(i\rho - i - z)\frac{\pi}{4}}}{\sqrt{2\rho}} \left[e^{i(\rho-1)\frac{\pi}{2}} L_{\frac{1}{2}}(e^{(z-i\rho)\pi}) - L_{\frac{1}{2}}(e^{(z+i\rho)\pi}) \right], \tag{2.11}$$

which is real valued. This form can be used to determine simple analytic approximations for the k^{th} singular ring, by noting the residue series expression for the polylogarithm [34]:

$$L_{\frac{1}{2}}(e^{\pi\mu}) = \sum_{q=-\infty}^{\infty} \frac{1}{\sqrt{2iq - \mu}}. \tag{2.12}$$

For the limit approaching ring k, the terms $q = \pm k$ dominate, leaving

$$\lim_{\substack{\rho \to 2k \\ z \to 0}} \tilde{V} = \lim_{\substack{\rho \to 2k \\ z \to 0}} \frac{i^k}{2\sqrt{k}} \left(\frac{1}{\sqrt{\rho + iz - 2k}} + \frac{(-)^k}{\sqrt{\rho - iz - 2k}} \right). \tag{2.13}$$

In Section 2.4.3 it is shown that a combination of 2 point charges located at $z = \pm 2i$ is an accurate approximation to the first ring. In fact, on the $z = 0$ plane these point charges share the same limit as (2.13) for $k = 1$. From this we can assume that similar point charges can be used to match the singularities for the higher rings. Explicit expressions for these image point charges are

$$V^0_{\text{im},k} = \frac{i^k}{\sqrt{\rho^2 + (z - 2ik)^2}} + \frac{(-i)^k}{\sqrt{\rho^2 + (z + 2ik)^2}}. \tag{2.14}$$

It is straightforward to show that $V^0_{\text{im},k}$ matches the limits in (2.13) for any k. Then summing these together gives an approximation for the potential $V \approx V^0_{\text{im}}$, with

$$V^0_{\text{im}} = \frac{1}{r} + \sum_{k=1}^{\infty} V^0_{\text{im},k}, \tag{2.15}$$

$V^0_{\text{im},k}$ are real valued and singular on the rings but also posses discontinuities on the $z = 0$ plane. In particular, for k even(odd), $V^0_{\text{im},k}$ is discontinuous on the inner(outer) disk $\rho < 2k$ ($\rho > 2k$). So V^0_{im} is discontinuous inside the cylinder and not a practical approximation to V near $z = 0$. In Figure 2.5, V^0_{im} is plotted along with the difference relative to V. While the difference is not negligible, it is finite everywhere. Figure 2.5 (b) shows increasing error for the outer rings, but tests out to $\rho = 1000$ indicate that the error does eventually decrease, consistent with the approximation (2.9) becoming more accurate as $\rho \to \infty$.

By comparing the series for V^0_{im} to the image series solution for the two planes problem (2.2), and noting that this is also equal to the Bessel series (2.3), we can derive with some algebra the following Bessel series for V^0_{im}:

$$V^0_{\text{im}} = \pi \sum_{n=1}^{\infty} J_0((n - 1/4)\pi\rho) e^{-(n-1/4)\pi|z|} \tag{2.16}$$

which more closely resembles the series (2.1), with nonuniform convergence as $n^{-1/2}$ for $z = 0$. This series has the same asymptotic limit as $n \to \infty$ as the series for both V and $\tilde{V}$.

2.4 More solutions and approximations

There are other solutions to this problem involving different basis functions which can be used to derive approximations.

2.4.1 Integral solution

The integral solution involves splitting the potential into $V = V_e + V_r$ where V_e is the excitation of the point charge and V_r is reflected by the cylinder. V_e can be expressed as an integral of cylindrical harmonics:

$$V_e = \frac{1}{r} = \frac{2}{\pi}\int_0^\infty K_0(t\rho)\cos(tz)\mathrm{d}t, \tag{2.17}$$

where I_0 and K_0 are the modified Bessel functions of the first and second kinds. V_r is constructed to fit the boundary condition $V = 0$ at $\rho = 1$ [31]:

$$V_r = -\frac{2}{\pi}\int_0^\infty \frac{K_0(t)}{I_0(t)} I_0(t\rho)\cos(tz)\mathrm{d}t. \tag{2.18}$$

The integrand is finite except at $t \to 0,\ t \to \infty$, so we can determine the physical domain where this integral converges by analysis of the behavior of the integrand near the end points. The Bessel functions behave as

$$I_0(t \to 0) \to 1 \tag{2.19}$$

$$K_0(t \to 0) \to \log\frac{1}{t} \tag{2.20}$$

$$I_0(t \to \infty) \to \frac{e^t}{\sqrt{2\pi t}}\left(1 + \frac{1}{8t}\right) \tag{2.21}$$

$$K_0(t \to \infty) \to e^{-t}\sqrt{\frac{\pi}{2t}}\left(1 - \frac{1}{8t}\right). \tag{2.22}$$

Then as $t \to \infty$ the integrand behaves as $e^{(\rho-2)t}/\sqrt{t}$ and converges for $\rho < 2$, independent of z, which is inside a cylindrical boundary of twice the radius of the physical cylinder. This is consistent with the image having its innermost ring at $\rho = 2$.

2.4.2 Spherical series solution

The integral solution may be transformed into a series of solid spherical harmonics, which will then be useful to determine approximations to V_r. The coefficients can be obtained via the following expansion relating cylindrical and spherical harmonics:

$$I_0(t\rho)\cos(tz) = \sum_{n=0:2}^{\infty} \frac{(itr)^n}{n!} P_n(\cos\theta), \tag{2.23}$$

where the notation $n = 0:2$ means n increases in steps of 2. Substituting (2.23) into the integral (2.18) and rearranging gives

$$V_r = -\sum_{n=0:2}^{\infty} h_n \left(\frac{ir}{2}\right)^n P_n(\cos\theta), \tag{2.24}$$

where

$$h_n = \frac{2^{n+1}}{\pi n!}\int_0^\infty \frac{K_0(t)}{I_0(t)} t^n \mathrm{d}t. \tag{2.25}$$

Note that in [31, 35], a different expression for h_n is derived, which is equivalent through partial integration and applying the Wronskian $I_0(t)K_0'(t) - I_0'(t)K_0(t) = -1/t$.

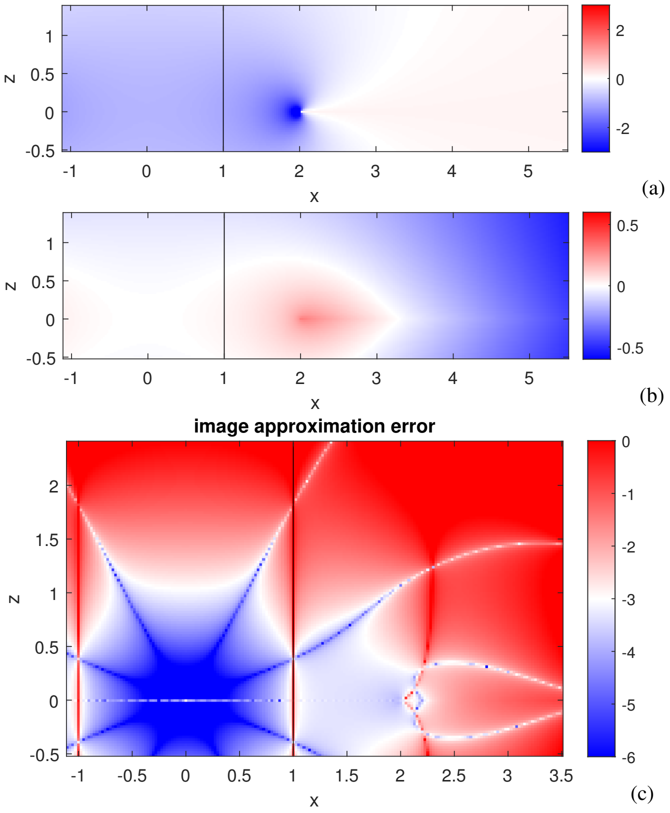

Figure 2.6: (a): approximation $V^{(0)}$, (b): correction $V^{(1)}$, (c): $\log_{10}$ of the relative error $(V^{(0)}+V^{(1)}-V)/V$.

2.4.3 A first order approximation

From the spherical series solution (2.24) we can find a simple approximation that happens to match the image well. The integrand of (2.25) may be expanded for $t \to \infty$ as:

$$\frac{K_0(t)}{I_0(t)}t^n \to \pi\left(1-\frac{1}{4t}+\mathcal{O}(t^{-2})\right)e^{-2t}t^n, \tag{2.26}$$

which also is fairly accurate for small t. Because of the factor t^n, as $n \to \infty$ the contributions in the integral only come from large t. This approximation leads to $h_{n\to\infty} \to 1-\frac{1}{2n}$.

The zeroth order approximation has $h_n \approx 1$. The first two terms for $n = 0,2$ are however not well represented by this approximation so should be subtracted and the exact terms with $h_0 \approx 0.8706901$ $h_2 \approx 0.8236450$ and added on explicitly:

$$\begin{aligned} V^{(0)} &= -\sum_{n=4:2}^{\infty}\left(\frac{r}{2i}\right)^n P_n(\cos\theta) - h_0 - h_2 r^2 P_2(\cos\theta) \\ &= \frac{i}{\sqrt{\rho^2+(z+2i)^2}} - \frac{i}{\sqrt{\rho^2+(z-2i)^2}} + 1 - h_0 - \left(\frac{1}{4}-h_2\right) r^2 P_2(\cos\theta), \end{aligned} \tag{2.27}$$

which is two point charges located at $z = \pm 2i$ that appear in $V^0_{\mathrm{im},1}$ (Eq. (2.14)), plus smooth terms. $V^{(0)}$ is real, singular at $\rho = 2,\ z = 0$ and discontinuous across $\rho \geq 2,\ z = 0$, as seen in Figure 2.6 (a), with surface charge $4/(\rho^2-4)^{3/2}$. Just like $V^0_{\mathrm{im}1}$, $V^{(0)} - V$ is finite at the innermost ring. This approximation was also derived in [31] but with the wrong prefactor and without correction of the $n = 0,2$ terms.

For the first order correction again we take off the $n = 2$ term:

$$\begin{aligned} V^{(1)} &= \sum_{n=4:2}^{\infty}\frac{1}{2n}\left(\frac{r}{2i}\right)^n P_n(\cos\theta) \\ &= \frac{1}{2}\mathrm{Re}\left\{\log\frac{2}{2-iz+\sqrt{-\rho^2-(z+2)^2}}\right\} + \frac{1}{16}r^2 P_2(\cos\theta). \end{aligned} \tag{2.28}$$

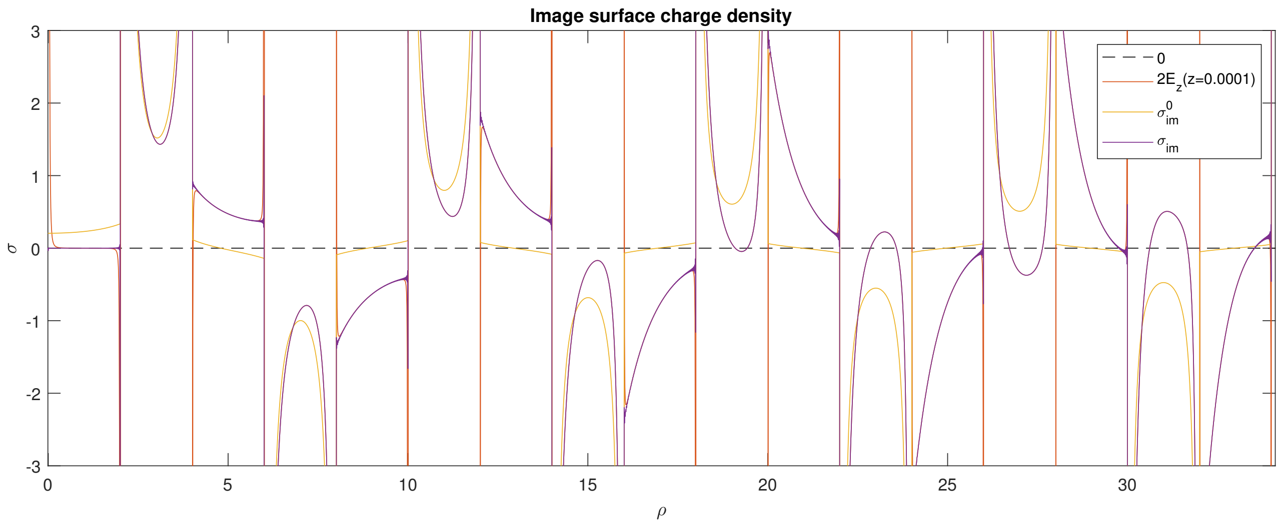

Figure 2.7: The surface charge density σ_{im} compared to the approximation σ^0_{im} and the electric field E_z evaluated at $z = 0.0001$. E_z and σ_{im} are computed with 20,000 terms in the Bessel series (2.29) and (2.32), while σ^0_{im} is computed with 80 terms in the series (2.30), enough to converge to visible accuracy.

This is also discontinuous across $\rho \geq 2,\ z = 0$. The logarithm can be derived from a coordinate transformation applied to the expansion of a similar function in [36]. $V^{(1)}$ has a positive surface charge density of $1/\sqrt{\rho^2 - 4}$ on the disk $\rho \geq 2, z = 0$, but also consists of negative charge at $r \to \infty$ so that even on the disk the potential can be negative, as seen in Figure 2.6 (b). The potential is finite everywhere even at $\rho = 2, z = 0$, but diverges logarithmically as $r \to \infty$.

The approximation $V^{(0)} + V^{(1)}$ is very accurate for $|z| \lesssim 1.5$, as shown in Figure 2.6 (c). Numerical evidence suggests that difference $V_r - (V^{(0)} + V^{(1)})$ and its low order derivatives at least are continuous across the innermost image ring.

This seems to be the extent of these image approximations since this expansion of h_n about $n \to \infty$ appears to not match well for small n. Already in our approximation we have had to correct for $n = 0, 2$, and more corrections are likely needed for higher orders if continuing in this fashion. And unfortunately adding similar terms for the next ring at $\rho = 4$ only degrades the approximation - as noted before $V^0_{\mathrm{im},2}$ is discontinuous across the middle of the cylinder.

2.5 Image surface charge density

To complete the description of the image disk, we must determine its charge distribution. The surface charge is equivalent to the discontinuity in the electric field component $E_z = -\partial_z V$ across $z = 0$. Since the series for E_z at $z = 0$ actually diverges – the terms increase as $\sqrt{n}$ – we must instead consider the limit:

$$\sigma_{\mathrm{im}} = 2 \lim_{z \to 0} E_z = -\lim_{z \to 0} 4 \sum_{n=1}^{\infty} \frac{J_0(k_n \rho) e^{-k_n z}}{J_1(k_n)^2}. \tag{2.29}$$

In order to calculate this limit, we can modify the series using Kummer acceleration - subtract off an analytically known term that has a similar series expansion, so that the difference of the two series coefficients decreases faster as $n \to \infty$. We will in fact subtract off the surface charge density of the approximation V^0_{im}. This can be obtained from (2.15):

$$\sigma^0_{\mathrm{im}} = 8 \sum_{k=1}^{\infty} \Re \left\{ \frac{i^k k}{(4k^2 - \rho^2)^{3/2}} \right\} \tag{2.30}$$

Note that the direct substitution of $z = 0$ in the z-derivative of (2.14) leads to a different branch cut, while (2.30) provides the correct limit – thanks to Carlo Beenakker on MathOverflow for this. And Eq. (2.30) is equivalent

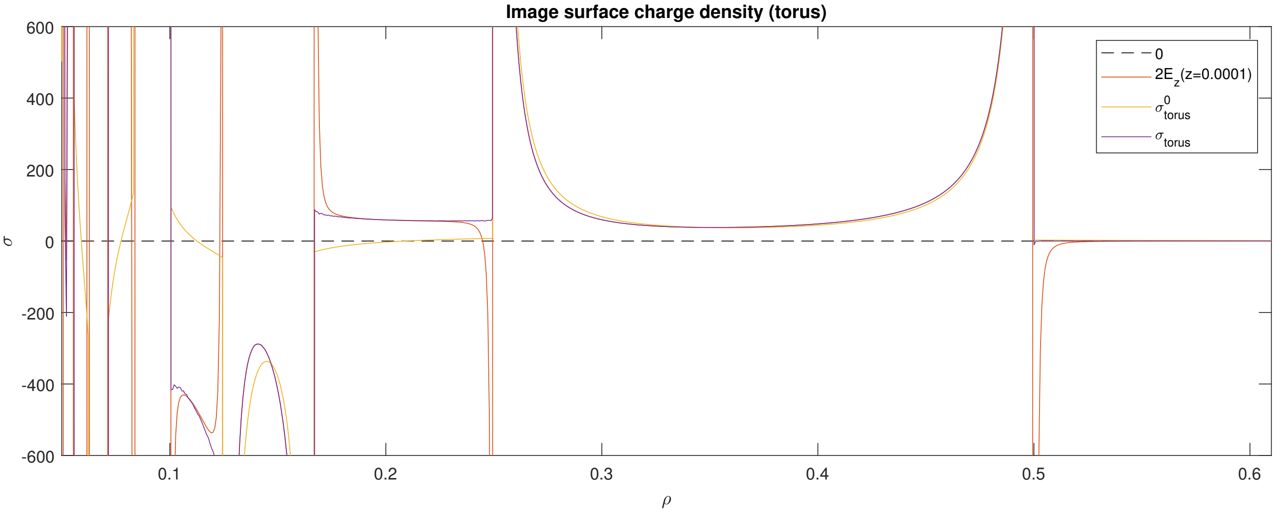

Figure 2.8: The surface charge density σ_{torus} compared to the approximation σ^0_{torus} and the electric field E_z evaluated at $z = 0.0001$. E_z and σ_{torus} are computed with 50,000 terms in the Bessel series (2.34) and (2.36), while σ^0_{torus} is computed with 500 terms in the series (2.35), enough to converge to visible accuracy. The plot is truncated at $x = 0.05$ since the information for $x < 0.05$ is illegible.

to the Bessel series (2.16):

$$\sigma^0_{\text{im}} = -\lim_{z\to 0} 2\pi^2 \sum_{n=1}^{\infty} J_0((n-1/4)\pi\rho)e^{-(n-1/4)\pi z} \tag{2.31}$$

which is again divergent for $z = 0$, with terms increasing as $\sqrt{n}$. In fact, as $n \to \infty$, the series coefficients in (2.29) and (2.31) have the same leading order, while their difference goes as $1/\sqrt{n}$, which converges (slowly). Combining Eqs. (2.29), (2.30) and (2.31) then gives the following convergent expression for the image surface charge:

$$\begin{aligned}\sigma_{\text{im}} &= \sigma^0_{\text{im}} - 2\lim_{z\to 0}\partial_z(V - V^{(0)}) \\ &= \sigma^0_{\text{im}} - 2\sum_{n=1}^{\infty}\left(2\frac{J_0(k_n\rho)}{J_1(k_n)^2} - \pi^2(n-1/4)J_0((n-1/4)\pi\rho)\right)\end{aligned} \tag{2.32}$$

which converges except at the rings $\rho = 2, 4, 6, 8...$, and is plotted in Figure 2.7 with comparison to both the approximation (2.30) and the numerical limit of (2.29), that is $2E_z$ for a very small value of $z = 0.0001$. All three show a similar pattern - diverging U shaped regions of alternating sign, with relatively smooth regions in between, which become steeper as ρ increases. For the region $0 < \rho < 2$, σ_{im} is zero, while σ^0_{im} is small but finite in this region (V^0_{im} is discontinuous there). This surface charge is represented schematically in Figure 2.1 with blocks of color matching sign.

2.6 Comparison to 2D problem

The 2D analogue of our problem is an infinite line charge at the center of the cylinder. The solution to this problem is simply $V_{\text{r,line}} = -\log\rho$ because it is logarithmically infinite at the line charge and zero on the cylinder surface at $\rho = 1$. The image actually resides at $\rho = \infty$. How do we reconcile this with the image for the point charge which is singular at $\rho = 2$? The line charge is the limit of an infinite number of point charges on the z-axis, and the potentials of different sources add, so we might naively expect the line to also have an image at $\rho = 2$. An intuitive explanation for this is that the line charge is thinned out, since the total charge is spread over an infinite line. The same then applies to the image; if we were to construct the image of the line charge from the image of the point charge, we would spread the rings and disks along the z-axis to become cylindrical surfaces with volume charge in between. But since the surface of the inner image cylinder at $\rho = 2$ is closed, it can be analytically continued through to reveal a more distant image, in this case all the way to $\rho = \infty$.

2.7 Charged tight torus

The problem of a point charge at the center of a cylinder has a one to one correspondence with the potential of a charged conducting tight torus in free space. This is realized through radial inversion/ Kelvin transform, the transformation $r \to 1/r$, which takes the outside of the cylinder to the inside of the torus. The potential transforms as $V(r,\theta,\phi) \to 1/r\, V(1/r,\theta,\phi)$, and by applying this transformation to (2.1) gives

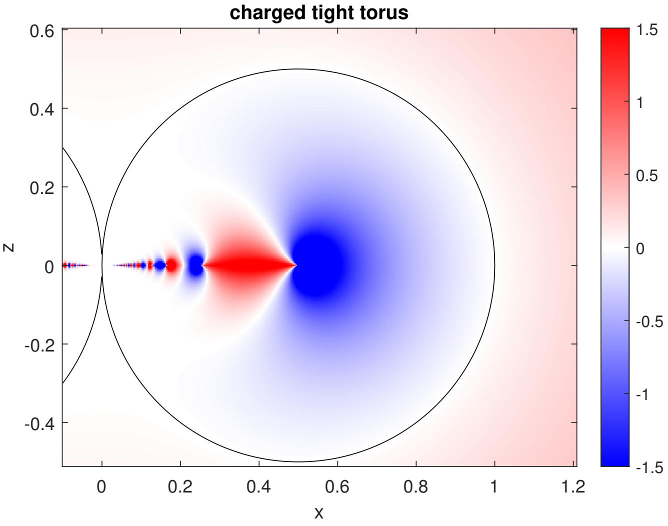

Figure 2.9: Analytic continuation of the potential of a charged conducting tight torus as computed by (2.33).

$$V_{\text{torus}} = \frac{2}{r}\sum_{n=1}^{\infty} \frac{J_0(k_n(\rho/r^2)e^{-k_n|z|/r^2}}{J_1(k_n)^2}. \tag{2.33}$$

which is plotted in Figure 2.9, and reveals a singular disk for $\rho < 1/2$ - we will call this singularity the 'image' of the torus in free space. The Kelvin transform modifies the location of the image by $\rho \to 1/\rho$, so that the image of the torus lies on the disk $\rho < 1/2$, $z = 0$ with singular rings located at $\rho = 1/2, 1/4, 1/6 \ldots$. To calculate the corresponding image surface charge density σ_{torus}, we need the limit of the electric field approaching $z = 0$:

$$\sigma_{\text{torus}} = 2\lim_{z\to 0} E_z = -\lim_{z\to 0}\sum_{n=1}^{\infty} \frac{4e^{-k_n|z|/r^2}}{r^5 k_n J_1(k_n)^2}\left((k_n(\rho^2-z^2)+|z|r^2)J_0(k_n\rho/r^2) - 2k_n|z|\rho J_1(k_n\rho/r^2)\right), \tag{2.34}$$

but as for the cylinder, the series diverges for $z = 0$ (the terms increase as $\sqrt{n}$), so we follow the above approach of taking the difference of two diverging series – subtracting off a function σ^0_{torus} which has a Bessel series of similar form to σ_{torus}, but which has an alternate form which is well defined analytically. Such a function is

$$\sigma^0_{\text{torus}} = \frac{1}{\rho^3}\sum_{n=1}^{\infty} 2\pi^2(n-1/4)J_0((n-1/4)\pi/\rho) = 4\sum_{k=1}^{\infty}\Re\left\{\frac{i^k/(2k)^2}{(\rho^2-1/(2k)^2)^{3/2}}\right\}, \tag{2.35}$$

which is in some sense a zeroth order approximation to the image charge distribution. The left series diverges at the same rate as (2.34), but is equivalent to the series on the right which converges. Their equivalence can be seen through similar manipulations used to derive (2.15). So a convergent expression for σ_{torus}, with terms decrease as $1/\sqrt{n}$, is

$$\sigma_{\text{torus}} = \sigma^0_{\text{torus}} + \frac{1}{\rho^3}\sum_{n=1}^{\infty} 4\frac{J_0(k_n/\rho)}{J_1(k_n)^2} - 2\pi^2(n-1/4)J_0((n-1/4)\pi/\rho). \tag{2.36}$$

This is plotted in Figure 2.8, showing close agreement with the electric field evaluated at $z = 0.0001$, except near the singular rings. This discrepancy has been checked to decrease as $z \to 0$ as it should. The magnitude of σ_{torus} is far higher than for the cylinder, but the surface area is also much smaller.

For more analysis on the tight torus, see [37]. The image for a non-tight torus in free space is not known [38], and maybe this solution can provide a starting point. Also, the convergence of the T-matrix for the torus in Chapter 7 depends on the location of this singularity.

2.8 Eccentric point charge

For a point charge located at $\rho = \rho_0$ with azimuthal angle $\phi = 0$, the solution as a series of Bessel functions is derived in [31, 39] to be (correcting a typo in [31] eq. 42):

$$V_{\text{eccentric}} = 2\sum_{m=0}^{\infty}\sum_{n=1}^{\infty}(2-\delta_{m0})\frac{J_m(k_{nm}\rho_0)J_m(k_{nm}\rho)}{k_{nm}J_{m+1}(k_{nm})^2}\cos(m\phi)e^{-k_{nm}|z|}, \tag{2.37}$$

where k_{nm} is the n^{th} zero of J_m. This formula converges everywhere except on $z = 0$ where convergence is non-uniform (dependent on x and y). $V_{\text{eccentric}}$ is plotted on the plane $z = 0$ in Figure 2.10 to reveal the image structure, which is extremely complicated, consisting of distorted rings which overlap chaotically.

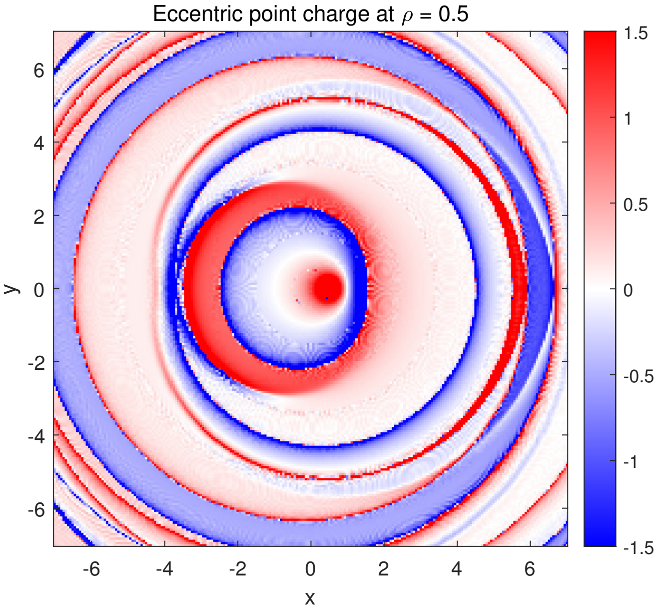

Figure 2.10: Potential for an eccentric point charge at $x = 0.5$, $y = 0$, in a conducting cylinder of radius 1. $V_{\text{eccentric}}$ was computed up to $m = 90$ and $n = 340$, enough to converge to reveal the main features of the image, but with some noise.

2.9 Conclusion

We have investigated the image of a point charge at the center of a conducting cylinder and found an exact expression for the image surface charge, (2.32).

We also derived a simple and accurate approximation (2.27) which matches the inner ring of the image, which corrects an approximation given in Ref. [31]. We then derived the next order term (2.28), and demonstrated the accuracy of (2.27)+(2.28), which may be attributed to the similar singularities of this approximation and the singularity of the image (2.32).

By applying the Kelvin transformation, we also derived the image charge distribution of a conducting tight torus, (2.36).

This analysis should extend to finite cylinders by taking copies of the image disks and repeating them at discrete heights along the z-axis, just as done for the point charge between two parallel planes. And in fact the Bessel series solution for a spherical acoustic wave in the cylinder is mot much more complicated and converges for $z \neq 0$. So it may be possible to extend the results in this chapter to the Helmholtz equation.

Chapter 3

Conducting spheroid

The interaction of a point source near a nano-particle is prevalent in photonics and Raman spectroscopy, and the spheroid is of interest to study being the simplest non-spherical particle. The first exact formulation of the image of a point charge on the axis of a spheroid was in 1995 - partial success was found in [40] where the image consisted of a line charge lying on the focal segment. A later investigation of the image solution for the elliptic cylinder [41] revealed that the image lies on a focal strip, but if the source is close enough, a disjoint point image must be added to the image system. In fact the potential computed by this image system gives the full analytic continuation of the potential. In this sense the image is “reduced”, meaning the singularities encompass the smallest possible spatial domain. But for the spheroid, the authors of [40] later realized that the series expression for the image charge density diverges when the point charge is too close to the surface [42], and attempted to amend the image solution by subtracting an image point charge. This point charge is a good approximation, but unlike the case of the elliptic cylinder, the series for the charge density of this proposed image system still diverges, just slower. The authors later studied the same problem for the *dielectric* spheroid [43] and tried an approximate correction by subtracting an approximate image line segment extending from the focal segment up to the location of the point image, to imitate the line image for the dielectric sphere. But again the remaining series for the charge distribution still diverges, due to an incorrect assumption of its domain. For the non-rotational ellipsoid, the first proposed image solution consisted of a point charge plus a surface charge on an interior ellipsoid [44]. This image formulation was then presented for the particular case of the prolate spheroid in [45]. But the spheroidal surface charge image cloaks the true form of the image lying inside; the potential is actually finite at all but one point of the surface image, so it is theoretically possible to analytically continue the potential within this boundary. For the non-rotational ellipsoid with *Neumann boundary condition*, the first attempt at finding an image solution is in [46], where they assumed a point image plus a curved line of image charge extending along a spheroidal coordinate line, but they still needed to correct for this by adding a surface charge on an ellipsoidal surface that encloses the point and line image. This image formulation is specialized for the prolate spheroid in [47].

This chapter looks at the reduced form of the image of a point charge near or inside a conducting spheroid, and compare these problems to similar geometries - the elliptic cylinder and the circular disk. We cover the progress made by [42] for the point charge on the axis of a prolate spheroid, and devise a series expansion that uncovers the true form of the image, and explain why their expression for the line charge density diverges. We also investigate the similar problem of a point charge at the center of a prolate spheroid, finding numerical evidence that the reduced image lies on an infinitely wide, flat sheet with a hole around the spheroid. We finally ask what it means for an image to be unique, and show a specific example where two fairly disjoint different image solutions can solve the same problem.

The goal here is not necessarily to find a fast and accurate approximation of a potential function, but to find its analytic continuation by any means. With knowledge of the location and charge distribution on the fundamental singularities, it may be possible to construct efficient approximate solutions.

3.1 Elliptic cylinder - 2D analogue

For context we will first look at the 2D analogue of our spheroid problem, where it is possible to find the exact form of the image [41]. In this problem there is an infinite uniform line charge parallel to an infinitely long elliptic cylinder in 3D, but due to the uniformity along one coordinate, the problem is essentially 2D.

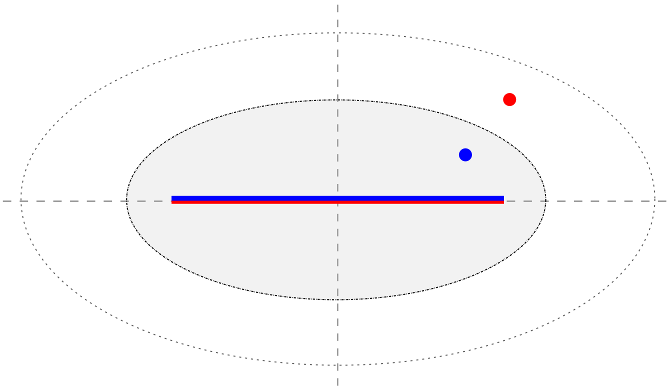

Figure 3.1: schematic of the image solution for a line charge near a 2d elliptic cylinder.

The elliptic coordinates ξ, η are analogous to spheroidal coordinates, with the parameter ξ describing concentric ellipses. The conducting or dielectric elliptic cylinder is defined by $\xi = \xi_0$, and the line charge lies outside at ξ_d, η_d. The standard solution is given by a series of elliptic cylindrical harmonics, which are simply trigonometric and exponential functions. In terms of the image representation, there is a critical ellipse $\xi = 2\xi_0$, where if the source lies outside, i.e. $\xi_d > 2\xi_0$, the image charge distribution then lies entirely on the focal strip, and the image surface distribution is given as a series of trigonometric functions. But for a close source with $\xi_d < 2\xi_0$, the image system has two disjoint parts - a focal strip image plus a point image at $2\xi_a - \xi_d, \eta_d$, as depicted in Figure 3.1. The potential of these images represents the analytic continuation of the reflected potential by the cylinder to all space. The image formulation for a spheroid is not so simple.

3.2 Point charge on axis of conducting prolate spheroid

Consider a conducting prolate spheroid of half-focal length f, half-height c and half-width $a = \sqrt{c^2 - f^2}$, excited by a point charge located at d on the z-axis, as depicted in Figure 3.2. We will use spheroidal coordinates ξ, η:

$$\xi = \frac{\sqrt{\rho^2 + (z+f)^2} + \sqrt{\rho^2 + (z-f)^2}}{2f} \tag{3.1}$$

$$\eta = \frac{\sqrt{\rho^2 + (z+f)^2} - \sqrt{\rho^2 + (z-f)^2}}{2f}, \tag{3.2}$$

so that the boundary of the spheroid is simply $\xi = \xi_0 = c/f$. The exciting potential is

$$V_{\mathrm{e}} = \frac{c}{\sqrt{\rho^2 + (z-d)^2}} = \sum_{n=0}^{\infty} (2n+1) Q_n(\xi_d) P_n(\xi) P_n(\eta). \qquad \xi < \xi_d \tag{3.3}$$

The boundary condition is $V = 0$ at $\xi = \xi_0$, where $V = V_{\mathrm{e}} + V_{\mathrm{r}}$ is the total potential outside the spheroid and V_{r} is the reflected potential. Using standard techniques, V_{r} is found to be

$$V_{\mathrm{r}} = -\sum_{n=0}^{\infty} (2n+1) \frac{P_n(\xi_0)}{Q_n(\xi_0)} Q_n(\xi_d) Q_n(\xi) P_n(\eta). \tag{3.4}$$

where $\xi_d = d/f$. We will now investigate the analytic continuation of the series (3.4) inside the spheroid.

3.2.1 Summary of progress in [42] - zeroth order approximation

The Legendre functions behave for large n as

$$P_n(x) \to \sqrt{\frac{1}{2n\pi}} \frac{(x + \sqrt{x^2-1})^{n+1/2}}{(x^2-1)^{1/4}} \left[1 + \frac{1}{8n} \left(\frac{x}{x^2-1} - 2 \right) + \mathscr{O}(n^{-2}) \right] \qquad |x| > 1 \tag{3.5}$$

$$Q_n(x) \to \sqrt{\frac{\pi}{2n}} \frac{(x + \sqrt{x^2-1})^{-n-1/2}}{(x^2-1)^{1/4}} \left[1 - \frac{1}{8n} \left(\frac{x}{x^2-1} + 2 \right) + \mathscr{O}(n^{-2}) \right] \qquad |x| > 1 \tag{3.6}$$

which are modified first order expressions from [48]. Then the terms in the series (3.4) behave to zeroth order for large n as

$$\frac{P_n(\xi_0)}{Q_n(\xi_0)}Q_n(\xi_d) = \frac{1}{\sqrt{2\pi n}(\xi_d^2-1)^{1/4}}\left(\frac{\left(\xi_0+\sqrt{\xi_0^2-1}\right)^2}{\xi_d+\sqrt{\xi_d^2-1}}\right)^n\left[1+\mathscr{O}(n^{-1})\right]. \tag{3.7}$$

If the point source is further than a critical distance, $d > d_c$ where

$$d_c = 2\frac{c^2}{f} - a, \tag{3.8}$$

then the series converges in all space except the focal segment, and the corresponding image may be expressed as a series using the Havelock formula for the prolate spheroidal harmonics.

The corresponding image line charge distribution λ can be found by applying the Havelock formula, which essentially expresses each spheroidal harmonic in terms of a distribution of line charge on the focal segment:

$$\lambda(z) = -\frac{1}{2}\sum_{n=0}^{\infty}(2n+1)\frac{P_n(\xi_0)}{Q_n(\xi_0)}Q_n(\xi_d)P_n(z/f), \qquad |z| < f \tag{3.9}$$

which converges if $d > d_c$.

But for $d < d_c$, the series (3.4) diverges inside the spheroid $\xi < \xi_h$ where

$$\xi_h = (2\xi_0^2-1)\xi_d - \xi_0\sqrt{\xi_0^2-1}\sqrt{\xi_d^2-1}. \tag{3.10}$$

This is shown schematically in Figure 3.2, where the spheroidal series diverges inside the inner spheroid.

To work around this, the authors noted that the leading asymptotic order of the series terms in (3.4) is similar to that for the spheroidal harmonic expansion of a point charge at $z = h$:

$$V^{(0)} = \frac{q_h f}{\sqrt{\rho^2+(z-h)^2}}, \tag{3.11}$$

$$= q_h\sum_{n=0}^{\infty}(2n+1)P_n(\xi_h)Q_n(\xi)P_n(\eta), \tag{3.12}$$

$$\text{where} \quad q_h = -\sqrt[4]{\frac{h^2-f^2}{d^2-f^2}}.$$

This is the blue dot in Figure 3.2. Then (3.12) was extracted from the series (3.4) so that the remaining series converged faster:

$$V \equiv V' = V_\mathrm{e} + V^{(0)} - \sum_{n=0}^{\infty}(2n+1)\left(\frac{P_n(\xi_0)}{Q_n(\xi_0)}Q_n(\xi_d) + q_hP_n(\xi_h)\right)Q_n(\xi)P_n(\eta). \tag{3.13}$$

However, the authors incorrectly assumed that the remaining image lies on the focal segment, and attempted to write down the image charge density on this strip as:

$$\lambda(z) \neq -\frac{1}{2}\sum_{n=0}^{\infty}(2n+1)\left(\frac{P_n(\xi_0)}{Q_n(\xi_0)}Q_n(\xi_d) + q_hP_n(\xi_h)\right)P_n(z/f), \qquad |z| < f \tag{3.14}$$

But the terms increase exponentially as $n \to \infty$, so the series diverges. They state that this series is asymptotic, initially converging then diverging, but it could not converge to any meaningful distribution since, as we will see, the analytic continuation of the potential is actually singular in a region off this focus too. No charge distribution can produce a singularity outside its support. Perhaps one could argue that the image is still valid in some sense because it can be represented by a series of spheroidal harmonics which converges for $\xi > \xi_h$, but then nothing is gained from this "image" representation since it is only useful to reproduce the series it was obtained from in the first place.

[1]

---

[1] Note that in [42] there is a minor error in stating that the requirement that $h > f$ (image charge lying off the focal segment) is equivalent to $d < d_c$. But in fact $h > f$ and is real regardless of $d < d_c$, as shown in Figure 3.3. Although it can happen that $h > c$ for some much larger d. The same for q_h - it is still real for $d > d_c$. Nevertheless, there is no point in extracting an image point charge at $z = h > f$ when the image lies entirely on the focal segment anyway. (In their notation $c \leftrightarrow a$, $f \to c$ and $d_c \to d_o$.)

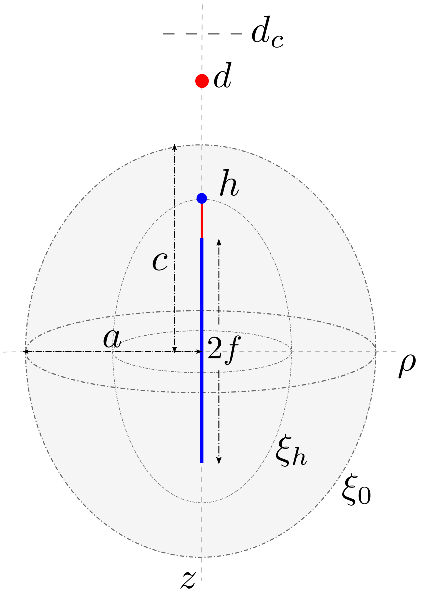

Figure 3.2: Schematic of the problem of a point charge near a prolate spheroid, showing the extended image singularity in the case of a close source charge. Red represents positive charge and blue negative.

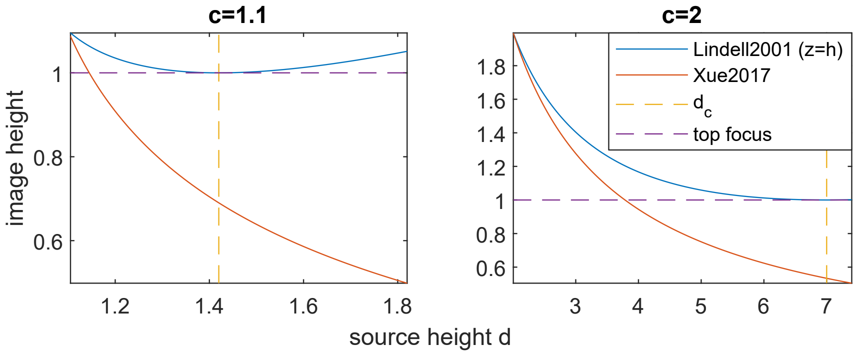

Figure 3.3: Comparison of the height h of the image point charge in [42] to that from [45]. The height is plotted as a function of the source charge height d, for two spheroids of very different aspect ratio. The top of the focal segment lies at $f = 1$, and d_c is the critical height for the source charge - the blue line is only used for $d < d_c$.

3.2.2 Comparison to approach in [45]

In [45] the authors separated out a different image point charge, but in this case its location and charge were chosen so as to cancel out just the $n = 0$ and $n = 1$ terms of the series (3.4) exactly.As shown in Figure 3.3, the height of the image charge in [45] decreases faster towards the center of the spheroid, and may even lie on the focal segment, unlike the point image from [42]. This is a good approximation in cases where the spheroidal series converges very quickly so that the first two terms are dominant, but from the point of view of analytical continuation, but this point charge does not appear in the reduced image.

3.2.3 Analytic continuation of the potential for close source charges

For point sources within the critical distance $d < d_c$, the potential diverges within the spheroid $\xi < \xi_h$, which extends along the z-axis to $z = \pm h$. We will make the intuitive guess that V is singular on the z-axis from $z = -f$ to h, shown in Figure 3.2; there seems no reason why the image would have to extend to $z < -f$, when the image should concentrate towards the top surface as the source comes very close, mimicking the image solution for the plane. And it is a fair assumption that the image lies on the axis, since this is the case for $d > d_c$, as seen in the previous section.

So we'll define a 'stretched' prolate coordinate system whose focal segment lies on the z-axis from $z = -f$

to h, exactly on the proposed singularity:

$$\bar{\xi} = \frac{\sqrt{\rho^2+(z+f)^2}+\sqrt{\rho^2+(z-h)^2}}{f+h} \tag{3.15}$$

$$\bar{\eta} = \frac{\sqrt{\rho^2+(z+f)^2}-\sqrt{\rho^2+(z-h)^2}}{f+h}, \tag{3.16}$$

with the goal of expressing V_{r} as a series of the corresponding spheroidal harmonics. There should be no reason for such a series to diverge anywhere except on this singularity.

In order to find such a series, we can use the transformations between spheroidal and spherical harmonics, first transforming the series in to a sum of spherical harmonics, with the following transformation [26]:

$$Q_n(\xi)P_n(\eta) = \sum_{p=n}^{\infty} \frac{p!^2}{2(p-n)!(p+n+1)!}\left(\frac{2f}{r}\right)^{p+1} P_p(\cos\theta) \tag{3.17}$$

then onto a basis of the stretched spheroidal harmonics [5]:

$$\left(\frac{h+f}{r'}\right)^{p+1} P_p(\cos\theta') = \sum_{k=p}^{\infty} \frac{2(-)^{k+p}(2k+1)(k+p)!}{p!^2(k-p)!} Q_k(\bar{\xi})P_k(\bar{\eta}), \tag{3.18}$$

where $r' = \sqrt{\rho^2+(z+f)^2}$, $\cos\theta' = (z+f)/r'$.

Then the series (3.13) may be re-expressed as

$$V \equiv V'' = V_{\mathrm{e}} + V^{(0)} - \sum_{k=0}^{\infty}(2k+1)\sum_{n=0}^{k}\beta_{kn}(2n+1)\left[\frac{Q_n(\xi_d)P_n(\xi_0)}{Q_n(\xi_0)} + q_h P_n(\xi_h)\right] Q_k(\bar{\xi})P_k(\bar{\eta}), \tag{3.19}$$

where

$$\beta_{kn} = \sum_{p=n}^{k} \frac{(-)^{p+k}(k+p)!}{(k-p)!(p-n)!(p+n+1)!}\left(\frac{2f}{f+h}\right)^{p+1}. \tag{3.20}$$

These series suffer numerically from catastrophic cancellation, where the individual terms are large but with alternating sign, and their magnitudes are just so that their combined sum is many orders of magnitude smaller than the terms themselves. This cancellation is so dramatic that 15 digits is not enough precision to compute the sum with any accuracy for $k,n \gtrsim 20$. Fortunately β_{kn} can instead be computed via the following stable recurrence:

$$\beta_{k+1,n} = \frac{k+1}{(n+k+2)(k-n+1)}\left\{(2k+1)\left[2x_h - \frac{n(n+1)}{k(k+1)} - 1\right]\beta_{kn} + \frac{(n-k+1)(k+n)}{k}\beta_{k-1,n}\right\}, \tag{3.21}$$

$$x_h = \frac{2f}{h+f}$$

with initial values

$$\beta_{nn} = \frac{1}{2n+1}x_h^{n+1} \tag{3.22}$$

$$\beta_{n+1,n} = x_h^{n+2} - x_h^{n+1}. \tag{3.23}$$

But another source of numerical instability in (3.19) lies in the sum over n, which again suffers from catastrophic cancellation, and this time there seems no way to find an analytic stable method of computation due to the complexity of the terms. The numerical errors become significant for higher k, depending on the geometry of the problem.

The series for the line charge distribution (3.19) is obtained by applying the Havelock formula:

$$\lambda(z) = -\sum_{k=0}^{\infty}\frac{2k+1}{2}\sum_{n=0}^{k}\beta_{kn}(2n+1)\left[\frac{Q_n(\xi_d)P_n(\xi_0)}{Q_n(\xi_0)} + q_h P_n(\xi_h)\right] P_k\left(\frac{2z+f-h}{h+f}\right), \qquad -f \le z < h \tag{3.24}$$

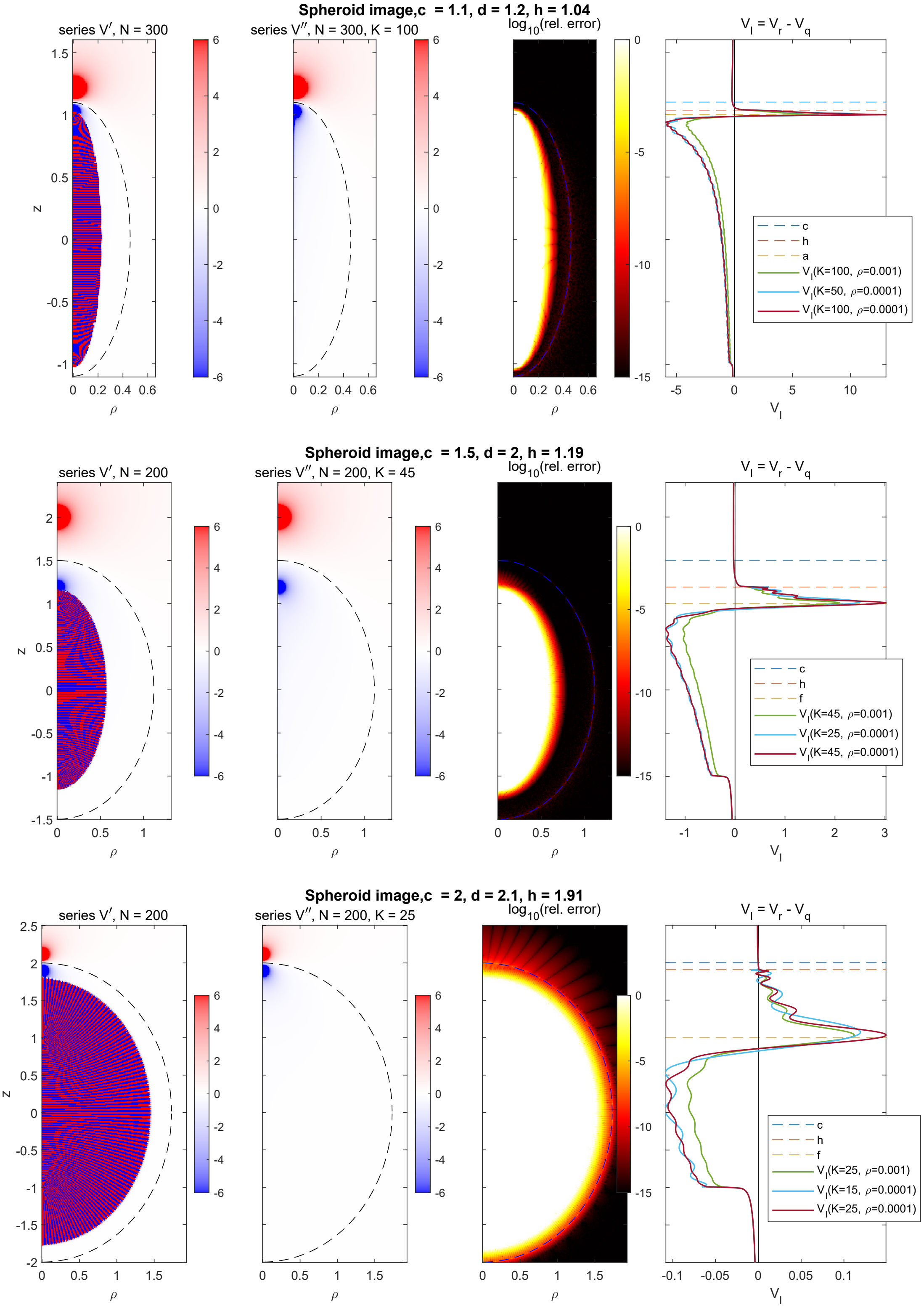
Spheroid image,c = 1.1, d = 1.2, h = 1.04
series V′, N = 300
series V″, N = 300, K = 100
log$_{10}$(rel. error)
V$_l$ = V$_r$ - V$_q$
z
ρ
V$_l$
c
h
a
V$_l$(K=100, ρ=0.001)
V$_l$(K=50, ρ=0.0001)
V$_l$(K=100, ρ=0.0001)
Spheroid image,c = 1.5, d = 2, h = 1.19
series V′, N = 200
series V″, N = 200, K = 45
log$_{10}$(rel. error)
V$_l$ = V$_r$ - V$_q$
z
ρ
V$_l$
c
h
f
V$_l$(K=45, ρ=0.001)
V$_l$(K=25, ρ=0.0001)
V$_l$(K=45, ρ=0.0001)
Spheroid image,c = 2, d = 2.1, h = 1.91
series V′, N = 200
series V″, N = 200, K = 25
log$_{10}$(rel. error)
V$_l$ = V$_r$ - V$_q$
z
ρ
V$_l$
c
h
f
V$_l$(K=25, ρ=0.001)
V$_l$(K=15, ρ=0.0001)
V$_l$(K=25, ρ=0.0001)

Figure 3.4:

which appears to converge as $1/k$ - not fast enough to obtain much detail before numerical problems appear. Even multiple precision has been tried but offers only mild improvement due to it being impractically slow.

In Figure 3.4 the analytic continuation of the potential is plotted for three different configurations of spheroids and point charges. The three left panels confirm numerically that V'' is the analytic continuation of V' and therefore of V. V'' is smooth all the way down to the line segment $-f \leq z \leq h$. The far right panels are an attempt to get an idea of what the corresponding image line charge distribution looks like, by plotting the potential very close to the image line singularity; the potential approaching any line of charge becomes proportional to the line charge density. On these far right panels, the point charges V_{e} and $V^{(0)}$ are subtracted from the total potential V'' since they tend to overpower the line source. These plots indicate that there are no other point sources in the image system, unless they have a very small amount of charge. For all three plotted configurations, the main features of the image line charge distribution are: a positive charge distribution on the segment $f \leq z < h$, which spikes at $z = +f$, then decreases past zero at some $z \lesssim f$ to negative values, and steadily decreases in magnitude as z approaches $-f$.

3.2.4 First order approximation

Towards the goal of making the series (3.24) converge faster so that it may be plotted accurately using double precision, we will look for a first order approximation to subtract from the series. Ideally this is done by analytically determining the next order in the limit of the series coefficients in (3.19), but this seems intangible. Instead we will follow the approach used to determine $V^{(0)}$, considering the next order in the original series (3.4). In that case, subtracting off $V^{(0)}$ from the "stretched" series (3.19) made the series converge much faster, since the limit of series coefficients for $V^{(0)}$ expressed in terms of stretched spheroidal harmonics also happened to match the limit of the coefficients for V expressed in terms of stretched spheroidal harmonics. However, this does not happen in the following attempt to extract the next order of V.

From the expansions of the Legendre functions given in (3.6), we see that the first order goes as $1/n$ relative to the zeroth, so a simple guess for the first order would be:

$$V^{(1)} = p_h \sum_{n=0}^{\infty} P_n(\xi_h) Q_n(\xi) P_n(\eta) \tag{3.25}$$

for some constant p_h, which can be determined by matching the limit of the series coefficients of $V^{(1)}$ to those in $V_{\mathrm{r}} - V^{(0)}$, to be

$$p_h = \frac{q_h}{4} \left(\frac{2\xi_0}{\sqrt{\xi_0^2 - 1}} - \frac{\xi_d}{\sqrt{\xi_0^2 - 1}} - \frac{\xi_h}{\sqrt{\xi_0^2 - 1}} \right) \tag{3.26}$$

Then the series coefficients for $V_{\mathrm{r}} - V^{(0)} - V^{(1)}$ converge as $1/n$ relative to the coefficients for $V_{\mathrm{r}} - V^{(0)}$. The series (3.25) diverges inside the spheroid ξ, ξ_h just as does the series for V_{r}. We can express (3.25) as a series of the stretched spheroidal harmonics:

$$V^{(1)} = p_h x_h \sum_{k=0}^{\infty} P_n(2x_h - 1) Q_k(\bar{\xi}) P_k(\bar{\eta}) \tag{3.27}$$

which converges everywhere except the segment $-f \leq z \leq h$, and its line charge distribution can be computed with no numerical problems. The problem is that, unlike the case for $V^{(0)}$, the coefficients of the series' of stretched spheroidal harmonics for V in (3.19) and in (3.27) do *not* match (numerically at least), even though their coefficients expressed in the original series (3.4) and (3.25) *do* match. So unfortunately, subtracting $V^{(1)}$ from $V_{\mathrm{r}} - V^{(0)}$ has no effect on the rate of convergence of the series (3.19) or (3.24). But there may exist a first order approximation to both series that differs in higher orders in n so that it still matches the first order in (3.4) but may also match the first order in (3.19).

3.2.5 Off-axis source charge

For an off-axis point charge at ξ_d, η_d, there is a critical spheroidal surface ξ_c, where for the source outside this surface, $\xi_d > \xi_c$, the image lies completely on the focal segment, but for $\xi_d < \xi_c$ the series solution diverges

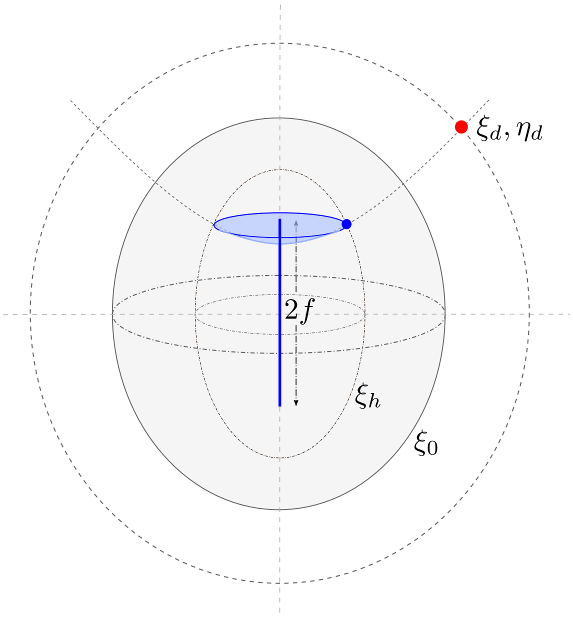

Figure 3.5: schematic of a guess of the location of the image for a point charge near a prolate spheroid, consisting of an image point charge, a parabolic bowl, and the focus. The sign of the image charge may not be all negative.

everywhere inside some inner spheroid. The location of the fundamental singularity/singularities is unknown. We may let the point charge lye on $y = 0$. The series solution is

$$V = \frac{f}{\sqrt{(x-x_d)^2 + y^2 + (z-z_d)^2}} - \sum_{n=0}^{\infty} \sum_{m=-n}^{n} (2n+1)(-)^m \frac{(n-m)!^2}{(n+m)!^2} \frac{P_n^m(\xi_0)}{Q_n^m(\xi_0)} Q_n^m(\xi_d) P_n^m(\xi_d) Q_n^m(\xi) P_n^m(\eta) e^{im\phi}. \tag{3.28}$$

It may be possible to analytically this using the Watson transformation which was applied to the time-harmonic scattering problem for a dipole near a sphere [49, 50] - see also the Chapter 5. An initial guess is that the series would look something like

$$V = \sum_{\nu} \sum_{m=0}^{\infty} \frac{(2\nu+1)P_\nu(\xi_0)}{\sin(\nu\pi)\partial_\nu Q_\nu(\xi_0)} Q_\nu^m(\xi_d) P_\nu^m(\eta_d) Q_\nu^m(\xi) P_\nu^m(\eta) e^{im\phi}? \tag{3.29}$$

where ν are the complex zeros of $Q_\nu^m(\xi)$ for fixed m and ξ. The convergence of a Watson transformed series tends to depend on a different coordinate, as seen for the sphere and cylinder - so in this case series should hopefully depend on η instead of ξ. A plausible guess is that the image lies on the surface $\eta = \eta_d, \xi < \xi_h$ which is a parabolic bowl, plus the focus, as shown in Figure 3.5 - this would be consistent with the on-axis case. Then (3.29) should converge everywhere except this bowl and the focus (since $Q_\nu(\xi = 1)$ diverges), giving the full analytic continuation of V. But actually evaluating (3.29) seems a nightmare - the zeros ν are not given by an exact formula - they would likely have to be calculated by some algorithm for finding complex zeros. Also, we find for the sphere in Chapter 5 that the Watson series is numerically unstable near the singularity.

3.3 Point charge at center of conducting prolate spheroid

This problem is also simple enough to derive an analytic continuation for, by using basis re-expansions. Now the excitation potential is

$$V_{\mathrm{e}} = \frac{f}{r} = \sum_{n=0}^{\infty} (2n+1) P_n(0) Q_n(\xi) P_n(\eta). \tag{3.30}$$

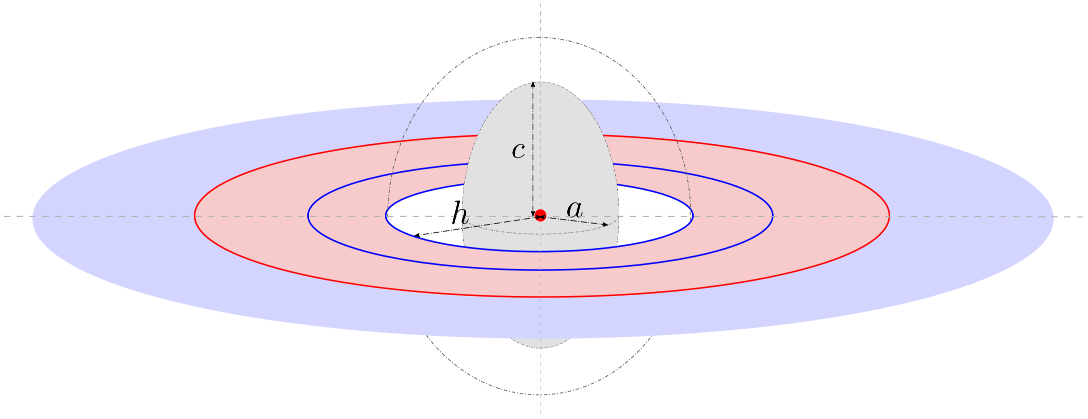

Figure 3.6: Schematic of the problem of a point charge centered in a prolate spheroid, roughly showing the proposed disk image with singular rings that extends out to infinity. Red represents positive charge and blue negative. Beyond the initial negative ring, the actual pattern of charge on the disk is a guess based on the limiting case of a cylinder.

Note that for n odd, $P_n(0) = 0$. The total potential inside is $V = V_\mathrm{e} + V_\mathrm{r}$, where

$$V_\mathrm{r} = -\sum_{n=0}^{\infty}(2n+1)\frac{Q_n(\xi_0)}{P_n(\xi_0)}P_n(0)P_n(\xi)P_n(\eta), \tag{3.31}$$

which converges inside a spheroidal volume with surface $\xi = \xi_h = 2\xi_0^2 - 1$. Now we want to determine the form of the image, which must lie outside this spheroid $\xi = \xi_h$. For the similar problem of a charge located inside a cylinder [51], the image lies on the $z = 0$ plane with a circular hole. So at least for thin long spheroids we should expect a similar disk image, where the hole touches the spheroid of divergence. So we will assume that the image lies on

$$\rho \geq h = f\sqrt{\xi_h^2 - 1}, \quad z = 0, \tag{3.32}$$

which is depicted in Figure 3.6. Now to find a mathematical expression for the analytic continuation of V_r, we could follow the approach for the infinite cylinder and search for an expression as a sum or integral of cylindrical harmonics $J_0(k\rho)e^{-k|z|}$, since this expression should converge everywhere except this image disk. However, there isn't a clear ansatz for this is - for the cylinder the solution is a discrete sum over $k = k_n$, the n^{th} zeros of J_0, but there seems no reason why V_r couldn't be a sum over different values of k, or even an integral over $0 \leq k < \infty$. So instead we will use different basis that also shares this plane singularity - radially inverted irregular oblate spheroidal harmonics (RIIOSHs). These are singular on the $z = 0$ plane with a hole in the middle, which can be fitted to match the assumed image domain (3.32) exactly. The RIIOSHs are $\frac{1}{r}Q_n(i\bar{\chi})P_n(\bar{\zeta})$, where $\hat{\chi}, \hat{\zeta}$ are radially inverted oblate spheroidal coordinates:

$$\hat{\chi} = \frac{1}{\sqrt{2}h}\sqrt{\hat{r}^2 - h^2 + \sqrt{(\hat{r}^2 - h^2)^2 + (2hu\hat{r})^2}}, \qquad \hat{\zeta} = \frac{u\hat{r}}{h\hat{\chi}}, \qquad \hat{r} = \frac{h^2}{r}. \tag{3.33}$$

h is the focal disk radius which has been set so that the RIIOSHs are then singular on the domain (3.32). To expand V_r in terms of RIIOSHs, we must first expand the prolate spheroidal harmonics in (3.31) in terms of regular spherical harmonics - this expansion is well known [52]. Then we can expand the spherical harmonics in terms of RIIOSHs. The required expansion can be obtained by applying radial inversion to a well known transformation formula between the *irregular* spherical harmonics and the irregular oblate spheroidal harmonics [52]. Inserting these expansions into (3.31) and rearranging the summation order gives

$$\begin{aligned} V_\mathrm{r} = \sum_{k=0:2}^{\infty}\Bigg\{\sum_{p=0:2}^{k}\Bigg[\sum_{n=p:2}^{\infty}(2n+1)\frac{Q_n(\xi_0)}{P_n(\xi_0)}P_n(0)\frac{(-)^{\frac{n-p}{2}}(n+p-1)!!}{p!(n-p)!!}\Bigg] \\ \times\frac{(k+p-1)!!}{p!(k-p)!!}\left(\frac{h}{f}\right)^k\Bigg\}(2k+1)i^{k+1}\,\frac{h}{r}Q_k(i\hat{\chi})P_k(\hat{\zeta}). \end{aligned} \tag{3.34}$$

The series over n appears to converge quickly and be numerically stable (checked for $p \leq 100$). But the sum over p suffers from catastrophic cancellation like in (3.19) - the terms are only accurate for $k \lesssim 44$ (depending on aspect ratio). In some regions of space - in particular inside the physical spheroid, 44 terms is enough to converge to many digits of accuracy, and (3.34) has been checked to agree with the original series (3.31) inside the spheroid.

3.3.1 Zeroth order approximation

We can improve the numerical stability of (3.34) slightly by considering a simple approximation to V_r, similar to both the image charge $V^{(0)}$ in Sec. 3.2.1 and the image disk in [51] for the cylinder.

In addition to the limits for the Legendre functions given in (3.6), we need the limit for $P_n(0)$:

$$P_n(0) \to \sqrt{\frac{2}{n\pi}}(-)^{n/2}\left[1 - \frac{1}{4n} + \mathscr{O}(n^{-2})\right]. \tag{3.35}$$

Then the coefficients in the series (3.31) go as (to zeroth order):

$$\frac{Q_n(\xi_0)}{P_n(\xi_0)}P_n(0) \to \frac{\sqrt{2\pi/n}(-)^{n/2}}{(\xi_0 + \sqrt{\xi_0^2 - 1})^{2n+1}}. \tag{3.36}$$

We want to find a simple function that matches this limit, that when substituted in (3.31), has a simple closed form for the corresponding series. For the infinite conducting cylinder, the zeroth order approximation is two point charges offset on the imaginary z-axis at $z = \pm 2i$, which appears in real space as a ring/outer disk, mimicking the exact image. So for the spheroid, the zeroth order image should be two point charges offset by $z = \pm ih$. The spheroidal series expansion for this is easily found from the inverse distance expansion [53]:

$$\begin{aligned} V^{(0)} &= \frac{ic\sqrt{\xi_h}}{\sqrt{\rho^2 + (z - ih)^2}} - \frac{ic\sqrt{\xi_h}}{\sqrt{\rho^2 + (z + ih)^2}} \\ &= -2i\sqrt{\xi_h}\sum_{n=0}^{\infty}(2n+1)Q_n(i\xi_h)P_n(\xi)P_n(\eta), \qquad \xi_h = h/f. \end{aligned} \tag{3.37}$$

Although not immediately apparent, the series coefficients in (3.37) have the same asymptotic limit as (3.36), since $(\xi_h + \sqrt{\xi_h^2 + 1})^{n+1/2} = (\xi_0 + \sqrt{\xi_0^2 - 1})^{2n+1}$. $V^{(0)}$ is a good approximation to V_r for fatter spheroids, accurate to within 1% (note a constant correction term should be applied to $V^{(0)}$, replacing the $n = 0$ term in (3.37) with the term in (3.31)).

3.3.2 First order approximation

A first order approximation can be found in a similar manner, by considering the next order in the coefficients for the Legendre functions, which allows us to deduce the limit of the coefficients in $V - V^{(0)}$:

$$(2n+1)\left[\frac{Q_n(\xi_0)}{P_n(\xi_0)}P_n(0) - 2i\sqrt{\xi_h}Q_n(ih/f)\right] \to \sqrt{\frac{\pi}{2n}}(-)^{n/2}\frac{\xi_0^3}{\xi_h^{3/2}}\frac{\left(\xi_0 + \sqrt{\xi_0^2 - 1}\right)^{-2n-1}}{\sqrt{\xi_0^2 - 1}}. \tag{3.38}$$

Now consider the limit of

$$(2n+1)\int Q_n(x)\mathrm{d}x \; = \; Q_{n+1}(x) - Q_{n-1}(x) \; \to \; \sqrt{\frac{2\pi}{n}}\frac{(x^2-1)^{1/4}}{(x + \sqrt{x^2 - 1})^{n+1/2}}, \tag{3.39}$$

which can be matched to the limit of (3.38) with $x = ih/f$ and the right prefactor. This leads to the first order correction, writing $V_\mathrm{r} \approx V^{(0)} + V^{(1)}$:

$$V^{(1)} = -\frac{\xi_0^3}{2\xi_h^{3/2}\sqrt{\xi_0^2 - 1}}\sum_{n=0}^{\infty}(2n+1)\int^{ih/f} Q_n(x)\mathrm{d}x \, P_n(\xi)P_n(\eta). \tag{3.40}$$

For $n = 0$, $\int^{ih/f} Q_0(x)\mathrm{d}x = 1 - h/f \tan^{-1}(f/h) - \log(1 + f^2/h^2)/2$. The series for $V^{(1)}$ has a simple closed form expression:

$$V^{(1)} = \frac{\xi_0^3}{2\xi_h^{3/2}\sqrt{\xi_0^2 - 1}} \mathrm{Re}\Big\{ \log \frac{2h}{h - iz + \sqrt{h^2 - 2izh - r^2}} \Big\}, \tag{3.41}$$

which is also singular on the inverted disk $\rho > h, z = 0$. (3.41) can be verified by expanding (3.40) onto spherical harmonics and comparing with the first order approximation for the cylinder in [51]. But unfortunately like in Section 3.2.4, subtracting $V^{(1)}$ does not actually make the RIIOSH series converge faster.

3.3.3 Numerical improvement of (3.34)

We can now use this approximation to improve the rate of convergence of (3.34) by adding and subtracting the two forms for $V^{(0)}$ in (3.37):

$$\begin{aligned} V_\mathrm{r} = V^{(0)} - \sum_{k=0:2}^{\infty} \Bigg\{ \sum_{p=0:2}^{k} \Bigg[\sum_{n=p:2}^{\infty} (2n+1) \left(\frac{Q_n(\xi_0)}{P_n(\xi_0)} P_n(0) - 2i\sqrt{\xi_h} Q_n(ih/f) \right) \\ \times \frac{(-)^{\frac{n-p}{2}} (n+p-1)!!}{p!(n-p)!!} \Bigg] \frac{(k+p-1)!!}{p!(k-p)!!} \left(\frac{h}{f} \right)^p \Bigg\} (2k+1) i^{k+1} \frac{h}{r} Q_k(i\hat{\chi}) P_k(\hat{\zeta}). \end{aligned} \tag{3.42}$$

The faster convergence means (3.42) can accurately compute V_r in a larger domain relative to (3.34) before numerical cancellations become a problem. Eq. (3.42) is plotted in Figure 3.7 for spheroids of different aspect ratios. Numerical errors are high where $\hat{\chi}$ is small, near the image disk, but we can still make loose deductions of image charge density from the plots. V_r changes sign as it moves out in the ρ direction, indicating that the image disk charges also change sign in this way. A similar pattern is seen for the infinite cylinder, but there the image changes sign at regularly spaced intervals, while the pattern here appears to stretch as ρ increases.

In order to prove that the image lies completely on the $z = 0$ plane, we would have to show that the coefficients in either series (3.34) or (3.42) grow at a polynomial rate in k as $k \to \infty$, which does appear to be true numerically for low k. But they appear far too complicated to show this analytically.

For a point charge located off-center in the prolate spheroid at some η_d, but still on the rotation axis, we can only guess where the image lies. Plots of the standard series solutions, reveal just the edge of the image, and it appears that this edge lies on the same coordinate line $\eta = \eta_d$. Perhaps the image lies on the surface $\eta = \eta_d$, $\xi > \xi_h$ - an infinite parabolic curved sheet with a circular hole around the spheroid. For $\eta_d = 0$, this reduces to the flat disk image proposed in this section, and for a point charge located at the focus $\eta = 1$, the image would be a straight line extending up the z axis for $\xi > \xi_h$.

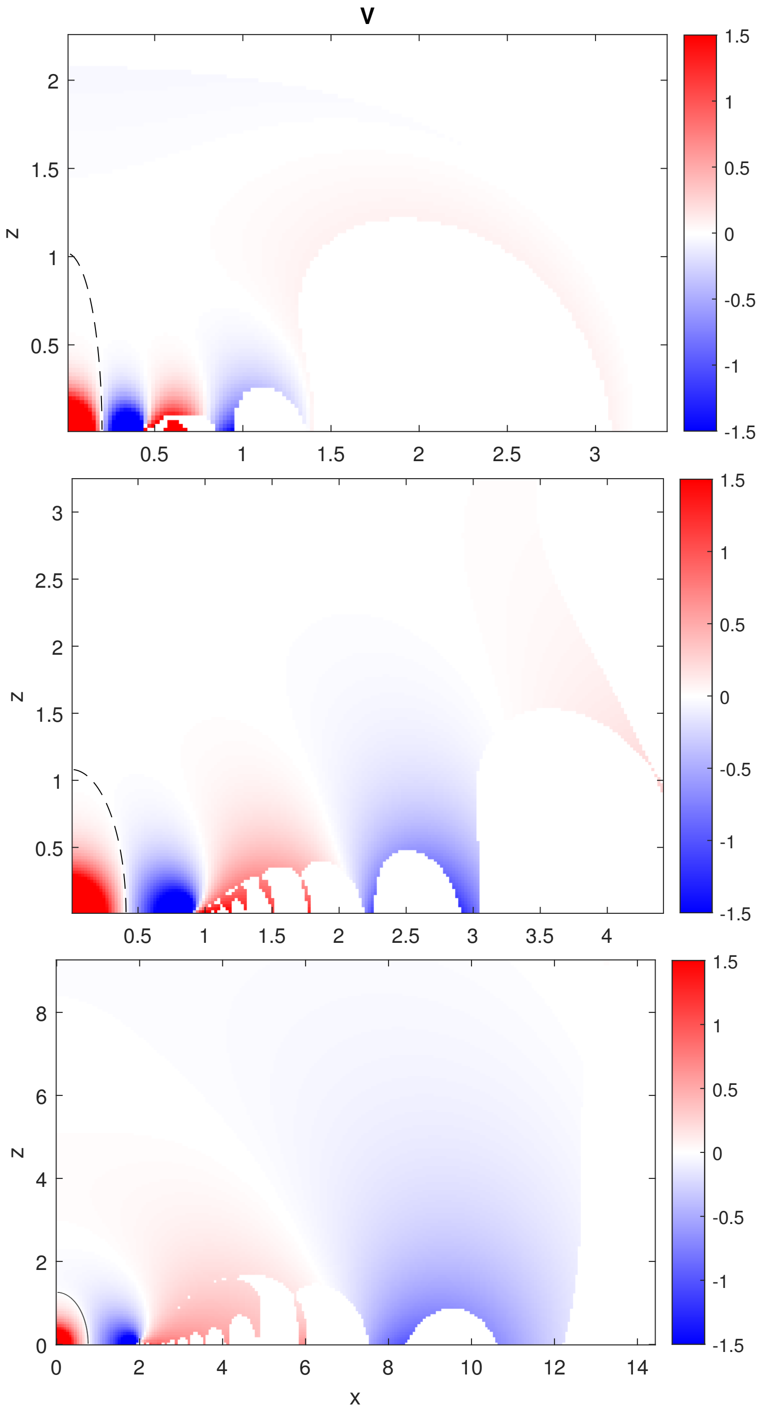

Figure 3.7: Plots of the analytic continuation of V using Eq. (3.42), for spheroids of different aspect ratios, which extend out on the x-axis to $\rho = 0.2, 0.4, 0.7$ respectively, with $f = 1$ in each. The series (3.42) is computed up to $k = K$ for two similar values of K, and these are compared to check that the series has converged sufficiently and has not encountered numerical cancellations. Regions where the two series have converged to less than 10% of each other have been whited-out to avoid showing this incorrect data. There is no guarantee that the remaining plot is accurate to within 10% error, since the two series may just happen to coincide, likely in the areas between the white blobs. The K values for each plot are - top: $K = 14, 20$, middle: $K = 24, 30$, bottom: $K = 34, 44$.

3.4 External oblate harmonics expanded on internal spherical harmonics

On a related note, we present the following potential tool. Since the external oblate spheroidal harmonics $Q_n(i\chi)P_n(\zeta)$ are finite everywhere in space, they can actually be expanded as a series of internal spherical harmonics. On the z-axis, $\chi = |z|/f$, $\zeta = 1$, where f is the focal disk radius. We assume a regular spherical harmonic expansion and match the coefficients of the series to hypergeometric expansion of the $Q_n(i\chi)$ on the z-axis about $z = 0$. Skipping the details, the result is for the azimuthally independent $m = 0$ functions:

$$\begin{aligned} i^{n-1}Q_n(i\chi)P_n(\zeta) = &-\frac{\pi}{2}\sum_{k=0:2}^{n}\prod_{p=1}^{k}\frac{n-k-1+2p}{p}\prod_{p=1}^{\frac{n-k}{2}}\frac{2p-1}{2p}\left(\frac{r}{f}\right)^k P_k(\cos\theta) \\ &+\left(\prod_{p=1}^{\frac{n}{2}}\frac{2p}{2p-1}\right)\sum_{k=1:2}^{\infty}\prod_{p=0}^{\frac{k-3}{2}}\frac{(2p+n+2)(2p-n-1)}{(2p+2)(2p+3)}(-)^{\frac{k-1}{2}}\left(\frac{r}{f}\right)^k P_k(\cos\theta)\mathrm{sign}(z) \end{aligned} \tag{3.43}$$

for n even, and

$$\begin{aligned} i^{n-1}Q_n(i\chi)P_n(\zeta) = &\frac{\pi}{2}\sum_{k=1:2}^{n}\prod_{p=1}^{k}\frac{n-k-1+2p}{p}\prod_{p=1}^{\frac{n-k}{2}}\frac{2p-1}{2p}\left(\frac{r}{f}\right)^k P_k(\cos\theta) \\ &-\left(\prod_{p=1}^{\frac{n-1}{2}}\frac{2p}{2p+1}\right)\sum_{k=0:2}^{\infty}\prod_{p=0}^{\frac{k}{2}-1}\frac{(2p+n+1)(2p-n)}{(2p+2)(2p+1)}(-)^{\frac{k}{2}}\left(\frac{r}{f}\right)^k P_k(\cos\theta)\mathrm{sign}(z) \end{aligned} \tag{3.44}$$

for n odd. (3.43) and (3.44) have been checked numerically – the left and right hand sides agree to many digits of accuracy.

If we can determine that a function has a non-singular surface discontinuity, say on the $z = 0$ plane as in the image of a point charge at the center of a spheroid, then in theory we can expand this as a series of spherical harmonics. If we conjecture that the image has singular rings but is finite in between, then a unique spherical harmonic series containing both interior and exterior harmonics should converge within each annulus between the singular rings. This could then be used to obtain the surface charge density simply by evaluating the derivative of the spherical harmonics across the surface. But it does not seem clear how to obtain a spherical harmonic expansion about some intermediate radius. Also, this would only work if the analytic continuation of the potential through the surface is also non-singular on the entire annulus.

3.5 Uniqueness of reduced image?

It is well known that the analytic continuation of any harmonic function is unique, but it may be multi-valued, lying on a Riemann surface. If a function can be expressed in all space except at line and point sources, these are the unique singularities. But as for surface discontinuities, a smooth potential defined outside any closed surface can be analytically continued inward – in fact this is what we have done for all problems this far – starting from a solution defined by a multipole series which converges outside a closed surface, we have analytically continued the function inside or outside. An *open* surface can also be continued through, shifting the surface discontinuity to one side. This is like the branch cut of a multivalued functions in the complex plane - their position can be chosen to reveal a different branch of the function in a particular region.

We can demonstrate this with a specific example. Consider a grounded conducting oblate spheroid defined by the oblate spheroidal coordinate $\chi = \chi_0$, in a uniform external potential $V_e = 1$. The total potential V_O outside is simply the oblate spheroidal harmonic of order zero, with an offset:

$$V_O = \tan^{-1}\chi - \tan^{-1}\chi_0. \tag{3.45}$$

In fact V_O is finite everywhere but with discontinuous derivatives across the focal disk. One could analytically continue V_O through either side of the disk to push the discontinuity to a different surface. For example we can construct a piece-wise function that is continuous through the disk, but at the same time equal to V_O, except in a hemisphere sub-tending from the disk:

$$V_O' = \begin{cases} \tan^{-1}\chi - \tan^{-1}\chi_0 & r \geq 1 \text{ or } z \geq 0 \\ -\tan^{-1}\chi - \tan^{-1}\chi_0 & r < 1 \text{ and } z > 0 \end{cases} \tag{3.46}$$

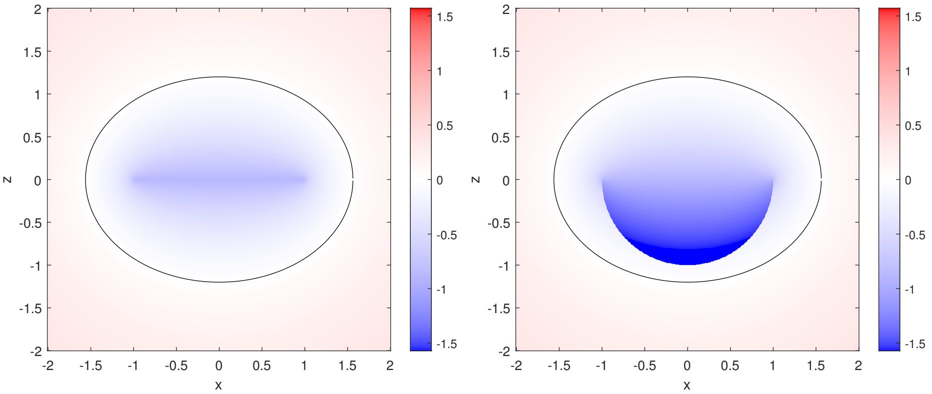

Figure 3.8: Two solutions for the potential of a grounded oblate spheroid with $\chi_0 = 1.2$. Left: V_O, right: V_O'.

which is equal to V_O outside the hemisphere $z > 0, r > 1$. For large enough χ_0, we have $V_O' = V_O$ outside the spheroid χ_0, so V_O' is a solution to the same physical problem. V_O and V_O' are plotted in Figure 3.8, inside a conducting spheroidal surface $\chi_0 = 1.2$. The surface charge for V_O is monopolar, while the surface charge for V_O' is a double layer - positive on one side and negative on the other, resulting in a finite discontinuity in V_O'. It can be verified analytically that all derivatives of V_O' are continuous across the focal disk, using the spherical harmonic expansion in (3.43) for $n = 0$ and omitting the $\operatorname{sign}(z)$ factor. So for this problem the reduced image is not unique unless we require it to have minimum surface area. In fact V_O and V_O' are just parts of a multivalued valued function, a Riemann surface of two sheets jut like the square root function in the complex plane. This Riemann surface is continuous everywhere except the branch point on the focal ring. To view only one branch at every point in space, a cut in real space must be made on some surface with the ring as its edge.

And there is another image solution that was briefly mentioned in Chapter 1. This is the line charge placed in complex space. The image has a uniform charge density distributed on the imaginary z-axis from $z = -i$ to i. The potential V_O'' created by this image is

$$V_O'' = \frac{\pi}{2} - \frac{1}{2}\int_{-1}^{1} \frac{\mathrm{d}v}{\sqrt{\rho^2 + (z - iv)^2}} - \tan^{-1}\chi_0, \tag{3.47}$$

which is equal to V_O. So if we allow for images to be placed in complex space, then this line segment on the imaginary z-axis could be interpreted as the reduced image.

We can also consider Sommerfeld images. For a point source above the center of a conducting disk, the concept of an image is more complicated since there is apparently no space to put an image. But intuitively there should be some sort of image opposite the disk, because if the disk is very large, the problem is comparable to a point charge near an infinite conducting plane, where the solution is a point charge on the opposite side. This problem can be solved with the Sommerfeld image technique by considering a double Riemann space where the disk is a branch surface joining the two spaces (or "branches") [14, 54]. In this double space, the Green function - potential of a point charge, is different but still expressible in terms of standard functions. The solution is the modified source charge source plus an oppositely charged point image opposite the disk, in the second space. When only the physical space is considered, a branch cut is taken across the disk, so the image source disappears and is replaced by a surface charge distribution on the disk.

3.6 Conclusion

We have investigated the reduced forms of images in spheroids and provided progress for two specific problems. For a point charge on the axis of a prolate spheroid, close to the surface, numerical analysis of the series of stretched spheroidal harmonics (3.19) strongly suggests that the reduced image lies on the segment extending from the lower focus up to the image point: $-f < z < h$. However, we cannot analytically prove that this series actually converges everywhere except this segment.

For a point charge at the center of a prolate spheroid, we provided some numerical evidence evidence that that the image lies on the external disk $z = 0$, $\rho \geq h$, by expanding the potential as a series of radially inverted oblate spheroidal harmonics in Eq. (3.42), but the series has severe numerical problems. Future work to improve the numerical stability of this series or evaluate it with higher precision would allow us to visualize the image in more detail.

Ideally we want to find the form of the image for an off-axis point source, but methods of analytic continuation tend to be numerically unstable as we have seen.

Chapter 4

Sphere with negative permittivity

The image of a point charge near a dielectric sphere has been solved by Carl Neumann and various later authors [15, 16, 55], as a point charge at the inversion point plus some charge distribution on the line segment from the origin to the inversion point. In electrostatics the permittivity is real and positive, and in this case the image formulation has no problems. But the electrostatic solution is also used in nano-photonics where the quasi-static approximation applies. The quasi-static approximation assumes a time harmonic field, where the sphere is too small to notice the spatial oscillations, while the permittivity depends on the frequency and may be complex (see Chapter 1). For example, the problem of a point dipole near a sphere is used to model the radiative rate of dipolar molecules aggregated on metallic nano-particles [56] which show permittivity with large negative real part at optical frequencies. For a sphere, there is a resonance for each multipole order $n = 1,2,3...$, which occur at negative $\varepsilon = \varepsilon_{\text{res}} = -1 - 1/n$, where mathematically the potential and electric field are infinite. Physically these can never be achieved exactly because all materials have some absorption which gives ε an imaginary part, but very strong field enhancements may be exploited near these resonances [57]. In particular, for silver particles in water, the relative permittivity at low optical frequencies has $\varepsilon' < -1$ and $\varepsilon'' \lesssim 0.2$. However, the image integral diverges for relative permittivity $\varepsilon = \varepsilon' + i\varepsilon''$ with $\varepsilon' < -1$, even if the potential is finite. A solution is proposed in this chapter, regularizing the image integral solution so that it reproduces the series solution for $\varepsilon' < -1$, by adding a finite number of infinite-magnitude multipoles.

4.0.1 Problem and image solution for $\varepsilon' > -1$

Consider a point charge Q located at $z = d$ above a sphere radius a, permittivity ε_{i} in a medium with permittivity ε_{o} as shown in Fig. 4.1. The relative permittivity is $\varepsilon = \varepsilon_{\text{i}}/\varepsilon_{\text{o}}$. Using spherical (r,θ,ϕ) and cylindrical (ρ,z,ϕ) coordinates, the excitation potential is

$$V_{\text{e}} = V_0 \frac{a}{r_d}; \qquad r_d = \sqrt{\rho^2 + (z-d)^2}, \qquad V_0 = \frac{Q}{4\pi\varepsilon_{\text{o}} a}. \tag{4.1}$$

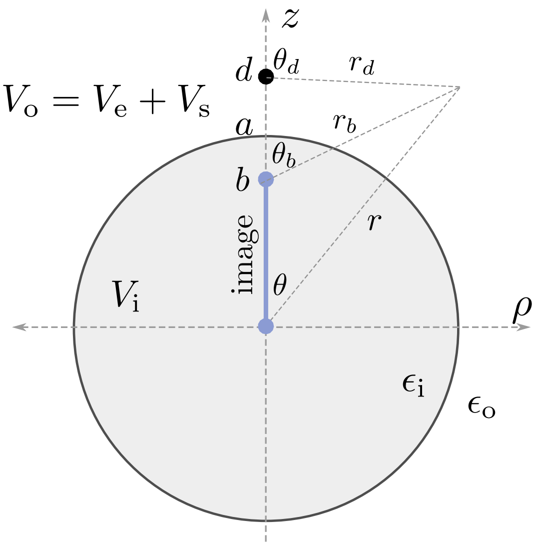

Figure 4.1: Schematic of the problem.

The total potential outside the sphere may be expressed as $V_{\text{o}} = V_{\text{e}} + V_{\text{s}}$, where V_{s} is the scattered potential. Note we have changed notation from V_{r} (“reflected” potential) in previous chapters to V_{s} (“scattered” potential) to follow the convention used in time harmonic scattering.

V_{s} may be derived by assuming a series of spherical harmonics and determining the coefficients from the boundary conditions $V_{\text{i}} = V_{\text{o}}$, $\varepsilon \partial_r V_{\text{i}} = \partial_r V_{\text{o}}$ at $r = a$, where V_{i} is the potential inside the sphere. The solution is

$$V_{\text{s}} = -V_0 \sum_{n=0}^{\infty} \frac{n(\varepsilon-1)}{n(\varepsilon+1)+1} \left(\frac{b}{r}\right)^{n+1} P_n(\cos\theta). \tag{4.2}$$

This series is also often modified by separating an image point charge at $z = b = a^2/d$:

$$V_{\text{s}} = -V_0 \frac{\varepsilon-1}{\varepsilon+1} \left[\frac{b}{r_b} - \sum_{n=0}^{\infty} \frac{\alpha}{n+\alpha} \left(\frac{b}{r}\right)^{n+1} P_n(\cos\theta) \right] \tag{4.3}$$

where

$$r_b = \sqrt{\rho^2 + (z-b)^2}, \qquad \alpha = \alpha' + i\alpha'' = \frac{1}{\varepsilon + 1}. \tag{4.4}$$

Both of these series converge for $r > b$, and provide the solution for all $\alpha \neq 0 - 1, -2...$; i.e. whenever the potential is finite. The reason then for using an alternate image solution is because these series converge very slowly when the point charge is near the surface.

The image singularity lies inside on the line segment $0 \leq z \leq b$, $\rho = 0$. Its charge distribution can be derived by using this ansatz for the image domain, expanding the Green function in the line integral in terms of spherical harmonics, and comparing with (4.3) [16]:

$$V_\mathrm{s} = -V_0 \frac{\varepsilon - 1}{\varepsilon + 1} \left[\frac{b}{r_b} - \frac{b}{\varepsilon + 1} \int_0^1 \frac{u^{\alpha - 1} \mathrm{d}u}{\sqrt{\rho^2 + (z - bu)^2}} \right]. \tag{4.5}$$

The equality of the series and integral expressions comes from recognizing the generating function for the Legendre polynomials in the integrand:

$$\frac{1}{\sqrt{\rho^2 + (z - bu)^2}} = \sum_{n=0}^{\infty} \frac{b^n u^n}{r^{n+1}} P_n(\cos\theta). \tag{4.6}$$

Before investigating the image solution, we should consider what happens to the potential near the plasmon resonances. The simplest is the “Fröhlich” resonance at $\varepsilon = -2$, where the dipole moment of the sphere (the $n = 1$ term) diverges. The next is the quadrupole resonance at $\varepsilon = -1.5$, then the octopole resonance at $\varepsilon = 1.333$ and so on; there are an infinite number of resonances of increasing complexity as $\varepsilon \to -1$. Despite this, $\varepsilon = -1$ itself is not a resonance – from Eq. (4.2) one can deduce that $V_s(\varepsilon = -1) = 0$. Of course physically in the quasistatic approximation, ε is complex and the closest approach to any resonance will be $\varepsilon = -\varepsilon_\mathrm{res} + i\delta$ for small δ.

But the problem with the solution (4.5) is that the integral diverges for *all* complex $\varepsilon < -1$. In the next section we will remedy this by modifying the image expression.

4.0.2 Regularized image for $\varepsilon' < -1$

If $\alpha' < 0$ ($\varepsilon' < -1$) the integral (4.5) diverges, due to the antiderivative being infinite at $u = 0$. This is clearly seen if we substitute the expansion (4.6) into the integral - then all terms with $n < -\alpha'$ diverge. In fact the integral would be equal to the series (4.3) if we ignored the $u = 0$ integration bound, but we cannot do this if we want to make physical sense of the integral as a charge distribution. To counter this problem, we subtract off the infinite part of the integral, that is all terms with $n < -\alpha'$. For $\alpha' < 0$, $\alpha \neq 0, -1, -2, -3...$, (the case $\alpha = 0$ is finite but should be treated separately) we may write

$$\sum_{n=0}^{\infty} \left(\frac{b}{r}\right)^{n+1} \frac{1}{n + \alpha} P_n(\cos\theta) = \lim_{v \to 0} \left[b \int_v^1 \frac{u^{\alpha - 1} \mathrm{d}u}{\sqrt{\rho^2 + (z - bu)^2}} + \sum_{n=0}^{\lfloor -\alpha \rfloor} \frac{v^{n+\alpha}}{n + \alpha} \left(\frac{b}{r}\right)^{n+1} P_n(\cos\theta) \right]. \tag{4.7}$$

Where $\lfloor x \rfloor$ is the floor of x, the largest integer $\leq \Re\{x\}$. As $v \to 0$, the integral and series both diverge, but their difference is finite and equal to the integral evaluated at the top end point which is equal to the left hand side. This approach of regularization has been used recently for the Stieltjes transformation, and discussed in more detail in [58] (see their eq 2.18). The image consists of an image point charge at the inversion point, plus a line charge, plus, if $\alpha' < 0$ ($\varepsilon' < -1$), a finite number ($\lfloor -\alpha + 1 \rfloor$) of infinite-magnitude multipoles at the origin that regularize the divergence of the line source. For $\alpha = -1/2$ for instance (top center of Figure 4.3), an image point charge at the origin is introduced with opposite sign to the line charge distribution (same sign as the source charge). Then the correct form of the potential for $\alpha \neq 0, -1, -2...$ is

$$V_\mathrm{s} = V_0 \frac{\varepsilon - 1}{\varepsilon + 1} \left[-\frac{b}{r_b} + \frac{1}{\varepsilon + 1} \lim_{v \to 0} \left(b \int_v^1 \frac{u^{\alpha - 1} \mathrm{d}u}{\sqrt{\rho^2 + (z - bu)^2}} + \sum_{n=0}^{\lfloor -\alpha \rfloor} \frac{v^{n+\alpha}}{n + \alpha} \left(\frac{b}{r}\right)^{n+1} P_n(\cos\theta) \right) \right]. \tag{4.8}$$

When $\alpha' > 0$ ($\varepsilon' > -1$), the sum vanishes and the expression reduces to (4.4). The concept of a divergent charge distribution is very common in electrostatics - for example the ideal dipole is the limit of two opposite

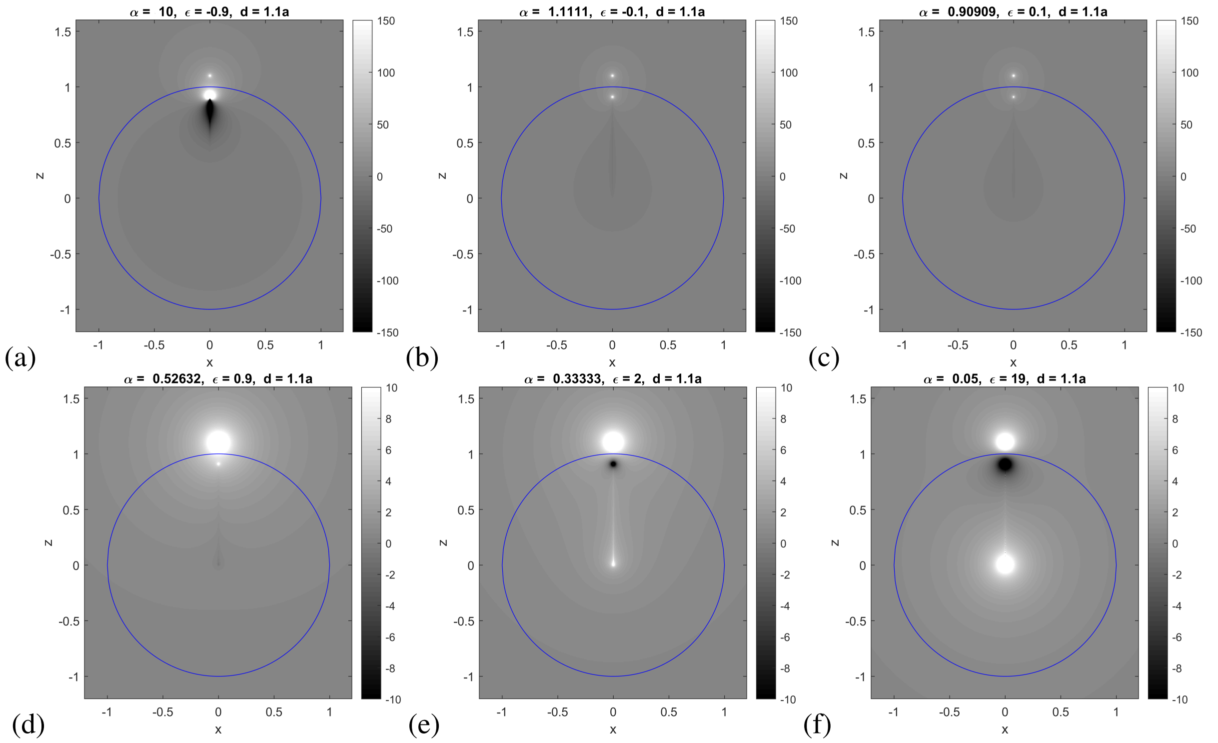

Figure 4.2: Plots of the analytic continuation of the potential $V_\mathrm{s} + V_\mathrm{e}$ for various $\varepsilon > -1$. Here there are no infinite multipoles. Note the lower intensity scale in (d)-(f).

charges placed infinitely close together while their charge magnitude diverges so that the electric field is finite.

An interesting case is $\varepsilon = -1$ ($|\alpha| = \infty$), where the limit as $\varepsilon \to -1$ from below oscillates rapidly, but from above the image can be obtained from the spherical harmonic series solution:

$$V_\mathrm{s}(\varepsilon = -1) = 2V_0 \sum_{n=0}^{\infty} n \left(\frac{b}{r}\right)^{n+1} P_n(\cos\theta) = 2V_0 \frac{b^2}{r_b^2} \cos\theta_b \tag{4.9}$$

where θ_b is the colatitude from the inversion point. This is a dipole at the inversion point pointing towards the source (seen the top left of Figure 4.2 for $\varepsilon = -0.9$). And for the conducting sphere, $|\varepsilon| = \infty$ in any direction in the complex plane ($\alpha = 0$):

$$V_\mathrm{s}(|\varepsilon| = \infty) = -V_0 \sum_{n=0}^{\infty} \left(\frac{b}{r}\right)^{n+1} P_n(\cos\theta) = -V_0 \frac{b}{r_b}. \tag{4.10}$$

The form of the image (4.8) can be verified by plotting the spheroidal harmonic series solution [5] which converges everywhere except the image line, for all $\alpha \neq -1, -2, -3, \ldots$:

$$V_\mathrm{s} = V_0 \frac{\varepsilon - 1}{\varepsilon + 1} \left[-\frac{b}{r_b} + 2\sum_{n=0}^{\infty} (2n+1) \prod_{k=1}^{n} \frac{\alpha - k}{\alpha + k} \, Q_n(\bar{\xi}) P_n(\bar{\eta}) \right] \tag{4.11}$$

$$\text{where } \bar{\xi} = \frac{r + r_b}{b}, \quad \bar{\eta} = \frac{r - r_b}{b}.$$

The familiar potentials for $\varepsilon' > -1$ are plotted in Figure 4.2, and the potentials for various $\varepsilon' < -1$ are plotted in Figure 4.3. In both figures V_s is computed with (4.11). The cases $\varepsilon \to \infty$ (bottom right of Figure 4.2) and $\varepsilon \to -\infty$ (top left of Figure 4.3) both produce the identical result of the Kelvin image charge found for the conducting sphere. Figure 4.2 shows some interesting features even for $\varepsilon' > -1$, for example the image system flip sign as ε passes through 1 (see plots for $\varepsilon = 0.9, 2$), but there is no real difference between $\varepsilon = 0.1$ and $\varepsilon = -0.1$. In Figure 4.3, as $\varepsilon \to -1$ from below we see the addition of a new infinite multipole at the origin each time ε passes a resonance $\varepsilon_\mathrm{res} = -1 - 1/n$.

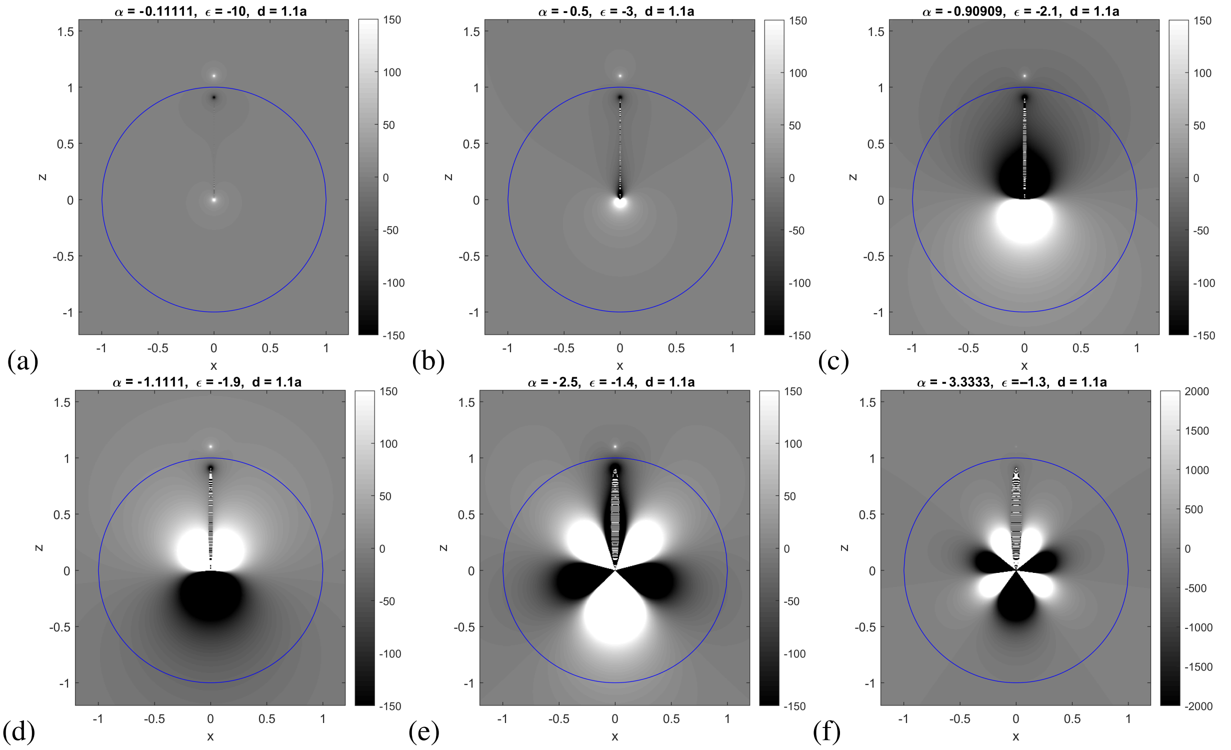

Figure 4.3: Plots of the analytic continuation of the potential $V_s + V_e$ for various ε, as computed by the spheroidal harmonic series 4.11 with a truncation order of $n = 300$. The grayscale has been truncated for clarity. The series converges very slowly near the image line for $\varepsilon \to -1$, creating the thin striped spheroidal region which should be ignored. For $\varepsilon = 1.9$ (d), there are actually 2 positive lobes either side of the image line.

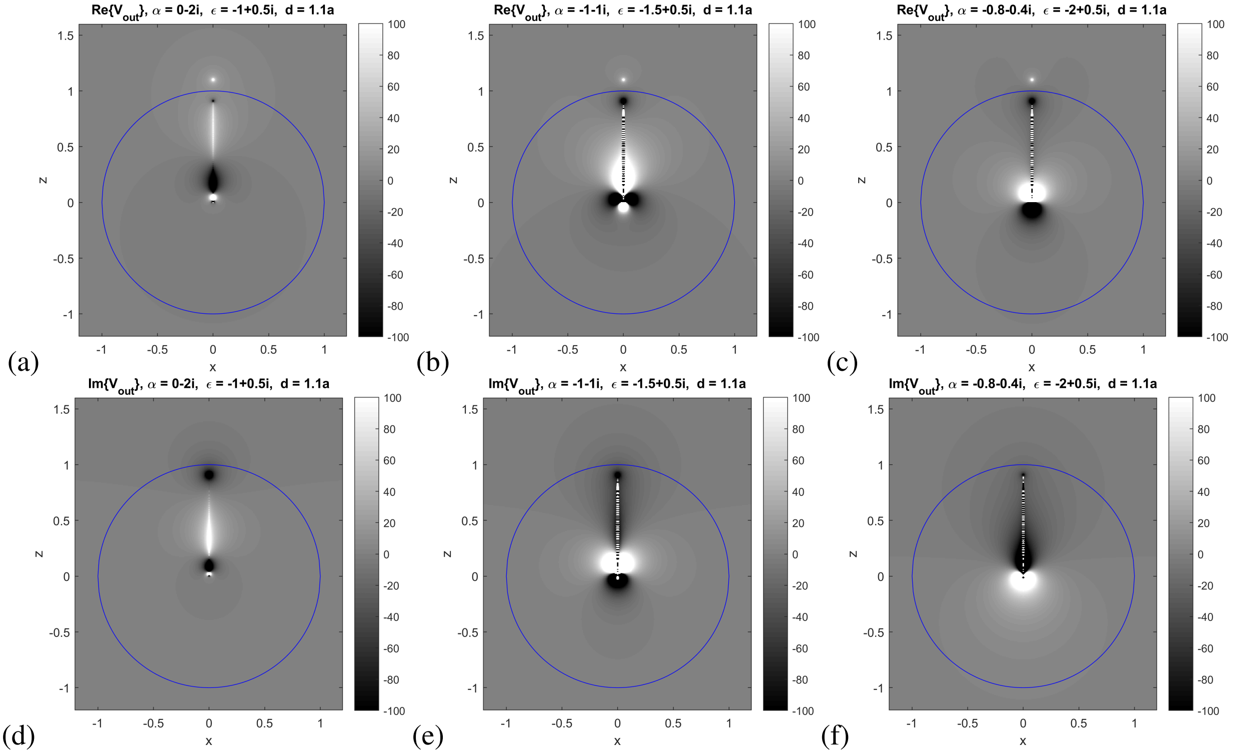

Figure 4.4: Real and imaginary parts of the analytic continuation of $V_{\text{out}} = V_s + V_e$ for complex ε.

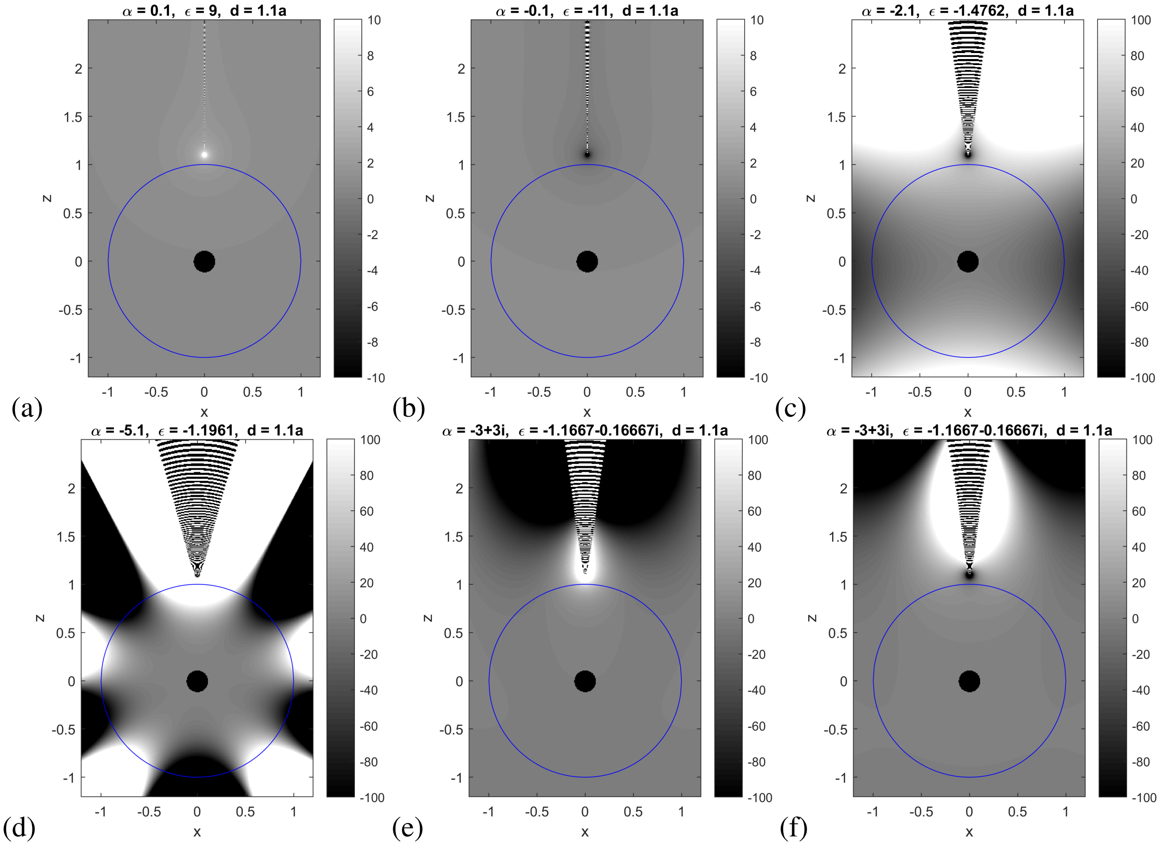

Figure 4.6: Plots of the analytic continuation of the internal potential V_{in} as computed with the inverted spheroidal harmonic series (4.14). A truncation order of $n = 300$ was chosen. The black circle near the origin is an artifact from overflow (this gets worse for high n), and the striped areas are an artifact from the slow convergence of the series near the image line. Note that (a),(b) have a different intensity scale. (e),(f) are real and imaginary parts for a single complex ε.

There is a drastic difference for ε being slightly either side of each resonance, which is very apparent for the plots with $\varepsilon = -2.1$ and $\varepsilon = -1.9$. The black and white striped regions are due to the finite truncation of the spheroidal harmonic series (higher orders may be summed to minimise this striped region, but this eventually introduces numerical underflow in $Q_n(\bar{\xi})$ away from the line segment). The spheroidal series can be proven to converge in all space except the line segment $\bar{\xi} = 1$ by analysis of the limit of each term as $n \to \infty$.

Which converges for $\bar{\xi} > 1$, although slowly for $\alpha \to -\infty$ ($\varepsilon \to -1$).

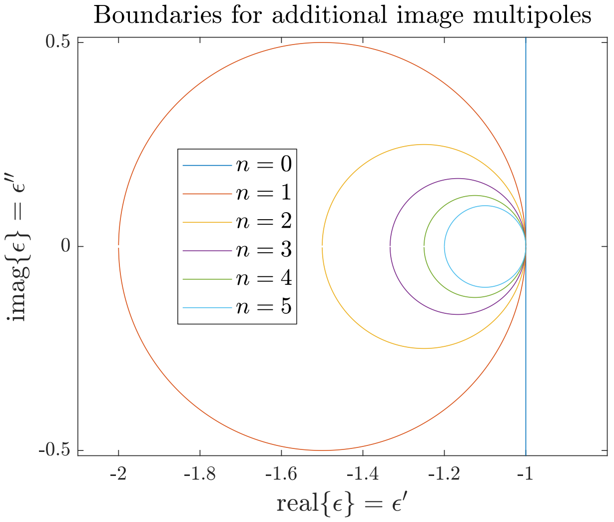

Figure 4.5: Circles that define the number of additional multipoles to be added to the sum in (4.8). To the right of $\varepsilon' = -1$ there are no additional multipoles, and from there, crossing inside each circle adds one multipole.

For complex ε, the real and imaginary parts of V_s are plotted for $\varepsilon' = -1, -1.5, -2$, $\varepsilon'' = 0.5$ in Figure 4.4. As mentioned above, the number of infinite-magnitude multipoles increases by one as α' crosses left of $-n$. The conditions $\alpha' = -n$ are equivalent to $\varepsilon''^2 = -(\varepsilon' + 1)/n - (\varepsilon' + 1)^2$, which are equations for circles in the complex plane for each n, shown in Figure 4.5. For $\varepsilon'' \neq 0$ the potential changes smoothly as ε crosses these boundaries.

4.0.3 Solution inside the sphere

Here the image is an integral over the semi-infinite line segment extending from the source, and now the integral diverges at $r = \infty$ for $\alpha < 1$ $(\varepsilon < 0)$. We present the final results for the potential as a spherical harmonic series, a regularised image system, and a spheroidal harmonic series [26]:

$$V_\mathrm{i} = \frac{V_0 a}{\varepsilon+1}\left[\frac{2}{r_d} + \frac{1}{d}\sum_{n=0}^{\infty}\frac{\varepsilon-1}{n(\varepsilon+1)+1}\left(\frac{r}{d}\right)^n P_n(\cos\theta)\right] \tag{4.12}$$

$$= \frac{V_0 a}{\varepsilon+1}\left[\frac{2}{r_d} + \frac{\varepsilon-1}{(\varepsilon+1)^2}\lim_{\nu\to\infty}\left(\int_1^{\nu}\frac{u^{-\alpha}\mathrm{d}u}{\sqrt{\rho^2+(z-du)^2}} - \frac{a}{d}\sum_{n=0}^{\lfloor-\alpha\rfloor+1}\frac{\nu^{-n-\alpha}}{n+\alpha}\left(\frac{r}{d}\right)^n P_n(\cos\theta)\right)\right] \tag{4.13}$$

$$= \frac{V_0 a}{\varepsilon+1}\left[\frac{2}{r_d} + (\varepsilon-1)\frac{2}{r}\sum_{n=0}^{\infty}(2n+1)\prod_{k=1}^{n}\frac{\alpha-k}{\alpha+k}\,Q_n(\check{\xi})P_n(\check{\eta})\right], \tag{4.14}$$

where $\check{\xi} = \bar{\xi}(r \to a^2/r)$, $\check{\eta} = \bar{\eta}(r \to a^2/r)$ are radially inverted offset spheroidal coordinates. This time the regularization is a sum of infinite magnitude *external* multipoles. The spheroidal series (4.14) is plotted for a range of complex ε in Figure 4.6.

The results for dipole sources are similar and presented in [23].

4.1 Conclusion

The canonical image system for a point source near a dielectric sphere has been shown to break down for negative values of the real part of the relative permittivity. This can be fixed analytically with the addition of regularizations in the form of infinite-magnitude multipoles (Eq. 4.8), so that the image system reproduces the solution to the problem. However the potential created by the image system may be complicated to compute numerically. So instead we have used the efficient spheroidal harmonic expansions of Ref. [5] which apply for all values of ε, to visually reaffirm the existence of the additional regularizations. This has shown that the image system changes drastically, increasing the number of positive and negative lobes as ε crosses the poles $\varepsilon_\mathrm{res} = -2, -1.5, -1.33...$, just as does the nature of the surface fields.

Chapter 5

Oscillating point source near a sphere

The Helmholtz equation governing harmonic time dependent fields also exhibits image singularities, and in fact this equation connects with the high frequency geometric optics limit, where images may be determined using ray optics. For the conducting plane, the image of a radiating dipole is similar to that of an electrostatic point charge, and that of a visible point object - a copy of the source object exactly opposite the plane, with inverted charge or phase. For a conducting sphere the electrostatic image is a charge at the inversion point, and the image for a visible object using geometric optics is given in [59], but the image for a radiating dipole of a finite frequency near a sphere is unknown, although images have been derived in the zeroth and first order long wavelength approximations [60].

The problem of an oscillating point source (monopole or dipole) scattering from a sphere for the Helmholtz equation can be solved with generalized Mie theory as a series spherical wavefunctions. However the series converges slowly for emitters close to the surface, so we would like some kind of image solution instead.

Here we attempt to determine the image of an acoustic spherical wave near a soft sphere. This problem is similar to the electromagnetic scattering problem, but simpler – it can be used to analyze the problem with more clarity, and the results should be extendable to the electromagnetic case. First, we assume there to be an image spherical wave located at the standard Kelvin inversion point, and find the correct weighting of the image so that when subtracted from the original series, the remaining series converges faster. The technique was used in the context of a static point source near a spheroid in Chapter 3 – a point image was separated from the series of spheroidal harmonics by subtracting terms that matched the leading order of the series coefficients, and from these terms recognizing the expression for an offset point charge [61]. The remaining series coefficients are messier but the series converges faster. Then towards finding a complete image system, we consider a low frequency expansion of the potential, finding the complete image system to the second non-zero order in the wavenumber expansion. Finally we consider the Watson transformation - a series which converges depending on θ rather than r, and analysis of this series suggests that the image lies on a finite segment on the positive z-axis.

5.1 Acoustic spherical wave near soft sphere

Consider a sphere radius a excited by a spherical wave on the z axis at $z = d > a$. The excitation potential V_e can be expressed as a series of spherical wave functions $j_n(kr)P_n(\cos\theta)$ [53]:

$$V_\mathrm{e} = \frac{e^{ikr_d}}{ikr_d} = h_0(kr_d) = \sum_{n=0}^{\infty}(2n+1)h_n(kd)j_n(kr)P_n(\cos\theta), \qquad r_d = \sqrt{\rho^2+(z-d)^2}, \tag{5.1}$$

where j_n and h_n are the spherical Bessel and Hankel functions. Writing $V = V_\mathrm{e} + V_\mathrm{s}$ where V_s is scattered by the sphere, the boundary condition for a soft scatterer is $V_\mathrm{s} = -V_\mathrm{e}$ at $r = a$. The solution is easily shown to be

$$V_\mathrm{s} = -\sum_{n=0}^{\infty}(2n+1)\frac{j_n(ka)}{h_n(ka)}h_n(kd)h_n(kr)P_n(\cos\theta), \tag{5.2}$$

which converges for $r > b = a^2/d$. We look to extract an image monopole at the standard Kelvin inversion point $z = b$, just as is done in the static case. We want the magnitude of this image to be so that extracting it cancels out the leading order (in n) in the remaining series. The expansion of the image monopole is

$$V_{\text{image monopole}} \propto \frac{e^{ikr_b}}{ikr_b} = \sum_{n=0}^{\infty}(2n+1)j_n(kb)h_n(kr)P_n(\cos\theta), \qquad r_b = \sqrt{\rho^2+(z-b)^2}. \tag{5.3}$$

For $n \to \infty$ we have to leading order [62]:

$$(2n+1)\frac{j_n(ka)}{h_n(ka)}h_n(kd) = \frac{k^n b^{n+1}}{(2n-1)!!a}(1+\mathscr{O}(1/n)) \tag{5.4}$$

$$\frac{a}{d}(2n+1)j_n(kb) = \frac{k^n b^{n+1}}{(2n-1)!!a}(1+\mathscr{O}(1/n)) \tag{5.5}$$

$$\Rightarrow (2n+1)\frac{j_n(ka)}{h_n(ka)}h_n(kd) = \frac{a}{d}(2n+1)j_n(kb)(1+\mathscr{O}(1/n)). \tag{5.6}$$

So we weight the image in (5.3) by a/d and rewrite the potential as

$$V_{\text{s}} = -\frac{a}{d}h_0(kr_b) - \sum_{n=0}^{\infty}(2n+1)\left[\frac{j_n(ka)}{h_n(ka)}h_n(kd) - \frac{a}{d}j_n(kb)\right]h_n(kr)P_n(\cos\theta). \tag{5.7}$$

The resulting series converges faster by a factor $1/n$, due to the leading order being canceled, but the series still diverges for $r < b$ because the terms behave as $(b/r)^n$. In the static limit the two terms in the series cancel completely, leaving just the offset point image. We would like to make further deductions about the image, but this approach of extracting terms seems unlikely to result in an expression that converges for $r < b$.

5.2 Integral equation of the first kind

A reasonable assumption for the location of the image is on the finite segment from the origin to the inversion point of the source with some linear density $\lambda(z)$. Then we may express the scattered potential as an integral over this source:

$$V_{\text{s}} = -\int_0^b \lambda(v,ka,kd)\frac{e^{ikr'}}{ikr'}\mathrm{d}v, \tag{5.8}$$

$$r' = \sqrt{r^2-2ruv+v^2}, \qquad u = \cos\theta. \tag{5.9}$$

λ may be able to be determined from the boundary condition $V_{\text{s}} = -V_{\text{e}}$ at $r = a$:

$$\int_0^b \lambda(v,ka,kd)\frac{e^{ikr'}}{r'}\mathrm{d}v = \frac{e^{ikr_d}}{r_d} \qquad \text{at } r = a. \tag{5.10}$$

Assuming that the image lies on this segment, (5.10) should have a unique solution. This is a Fredholm equation of the first kind,

$$\int_0^b \lambda(v)K(u,v)\mathrm{d}v = f(u); \tag{5.11}$$

where $K(v,u,ka,kd)$ is the kernel and $f(u)$ is the inhomogeneous part:

$$K(v,u,ka,kd) = \frac{e^{ik\sqrt{a^2-2auv+v^2}}}{\sqrt{a^2-2auv+v^2}}, \quad f(u) = \frac{e^{ik\sqrt{a^2-2aud+d^2}}}{\sqrt{a^2-2aud+d^2}}. \tag{5.12}$$

We should subtract the image point charge at the inversion point as in (5.7), since this would appear as a delta function in λ. Then we would solve for some $\bar{\lambda}$, which is identical to λ except at $v = b$:

$$\int_0^b \bar{\lambda}(v,ka,kd)\frac{e^{ikr'}}{r'}\mathrm{d}v = \frac{e^{ikr_d}}{r_d} - \frac{a}{d}\frac{e^{ikr_b}}{r_b} \qquad \text{at } r = a. \tag{5.13}$$

We can expand K and f using the offset spherical wave expansion (5.3), and subtract the inversion point image:

$$\int_0^b \bar{\lambda}(v) j_n(kv)\mathrm{d}v = \frac{j_n(ka)}{h_n(ka)} h_n(kd) - \frac{a}{d} j_n(kb). \tag{5.14}$$

This essentially changes the independent variable u to n.
But this approach is not practical - likely one would have to solve this numerically which is not ideal, and integral equations of the first kind are known to be unstable. So instead, in the next section we will look at directly extracting images from the low frequency expansion of the series.

5.3 Low frequency image system

We shall expand the series (5.2) in powers of k, assuming ka and kd are small. The expansion of the Bessel functions for small argument read

$$j_n(x) \approx \frac{x^n}{(2n+1)!!}\left(1 - \frac{x^2}{2(2n+3)} + \mathscr{O}(x^4)\right), \tag{5.15}$$

$$h_n(x) \approx -i\frac{(2n-1)!!}{x^{n+1}}\left(1 + \frac{x^2}{2(2n-1)} + \mathscr{O}(x^4)\right) + \delta_{n0}\left(1 - \frac{x^2}{6}\right) + \delta_{n1}\frac{x}{3}. \tag{5.16}$$

The Kronecker deltas δ_{nm} account for the real parts of $h_0(x)$ and $h_1(x)$ being significant to this order. Then the potential can be expanded to second order in k as

$$\begin{aligned} V_\mathrm{s} =& \frac{1}{k} V_\mathrm{s}^{(0)} + V_\mathrm{s}^{(1)} + k V_\mathrm{s}^{(2)} + \mathscr{O}(k^2) \\ =& -\frac{ia}{kdr_b} + \frac{a}{d}\left(1 - \frac{d-a}{r}\right) + \frac{ika}{d}(d-a)\left(\frac{a}{r} - 1\right) \\ &+ \frac{ik}{2a}\sum_{n=0}^{\infty}\left(\frac{b}{r}\right)^{n+1}\left(\frac{d^2+r^2-a^2}{2n-1} - \frac{a^2}{2n+3}\right) P_n(\cos\theta) + \mathscr{O}(k^2). \end{aligned} \tag{5.17}$$

The k^{-1} and k^0 terms are singular at the inversion point and the origin respectively. But the k^1 term is a series which converges only for $r > b$, which does not reveal the image or ”support” of the function. To find its image, we use the result of [16] that

$$\sum_{n=0}^{\infty} \frac{1}{n+\mu}\left(\frac{b}{r}\right)^{n+1} P_n(\cos\theta) = \int_0^1 \frac{bu^{\mu-1}\mathrm{d}u}{\sqrt{\rho^2 + (z-bu)^2}} \qquad \Re\{\mu\} > 0. \tag{5.18}$$

We require the two cases $\mu = 3/2, -1/2$. For $\mu = 3/2$:

$$\sum_{n=0}^{\infty} \frac{1}{2n+3}\left(\frac{b}{r}\right)^{n+1} P_n(\cos\theta) = \frac{b}{2}\int_0^1 \frac{u^{1/2}\mathrm{d}u}{\sqrt{\rho^2 + (z-bu)^2}}. \tag{5.19}$$

But for $\mu = -1/2$ the anti-derivative is singular at the endpoint $u = 0$. For this we can subtract the infinite part, as done in the previous chapter:

$$\sum_{n=0}^{\infty} \frac{1}{2n-1}\left(\frac{b}{r}\right)^{n+1} P_n(\cos\theta) = \lim_{v\to 0}\left[\frac{b}{2}\int_v^1 \frac{u^{-3/2}\mathrm{d}u}{\sqrt{\rho^2 + (z-bu)^2}} - \frac{b}{r}v^{-1/2}\right]. \tag{5.20}$$

The right hand side is the difference between two divergent potential functions - a line source with charge distribution $\propto z^{-3/2}$ (which has infinite total charge), and a point charge of infinite strength $2/\sqrt{0}$. To check this image distribution numerically, we express this potential as a series of offset spheroidal harmonics, as done for the point charge near a dielectric sphere [5]:

$$\sum_{n=0}^{\infty} \frac{\mu}{n+\mu}\left(\frac{b}{r}\right)^{n+1} P_n(\cos\theta) = 2\sum_{n=0}^{\infty}(2n+1)\prod_{k=1}^{n}\frac{\mu-k}{\mu+k} Q_n(\bar{\xi})P_n(\bar{\eta}) \qquad \mu \neq -1, -2, -3... \tag{5.21}$$

where

$$\bar{\xi} = \frac{r + r_b}{b} \qquad \eta = \frac{r - r_b}{b}. \tag{5.22}$$

The foci of the spheroidal coordinate system here is on the z-axis from the origin to $z = b$, coinciding with the singularity of $V_{\mathrm{s}}^{(2)}$. Then we have

$$V_{\mathrm{s}}^{(2)} = +\frac{ia}{d}(d-a)\left(\frac{a}{r} - 1\right) + \frac{i}{a}\sum_{n=0}^{\infty}(-)^n\left(\frac{a^2}{(2n+3)(2n-1)} + (a^2 - d^2 - r^2)(2n+1)^2\right)Q_n(\bar{\xi})P_n(\bar{\eta}) \tag{5.23}$$

which converges in all space except the image at $\bar{\xi} = 1$. (5.23) allows us to justify the image form of the potential through an independent calculation of the image charge distribution. The Havelock formula expresses the spheroidal harmonics as an integral of a source distribution over the focal line:

$$Q_n(\bar{\xi})P_n(\bar{\eta}) = \frac{b}{2}\int_0^1 \frac{P_n(2u-1)\mathrm{d}u}{\sqrt{\rho^2 + (z - bu)^2}}. \tag{5.24}$$

We the obtain series expressions for the image line distributions:

$$\lambda_1 = \sum_{n=0}^{\infty} \frac{(-)^n}{(2n-1)(2n+3)} P_n(2u-1), \tag{5.25}$$

$$\lambda_2 = \sum_{n=0}^{\infty} (-)^n (2n+1)^2 P_n(2u-1). \tag{5.26}$$

[63] (8.922) gives $\lambda_1 = -\sqrt{u}$ which agrees with the integral in (5.19). For λ_2, the series diverges, but we can use the recurrence relation and generating function for the Legendre polynomials to deduce that $\lambda_2(u > 0) = -u^{-3/2}/2$, agreeing with the integral in (5.20).

At $u = 0$, $\frac{\mathrm{d}}{\mathrm{d}u}u^{-1/2}$ diverges. This is hard to compare to the result in (5.20), but atleast shows the same form of a $u^{-3/2}$ dependence with a point source at the origin of opposite sign. This also agrees qualitatively with the plot of the corresponding series of spheroidal harmonics (5.23) in Figure 5.1.

The main takeaway from this analysis is that the image in the low frequency limit lies on the segment $\bar{\xi} > 1$, or $0 \le z \le b, \rho = 0$. Since the low frequency expansions of the Bessel functions only involve polynomial coefficients in terms of n for each order, we would naturally expect that the higher orders could also be expressible in terms of a spheroidal harmonic series similar to (5.23), with polynomial or rational coefficients in terms on n - a series of this type converges except for $\bar{\xi} = 1$ on the singularity. This suggests that the exact problem for any frequency is also singular on this segment only.

5.4 Watson transformation

In 1918 Watson [49] devised a way to transform the standard multipole expansion into a series that converges faster on the sphere surface. The analysis is complicated but basically in the series for $V = V_{\mathrm{e}} + V_{\mathrm{s}}$ each term is recognized as the residue of $(2\nu+1)\frac{j_\nu(ka)h_\nu(kr) - h_\nu(ka)j_\nu(kr)}{h_\nu(ka)\sin\nu\pi}h_\nu(kd)P_\nu(\cos\theta)$ at $\nu = n$, so the series can be replaced by a contour integral that encloses all poles at $n = 0, 1, 2, 3...$:

$$V = \int (2\nu+1)\frac{j_\nu(ka)h_\nu(kr) - h_\nu(ka)j_\nu(kr)}{h_\nu(ka)\sin\nu\pi}h_\nu(kd)P_\nu(\cos\theta)\mathrm{d}\nu. \tag{5.27}$$

In turn this contour integral is recognized as the sum of residues over a different set of poles at $h_\nu(ka) = 0$, which occur at complex values of ν. Skipping the details, the final result is

$$V = \pi\sum_{s=1}^{\infty}(2\nu_s+1)\frac{j_{\nu_s}(ka)h_{\nu_s}(kd)}{\sin(\nu_s\pi)\partial_{\nu_s}h_{\nu_s}(ka)}h_{\nu_s}(kr)P_{\nu_s}(-\cos\theta). \tag{5.28}$$

where ν_s is the s^{th} complex zero of $h_\nu(ka) = 0$, ordered in increasing magnitude and ignoring zeros below the real line. This has not been proved but has been checked numerically, and is similar to the result in [50] for a

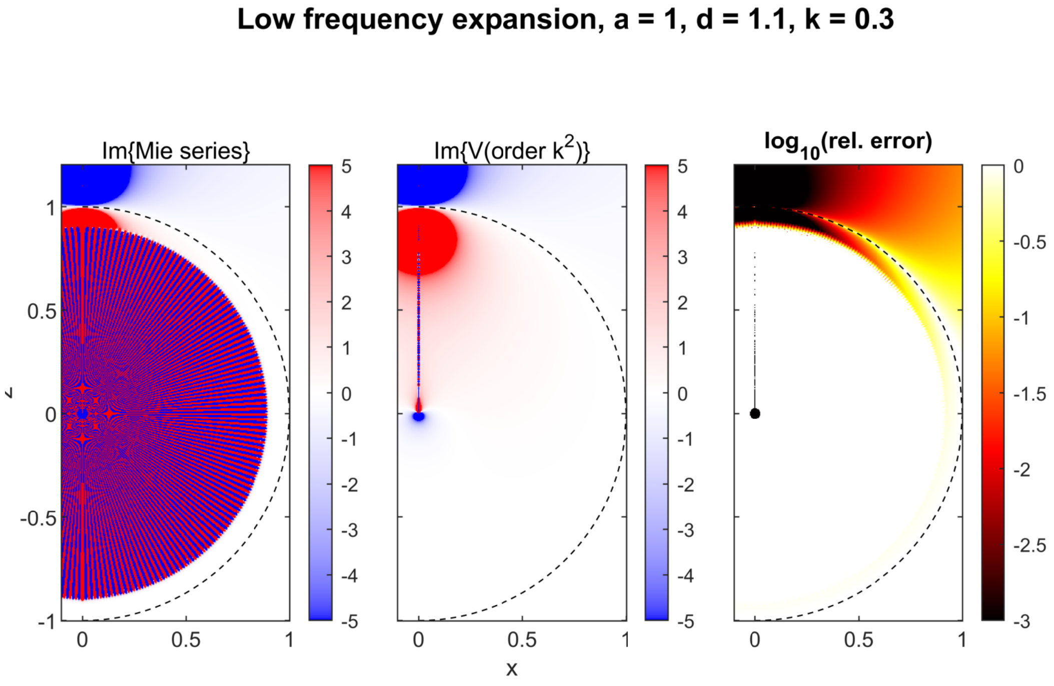

Figure 5.1: Comparison of the potential V computed by the Mie series (5.2) to the low frequency expansion, computed as a series of spheroidal harmonics (5.23), for a small $ka = .3$. The real parts are ignored since they are very small. The low frequency line image is revealed, along with the "divergent" point image at the origin that regularizes the line distribution in (5.20).

different boundary condition. As a basic analytical check, we can at least see that $V(r = a) = 0$. The zeros of the Hankel functions must be found as a function of ν for a fixed argument ka; only approximate formulas are available [64, 65, 66], so a root finding algorithm must be used to acquire full accuracy. This transformation was initially introduced to deal with the slow convergence of the multipole series, both near the surface and in the high frequency limit. But it may also provide the analytic continuation of V inside the sphere - the rate of convergence of the series depends primarily on θ, unlike the standard multipole series whose convergence depends on r. If V is only singular for $\theta = 0$ (on the z axis for $z > 0$), then this transformed series should converge everywhere except $\theta = 0$.

For context, we'll look at the Watson transform applied to the problem of a point charge inside an infinite conducting cylinder, where the transformed series converges everywhere except the image singularity which is an open disk on the $z = 0$ plane as seen in Chapter 2. Recapitulating this result for the source charge on the axis: the integral solution for the total potential is

$$V_{\text{cylinder}} = \frac{2}{\pi}\int_0^\infty \frac{I_0(t)K_0(t\rho) - K_0(t)I_0(t\rho)}{I_0(t)}\cos(tz)\mathrm{d}t, \tag{5.29}$$

whose convergence depends on ρ, diverging for $\rho > 2$ (twice the cylinder radius). The Watson-transformed series is [30, 31]

$$V_{\text{cylinder}} = 2\sum_{s=1}^{\infty} \frac{J_0(k_s\rho)e^{-k_s|z|}}{k_s J_1(k_s)^2}, \tag{5.30}$$

whose convergence depends on z, and converges for all $z \neq 0$ where the image lies. k_s is the s^{th} (real) zero of $J_0(k)$. The series (5.30) is much easier to compute than (5.28) since the zeros are calculated as a function of the argument - these are much better understood and many codes are available, and also only the zeroth and first degree of the Bessel functions are needed. It seems that (5.28) is rarely computed exactly and is mostly used for studying the high frequency limit.

Figure 5.2 plots the series (5.28). The zeros were found using the Matlab function `fsolve` with starting values given by approximate formulas for the zeros in [66] (using terms up to $z^{-5/3}$ – their $z^{-7/3}$ term somehow didn't decrease the magnitude of h_ν) for small s, and in [64] for large s. The Bessel functions of complex order could be evaluated to double precision using the `CaiBessel` package on file exchange, and $\partial_\nu h_\nu(ka)$ was differentiated numerically. The Legendre function was computed from its hypergeometric series. One of the main problems is that the starting values may not be accurate enough – `fsolve` may find the same zeros for different s. In Figure 5.2 the terms for each s were calculated accurately, but the series itself cannot be calculated near the z-axis using floating point arithmetic due to catastrophic cancellation, despite the series converging analytically as seen in the next section. The Watson series should fail in the static limit, since then the radial eigenfunctions are r^ν, but $a^\nu \neq 0$ for any finite ν.

5.4.1 Convergence of Watson series

The series converges slowest near $\theta = 0$ due to the behavior of $P_{\nu_s}(x \to -1)$ for large s. To derive the region of space where the series actually converges, we attempt to find the analytic limit of the series terms in (5.28) as $s \to \infty$. From inverting the limit of the z-zeros as a function of ν for large $|\nu|$ (equivalently large s) [66], we obtain the limit of the zeros in terms of the product log function ("Lambert W function") $W(x)$:

$$\nu_s \to -\frac{1}{2} + \frac{i\pi\left(s-\frac{1}{4}\right)}{W\left(\left(s-\frac{1}{4}\right)\frac{2\pi}{ez}\right)}. \tag{5.31}$$

This can be further simplified using the first term in the asymptotic expansion $W(x) \to \log x - 1/\log\log x + \mathcal{O}(\log\log x/\log x)$ [67]:

$$\nu_s \to -\frac{1}{2} + \pi\left(s-\frac{1}{4}\right)\left[\frac{\pi}{2}\log\left(\left(s-\frac{1}{4}\right)\frac{2\pi}{ez}\right)^{-2} + i\log\left(\left(s-\frac{1}{4}\right)\frac{2\pi}{ez}\right)^{-1}\right] \tag{5.32}$$

which coincides with the result of [64]. It gives mildly larger imaginary and real parts than (5.31), according the second order $-1/\log\log x$ term. We have to be careful in taking the limit of the zeros themselves since it is not clear how the second order terms in the approximation will affect the limits of the Bessel and Legendre functions. For example, the limiting behavior of the Hankel functions very much depends of the argument of ν in the complex plane - for $\nu \to +\infty$ (real), it increases as the Bessel function of the second kind $y_\nu(z)$, but for $\nu \to i\infty$, it increases as the Bessel function of the first kind $j_\nu(z)$. As noted in [64] and from inspection of (5.32), the imaginary part of the zeros grows faster than the real part so that $\arg(\nu) \to \pi/2$, but the real part still grows as $s \to \infty$. The limit of the spherical Bessel function $j_\nu(z)$ for $|\nu| \to \infty$ is, directly from its series expression

$$j_\nu(z) \to \frac{\sqrt{\pi}/2}{\Gamma(\nu+3/2)}\left(\frac{z}{2}\right)^\nu \tag{5.33}$$

and the spherical Hankel function $h_\nu(z)$ can be obtained from the relation

$$h_\nu(z) = \frac{j_{-\nu-1}(z) - e^{-i\pi(\nu+1/2)}j_\nu(z)}{i\sin(\pi(\nu+1/2))}. \tag{5.34}$$

The limit of $h_\nu(z)$ is dominated by either j_ν or $j_{-\nu-1}$, depending on z and ν. In our case we find numerically that the j_ν part dominates for $z = kr > a$, and the $j_{-\nu}$ part dominates for $kr < a$. In terms of computing the field in the physical region outside the sphere, then we can take $h_\nu(kr) \to 2j_\nu(kr)$, whereas for inside the sphere, we can take $h_\nu(kr) \to j_{-\nu-1}(kr)/i/\sin(\pi\nu)$.

And for the limit for $\partial_\nu h_\nu(ka)$, we can differentiate (5.34), and it appears numerically that the j_ν term dominates the $j_{-\nu-1}$ term (proof of this is needed). With this assumption, the limit can then be simplified to

$$\partial_\nu h_\nu(z) \to -\left(\frac{z}{2}\right)^\nu \frac{\sqrt{\pi}/2}{\Gamma(\nu+3/2)}\log\left(\frac{2\nu+3}{z}\right). \tag{5.35}$$

The Legendre function goes as, for $|\nu| \to \infty$ [48]

$$P_\nu(-\cos\theta) \to \sqrt{\frac{2}{\pi\nu\sin\theta}}\cos\left(\left(\nu+\frac{1}{2}\right)(\pi-\theta) - \frac{\pi}{4}\right). \tag{5.36}$$

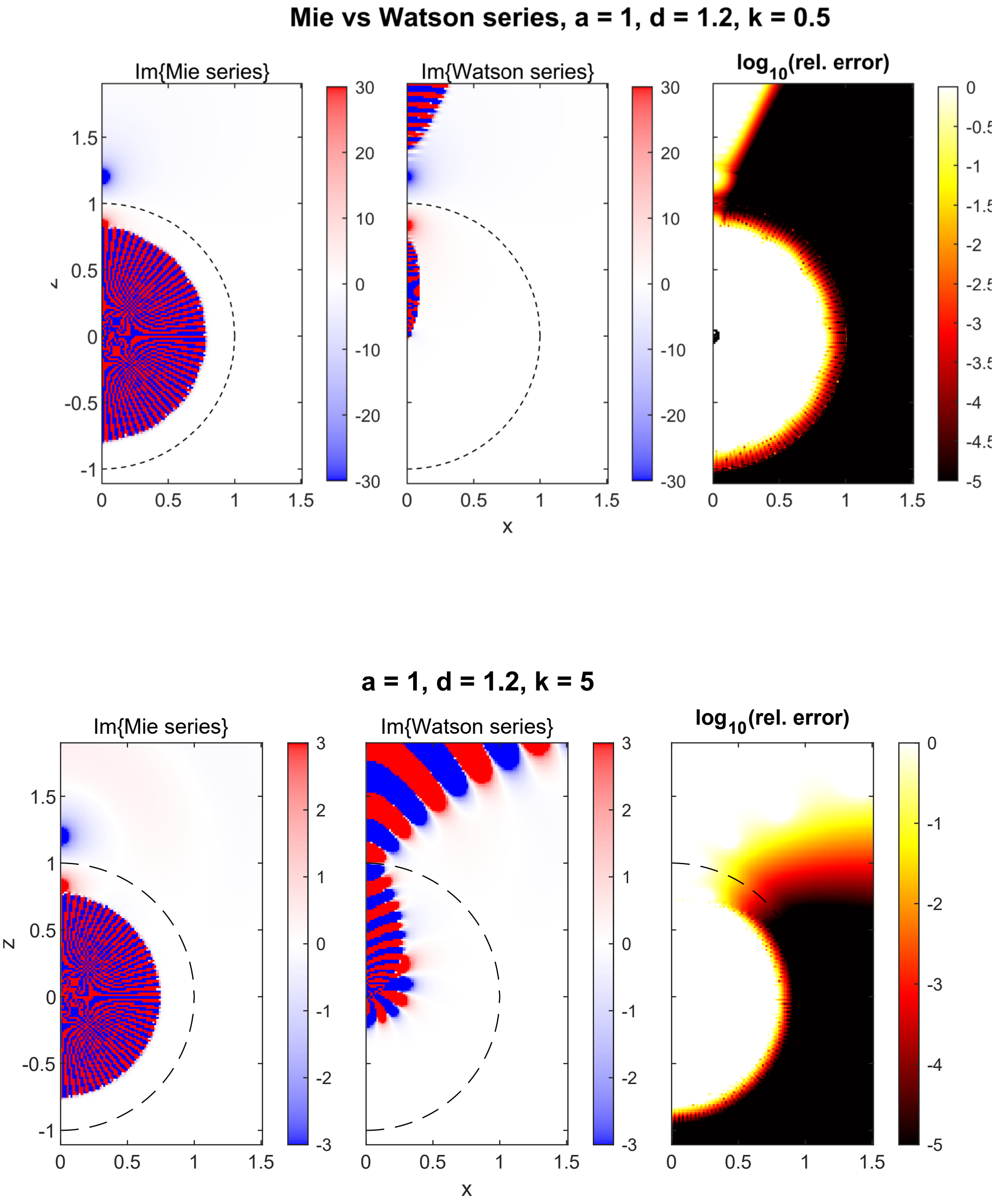

Figure 5.2: Comparison of the Mie series (5.2) to the Watson series (5.28) for $k = 0.5$ and $k = 5$ (looking at the imaginary parts is sufficient). Left: the potential calculated via the Mie series is plotted in all space including the region $r < b$ where it diverges, using up to $n = 90$ terms for both both values of k. Center: the Watson series is evaluated with up to $s = 250$ terms for $k = 0.5$, and to $s = 100$ for $k = 5$, which has not converged to any accuracy in regions near $\theta = 0$ – convergence is too slow for floating point computation due to overflow, but a rough derivation at the end of this chapter suggests that the series does converge for $\theta > 0$. Right: the relative error between the two series, showing that the series are equal where they have converged. This shows that the Watson series provides the analytical continuation of the potential for at least some region within the sphere $r < b$.

Then altogether the limit of the series coefficients in (5.28) is governed by

$$(2\nu+1)\frac{j_\nu(ka)h_\nu(kd)}{\sin(\nu\pi)\partial_\nu h_\nu(ka)}h_\nu(kr)P_\nu(-\cos\theta) \to \begin{cases} c_1\frac{e^{i\nu\theta}}{\Gamma(\nu+3/2)^2}\left(\frac{k^2dr}{4}\right)^\nu \log\nu\sqrt{\nu} & r > a \\ c_2 e^{i\nu\theta}\left(\frac{d}{r}\right)^\nu \frac{\log\nu}{\sqrt{\nu}} & r < a \end{cases} \tag{5.37}$$

for constants c_1, c_2.

For $\theta > 0$, the coefficients in (5.37) decay exponentially for both $r > a$ and $r < a$ - for $r > a$ this can be shown via the Stirling approximation for the Gamma function and considering the absolute value. The coefficients decrease to zero reasonably quickly for most values of θ, but for $\theta \to 0$, may grow extremely large, beyond floating point precision of $\sim 10^{300}$, for intermediate $|\nu|$. These large intermediate terms make the series impractical for studying the nature of the image numerically, since the terms must cancel to converge to a much smaller V, but with only 15 digits of precision this is not possible.

So, with the above evidence that the series (5.28) does actually converge except at $\theta = 0$, the image must be confined to the segment $0 \le z \le b, \rho = 0$. Determining an expression for the image is a future goal, since (5.28) diverges on this segment.

5.5 Conclusion

We have attempted to determine the nature of the image for the problem of an acoustic spherical wave near a soft sphere, and extracted an image spherical wave to make the remaining series converge faster. The low frequency expansion can be expressed as a line integral over $0 \le z \le b$ which suggests that the image for the exact solution also lies on this segment. The Watson series supposedly provides the full analytic continuation, and so may be a key to determining the image density.

Part II

Quasi-static T-matrices

Chapter 6

Quasi-static T-matrix for the Spheroid

The T-matrix is a widely used semi-analytic technique for the study of electromagnetic scattering by particles [7, 68, 69, 70, 71, 8, 72], used to calculate the near and far field properties of the scattering of plane waves or localized sources by one or more particles. In this approach, the electric and magnetic fields are expanded as series of orthogonal basis functions, usually the vector spherical wave-functions, and the T-matrix defines the linear relationship between the expansion coefficients of the incident and scattered fields. The T-matrix is uniquely defined for a given particle, depending only on its shape and material properties. The T-matrix method is computationally much faster than finite element methods, and can easily be used to obtain orientation averaged properties, useful for particle dispersions [73], or used to study clusters, by inverting a system of T-matrices, one for each particle [74]. The T-matrix is typically obtained from the extended boundary condition method (EBCM), where it is calculated as a matrix division of the auxiliary Q- and P-matrices, whose elements are calculated numerically via surface integrals of the basis functions. It may also be possible for simple shapes to obtain the T-matrix analytically from solving the boundary problem, for example spheroidal vector wave functions have been used to calculate the T-matrix for a spheroid [75]. The T-matrix is typically used to study time harmonic wave phenomena in electrodynamics and acoustics governed by the scalar or vector Helmholtz equation [8], but has recently been specified to static or quasi-static fields governed by Laplace's equation [76, 77, 78]. For plane wave scattering, the solution for a spheroid has been expanded to 3rd order in size-parameter in 1953 [79], and more recently in with connection to the T-matrix [27]. The 3rd order expansion for plane wave incidence only requires the first few elements in the T-matrix corresponding to electric dipoles, quadrupoles and octopoles, and magnetic dipoles. But for close sources, mathematically the entire T-matrix may be necessary to compute the field to a desired order in size parameter. This is evident from considering the electrostatic problem of a point dipole near a sphere, where the solution is given as a series of all multipoles, and the magnitude of each multipole is equivalent to an element of the T-matrix for the sphere. This is the problem we tackle in this chapter, but for a spheroid excited by a slowly oscillating electric or magnetic dipole.

In Ref. [80] analytic expressions were obtained for the long-wavelength limit of the T-matrix block for electric-electric multipole coupling, $\mathbf{T}^{22}$, of a prolate spheroid. There the zeroth order in the low frequency expansion was considered which is equivalent to an electrostatic problem. The matrix elements were determined by solving the corresponding boundary problem for Laplace's equation using spheroidal harmonics, and applying the expansions relating spherical/spheroidal harmonics [52, 81, 82] to express the scattered field in terms of spherical harmonics and from there extract the entries of the T-matrix. Here we extend the approach to the next two orders in frequency, including the blocks governing interactions between electric and magnetic multipoles. The problem is more complicated as it can no longer be reduced to simply solving Laplace's equation, but analytic results can still be found. Unlike for $\mathbf{T}^{22}$, where the quasi-static limit coincides with an exact electrostatics problem, the quasi-static limits of the other blocks are only physically meaningful as approximations of the corresponding time harmonic problem.

In this chapter we briefly recap of the T-matrix formalism and of the main notations, then summarize the results obtained in Ref. [80] for $\mathbf{T}^{22}$. Then we derive the quasi-static limit of $\mathbf{T}^{21}$,$\mathbf{T}^{12}$ $\mathbf{T}^{11}$ for general axisymmetric particles and derive analytic expressions for the matrix elements. Finally we use these expressions to derive simple conditions for the plasmon resonances in terms of generalized depolarization factors for spheroids, and show that higher multipole resonances actually have more than one resonant wavelength.

6.1 General approach/notations

6.1.1 T-matrix formalism

We first summarize the T-matrix formalism for electromagnetic scattering as presented in Mishchenko [83], which solves the scattering problem of some arbitrary but known time-harmonic excitation field $\mathbf{E}_\mathrm{e}, \mathbf{H}_\mathrm{e}$ incident on some particle. We will consider a particle with finite size, homogeneous and non-magnetic, in a non-absorbing medium. A time dependence $e^{-i\omega t}$ is implied and omitted from the notation. The permittivity inside and outside the particle are denoted ε_i , ε_o, with their ratio $\varepsilon = \varepsilon_\mathrm{i}/\varepsilon_\mathrm{o}$ and relative refractive index $s = \sqrt{\varepsilon}$ (possibly complex). The wavenumber inside and outside the particle are denoted k_i and k_o with $k_\mathrm{i} = sk_\mathrm{o}$. The external field creates an internal field $\mathbf{E}_\mathrm{i}, \mathbf{H}_\mathrm{i}$ inside the scatterer and a scattered field $\mathbf{E}_\mathrm{s}, \mathbf{H}_\mathrm{s}$, so that the field outside the particle is $\mathbf{E}_\mathrm{o} = \mathbf{E}_\mathrm{e} + \mathbf{E}_\mathrm{s}$, $\mathbf{H}_\mathrm{o} = \mathbf{H}_\mathrm{e} + \mathbf{H}_\mathrm{s}$. These fields satisfy the boundary conditions at the surface of the scatterer, with $\hat{\mathbf{n}}$ the unit normal vector:

$$\begin{aligned} \varepsilon\hat{\mathbf{n}} \cdot \mathbf{E}_\mathrm{i} &= \hat{\mathbf{n}} \cdot \mathbf{E}_\mathrm{o}, \qquad & \hat{\mathbf{n}} \times \mathbf{E}_\mathrm{i} &= \hat{\mathbf{n}} \times \mathbf{E}_\mathrm{o}, \\ \hat{\mathbf{n}} \cdot \mathbf{H}_\mathrm{i} &= \hat{\mathbf{n}} \cdot \mathbf{H}_\mathrm{o}, \qquad & \hat{\mathbf{n}} \times \mathbf{H}_\mathrm{i} &= \hat{\mathbf{n}} \times \mathbf{H}_\mathrm{o}, \end{aligned} \tag{6.1}$$

and the Sommerfeld radiation condition for the scattered field at infinity, that energy may only be radiated outward. In the electrostatic limit this means the scattered field has no singularities outside the particle and decreases to zero as $r \to \infty$. The main ansatz of the T-matrix formalism is that due to the linearity of the Helmholtz equation, the fields can be expanded as series of vector spherical wave functions:

$$\mathbf{E}_\mathrm{e} = E_0 \sum_{n,m} a_n^m \mathbf{RgM}_n^m(k_\mathrm{o}\mathbf{r}) + b_n^m \mathbf{RgN}_n^m(k_\mathrm{o}\mathbf{r}), \tag{6.2}$$

$$\mathbf{H}_\mathrm{e} = H_0 \sum_{n,m} a_n^m \mathbf{RgN}_n^m(k_\mathrm{o}\mathbf{r}) + b_n^m \mathbf{RgM}_n^m(k_\mathrm{o}\mathbf{r}), \tag{6.3}$$

$$\mathbf{E}_\mathrm{i} = E_0 \sum_{n,m} c_n^m \mathbf{RgM}_n^m(k_\mathrm{i}\mathbf{r}) + d_n^m \mathbf{RgN}_n^m(k_\mathrm{i}\mathbf{r}), \tag{6.4}$$

$$\mathbf{H}_\mathrm{i} = H_0 s \sum_{n,m} c_n^m \mathbf{RgN}_n^m(k_\mathrm{i}\mathbf{r}) + d_n^m \mathbf{RgM}_n^m(k_\mathrm{i}\mathbf{r}), \tag{6.5}$$

$$\mathbf{E}_\mathrm{s} = E_0 \sum_{n,m} p_n^m \mathbf{M}_n^m(k_\mathrm{o}\mathbf{r}) + q_n^m \mathbf{N}_n^m(k_\mathrm{o}\mathbf{r}), \tag{6.6}$$

$$\mathbf{H}_\mathrm{s} = H_0 \sum_{n,m} p_n^m \mathbf{N}_n^m(k_\mathrm{o}\mathbf{r}) + q_n^m \mathbf{M}_n^m(k_\mathrm{o}\mathbf{r}), \tag{6.7}$$

where E_0 is the incident electric field strength and $H_0 = E_0 k_\mathrm{o}/(i\omega\mu_0)$. With this ansatz, the scattered field automatically satisfies the Sommerfeld radiation condition. $\mathbf{M}$, $\mathbf{N}$ are the radiating spherical vector wave-functions and $\mathbf{RgM}$, $\mathbf{RgN}$ are the regular wave-functions, corresponding to magnetic and electric multipolar fields, respectively. These are defined as:

$$\mathbf{M}_{nm}^c = \gamma_n^m \boldsymbol{\nabla} \times [\mathbf{r}\, h_n(kr) P_n^m(\cos\theta) e^{im\phi}], \qquad \mathbf{N}_{nm}^c = \frac{1}{k} \boldsymbol{\nabla} \times \mathbf{M}_{nm}^c, \tag{6.8}$$

$$\mathbf{RgM}_{nm}^c = \gamma_n^m \boldsymbol{\nabla} \times [\mathbf{r}\, j_n(kr) P_n^m(\cos\theta) e^{im\phi}], \qquad \mathbf{RgN}_{nm}^c = \frac{1}{k} \boldsymbol{\nabla} \times \mathbf{RgM}_{nm}^c, \tag{6.9}$$

$$\text{where } \gamma_n^m = \sqrt{\frac{2n+1}{4\pi n(n+1)} \frac{(n-m)!}{(n+m)!}}. \tag{6.10}$$

j_n and h_n are the spherical Bessel and Hankel functions of the first kinds. These are defined for integer $n \geq 0$ and $|m| \leq n$ (although the $n = 0$ functions are not physically relevant). The associated Legendre functions $P_n^m(\cos\theta)$ are here defined without the $(-)^m$ prefactor, so our wave-functions differ by $(-)^m$ to those in appendix C of [8].

The problem is to determine the coefficients $c_n^m, d_n^m, p_n^m, q_n^m$ that satisfy the boundary conditions (6.1). By linearity of Maxwell's equations, the coefficients are related by linear expressions commonly expressed in matrix form as:

$$\begin{bmatrix} \mathbf{p} \\ \mathbf{q} \end{bmatrix} = \begin{bmatrix} \mathbf{T}^{11} & \mathbf{T}^{12} \\ \mathbf{T}^{21} & \mathbf{T}^{22} \end{bmatrix} \begin{bmatrix} \mathbf{a} \\ \mathbf{b} \end{bmatrix} = \mathbf{T} \begin{bmatrix} \mathbf{a} \\ \mathbf{b} \end{bmatrix}, \tag{6.11}$$

which defines the T-matrix. The column vectors **a**, **b**, **c**, **d**, **p** and **q** contain a_n^m, b_n^m c_n^m, d_n^m, p_n^m and q_n^m as components, for all n and m. Within the EBCM, one typically also defines the P- and Q-matrices as:

$$\begin{bmatrix} \mathbf{a} \\ \mathbf{b} \end{bmatrix} = \begin{bmatrix} \mathbf{Q}^{11} & \mathbf{Q}^{12} \\ \mathbf{Q}^{21} & \mathbf{Q}^{22} \end{bmatrix} \begin{bmatrix} \mathbf{c} \\ \mathbf{d} \end{bmatrix}, \tag{6.12}$$

$$\begin{bmatrix} \mathbf{p} \\ \mathbf{q} \end{bmatrix} = - \begin{bmatrix} \mathbf{P}^{11} & \mathbf{P}^{12} \\ \mathbf{P}^{21} & \mathbf{P}^{22} \end{bmatrix} \begin{bmatrix} \mathbf{c} \\ \mathbf{d} \end{bmatrix}, \tag{6.13}$$

and we also introduce the matrix $\mathbf{R} = \mathbf{Q}^{-1}$ which is essentially the T-matrix for the internal field. Note that Ref. [83] uses **RgQ** instead of **P**.

For axisymmetric particles (such as spheroids), a major simplification is that all matrices are decoupled for each m, and we may therefore treat each m separately.

As an example, for an axisymmetric particle who's surface is defined as $r = r(\theta)$, the n,k entry of the $\mathbf{Q}^{12}$ block for some m may be calculated in the null-field approach via (but we will use a different approach):

$$Q^{12}_{nk|m} = \propto \int_0^\pi \mathrm{d}\theta P_n^m(\cos\theta) P_k^m(\cos\theta) r(\theta) h_n(k_\mathrm{o} r(\theta)) \frac{\partial}{\partial\theta}[r(\theta) j_k(k_\mathrm{i} r(\theta))] \frac{\partial r(\theta)}{\partial\theta}. \tag{6.14}$$

Moreover, for particles with reflection symmetry with respect to the $z = 0$ plane (like spheroids), half of the matrix elements are zero, namely:

$$A^{11}_{nk} = A^{22}_{nk} = 0 \quad n+k \text{ odd}, \tag{6.15}$$

$$A^{21}_{nk} = A^{12}_{nk} = 0 \quad n+k \text{ even}, \tag{6.16}$$

for $A = P, Q, R, T$.

6.1.2 Spheroidal coordinates

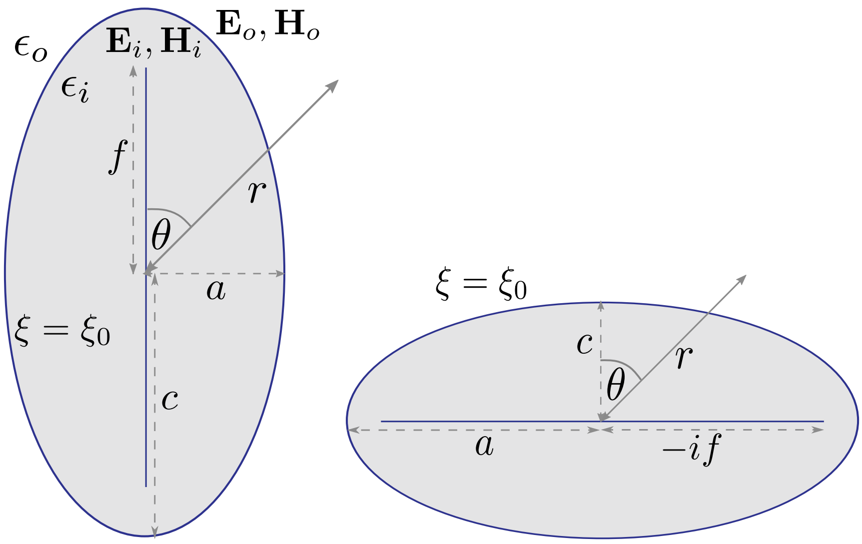

Figure 6.1: Schematics of the scattering problem for prolate and oblate spheroids.

Consider a dielectric spheroid (prolate or oblate) of semi-height c along the z-axis and semi-width a along x, y, as in Figure 6.1. It will be convenient to define oblate spheroidal coordinates and parameters by exactly the same formulae, since this choice means the T-matrix elements for prolate and oblate spheroids will also have exactly the same expressions. We define the focal parameter $f = \sqrt{c^2 - a^2}$. Then prolate spheroids have $c > a$, half focal-length f, and oblate spheroids have $a > c$, focal disk radius $-if = \sqrt{a^2 - c^2}$. The spheroidal coordinates ξ, η are defined in terms of r^+, r^-, the distance from the top and bottom focal points:

$$\xi = \frac{r^+ + r^-}{2f}, \qquad \eta = \frac{r^+ - r^-}{2f}$$

$$r^\pm = \sqrt{r^2 \pm 2fr\cos\theta + f^2}. \tag{6.17}$$

for both prolate and oblate. For the oblate spheroid, $\xi = i\chi$ where χ is the real oblate spheroidal coordinate from Chapter 3. $\xi = \xi_0 = c/\sqrt{c^2 - a^2}$ defines the surface of our scatterer. For prolate spheroidal coordinates, ξ_0 ranges from 1 (needle) to ∞ (large sphere), while for oblate coordinates, ξ_0 ranges from 0 (disk) to $-i\infty$ (large sphere).

The solution of Laplace's equation in spheroidal harmonics involves the product of Legendre functions of the first or second kind $P_n^m(\xi)P_n^m(\eta)$, or $Q_n^m(\xi)P_n^m(\eta)$. Their derivatives are denoted with a prime $'$.

6.1.3 Quasi-static/long-wavelength approximation

Quasi-static here means that the wavelength of the light both inside and outside the particle is long in comparison to the particle size. As per Ref. [27] we shall define a size parameter $X = k_o c$, where for small particles relative to the wavelength, $X \ll 1$ and the fields may be considered as asymptotic expansions in powers of X, and here we consider just the lowest two orders. This approximation also requires $k_i c = sX \ll 1$, so the relative refractive index s must not be too large. This definition for X is convenient here, but as shown in Ref. [27], it is usually more relevant to define the size parameter in terms of the radius of the sphere of equivalent volume. One should also note that spherical Bessel functions of higher order n can be well approximated by their dominant term (small X approximation) for up to $X \lesssim n$ [84], so our final expressions for matrix elements for large n,k will be valid for relatively large X.

In this analysis it is crucial to be aware of how the basis functions and matrix elements depend on X. In the near field, $X \approx k_o r$ (using the superscript $^{(\cdot)}$ notation to denote the order of the expansion in X rather than the type of Bessel function used in the wave functions):

$$\mathbf{RgM}_{nm}^{(0)} = \mathcal{O}(X^n), \qquad \mathbf{M}_{nm}^{(0)} = \mathcal{O}(X^{-n-1}), \tag{6.18}$$

$$\mathbf{RgN}_{nm}^{(0)} = \mathcal{O}(X^{n-1}), \qquad \mathbf{N}_{nm}^{(0)} = \mathcal{O}(X^{-n-2}), \tag{6.19}$$

and $E_0 = \mathcal{O}(X^0)$ while $H_0 = \mathcal{O}(X^1)$. The quasistatic limit of the Q-matrix and R-matrix elements take a special form for a spheroidal particle [85, 86] and the order of the dominant terms for all matrices are summarized below [85, 27]:

$$\begin{aligned} Q_{nk}^{11} &= \mathcal{O}(X^{[n<k](k-n+2)}), \quad Q_{nk}^{21} = \mathcal{O}(X^{[n<k](k-n+1)}), \\ Q_{nk}^{12} &= \mathcal{O}(X^{[n<k](k-n+1)}), \quad Q_{nk}^{22} = \mathcal{O}(X^{[n<k](k-n)}), \end{aligned} \tag{6.20}$$

where $[n<k] = 1$ if $n<k$ and 0 otherwise; this factor is a feature for spheroids only. For **P**:

$$\begin{aligned} P_{nk}^{11} &= \mathcal{O}(X^{k+n+3}), \qquad P_{nk}^{12} = \mathcal{O}(X^{k+n+2}), \\ P_{nk}^{21} &= \mathcal{O}(X^{k+n+2}), \qquad P_{nk}^{22} = \mathcal{O}(X^{k+n+1}). \end{aligned} \tag{6.21}$$

T has identical behavior as **P**, and **R** as **Q**, so:

$$R_{nk}^{ij} \propto Q_{nk}^{ij} \text{ and } T_{nk}^{ij} \propto P_{nk}^{ij} \quad \text{For } i,j = 1,2. \tag{6.22}$$

The aim of this work is to find analytic expressions for these dominant terms for all elements of **T**. In the process, we will also derive matrix elements for **P**, **Q**, and **R**, except for the lower triangular parts of **Q** and **R**, because they reduce to zero as $X \to 0$ for spheroids. Physically, the 22 block dominates the other blocks for small sizes because we have a dielectric particle with no magnetic response ($\mu = \mu_0$) – the magnetic multipoles are only excited due to electrodynamic coupling with the electric field, which requires a non-zero frequency.

6.2 Summary for 22 blocks

The 22 matrix blocks are the most important for low frequency scattering since their matrix elements dominate the other blocks, as per (6.22). Also, to zeroth order in wavelength, these blocks coincide (up to some prefactors) with the analogous T-matrix for electrostatics, where electrostatic potentials are used and expanded on bases of spherical harmonics. This chapter focuses on the other matrix blocks so we summarize the results and point out that the details are given in Ref. [80]. The problem of a spheroid in arbitrary electrostatic excitation is easily solved if the incident and scattered fields are expanded in terms of *spheroidal* harmonics - the scattered coefficients are simply multiplied by some constant relative to the incident coefficients. The expansion relations between spherical harmonics and spheroidal harmonics can be used to convert the solution in terms of spheroidal harmonics to a solution in terms of spherical harmonics, relating the coefficients of the scattered potential linearly to those of the known incident potential. Then the T-matrix is extracted from this linear relationship. The results for $\mathbf{P}^{22}$, $\mathbf{Q}^{22}$, $\mathbf{R}^{22}$, $\mathbf{T}^{22}$ are:

$$\begin{aligned} P^{22(0)}_{nk|m} &= -is^{k-1}(k_{\mathrm{o}}f)^{n+k+1}\, B^m_n B^m_k (s^2-1)(\xi_0^2-1)(-)^m \\ &\times \sum_{p=|m|}^{\min(n,k)} \frac{e_{nk}e_{np}(2p+1)\, P^{-m}_p(\xi_0)P^{m\prime}_p(\xi_0)}{(n-p)!!(n+p+1)!!(k-p)!!(k+p+1)!!}, \end{aligned} \tag{6.23}$$

$$\begin{aligned} Q^{22(0)}_{nk|m} &= s^{k-1}\delta_{nk} + s^{k-1}(k_{\mathrm{o}}f)^{k-n}\, \frac{B^m_k}{B^m_n}(s^2-1)(\xi_0^2-1) \\ &\times \sum_{p=n}^{k} e_{nk}e_{np}\frac{(-)^{(p-n)/2}(2p+1)(n+p-1)!!}{(p-n)!!(k-p)!!(k+p+1)!!} Q^{-m}_p(\xi_0)P^{m\prime}_p(\xi_0), \end{aligned} \tag{6.24}$$

$$\begin{aligned} R^{22(0)}_{nk|m} &= s^{1-n}(k_{\mathrm{o}}f)^{k-n}\, \frac{B^m_k}{B^m_n} \\ &\times \sum_{p=n}^{k} e_{nk}e_{np}\frac{(-)^{(p-n)/2}(2p+1)(n+p-1)!!}{(p-n)!!(k-p)!!(k+p+1)!!}\frac{1}{1+(s^2-1)L^m_p(\xi_0)}, \end{aligned} \tag{6.25}$$

$$\begin{aligned} T^{22(0)}_{nk|m} &= i(k_{\mathrm{o}}f)^{n+k+1}\, B^m_n B^m_k (s^2-1)(\xi_0^2-1)(-)^m \\ &\times \sum_{p=|m|}^{\min(n,k)} \frac{e_{nk}e_{np}(2p+1)}{(n-p)!!(n+p+1)!!(k-p)!!(k+p+1)!!}\frac{P^{-m}_p(\xi_0)P^{m\prime}_p(\xi_0)}{1+(s^2-1)L^m_p(\xi_0)}, \end{aligned} \tag{6.26}$$

where

$$B^m_n = \frac{1}{(2n-1)!!}\sqrt{\frac{(n+1)(n+m)!(n-m)!}{n(2n+1)}}, \tag{6.27}$$

$$e_{nk} = \begin{cases} 1 & n+k \text{ even} \\ 0 & n+k \text{ odd} \end{cases}, \tag{6.28}$$

and we define “generalized depolarization factors”:

$$L^m_n = (\xi_0^2-1)P^{m\prime}_n(\xi_0)Q^{-m}_n(\xi_0) \tag{6.29}$$

which will be further discussed in Sec. 6.6.

6.3 Quasistatic limit of $\mathbf{T}^{21}$, $\mathbf{T}^{12}$

We can now derive the quasi-static limits of the matrix elements, first outlining the general approach for any geometry, then giving analytic results for spheroids.

6.3.1 General approach

While the quasi-static limit of $\mathbf{T}^{22}$ can be found by considering the lowest order in X, solving Laplace's equation, the blocks $\mathbf{T}^{21}$ and $\mathbf{T}^{12}$ are zero to lowest order in X, so the next order in X must be considered.

We focus on obtaining $\mathbf{T}^{21}$, as $\mathbf{T}^{12}$ can then be obtained through

$$T^{12}_{nk|m} = -T^{21}_{kn|m}. \tag{6.30}$$

To extract the quasi-static limit of $\mathbf{T}^{21}$, we consider a particular excitation consisting of only magnetic multipoles - that is

$$\mathbf{E}_\mathrm{e} = E_0 \sum_{nm} a_n^m \mathbf{RgM}_{nm}^{(0)}(k_\mathrm{o}\mathbf{r}), \tag{6.31}$$

$$\mathbf{H}_\mathrm{e} = H_0 \sum_{nm} a_n^m \mathbf{RgN}_{nm}^{(0)}(k_\mathrm{o}\mathbf{r}). \tag{6.32}$$

Furthermore, considering the orders of the spherical vector wave-functions given in (6.18)-(6.19), we will impose that the coefficients a_n^m go as $a_n^m \propto X^{1-n}$, so that all multipole terms in the expansions are of the same order in X, and as a result we have $\mathbf{E}_\mathrm{i}, \mathbf{H}_\mathrm{i} = \mathscr{O}(X^1)$, with every term in the sum being $\mathscr{O}(X^1)$. It can then be shown that all elements of $\mathbf{T}^{21}$ will be obtainable by reduction to the lowest non-zero order of X. A physical example where $a_n^m \propto X^{1-n}$ is a low frequency radiating magnetic dipole located outside the scatterer. If we instead considered a plane wave excitation, only the lowest order multipoles would be non-negligible, and we would only obtain information about the initial rows of the matrices.

We now analyze which terms in the series of the incident and scattered fields can be neglected, taking into account the dependence of lowest orders of the elements in $\mathbf{T}^{21}$, $\mathbf{R}^{21}$ from 6.20–6.22. The significant parts of the internal and scattered fields to $\mathscr{O}(X^1)$ will be

$$\begin{aligned}
\mathbf{E}_\mathrm{i} &= E_0 \sum_{n,m} c_n^m \mathbf{RgM}_{nm}^{(0)}(k_\mathrm{i}\mathbf{r}) + d_n^m \mathbf{RgN}_{nm}^{(0)}(k_\mathrm{i}\mathbf{r}),\\
\mathbf{H}_\mathrm{i} &= sH_0 \sum_{n,m} c_n^m \mathbf{RgN}_{nm}^{(0)}(k_\mathrm{i}\mathbf{r}),\\
\mathbf{E}_\mathrm{s} &= E_0 \sum_{n,m} q_n^m \mathbf{N}_{nm}^{(0)}(k_\mathrm{o}\mathbf{r}),\\
\mathbf{H}_\mathrm{s} &= \mathscr{O}(X^2).
\end{aligned} \tag{6.33}$$

In the long-wavelength limit the magnetic field does not interact with the particle. The magnetic boundary conditions are therefore solved simply by setting the internal magnetic field identical to the external field, that is

$$\begin{gathered}
c_n^m = s^{-n} a_n^m\\
\Leftrightarrow\ Q_{nk}^{11(0)} = \delta_{nk} s^n, \qquad R_{nk}^{11(0)} = \delta_{nk} s^{-n}.
\end{gathered} \tag{6.34}$$

This also means that the magnetic-multipolar part of the internal electric field is equal to the magnetic-multipolar part of the incident electric field. However, this alone does not satisfy the electric boundary conditions, so the problem now is to solve for the coefficients d_n^m and q_n^m, knowing both a_n^m and c_n^m. For this problem the matrix relations between the known and unknown coefficients are

$$\mathbf{q} = \mathbf{T}^{21}\mathbf{a}, \qquad \mathbf{d} = \mathbf{R}^{21}\mathbf{a}, \tag{6.35}$$

In the long-wavelength limit the vector spherical wave functions are

$$\mathbf{RgM}_{nm}^{(0)} = \gamma_n^m \frac{k^n}{(2n+1)!!}\, \mathbf{r} \times \nabla[r^n P_n^m(\cos\theta) e^{im\phi}], \tag{6.36}$$

$$\mathbf{RgN}_{nm}^{(0)} = \gamma_n^m \frac{(n+1)k^{n-1}}{(2n+1)!!}\, \nabla[r^n P_n^m(\cos\theta) e^{im\phi}], \tag{6.37}$$

$$\mathbf{M}_{nm}^{(0)} = \gamma_n^m \frac{(2n-1)!!}{ik^{n+1}}\, \mathbf{r} \times \nabla[r^{-n-1} P_n^m(\cos\theta) e^{im\phi}], \tag{6.38}$$

$$\mathbf{N}_{nm}^{(0)} = \gamma_n^m \frac{in(2n-1)!!}{k^{n+2}} \nabla[r^{-n-1} P_n^m(\cos\theta) e^{im\phi}]. \tag{6.39}$$

This means we can express the electric field as:

$$\mathbf{E}_\mathrm{e} = \mathbf{r} \times \nabla U, \tag{6.40}$$

$$\mathbf{E}_\mathrm{i} = \mathbf{r} \times \nabla U - \nabla V_\mathrm{i}, \tag{6.41}$$

$$\mathbf{E}_\mathrm{s} = -\nabla V_\mathrm{s}, \tag{6.42}$$

$$\text{with } \nabla^2 U = \nabla^2 V_\mathrm{i} = \nabla^2 V_\mathrm{s} = 0. \tag{6.43}$$

Inserting (6.40)-(6.42) into the electric boundary conditions [1]:

$$\varepsilon \partial_n V_{\mathrm{i}} - \partial_n V_{\mathrm{s}} = (\varepsilon - 1)\hat{\mathbf{n}} \cdot \mathbf{E}_{\mathrm{e}}|_S, \qquad V_{\mathrm{i}} = V_{\mathrm{s}}|_S, \tag{6.44}$$

with $\partial_n = \hat{\mathbf{n}} \cdot \nabla$. For axisymmetric particles, $\hat{\mathbf{n}} \cdot \hat{\phi} = 0$ leaving

$$\hat{\mathbf{n}} \cdot \mathbf{E}_{\mathrm{e}} = (\mathbf{r} \times \hat{\mathbf{n}}) \cdot \nabla U = \frac{\hat{\mathbf{n}} \cdot \hat{\theta}}{\sin\theta} \frac{\partial U}{\partial \phi}. \tag{6.45}$$

We can obtain expressions for $\mathbf{T}^{21}$ by solving for V_{s} to obtain $\mathbf{q}$ in terms of $\mathbf{a}$, and comparing this solution with the matrix expression (6.35).

6.3.2 Analytic expressions for spheroids

Spheroidal particles are a special case where there exists a full analytic solution to (6.44). We follow a similar approach to Ref. [80]: solve the boundary problem in terms of spheroidal harmonics and re-express this in terms of spherical harmonics by applying basis transformations. Explicitly, we want to solve for the potentials $V_{\mathrm{i}}, V_{\mathrm{s}}$, knowing U. Since U, V_{i}, V_{s} satisfy Laplace's equation, we can express them as series of spheroidal harmonics:

$$U = E_0 \sum_{n,m} A_n^m P_n^m(\xi) P_n^m(\eta) e^{im\phi}, \tag{6.46}$$

$$V_{\mathrm{i}} = E_0 \sum_{n,m} B_n^m P_n^m(\xi) P_n^m(\eta) e^{im\phi}, \tag{6.47}$$

$$V_{\mathrm{s}} = E_0 \sum_{n,m} C_n^m Q_n^m(\xi) P_n^m(\eta) e^{im\phi}. \tag{6.48}$$

(The series coefficients have dimensions of length). In light of evaluating the boundary conditions, for a spheroid we have $\hat{\mathbf{n}} = \hat{\xi}$, and

$$\hat{\xi} \cdot \hat{\theta} = \frac{\sin\theta \ \eta}{\sqrt{(\xi^2 - \eta^2)(\xi^2 - 1)}}, \tag{6.49}$$

$$\frac{\partial}{\partial n} = \frac{1}{f} \sqrt{\frac{\xi^2 - 1}{\xi^2 - \eta^2}} \frac{\partial}{\partial \xi}. \tag{6.50}$$

Due to their orthogonality, we can equate the coefficients of $P_n^m(\eta)$ in the expansions, but there is an extra factor of η in (6.49), which can be dealt with the following identity:

$$\eta P_n^m(\eta) = \frac{(n - m + 1) P_{n+1}^m(\eta) + (n + m) P_{n-1}^m(\eta)}{2n + 1}, \tag{6.51}$$

and re-indexing the sums so that all terms contain $P_n^m(\eta)$. Then the problem is solved by setting

$$B_n^m = \frac{Q_n^m(\xi_0)}{P_n^m(\xi_0)} C_n^m, \tag{6.52}$$

$$C_n^m = \frac{ifm(\varepsilon - 1) P_n^{-m}(\xi_0)}{1 + (s^2 - 1) L_n^m(\xi_0)} \left(\frac{n-m}{2n-1} P_{n-1}^m(\xi_0) A_{n-1}^m + \frac{n+m+1}{2n+3} P_{n+1}^m(\xi_0) A_{n+1}^m \right). \tag{6.53}$$

Now we must express this solution on a spherical harmonic basis. The relevant relationships between the spherical and spheroidal harmonics are

$$\left(\frac{r}{f}\right)^n P_n^m(\cos\theta) = \sum_{k=0}^{n} \alpha_{nk}^m P_k^m(\xi) P_k^m(\eta), \tag{6.54}$$

$$Q_n^m(\xi) P_n^m(\eta) = \sum_{k=n}^{\infty} \beta_{nk}^m \left(\frac{f}{r}\right)^{k+1} P_k^m(\cos\theta), \tag{6.55}$$

---

[1] The last equality comes from requiring the tangential derivatives of V_{i} and V_{s} be equal at the surface, which implies V_{i} and V_{s} are equal up to a constant which can be neglected.

where the coefficients $\alpha^m_{nk}, \beta^m_{nk}$ are

$$\alpha^m_{nk} = \begin{cases} \dfrac{(n+m)!(2k+1)}{(n-k)!!(n+k+1)!!}\dfrac{(k-m)!}{(k+m)!} & n \geq k \\ 0 \qquad n<k \;\text{ or }\; n+k \,\text{odd} \end{cases} \tag{6.56}$$

$$\beta^m_{nk} \begin{cases} (-)^{(n-k)/2+m}\dfrac{(2k+1)(n+k-1)!!}{(n-m)!(k-n)!!}\dfrac{(k-m)!}{(k+m)!} & n \leq k \\ 0 \qquad n>k \;\text{ or }\; n+k \,\text{odd.} \end{cases} \tag{6.57}$$

By substituting these expressions into the potential and electric field expressions, we find that the series coefficients satisfy

$$A^m_p = \sum_{k=p}^{\infty} \alpha^m_{kp} \frac{(k_\mathrm{o}f)^k}{(2k+1)!!}\gamma^m_k a^m_k, \tag{6.58}$$

$$q^m_n = \frac{1}{\gamma^m_n}\frac{ik_\mathrm{o}(k_\mathrm{o}f)^{p+1}}{n(2n-1)!!}\sum_{p=|m|}^{n} \beta^m_{pn} C^m_p. \tag{6.59}$$

Combining these with the relationship between C^m_n and A^m_n, we obtain an expression relating $\mathbf{q}$ and $\mathbf{a}$ which can be compared to (6.35) to obtain $\mathbf{T}^{21}$. We can also follow a similar derivation and obtain the quasi-static limit of $\mathbf{R}^{21}$. We can then obtain expressions for $\mathbf{P}^{21}$ and $\mathbf{Q}^{21}$ from their matrix relationships to $\mathbf{T}$ and $\mathbf{R}$. We have $\mathbf{Q}^{21} = -\mathbf{Q}^{22}\mathbf{R}^{21}\mathbf{Q}^{11}$, which comes from the block-wise matrix inverse formula. Similarly, we can find $\mathbf{R}^{12} = -\mathbf{R}^{11}\mathbf{Q}^{12}\mathbf{R}^{22}$ and $\mathbf{P}^{12} = -\mathbf{T}^{21}\mathbf{Q}^{11} - \mathbf{T}^{22}\mathbf{Q}^{21}$. Below we summarize the results for all matrices:

$$\begin{aligned} P^{21(0)}_{nk|m} =& (s^2-1)s^k \frac{B^m_n B^m_k}{k+1}(k_\mathrm{o}f)^{n+k+2}(-)^m m \sum_{p=|m|}^{\min(n,k+1)} e_{np}\, e_{k+1,p}\, P^{-m}_p(\xi_0)\times \\ & \frac{(p+m)(k+p+2)P^m_{p-1}(\xi_0)+(p-m+1)(k-p+1)P^m_{p+1}(\xi_0)}{(k-p+1)!!(k+p+2)!!(n-p)!!(n+p+1)!!}, \end{aligned} \tag{6.60}$$

$$\begin{aligned} Q^{21(0)}_{nk|m} =& -(s^2-1)s^k \frac{B^m_k}{B^m_n}\frac{im(k_\mathrm{o}f)^{k-n+1}}{k+1}\sum_{p=n}^{k+1} e_{np}\, e_{k+1,p}\, Q^{-m}_p(\xi_0)\times \\ & (-)^{(n-p)/2+m}(p+n-1)!!\frac{(p+m)(k+p+2)P^m_{p-1}(\xi_0)+(p-m+1)(k-p+1)P^m_{p+1}(\xi_0)}{(k-p+1)!!(k+p+2)!!(p-n)!!}, \end{aligned} \tag{6.61}$$

$$\begin{aligned} R^{21(0)}_{nk|m} =& -(s^2-1)\frac{B^m_k}{B^m_n}\frac{im(k_\mathrm{o}f)^{k-n+1}}{s^{n-1}(k+1)}\sum_{p=n}^{k+1} e_{np}\, e_{k+1,p}\, \frac{Q^{-m}_p(\xi_0)}{1+(s^2-1)L^m_p(\xi_0)}\times \\ & (-)^{(n-p)/2+m}(p+n-1)!!\frac{(p+m)(k+p+2)P^m_{p-1}(\xi_0)+(p-m+1)(k-p+1)P^m_{p+1}(\xi_0)}{(k-p+1)!!(k+p+2)!!(p-n)!!}, \end{aligned} \tag{6.62}$$

$$\begin{aligned} R^{12(0)}_{nk|m} =& -(s^2-1)\frac{B^m_k}{B^m_n}\frac{im(k_\mathrm{o}f)^{k-n+1}}{s^n n}\sum_{p=n}^{k+1} e_{np}\, e_{k+1,p}\, Q^m_p(\xi_0)\times \\ & \frac{(-)^{(n-p)/2}(p+n-1)!!}{(k-p+1)!!(k+p+2)!!(p-n)!!}\left[\frac{(p-m)(k+p+2)P^{-m}_{p-1}(\xi_0)}{1+(s^2-1)L^m_{p-1}(\xi_0)}+\frac{(p+m+1)(k-p+1)P^{-m}_{p+1}(\xi_0)}{1+(s^2-1)L^m_{p+1}(\xi_0)}\right], \end{aligned} \tag{6.63}$$

$$\begin{aligned} T^{21(0)}_{nk|m} =& -(s^2-1)\frac{B^m_n B^m_k}{k+1}(k_\mathrm{o}f)^{n+k+2}(-)^m m \sum_{p=|m|}^{\min(n,k+1)} e_{np}\, e_{k+1,p}\, \frac{P^{-m}_p(\xi_0)}{1+(s^2-1)L^m_p(\xi_0)}\times \\ & \frac{(p+m)(k+p+2)P^m_{p-1}(\xi_0)+(p-m+1)(k-p+1)P^m_{p+1}(\xi_0)}{(k-p+1)!!(k+p+2)!!(n-p)!!(n+p+1)!!}. \end{aligned} \tag{6.64}$$

The expressions for $\mathbf{P}^{21}$, $\mathbf{Q}^{21}$ and $\mathbf{R}^{12}$ were simplified using the following identity:

$$\sum_{q=p}^{r} e_{qr} \frac{(-)^{(r-q)/2}(r+q-1)!!}{(q-p)!!(q+p+1)!!(r-q)!!} = \frac{\delta_{pr}}{2r+1} \tag{6.65}$$

which can be extracted by expanding the Legendre polynomials in terms of monomials, then back in terms of Legendre polynomials, and noting their orthogonality.

$\mathbf{P}^{12}$ and $\mathbf{Q}^{12}$ can be obtained through:

$$P^{12(0)}_{nk|m} = \frac{1}{s}\frac{k+1}{n+1} P^{21(0)}_{nk|m}, \tag{6.66}$$

$$Q^{12(0)}_{nk|m} = \frac{1}{s}\frac{k+1}{n} Q^{21(0)}_{nk|m} \qquad n \leq k+1. \tag{6.67}$$

which can be derived for a general axisymmetric scatterer from the integral expressions given in Refs. [80, 87].

6.4 Quasistatic limit for $\mathbf{T}^{11}$

This block determines the scattered magnetic multipole field scattered by an external magnetic multipole field. For non-magnetic particles, this matrix is zero in the static case and only arises from non-zero frequency interactions. We can obtain the matrix elements using a similar method to that for $\mathbf{T}^{21}$, this time formulating the problem in terms of magnetic fields.

6.4.1 General formulation

Following the approach for $\mathbf{T}^{21}$, the matrix $\mathbf{T}^{11}$ can be found by considering an incident field of magnetic multipoles, but here the spherical vector wave functions must be expanded to second order:

$$\mathbf{H}_{\mathrm{e}} = \sum_{n=m}^{\infty} a_{nm}[\mathbf{RgN}^{(0)}_{nm}(k_{\mathrm{o}}\mathbf{r}) + \mathbf{RgN}^{(2)}_{nm}(k_{\mathrm{o}}\mathbf{r})], \tag{6.68}$$

$$\mathbf{H}_{\mathrm{i}} = s\sum_{n=m}^{\infty} c^{(0)}_{nm}[\mathbf{RgN}^{(0)}_{nm}(k_{\mathrm{i}}\mathbf{r}) + \mathbf{RgN}^{(2)}_{nm}(k_{\mathrm{i}}\mathbf{r})] + c^{(2)}_{nm}\mathbf{RgN}^{(0)}_{nm}(k_{\mathrm{i}}\mathbf{r}) + d_{nm}\mathbf{RgM}^{(0)}_{nm}(k_{\mathrm{i}}\mathbf{r}), \tag{6.69}$$

$$\mathbf{H}_{\mathrm{s}} = \sum_{n=m}^{\infty} p_{nm}\mathbf{N}^{(0)}_{nm}(k_{\mathrm{o}}\mathbf{r}) + q_{nm}\mathbf{M}^{(0)}_{nm}(k_{\mathrm{o}}\mathbf{r}). \tag{6.70}$$

This approach differs for the cases $m=0$ and $m \neq 0$, since the off diagonal T-matrix blocks are zero for $m=0$. To lowest order, $c^{(0)}_{nm} = s^{-n}a_{nm}$ as in (6.34), and the leftmost terms in $\mathbf{H}_{\mathrm{e}}$ and $\mathbf{H}_{\mathrm{i}}$ are identical. d_{nm}, p_{nm} and q_{nm} are all kept to lowest order only. The problem is to solve for p_{nm} and $c^{(2)}_{nm}$.

To express $\mathbf{RgN}^{(2)}_{nm}$ with harmonic functions, we note that for a solution of the Helmholtz equation [88]

$$\nabla \times \nabla \times (\mathbf{r}\psi) = \nabla[(1 + r\partial_r)\psi] + \mathbf{r}k^2\psi. \tag{6.71}$$

Then we express the incident field to second order as:

$$\mathbf{H}_{\mathrm{e}} = \mathbf{H}^{(0)}_{\mathrm{e}} + \nabla(k_{\mathrm{o}}^2 r^2 U^{\nabla}_{\mathrm{e}}) + \mathbf{r}k_{\mathrm{o}}^2 U^{r}_{\mathrm{e}} \tag{6.72}$$

where both U^{∇}_{e} and U^{r}_{e} satisfy Laplace's equation. $\mathbf{H}^{(0)}_{\mathrm{e}}$ does not interact with the spheroid. For the other fields we may write

$$\mathbf{H}_{\mathrm{i}} = \mathbf{H}^{(0)}_{\mathrm{e}} + s^2k_{\mathrm{o}}^2\left[\nabla(r^2U^{\nabla}_{\mathrm{e}}) + \mathbf{r}U^{r}_{\mathrm{e}}\right] - \nabla U^{N}_{\mathrm{i}} + \nabla \times (\mathbf{r}U^{M}_{\mathrm{i}}), \tag{6.73}$$

$$\mathbf{H}_{\mathrm{s}} = -\nabla U^{N}_{\mathrm{s}} + \nabla \times (\mathbf{r}U^{M}_{\mathrm{s}}). \tag{6.74}$$

U^{∇}_{e} and U^{r}_{e} are given, and U^{M}_{i} and U^{M}_{s} are known from $\mathbf{R}^{21}$ and $\mathbf{T}^{21}$. This leaves us to determine the two potentials U^{N}_{i} and U^{N}_{s}. For this problem it appears most straightforward to solve via just the two boundary conditions on the magnetic field.

6.4.2 Prolate spheroids, $m = 0$

For $m = 0$, we assume an axially symmetric incident field. $\mathbf{T}^{21}$, $\mathbf{T}^{12}$, $\mathbf{R}^{21}$ and $\mathbf{R}^{12}$ are all zero and the problem is decoupled from any interactions between electric and magnetic multipoles. This means $U_\mathrm{i}^M = U_\mathrm{s}^M = 0$. Since $\hat{\phi} \cdot \mathbf{H} = 0$, the boundary conditions are $\hat{\xi} \cdot \mathbf{H}_\mathrm{i} = \hat{\xi} \cdot \mathbf{H}_\mathrm{o}$ and $\hat{\eta} \cdot \mathbf{H}_\mathrm{i} = \hat{\eta} \cdot \mathbf{H}_\mathrm{o}$, or in terms of the potentials:

$$(s^2-1)k_\mathrm{o}^2 f^2 \left[\partial_\xi[(\xi^2+\eta^2-1)U_\mathrm{e}^\nabla] - \xi U_\mathrm{e}^r\right] + \partial_\xi U_\mathrm{i}^N = \partial_\xi U_\mathrm{s}^N, \tag{6.75}$$

$$(s^2-1)k_\mathrm{o}^2 f^2 \left[\partial_\eta[(\xi^2+\eta^2-1)U_\mathrm{e}^\nabla] - \eta U_\mathrm{e}^r\right] + \partial_\eta U_\mathrm{i}^N = \partial_\eta U_\mathrm{s}^N. \tag{6.76}$$

For the second boundary condition it is convenient to integrate over η. Then we expand the fields as series of spheroidal harmonics, apply recurrence identities for the Legendre polynomials, and re-index the summations to express the η dependence of each term in the series as $P_n(\eta)$. There is a lot of algebra so we skip to the final result:

$$\begin{aligned} T_{nk|0}^{11(0)} &= -i(s^2-1)(\xi_0^2-1)(k_\mathrm{o}f)^{n+k+3}\frac{B_n^0 B_k^0}{k+1}\sum_{p=0}^{\min(n,k)}\frac{e_{nk}e_{np}}{(n-p)!!(n+p+1)!!(k-p)!!(k+p+1)!!} \\ &\times\left\{(2p+1)\left(\frac{P_p P_p'}{(2p+3)(2p-1)} - \frac{k}{2k+3}\xi_0 P_p P_p\right) - \frac{k-p}{k+p+3}\frac{p+2}{2p+3}P_{p+2}P_p' + \frac{n-p}{n+p+3}\frac{p+1}{2p+3}P_p P_{p+2}'\right. \\ &\left.-\frac{(k+3)(k-n)(p+1)(p+2)}{2(2k+3)(n+p+3)(k+p+3)}[P_p P_{p+2}' - P_{p+2}P_p']\right\} \end{aligned} \tag{6.77}$$

where $P_p \equiv P_p(\xi_0)$. Unlike the other T-matrix blocks, this has no log terms or singular points – it is a polynomial in ξ_0. Despite its appearance, one can check numerically that this expression is actually symmetric about n and k, as it should be. None of the terms individually are symmetric, making it hard to recognise a symmetric form of this expression. This suggests there could be simpler approach to obtaining the matrix, maybe where the 2$^{\text{nd}}$ order fields are split differently to (6.72) or a combination of one electric and one magnetic boundary condition could be applied instead.

6.4.3 Prolate spheroids, $m \neq 0$

For $m \neq 0$, the problem has the additional complication of coupling from the electric multipoles induced in both the internal and scattered fields. In this case the boundary condition on $\hat{\eta} \cdot \mathbf{H}$ is too complicated, but the condition for $\hat{\phi} \cdot \mathbf{H}$ is non-zero and manageable, so we have

$$(s^2-1)k_\mathrm{o}^2 f^2 \left[\partial_\xi[(\xi^2+\eta^2-1)U_\mathrm{e}^\nabla] - \xi U_\mathrm{e}^r\right] + \frac{\eta f}{\xi^2-1}\partial_\phi[U_\mathrm{s}^M - U_\mathrm{i}^M] = \partial_\xi[U_\mathrm{s}^N - U_\mathrm{i}^N], \tag{6.78}$$

$$(s^2-1)k_\mathrm{o}^2 r^2 U_\mathrm{e}^\nabla - r\sin\theta\,\partial_\theta[U_\mathrm{s}^M - U_\mathrm{i}^M] = \partial_\phi[U_\mathrm{s}^N - U_\mathrm{i}^N]. \tag{6.79}$$

The derivative ∂_θ can be applied directly to the spherical harmonics, which splits them into two different orders, adding another layer of complication. All potentials are harmonic and should be expanded on a basis of spheroidal harmonics, and then related to their corresponding expansion in spherical wave functions. The series coefficients d_n^m, q_n^m for U_i^M, U_s^M are given by $\mathbf{R}^{21}$ and $\mathbf{T}^{21}$. The final result is:

$$\begin{aligned} T_{nk|m}^{11(0)} &= \frac{-i(\xi_0^2-1)(k_\mathrm{o}f)^{n+k+3}(n-m)!}{\gamma_n^m n(2n-1)!!}\sum_{p=m}^{n}\frac{e_{nk}e_{np}}{(n-p)!!(n+p+1)!!}\left\{\frac{(s^2-1)\gamma_k^m}{(2k+3)!!}\,\alpha_{kp}^m\right. \\ &\times\left[\frac{(k-n)(p-m+1)(p-m+2)(k+3)}{2(2p+1)(n+p+3)(k+p+3)}[P_p^m P_{p+2}^{m\prime} - P_{p+2}^m P_p^{m\prime}] - k\xi_0 P_p^m P_p^m\right] \\ &+\sum_{q=\max(p-1,m)}^{k+1}\frac{i\gamma_q^m(k_\mathrm{o}f)^{q-k-1}s^{q+1}}{(2q+1)!!}R_{qk|m}^{21} \\ &\times\left[-\left(\frac{mP_p^m}{\xi_0^2-1} + \xi_0 P_p^{m\prime}\frac{q+1}{m}\right)\left(\frac{p-m}{2p-1}\alpha_{q,p-1}^m P_{p-1}^m + \frac{p+m+1}{2p+3}\alpha_{q,p+1}P_{p+1}^m\right) + \frac{q-m+1}{m}\alpha_{q+1,p}^m P_p^m P_p^{m\prime}\right] \\ &+\sum_{q=m}^{p+1}\frac{\gamma_q^m(2q-1)!!}{(k_\mathrm{o}f)^{q+k+2}}T_{qk|m}^{21} \end{aligned}$$

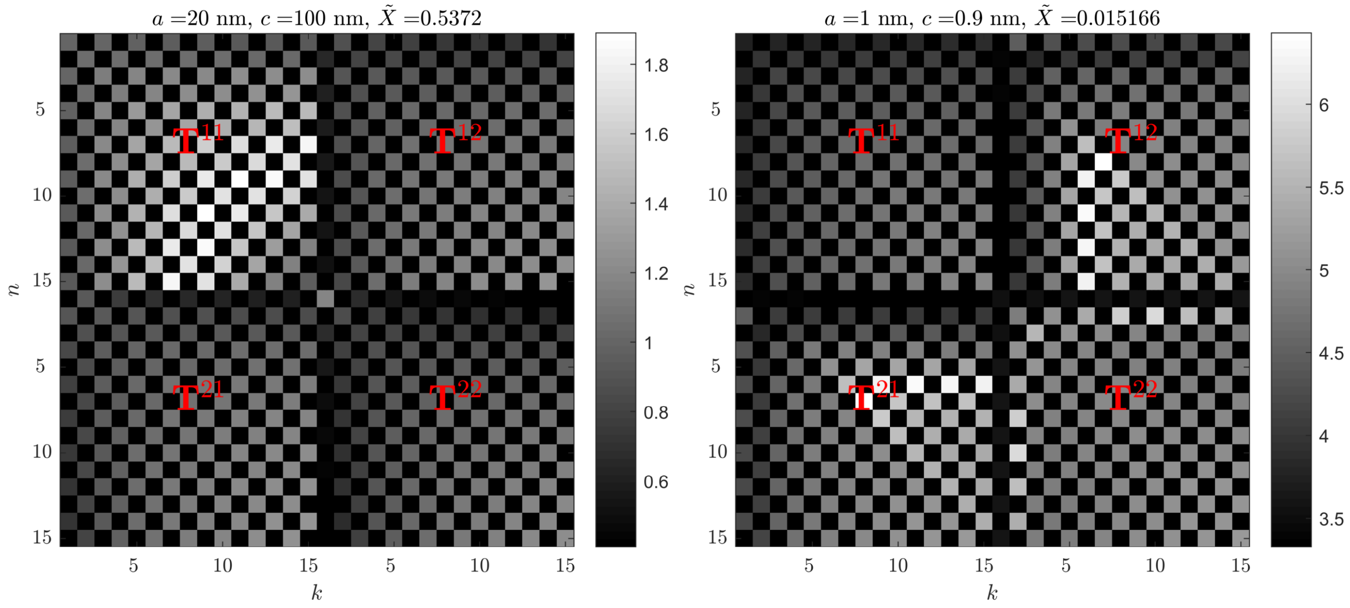

Figure 6.2: $-\log_{10}$(relative error) of the quasistatic T-matrix expressions compared to the exact solutions, for two silver spheroids in water, on the left a generic-sized nanoparticle, and on the right an unrealistically small particle used to demonstrate the validity of the long-wavelength expansion. The wavelength is 400 nm, ($\varepsilon = -6.4572 + 0.2993i$)

$$\times \left[\left(\frac{mP_p^m}{\xi_0^2 - 1} - \xi_0 P_p^{m\prime} \frac{q}{m} \right) \left(\frac{p-m}{2p-1} \beta^m_{q,p-1} Q^m_{p-1} + \frac{p+m+1}{2p+3} \beta_{q,p+1} Q^m_{p+1} \right) + \frac{q+m}{m} \beta^m_{q-1,p} Q^m_p P^{m\prime}_p \right] \Bigg\}. \qquad (6.80)$$

Again the matrix is symmetric despite its appearance, and it is likely that simplified expressions could be found.

6.5 Evaluating and checking expressions

All matrix elements were checked against the exact results, which can be computed to a high accuracy [89, 90], and the relative error is plotted in Figure 6.2. The radiative correction was also applied to the quasi-static T-matrix: $\mathbf{T} \rightarrow \mathbf{T}(\mathbf{I} - \mathbf{T})^{-1}$ [91], which had a noticeable increase in accuracy for larger particles. The volume-size parameter is $\tilde{X} = k_1 r_{\text{eq}} = k_1 \sqrt[3]{c^2 a}$ where r_{eq} is the radius of the volume equivalent sphere.

The accuracy generally improves as the size parameter $\tilde{X}$ decreases, indicating that the expressions are correct, and the approximations appear to somewhat favor low aspect ratios. Accuracy increases modestly with order, and tends to be more accurate for ε with positive real part. Practically this makes the quasi-static approximations useful as substitutes to higher order matrix elements, where the T-matrix begins to find numerical problems. They may also be useful as substitutes at an earlier stage in the Q- and P- matrices, so that one does not have to evaluate the surface integrals for as many high order matrix elements. This would require further investigation but similar accuracies are expected to that in Figure 6.2.

6.6 Depolarization factors

The T- and R-matrix expressions contain generalized depolarization factors, introduced earlier as

$$L_n^m(\xi) = (\xi^2 - 1) P_n^{m\prime}(\xi) Q_n^{-m}(\xi), \qquad (6.81)$$

which obey the sum rule

$$\sum_{m=-n}^{n} L_n^m = n. \qquad (6.82)$$

For $n = 1$ these reduce to the well known dipolar depolarization factors L_x, L_y, L_z, with sum rule $L_x + L_y + L_z = 1$.

We can also find surface integral expressions for the depolarization factors by comparison with the EBCM. In the quasi-static limit of the EBCM for axisymmetric particles the diagonal elements of $\mathbf{Q}^{22}$ may be expressed as (after some manipulation)

$$Q^{22(0)}_{nn|m} = s^{n-1}\left\{1 + (s^2-1)\left[\frac{n}{2n+1} - \frac{(-)^m}{2}\int_0^\pi \mathrm{d}\theta \sin\theta P_n^{-m}(\cos\theta)\frac{\mathrm{d}P_n^m(\cos\theta)}{\mathrm{d}\theta}\frac{1}{r(\theta)}\frac{\mathrm{d}r(\theta)}{\mathrm{d}\theta}\right]\right\}. \tag{6.83}$$

where $r(\theta)$ defines the surface of the scatterer. Eq. (6.83) reduces to the approximate (if the internal field is nearly uniform) dipolar responses in [92]. As $r(\theta)$ becomes constant (i.e. for a sphere), the integral goes to zero.

For spheroids

$$r(\theta) = c\sqrt{\frac{\xi_0^2 - 1}{\xi_0^2 - \cos^2\theta}} \Rightarrow \frac{1}{r}\frac{\mathrm{d}r}{\mathrm{d}\theta} = -\frac{\sin\theta\cos\theta}{\xi_0^2 - \cos^2\theta}. \tag{6.84}$$

and from (6.24) we have for the diagonal

$$Q^{22}_{nn|m} = s^{n-1}[1 + (s^2-1)L_n^m]. \tag{6.85}$$

Comparing (6.85) and (6.83) we find

$$L_n^m = \frac{n}{2n+1} + \frac{(-)^m}{2}\int_0^\pi \mathrm{d}\theta P_n^{-m}\frac{\mathrm{d}P_n^m}{\mathrm{d}\theta}\frac{\sin^2\theta\cos\theta}{\xi_0^2 - \cos^2\theta}. \tag{6.86}$$

This agrees numerically with (6.81), although analytically is not obvious. We have introduced (6.86) not as a practical device but as an extension of the integral expression in [92] for $n = 1$ and to highlight the connection with the EBCM.

6.7 Quasistatic resonances

For metallic scatterers, the real part of ε is negative which can cause very strong scattered fields for particular values of ε, depending on the geometry of the scatterer. For metals ε is wavelength dependent and these enhancements typically occur at optical and infrared frequencies. If material losses (imaginary part of ε) are small this results in a very strong optical response of the nanoparticle commonly referred to as a localized surface plasmon resonance [93]. For a sphere, these resonances occur for $\varepsilon = -2$ for the dipolar resonance and $\varepsilon = -(n+1)/n$ for n-multipolar resonances, as discussed in Chapter 4.

For the spheroid, we can derive some new results for the resonance conditions by looking at the quasi-static T-matrix elements in Equations (6.26), (6.64), (7.77), (7.78). The elements have the expression $1 + (\varepsilon - 1)L_n^m(\xi_0)$ as a denominator, so the resonances in spheroids are related to the generalized depolarization factors L_n^m:

$$\varepsilon_{\text{res}} = 1 - \frac{1}{L_n^m(\xi_0)} = \frac{P_n^m(\xi_0)Q_n^{m\prime}(\xi_0)}{P_n^{m\prime}(\xi_0)Q_n^m(\xi_0)}, \qquad n \geq 1,\ m \geq 0. \tag{6.87}$$

For $n = 1$, this reduces to the known dipolar resonance of a spheroid [93], where excitation along z corresponds to L_1^0, and along x or y corresponds to L_1^1.

The elements $T^{ij}_{nk|m}$ with $n \leq 2$ or $k \leq 2$ have just one resonance, and many elements share the same resonance condition, for example $T^{11}_{11|1}, T^{21}_{21|1}, T^{22}_{22|1}$ all resonate at $1 + (\varepsilon - 1)L_2^1(\xi_0) = 0$. These resonances are well known from the solution of the scattering problem in spheroidal coordinates [94], but now the resonances can be associated with their excitations from *spherical* multipoles through the T-matrix.

In the spherical limit, $\xi_0 \to \infty$, and the limits of the Legendre functions given in ([63], 8.776) reveal that $L_n^m(\xi_0 \to \infty) = \frac{n}{2n+1}$ which leads to the small sphere resonance conditions.

In the limit of a needle, $\xi_0 \to 1$ spheroid becomes arbitrarily thin. For $m = 0$, an asymptotic expression of the Legendre functions gives:

$$\varepsilon_{\text{res}}(\xi \to 1, m = 0)\ \frac{1 - \frac{2}{n(n+1)}\frac{1}{\xi_0^2 - 1}}{Q_0(\xi_0) - H_n} + 1. \tag{6.88}$$

which tend to $\varepsilon_{\text{res}} = -\infty$. For $m \geq 1$, the resonance conditions (6.87) all tend towards -1. For oblate spheroids, the limit $\xi_0 \to -0i$ is where the spheroid becomes a disk. We find that $\varepsilon_{\text{res}} \to 0$ or $-\infty$. Figure 6.3 plots the resonance conditions (6.87) are plotted for two aspect ratios h, compared to those for a sphere and a needle. We

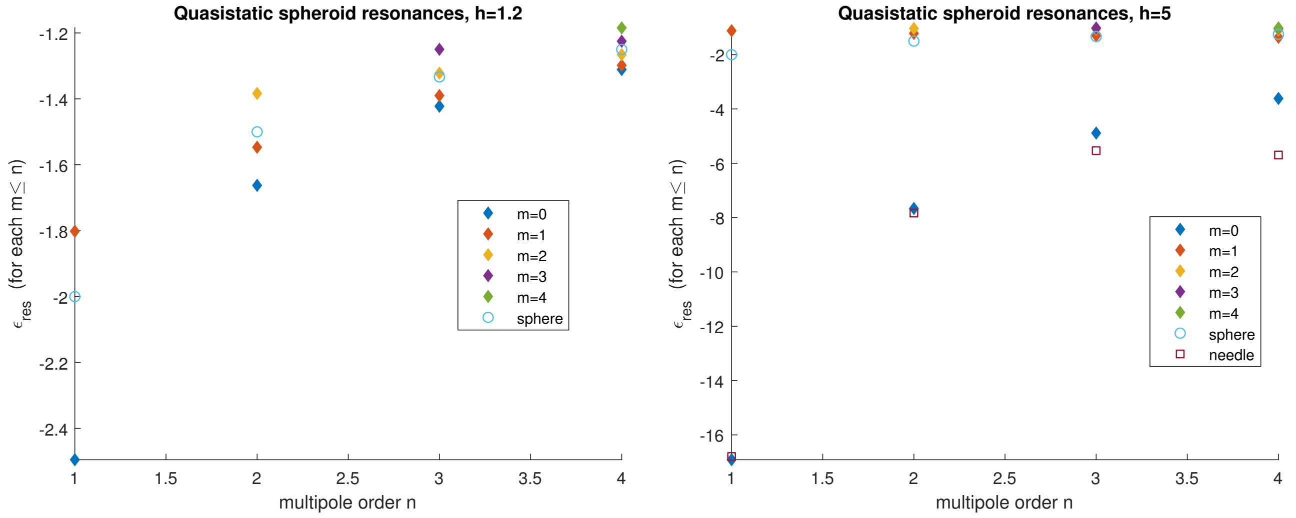

Figure 6.3: Resonance conditions for ε for small prolate spheroids. The resonances are plotted for multipole orders $n, m \leq 4$ from (6.87), and compared to the corresponding resonances for a sphere and the needle limit (6.88).

should also associate these resonances show up in each spherical multipole response in the T-matrix, and in fact each matrix element has several resonances depending on the degree of its multipolarity. The electric-electric element $T^{22}_{nk|m}$ has resonances at $\varepsilon = 1 - 1/L^m_p$ for all $p \leq \min(n,k)$ with p,n,k of the same parity. $T^{21}_{nk|m}$ has resonances for $p \leq \min(n,k+1)$ with p,n of the same parity, $T^{12}_{nk|m}$ has resonances for $p \leq \min(n+1,k)$ with p,k of the same parity, $T^{11}_{nk|0}$ has no resonances, and the form of $T^{11}_{nk|m>0}$ is too complex to know for sure, but the explicit expression for $T^{11}_{11|1}$ in [27] shows one resonance at $\varepsilon = 1 - 1/L^1_2$, which surprisingly has an index of $p = 2$, which one would normally associate with quadrupoles. Compare this to the sphere where T^{22}_{nn} has only one resonance at $\varepsilon = -(n+1)/n$, while the blocks $\mathbf{T}^{12}$ and $\mathbf{T}^{21}$ are zero, and there are no quasi-static resonances for T^{11}_{nn}.

6.8 Conclusion

We have provided an approach to find the quasistatic limit of $\mathbf{T}$ for any axisymmetric particle, and in the case of spheroids, this approach leads to analytic expressions. For non-magnetic particles, the magnetic multipole field does not interact with the object in the static limit. This means that this interaction cannot be seen without considering at least the lowest two orders of the spherical wave functions. The quasistatic limit of the electric susceptibilities is obtained from an electrostatics problem, while in this limit the magnetic susceptibilities are zero. For magnetic particles however, $\mathbf{T}^{11}$ is non-zero to the lowest order and could be obtained from a magnetostatics problem, with very similar formalism to the electrostatics problem for $\mathbf{T}^{22}$.

In [27] the T-matrix was found to 3rd lowest order for plane wave scattering, which is $\mathcal{O}(X^6)$ and involves only up to multipolarity $n,k = 3$. The results were derived by direct Taylor expansion of the EBCM. In contrast, here we have found the lowest non-zero order of the individual elements, by considering excitation from a localized source where every T-matrix element is equally important. Some of the results of these two approaches coincide, in particular the lowest orders of $T^{22}_{11|m}$, $T^{11}_{11|m}$, $T^{22}_{22|m}$, $T^{22}_{13|m}$, $T^{21}_{12|1}$, $T^{21}_{21|1}$ (and their symmetric counterparts) for $m = 0,1,2$. These results were used to confirm and simplify some of the ECBM-derived expressions.

The EBCM for spheroids in particular suffers from numerical problems in the surface integrals and matrix inversion for matrices larger than about 20 by 20, and stable computation methods are proposed in [21, 89]. But in the interest of computational speed for relatively small particles, the quasi-static formulas are a very good approximation for the matrix elements of high multipolarity [84] due to the $\sim X^{n+k+2}$ dependence, and could be used as substitutes to extend the matrix size when dealing with localized sources or closely packed particles. These quasi-static approximations can be used as checks and to investigate issues in matrix inversion.

We also found simple expressions for the resonance conditions of the matrix elements, and have shown that each spherical multipole element can have more than one resonance condition – i.e. more than one resonant wavelength, for octopole elements and higher.

The Rayleigh hypothesis is the assumption that the series for the scattered field converges everywhere on the particle surface [22]. It is not known exactly if this hypothesis must apply for a given particle for the T-matrix to work, and in fact it is not true for a spheroid but the EBCM works anyway. This is investigated numerically for spheroids in Ref. [95]. More difficult is the question of multiple particles. The applicability of the T-matrix method for two side by side spheroids is known to fail for close spheroids, but at what distance exactly, and are the problems numerical or analytical? [96]. The radius of convergence of a spherical wave-function series is the same in the electrostatic limit, which can be deduced from the limit as the degree tends to infinity, so the results for the $\mathbf{T}^{22}$ block can be used to study the convergence of the T-matrix for multiple particles, while reducing complexity and sources of numerical error.

Chapter 7

Electrostatic T-matrices for the Torus

The extended boundary condition method (EBCM) for calculating the T-matrix is known to be unstable for particles with highly non-spherical shape, and much work has been done on determining conditions for the T-matrix to be applicable [77, 97]. For the EBCM to work, the Rayleigh hypothesis is historically suggested as criteria, which is the assumption that the series of basis functions converge on the entire surface of the particle, although it is known that this is not necessary and weaker criteria have been suggested [77]. The EBCM may fail or becomes highly unstable for convex particles such as red blood cells [98], let alone multiply-connected particles such as a torus.

Using other methods, scattering by a torus has been considered analytically in the long wavelength limit using toroidal harmonics, the partially separable solutions to Laplace's equation in toroidal coordinates. Toroidal harmonics are a relatively new tool in computational physics due to their complexity. Also, being only partially separable solutions makes toroidal harmonics difficult to apply to problems even involving the torus. For conducting tori, fairly simple series solutions can be obtained in the static limit, but for dielectric tori, the series coefficients are not explicit. The coefficients are calculated using a three step recurrence relation, with initial values given by a continued fraction. Some specific simulations include a dielectric torus in a uniform field [99], a conducting torus illuminated by a low frequency plane wave [100], plasmon resonances [101] and electromagnetic trapping [102]. A detailed computational analysis of quasi-static scattering by solid and layered tori is conducted in [103]. Semi analytical results for low frequency dipole excitation a conducting torus have been obtained for the lowest three orders in frequency of the electric and magnetic fields, using toroidal harmonics [104].

Spherical harmonics are far easier to compute, better known and more applicable than toroidal harmonics, so it is of interest to obtain the T-matrix on a basis of spherical harmonics - in particular, this allows computation of the long wavelength limit of the T-matrix for electromagnetic or acoustic scattering, which is usually expressed on a basis of spherical wavefunctions. For the spheroid, the low frequency scattering problem has been re-expressed with spherical harmonics and the electromagnetic T-matrix has been obtained to third order in size parameter [80, 24, 27] by applying the series relationships between spherical and spheroidal harmonics. But the series relationships between spherical and toroidal harmonics are more complex and virtually unknown in the literature, except for the low degrees. For example toroidal harmonics of degree zero, corresponding to the potential of rings of sinusoidal charge distributions, are known as series of spherical harmonics, and spherical harmonics corresponding to point charges and dipoles are known as series of toroidal harmonics. The relationships for all degrees and orders have been derived in a Russian paper from 1983 [105], although this does not appear to be well known except for one other paper [106], which analyzed the electrostatic interaction between a conducting torus and a partial spherical shell - they used the relationships to construct what is effectively the T-matrix for the conducting torus (their equation 32), expressed on a spherical basis, as part of the kernel of an integral equation.

We begin by investigating properties of toroidal harmonics including deriving new expressions for their source distributions. Then we derive the T-matrix for a dielectric torus expressed on a basis of toroidal harmonics, and then present this on a spherical harmonic basis. We derive physical quantities; extinction cross sections, polarizabilities and resonance conditions, and finally derive asymptotic formulae for thin rings. Unlike the previous chapter for the spheroid, we will only focus on the lowest order of the quasi-static limit, i.e. the 22 block.

7.1 Toroidal coordinates and harmonics

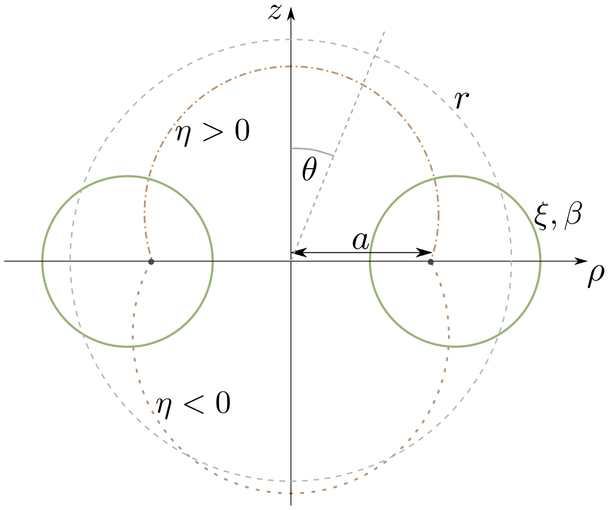

Figure 7.1: Cross section of the spherical, cylindrical and toroidal coordinate systems, showing some arbitrary coordinate surfaces.

The toroidal coordinate system uses a parameter a which defines the radius of the "focal ring" centred at the origin. Toroidal coordinates (ξ, η, ϕ) are then defined as

$$\eta = \operatorname{sign}(z) \arccos \frac{r^2 - a^2}{\sqrt{(r^2+a^2)^2 - 4\rho^2 a^2}}, \tag{7.1}$$

$$\xi = \frac{1}{2} \log \frac{(\rho+a)^2 + z^2}{(\rho-a)^2 + z^2}, \tag{7.2}$$

$$\beta = \cosh \xi, \tag{7.3}$$

with $\eta \in [-\pi, \pi]$, $\xi \in [0, \infty)$, $\beta \in [1, \infty)$. ξ and β correspond to the torus size; $\xi = 0$ and $\beta = 1$ is a tight torus covering all space and $\xi = \beta = \infty$ is the focal ring. η is related to the angle from the focal ring to a point on the torus, and its coordinate surfaces are partial spheres, as depicted in Figure 7.1.

Laplace's equation is partially separable in toroidal coordinates, so that the solutions have an additional prefactor. The toroidal harmonics are defined for integer n, m as

$$\psi_n^{mc} = \Delta Q_{n-1/2}^m(\beta) \cos n\eta \; e^{im\phi}, \tag{7.4}$$

$$\psi_n^{ms} = \Delta Q_{n-1/2}^m(\beta) \sin n\eta \; e^{im\phi}, \tag{7.5}$$

$$\Psi_n^{mc} = \Delta P_{n-1/2}^m(\beta) \cos n\eta \; e^{im\phi}, \tag{7.6}$$

$$\Psi_n^{ms} = \Delta P_{n-1/2}^m(\beta) \sin n\eta \; e^{im\phi}, \tag{7.7}$$

$$\text{with } \Delta = \sqrt{2(\beta - \cos\eta)}, \tag{7.8}$$

where $P_{n-1/2}^m$ and $Q_{n-1/2}^m$ are the Legendre functions of the first and second kinds. Using the superscript v to denote c or s, we will call Ψ_n^{mv} the "ring toroidal harmonics" and ψ_n^{mv} the "axial toroidal harmonics" since they are singular on the focal ring and z-axis respectively. There are two kinds of angular solutions: $\cos n\eta$ $(v = c)$ which are symmetric about the meridian plane and $\sin n\eta$ $(v = s)$ which are antisymmetric. Compare this to spherical harmonics which have angular solutions $P_n^m(\cos\theta)$ and $Q_n^m(\cos\theta)$ where the second type of angular solutions $Q_n^m(\cos\theta)$ are discarded due to their singularity at the poles of the sphere. Toroidal harmonics also are non-zero for $m > n$, as shown in the next section this occurs (with $n = 0$ for example) for a single ring with charge distribution $\cos(m\phi)$. So all Ψ_n^{mv} and ψ_n^{mv} for integer n, m and $v = c, s$ are physically applicable solutions

- smooth on the torus surface. Toroidal harmonics of negative n or m may be defined simply through

$$P^m_{-n-1/2} = P^m_{n-1/2} \qquad\qquad P^{-m}_{n-1/2} = \frac{\Gamma(n-m+\frac{1}{2})}{\Gamma(n+m+\frac{1}{2})} P^m_{n-1/2} \tag{7.9}$$

$$Q^m_{-n-1/2} = Q^m_{n-1/2} \qquad\qquad Q^{-m}_{n-1/2} = \frac{\Gamma(n-m+\frac{1}{2})}{\Gamma(n+m+\frac{1}{2})} Q^m_{n-1/2}. \tag{7.10}$$

7.1.1 Charge distributions of ring toroidal harmonics Ψ^{mv}_n

The charge distributions that create toroidal harmonics are quite interesting. Ψ^{mv}_n are finite everywhere except $\beta = \infty$, on the focal ring. We want to express the functions as integrals of charge distributions on this focal ring. We start with $n = 0$, looking at $\Psi^{mc}_0 = \Delta P^m_{-1/2}(\beta)e^{im\phi}$ (note that $\Psi^{ms}_0 = 0$). The Legendre functions approaching the ring behave as

$$P^m_{-1/2}(\beta \to \infty) \to \frac{(2m-1)!!}{(-2)^m \pi}\sqrt{\frac{2}{\beta}}\log\beta \tag{7.11}$$

while $\Delta \to \sqrt{2\beta}$. Approaching the focal ring, $1/\beta$ becomes equal to the distance d from the ring. Compare this to approaching infinitely close to a line source with arbitrary charge distribution, where the potential goes as $2\log d$ if the charge has unit density at the point of closest approach. Denoting points on the focal ring by $\mathbf{r}'$ and the observation point by $\mathbf{r}$, the distance $|\mathbf{r}'-\mathbf{r}|$ in cylindrical coordinates is $|\mathbf{r}'-\mathbf{r}| = \sqrt{\rho^2+a^2-2\rho a\cos(\phi-\phi')+z^2}$. Also the charge distribution must be proportional to $e^{im\phi}$, so we deduce that

$$\Psi^{mc}_0 = \frac{(2m-1)!!}{(-2)^m\pi}\int_0^{2\pi}\frac{e^{im\phi'}a\,\mathrm{d}\phi'}{\sqrt{r^2+a^2-2\rho a\cos(\phi-\phi')}}. \tag{7.12}$$

We should also check the limit as $r \to \infty$. Here $\beta \to 1$, $P_{n-1/2} \to 1$, $P^{m>0}_{n-1/2} \to 0$, and $\Delta \to 2a/r$, so we can rule out the possibility of sources at $r = \infty$.

The harmonics for $n = 1$ may be generated by application of the operators $\partial_z = \partial/\partial z$ and $r\partial_r$ (see appendix of [25] for details), so we apply these to the integral expression (7.12), first $r\partial_r$:

$$\begin{aligned}\Psi^{mc}_1 &= -\frac{1}{m-1/2}\left(2r\frac{\partial}{\partial r}+1\right)\Psi^{mc}_0\\ &= \frac{(2m-3)!!}{(-2)^m\pi}\int_0^{2\pi}\frac{a(a^2-r^2)e^{im\phi'}\mathrm{d}\phi'}{(r^2+a^2-2\rho a\cos(\phi-\phi'))^{3/2}}\end{aligned} \tag{7.13}$$

The charge distribution is two oppositely charged rings on the xy-plane, one with an infinitesimally greater radius than the other. This produces an infinitesimal charge imbalance - a net monopole moment, which is seen in the spherical-toroidal expansions (7.44).
And for Ψ^{ms}_1:

$$\begin{aligned}\Psi^{ms}_1 &= \frac{-a}{m-1/2}\frac{\partial}{\partial z}\Psi^{mc}_0\\ &= \frac{(2m-3)!!}{(-2)^m\pi}\int_0^{2\pi}\frac{-2a^2 z e^{im\phi'}\mathrm{d}\phi'}{(r^2+a^2-2\rho a\cos(\phi-\phi'))^{3/2}}\end{aligned} \tag{7.14}$$

This is the potential of two oppositely charged rings with an infinitesimal separation in the z-direction. These charge distributions are represented in Figure 7.2.

For higher n the harmonics can be generated by repeated application of the operator $r\partial_r$. The toroidal harmonics follow a recurrence relation involving $r\partial_r$, and this recurrence is also satisfied by coefficients c^m_{nk}, s^m_{nk} relating toroidal and spherical harmonics (see (7.48) and appendix of [25]). We can then deduce the differential

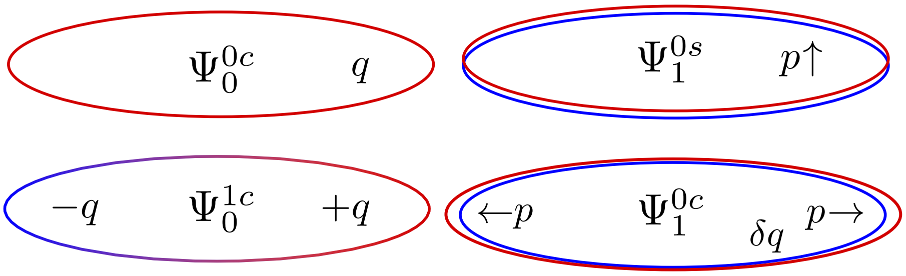

Figure 7.2: Representation of the source charge configurations for the low order ring toroidal harmonics. Red and blue represent positive and negative charge q, and dipole moments are denoted p. For Ψ^{0c}_1 the slightly larger radius of the outer ring creates a finite charge δq.

operators that generate the n^{th} order harmonic from the 0^{th} or 1^{st} order harmonics:

$$\Psi^{mc}_n = \frac{(-)^n}{2} c^m_n(r\partial_r)\Psi^{mc}_0 \tag{7.15}$$

$$\Psi^{ms}_n = \frac{(-)^{n+1}}{4} \frac{s^m_n(r\partial_r)}{r\partial_r + 1}\Psi^{ms}_1 \tag{7.16}$$

where $c^m_n(r\partial_r)$ is equal to c^m_{nk} with $k \to r\partial_r$ and similarly for s^m_n. (7.16) starts from $n = 1$ because $\Psi^{ms}_0 = 0$. Both $c^m_n(x)$ and $s^m_n(x)/(x+1)$ are degree n polynomials in x.

The corresponding integral expressions for Ψ^{mv}_n are given in operator form by applying (7.15) and (7.16) to the integral expression for Ψ^{mc}_0 (7.12) and Ψ^{ms}_1 (7.14). However, explicit evaluations of these derivatives do not appear to reveal any simple patterns. The integral expressions for Ψ^{mv}_n have been checked numerically up to $n = 3$. The ring harmonics are also plotted in Figure 7.3 on the plane $y = 0$, which confirms these source distributions.

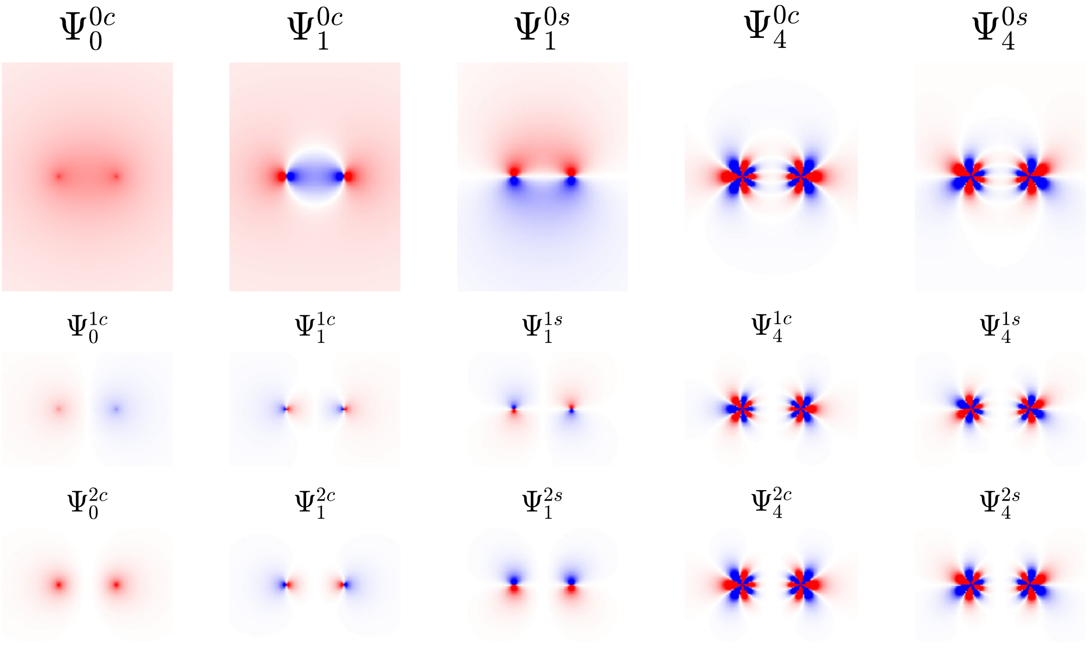

Figure 7.3: Plots of the ring toroidal harmonics for $n = 0, 1, 4$ and $m = 0, 1, 2$, on a slice of the x, z plane. The color scale is [-5,5] for $n = 0, 1$, and [-50,50] for $n = 4$.

7.1.2 Charge distributions of axial toroidal harmonics ψ_n^{mv}

Again we can determine the line charge distribution by matching it to the limit of the potential as it approaches the line. The exact proportionality is obtained by considering that the potential near an axial line source with unit magnitude goes as $2\log\rho$. The behavior of the components of the toroidal harmonics as $\rho \to 0$ are, using $v = z/a$:

$$\begin{aligned}\lim_{\rho\to 0}\Delta =& \frac{2}{\sqrt{v^2+1}} && (7.17)\\ \lim_{\rho\to 0}\eta =& \operatorname{sign}(v)\operatorname{acos}\frac{v^2-1}{v^2+1} \equiv \eta' && (7.18)\\ \lim_{\rho\to 0} Q_{n-1/2}(\beta) =& \log\frac{a}{\rho}. && (7.19)\end{aligned}$$

Then the line source distribution of $\psi_n^c + i\psi_n^s$ is $ae^{in\eta'}/\sqrt{v^2+1}$ (using complex notation to deal with ψ_n^c and ψ_n^s simultaneously):

$$\psi_n^c + i\psi_n^s = \int_{-\infty}^{\infty} \frac{a\, e^{in\eta'}\mathrm{d}v}{\sqrt{v^2+1}\sqrt{\rho^2+(z-av)^2}}. \tag{7.20}$$

And for $\rho \to \infty$, we have $\psi_n^v \to 0$ and there is no contribution from sources at $\rho \to \infty$. This is unlike the spherical harmonics of the second kind $r^n Q_n(\cos\theta)$, who are also singular on the z-axis, but are the difference between a line source that produces an infinite potential and a sum of multipoles at infinity of infinite strength [6].

For $m > 0$, the charge distributions are multi-line, which can be deduced from the $e^{im\phi}$ dependence. For example ψ_n^{1v} has a charge distribution of two line sources infinitely close together but of opposite charge. The behavior of the Legendre functions $Q_{n-1/2}^m(\beta)$ is:

$$\lim_{\rho\to 0} Q_{n-1/2}^m(\beta) = \frac{(-)^m}{2}(m-1)!\left(\frac{a(v^2+1)}{\rho}\right)^m. \tag{7.21}$$

so for $m > 0$ we have $\psi_n^{mv} \propto \rho^{-m}$ as $\rho \to 0$.

And in the limit $\rho \to \infty$, we have $\psi_n^{mv} \propto \rho^{m-1}$. Despite the divergence for $m > 1$, there is no contribution from sources at $\rho = \infty$, which can be explained as follows. If sources at $\rho = \infty$ existed, then we could split ψ_n^{mv} into its contributions from charges on the z-axis and at $\rho = \infty$. The potential due to charges at $\rho = \infty$, being finite at the origin, can then be expressed as a series of regular spherical harmonics $\hat{S}_n^m = r^n P_n^m(\cos\theta)e^{im\phi}$ of the same m as ψ_n^{mv}. However, $\hat{S}_n^m(\rho\to\infty) \propto \rho^k$ where $k \geq m$, so it is impossible to express the ρ^{m-1} dependence as a series of $\hat{S}_n^m$. Therefore there cannot exist charges at $\rho = \infty$.

We can compare ψ_n^{mv} to the potential near an m-fold line charge distribution which similarly goes as ρ^{-m} as $\rho \to 0$, with integral kernel $|\mathbf{r}-\mathbf{r}'|^{-2m-1}$. (7.21) for $m > 0$ also shows a non-constant z-dependence of $(v^2+1)^m$. Putting this together gives

$$\psi_n^{mc} + i\psi_n^{ms} = (2m-1)!!a\left(\frac{-a\rho}{2}\right)^m e^{im\phi}\int_{-\infty}^{\infty}\frac{(v^2+1)^{m-1/2}e^{in\eta'}}{(\rho^2+(z-av)^2)^{m+1/2}}\mathrm{d}v \tag{7.22}$$

Andrews ([107]- eq. 27) proved (7.22) via direct integration for all m, and $n = 0$ (in his notation $n \leftrightarrow m$). For $m = 0$ the total charge is infinite. For $n = m = 0$ the charge decreases as $v \to \pm\infty$ (away from the origin), but for all other cases, the charge increases as $v \to \pm\infty$. This behavior is seen in the plots in Figure 7.4.

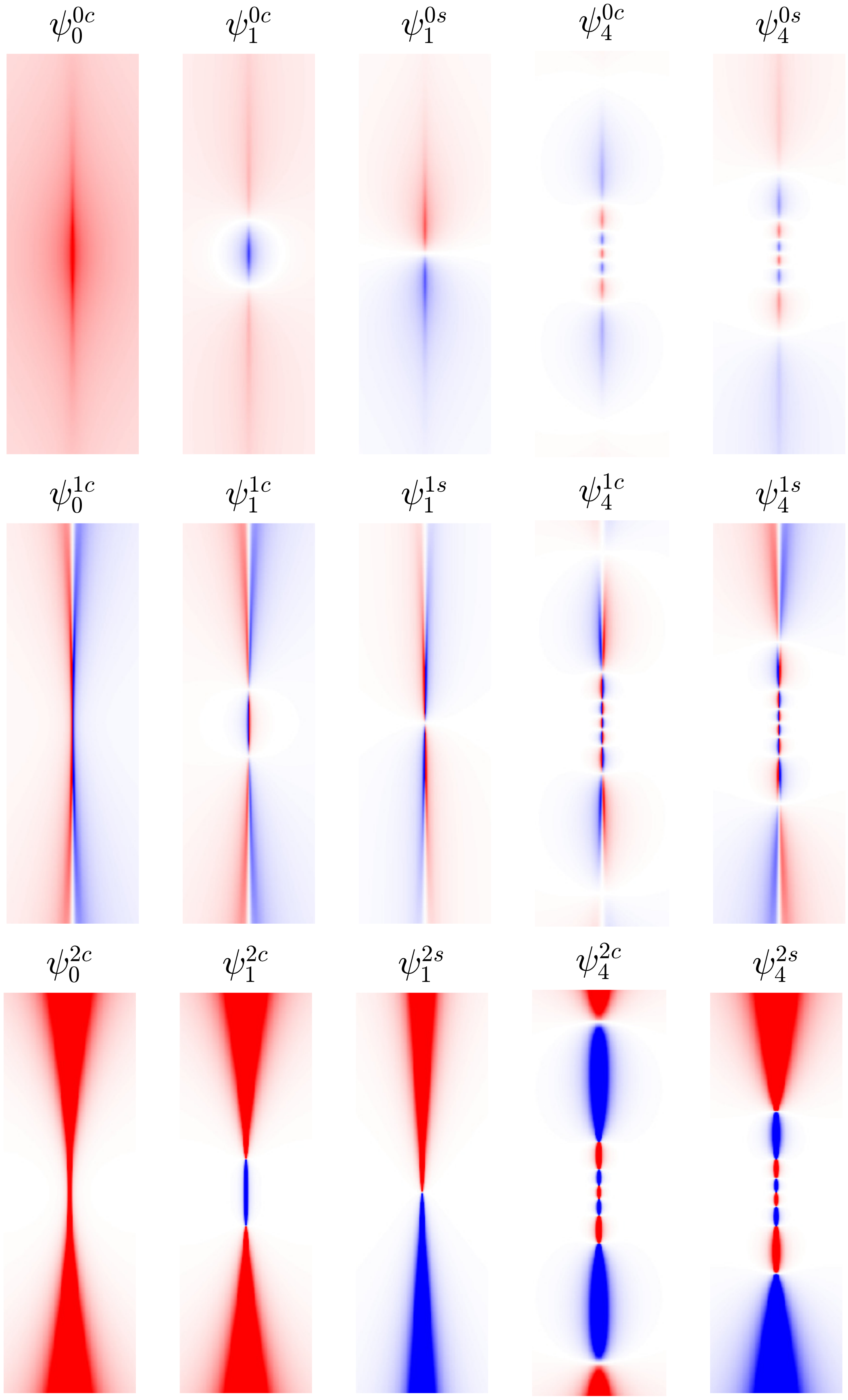

Figure 7.4: Plots of the axial toroidal harmonics for $n = 0,1,4$ and $m = 0,1,2$, on a slice of the x,z plane. The focal ring radius is 1/4 the width of each plot. The color scale is [-10,10] for $m = 0$, [-50,50] for $m = 1$ and [-500,500] for $m = 2$.

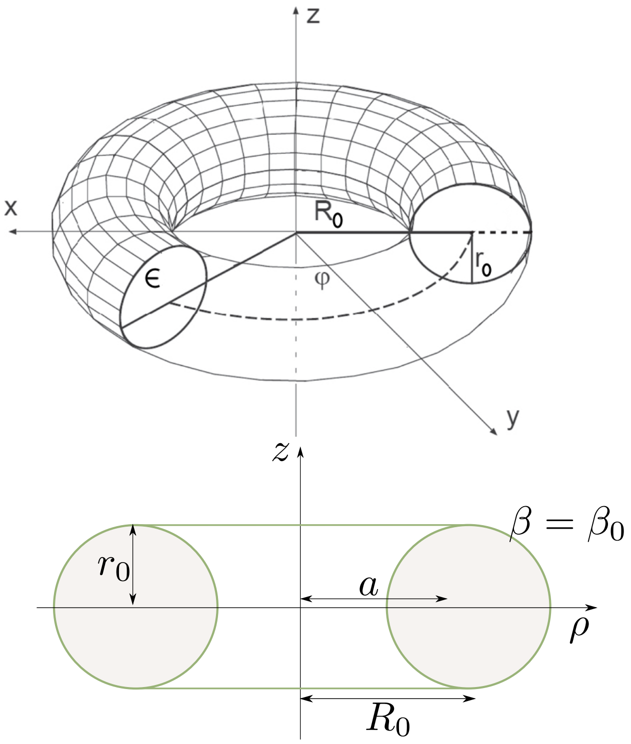

Figure 7.5: Top: Parameters defining the torus including relative permittivity to the surroundings ε. Bottom: relationships between toroidal geometry and the separable toroidal coordinate system.

7.2 T-matrix for a torus on a toroidal harmonic basis

Consider a circular torus with major radius R_0, minor radius r_0 and relative permittivity to the surroundings ε as shown in Figure 7.5. The surface is defined by the aspect ratio $\beta = \beta_0 = R_0/r_0$, and the focal ring radius is $a = \sqrt{R_0^2 - r_0^2}$. The torus is excited by an arbitrary external electric potential V_e, and we want to determine the scattered potential V_s (where $V_\mathrm{o} = V_\mathrm{e} + V_\mathrm{s}$), and internal potential V_i. The boundary conditions are:

$$V_\mathrm{i} = V_\mathrm{o}, \qquad \varepsilon \frac{\partial V_\mathrm{i}}{\partial \beta} = \frac{\partial V_\mathrm{o}}{\partial \beta}, \qquad \text{at } \beta = \beta_0. \tag{7.23}$$

The fields are assumed to be expanded in terms of toroidal harmonics as

$$V_\mathrm{e} = \sum_{n=0}^{\infty} \sum_{m=-\infty}^{\infty} \sum_{\nu=c,s} a_n^{m\nu} \psi_n^{m\nu}, \tag{7.24}$$

$$V_\mathrm{i} = \sum_{n=0}^{\infty} \sum_{m=-\infty}^{\infty} \sum_{\nu=c,s} b_n^{m\nu} \psi_n^{m\nu}, \tag{7.25}$$

$$V_\mathrm{s} = \sum_{n=0}^{\infty} \sum_{m=-\infty}^{\infty} \sum_{\nu=c,s} c_n^{m\nu} \Psi_n^{m\nu}. \tag{7.26}$$

In this section we derive the matrix relations between the incident, scattered, and internal expansion coefficients.

In general the boundary conditions are difficult to solve, and may lead to an inhomogeneous three term recurrence relation with initial conditions given by an infinite continued fraction [99]. Instead we will use the boundary integral equation formulation to find an analogue of the T-matrix in toroidal coordinates. The boundary integral equations are derived from Green's second identity on the torus surface S [76]:

$$\frac{\varepsilon - 1}{4\pi} \int_S \frac{\partial V_\mathrm{i}(\mathbf{r}')}{\partial n'} \frac{1}{|\mathbf{r} - \mathbf{r}'|} \mathrm{d}S' = \begin{cases} V_\mathrm{e}(\mathbf{r}) - V_\mathrm{i}(\mathbf{r}) & \mathbf{r} \in V \\ -V_\mathrm{s}(\mathbf{r}) & \mathbf{r} \notin V. \end{cases} \tag{7.27}$$

where $\partial/\partial n'$ is the derivative with respect to the surface normal and $\mathrm{d}S$ is the infinitesimal surface element. In the T-matrix approach, the Green function $1/|\mathbf{r} - \mathbf{r}'|$ is expanded as a series of separable harmonics; here we use toroidal harmonics:

$$\frac{1}{|\mathbf{r}-\mathbf{r}'|} = \frac{1}{2\pi a} \sum_{m=-\infty}^{\infty} \sum_{n=0}^{\infty} \sum_{v=c,s} \varepsilon_n (-)^m \begin{cases} \psi_n^{mv}(\mathbf{r}) \Psi_n^{-m,v}(\mathbf{r}') & \mathbf{r} \in V \\ \Psi_n^{mv}(\mathbf{r}) \psi_n^{-m,v}(\mathbf{r}') & \mathbf{r} \notin V \end{cases} \tag{7.28}$$

$$\text{with } \varepsilon_n = \begin{cases} 1 & n = 0 \\ 2 & n > 0 \end{cases} .$$

We now substitute (7.28) and the expansions of the potentials into the integral equation(7.27), and equate the coefficients of the toroidal harmonics. For example, equating the coefficients of $\psi_n^{mc}(\mathbf{r})$ for $\mathbf{r}$ inside the torus leads to (dropping the integration primes):

$$\varepsilon_n(-)^m \frac{\varepsilon-1}{8\pi^2 a} \sum_{k=0}^{\infty} \int_S \frac{\partial}{\partial n} \{\Delta Q_{k-1/2}^m(\beta_0)[b_k^{mc}\cos(k\eta) + b_k^{ms}\sin(k\eta)]\} \Delta P_{n-1/2}^{-m}(\beta_0)\cos(n\eta)\mathrm{d}S = a_n^{mc} - b_n^{mc}. \tag{7.29}$$

The sum over m has been omitted because the torus is rotationally symmetric and only terms with the same m in the expansions of the V_i and G survive the integration. This decouples the problem for each m. Furthermore, the integration is over an even interval of η so $\sin(k\eta)\cos(n\eta)$ integrates to zero, decoupling the sine and cosine expansion coefficients. The relationships between the expansion coefficients can be formulated with infinite dimensional matrices. For each $m \in \mathbb{Z},\ v = c,s$, the problem is solved by the following matrix relations:

$$\bar{\mathbf{a}} = \bar{\mathbf{Q}}\bar{\mathbf{b}}, \quad \bar{\mathbf{c}} = \bar{\mathbf{P}}\bar{\mathbf{b}}, \quad \bar{\mathbf{c}} = \bar{\mathbf{T}}\bar{\mathbf{a}} \tag{7.30}$$

which are analogous to the P, Q, T-matrices in the T-matrix method for scattering of waves. $\bar{\mathbf{a}}$ are $1 \times N$ (N being the numerical truncation order) column vectors containing the elements a_n^{mv} for fixed m, v. When convenient the superscripts m and v will be omitted.
For a conducting torus, $\varepsilon \to \infty$ and the T-matrix $\bar{\mathbf{T}} = \bar{\mathbf{T}}^\infty$ is diagonal:

$$\bar{T}_{nk}^\infty = -\frac{Q_{n-1/2}^m(\beta_0)}{P_{n-1/2}^m(\beta_0)} \delta_{nk} \tag{7.31}$$

which is equivalent to well known solutions for conducting tori, see for example [108].
For general ε, the integral equations 7.27 allow us to calculate $\bar{\mathbf{P}}$ and $\bar{\mathbf{Q}}$, while $\bar{\mathbf{T}}$ is obtained from

$$\bar{\mathbf{T}} = \bar{\mathbf{P}}\bar{\mathbf{Q}}^{-1}. \tag{7.32}$$

We now look for analytic expressions for the matrix elements. In toroidal coordinates the normal derivative and surface element are

$$\frac{\partial}{\partial n} = \frac{-\Delta^2 \sinh\xi}{2a} \frac{\partial}{\partial \beta}, \qquad \mathrm{d}S = \frac{4a^2 \sinh\xi}{\Delta^4} \mathrm{d}\eta \mathrm{d}\phi. \tag{7.33}$$

Putting these into (7.29) and simplifying leads to an integral expression for $\bar{\mathbf{Q}}^c$:

$$\bar{Q}_{nk}^{mc} = \delta_{nk} - \frac{\varepsilon-1}{2\pi} P_{n-1/2}^{-m}(\beta_0)\varepsilon_n \left[\frac{\partial Q_{k-1/2}^m(\beta_0)}{\partial \beta_0} \int_{-\pi}^{\pi} \cos(n\eta)\cos(k\eta)\mathrm{d}\eta + \frac{1}{2} Q_{k-1/2}^m(\beta_0) \int_{-\pi}^{\pi} \frac{\cos(n\eta)\cos(k\eta)}{\beta_0 - \cos\eta} \mathrm{d}\eta \right]. \tag{7.34}$$

The integrals can be evaluated analytically (see appendix of [25]), and the matrix elements are then

$$\bar{Q}_{nk}^{mc} = \delta_{nk} - (\varepsilon-1)\sinh^2\xi_0 P_{n-1/2}^{-m}(\beta_0) \left[\partial_{\beta_0} Q_{n-1/2}^m(\beta_0)\delta_{nk} + \frac{\varepsilon_n}{2} Q_{k-1/2}^m(\beta_0) \frac{e^{-|n-k|\xi_0} + e^{-(n+k)\xi_0}}{2\sinh\xi_0} \right], \tag{7.35}$$

$$\bar{Q}_{nk}^{ms} = \delta_{nk} - (\varepsilon-1)\sinh^2\xi_0 P_{n-1/2}^{-m}(\beta_0) \left[\partial_{\beta_0} Q_{n-1/2}^m(\beta_0)\delta_{nk}(1-\delta_{n0}) - Q_{k-1/2}^m(\beta_0) \frac{e^{-|n-k|\xi_0} - e^{-(n+k)\xi_0}}{2\sinh\xi_0} \right]. \tag{7.36}$$

A similar derivation shows that $\bar{\mathbf{P}}$ is related to $\bar{\mathbf{Q}}$ by $\bar{\mathbf{P}} = \bar{\mathbf{T}}^{\infty}(\bar{\mathbf{Q}} - \mathbf{I})$ for all m, v. Hence the T-matrix can also be expressed as

$$\bar{\mathbf{T}} = \bar{\mathbf{T}}^{\infty}(\mathbf{I} - \bar{\mathbf{Q}}^{-1}). \tag{7.37}$$

We suspect this form applies to the T-matrix for any particle whose geometry is a coordinate of a coordinate system with partially-separable solutions to Laplace's equation, including bispherical coordinates, as seen in the next chapter. $\bar{\mathbf{T}}$ may be calculated via (7.32) or (7.37); both give the same numerical accuracy. To avoid possible numerical instability in inverting $\bar{\mathbf{Q}}^{m=0,c}$, the matrix should be transposed, inverted then transposed back.

The static limit T-matrix for any scatterer is symmetric when expressed on a basis of normalized spherical harmonics or wave functions. This is proved in [109] by equating solutions from two surface integral equations similar to (7.27), given in [76]. The proof used a basis of normalized spherical harmonics but could be easily done with any orthonormal basis. The basis functions Ψ_n^{mv}, ψ_n^{mv} are orthogonal but not normalized - they have a norm of $\Gamma(n+m+\frac{1}{2})/\Gamma(n-m+\frac{1}{2})/\varepsilon_n$. Hence the toroidal T-matrix here has the following symmetry property:

$$\bar{T}_{kn}^{mv} = \frac{\varepsilon_k \Gamma(k-m+\frac{1}{2})\Gamma(n+m+\frac{1}{2})}{\varepsilon_n \Gamma(k+m+\frac{1}{2})\Gamma(n-m+\frac{1}{2})} \bar{T}_{nk}^{mv}. \tag{7.38}$$

7.2.1 Comparison to recurrence approach

Another way to solve electrostatic problems for the dielectric torus is to apply the boundary conditions in differential form (7.23) directly to the series expansions for the potentials (7.24-7.26), to obtain a recurrence relation for the coefficients. This has been done for a uniform electric field [99], and point charge [110]. For arbitrary excitation, we get

$$\begin{aligned} &c_{n+1}^{mv}\Lambda_{n+1}^{m} - c_n^{mv}\big(2\beta_0\Lambda_n^m + (\varepsilon-1)P_{n-1/2}^m\big) + c_{n-1}^{mv}\Lambda_{n-1}^m \\ &\qquad = (\varepsilon-1)\big[-a_{n+1}^{mv}Q_{n+1/2}^{m\prime} + a_n^{mv}(Q_{n-1/2}^m + 2\beta_0 Q_{n-1/2}^{m\prime}) - a_{n-1}^{mv}Q_{n-3/2}^{m\prime}\big] \\ &\text{where}\quad \Lambda_n^m = \varepsilon Q_{n-1/2}^{m\prime}(\beta_0)\frac{P_{n-1/2}^m(\beta_0)}{Q_{n-1/2}^m(\beta_0)} - P_{n-1/2}^{m\prime}(\beta_0). \end{aligned} \tag{7.39}$$

The difficulty in computing the coefficients using this scheme is finding the initial values; these are expressed as a series of products of continued fractions. Nevertheless, we can compare this to the T-matrix approach, combining recurrence (7.39) with the definition of the T-matrix, (7.30), we find

$$\begin{aligned} &\sum_{k=0}^{\infty}\left[\bar{T}_{n+1k}^{mv}\Lambda_{n+1}^m - \bar{T}_{nk}^{mv}\big(2\beta_0\Lambda_n^m + (\varepsilon-1)P_{n-1/2}^m\big) + \bar{T}_{n-1k}^{mv}\Lambda_{n-1}^m\right]a_k^{mv} \\ &\qquad = (\varepsilon-1)\big[-a_{n+1}^{mv}Q_{n+1/2}^{m\prime} + a_n^{mv}(Q_{n-1/2}^m + 2\beta_0 Q_{n-1/2}^{m\prime}) - a_{n-1}^{mv}Q_{n-3/2}^{m\prime}\big] \end{aligned} \tag{7.40}$$

which must hold for any set of coefficients a_n^{mv}. In particular if we choose an excitation with $a_n^{mv} = \delta_{np}$ for some p, a recurrence for the elements of the toroidal T-matrix can be found:

$$\begin{aligned} &\bar{T}_{n+1p}^{mv}\Lambda_{n+1}^m - \bar{T}_{np}^{mv}\big(2\beta_0\Lambda_n^m + (\varepsilon-1)P_{n-1/2}^m\big) + \bar{T}_{n-1p}^{mv}\Lambda_{n-1}^m \\ &\qquad = (\varepsilon-1)\big[\delta_{np}(Q_{p-1/2}^m + 2\beta_0 Q_{p-1/2}^{m\prime}) - (\delta_{n+1p} + \delta_{n-1p})Q_{p-1/2}^{m\prime}\big], \end{aligned} \tag{7.41}$$

which has been checked numerically.

7.3 Relationships between spherical and toroidal harmonics

In order to express the T-matrix on a basis of spherical harmonics, series relationships between spherical and toroidal harmonics are needed. We define the regular and irregular solid spherical harmonics as:

$$\hat{S}_n^m = \left(\frac{r}{a}\right)^n P_n^m(\cos\theta)e^{im\phi}, \tag{7.42}$$

$$S_n^m = \left(\frac{a}{r}\right)^{n+1} P_n^m(\cos\theta)e^{im\phi}, \tag{7.43}$$

and present the following linear relationships between spherical and toroidal harmonics (see appendix of [25]):

$$\Psi_n^{mc} = \sum_{k=m}^{\infty} c_{nk}^m P_k^{-m}(0) \begin{cases} (-)^n \hat{S}_k^m & r < a \\ S_k^m & r > a \end{cases} \tag{7.44}$$

$$\Psi_n^{ms} = \sum_{k=m}^{\infty} s_{nk}^m P_{k+1}^{-m}(0) \begin{cases} (-)^n \hat{S}_k^m & r < a \\ -S_k^m & r > a \end{cases} \tag{7.45}$$

$$\hat{S}_n^m = \frac{1}{\pi} \begin{cases} P_n^m(0) \displaystyle\sum_{k=0}^{\infty} \frac{\varepsilon_k}{2} c_{kn}^{-m} \psi_k^{mc} & n+m \text{ even} \\ -P_{n+1}^m(0) \displaystyle\sum_{k=1}^{\infty} s_{kn}^{-m} \psi_k^{ms} & n+m \text{ odd} \end{cases} \tag{7.46}$$

$$S_n^m = \frac{1}{\pi} \begin{cases} P_n^m(0) \displaystyle\sum_{k=0}^{\infty} \frac{\varepsilon_k}{2} (-)^k c_{kn}^{-m} \psi_k^{mc} & n+m \text{ even} \\ P_{n+1}^m(0) \displaystyle\sum_{k=1}^{\infty} (-)^k s_{kn}^{-m} \psi_k^{ms} & n+m \text{ odd.} \end{cases} \tag{7.47}$$

c_{nk}^m, s_{nk}^m are rational numbers with many equivalent explicit forms and recurrence relations. They may be defined by the stable recurrence:

$$\left(n - m + \frac{1}{2}\right) c_{n+1,k}^m = (2k+1) c_{nk}^m + \left(n + m - \frac{1}{2}\right) c_{n-1,k}^m \tag{7.48}$$

and the same for s_{nk}^m. The initial values are

$$\begin{aligned} c_{0k}^m &= \frac{(2m-1)!!}{2^{m-1}}, & c_{1k}^m &= -\frac{(2m-3)!!}{2^{m-1}}(2k+1), \\ s_{0k}^m &= 0, & s_{1k}^m &= -\frac{(2m-3)!!}{2^m}(k+m+1). \end{aligned} \tag{7.49}$$

(the double factorial can be extended to odd negative integers via recurrence, or equivalently through the gamma function). And for $m < 0$:

$$c_{nk}^{-m} = \frac{\Gamma(n - m + \frac{1}{2})}{\Gamma(n + m + \frac{1}{2})} c_{nk}^m, \qquad s_{nk}^{-m} = \frac{\Gamma(n - m + \frac{1}{2})}{\Gamma(n + m + \frac{1}{2})} \frac{k - m + 1}{k + m + 1} s_{nk}^m. \tag{7.50}$$

The Legendre functions at 0 are, for $m \in \mathbb{Z}$:

$$P_n^m(0) = \begin{cases} (-)^{(n-m)/2} \dfrac{(n+m-1)!!}{(n-m)!!} & n+m \text{ even} \\ 0 & n+m \text{ odd.} \end{cases} \tag{7.51}$$

We should discuss the existence of these expansions. Toroidal harmonics do not follow the same notion of internal and external as do spherical and spheroidal harmonics. We see that the ring harmonics Ψ_m^{mv} can be written as a series of either internal or external spherical harmonics; this is due to the fact that Ψ_m^{mv} are finite at both the origin and at $r = \infty$. However the axial toroidal harmonics ψ_n^{mv} are *singular* at both the origin and infinity, so cannot be expanded as a series of spherical harmonics at all [1]. Conversely, neither internal and external spherical harmonics can be expressed as a series of ring harmonics Ψ_n^{mv}. This is because a series of ring harmonics can only converge outside some toroidal boundary, and this boundary must enclose the singularities of the function being expanded - the external spherical harmonics S_n^m are singular at the origin, so this toroidal boundary must cover the origin and thus extend to all space, while the internal spherical harmonics $\hat{S}_n^m$ cannot be expanded for a similar reason - the torus must extend to all space to cover the "singularity" at $r = \infty$. However, both internal and external spherical harmonics can be expanded with axial toroidal harmonics ψ_n^{mv}; this is because a series of axial toroidal harmonics will converge *inside* some torus - for the internal spherical

---

[1] They can neither be expressed as a series of spherical harmonics of the second kind, $r^n Q_n(\cos\theta)$ or $r^{-n-1} Q_n(\cos\theta)$ which are also singular on the z axis. This is due to differences in parity about z.

harmonics, this toroidal boundary may extend up to infinity since the functions are continuous in all space. For external spherical harmonics the toroidal boundary may extend to the origin - so that the torus also covers all space. To check this we can determine the boundary of convergence of expansions (7.46) and (7.47) from the behavior of the k^{th} term in the series as $k \to \infty$. The Legendre functions grow as ([62] pg 191):

$$\lim_{k\to\infty} P^m_{k-1/2}(\cosh\xi) = \frac{k^m e^{k\xi}}{\sqrt{(2k-1)\sinh\xi}} \tag{7.52}$$

$$\lim_{k\to\infty} Q^m_{k-1/2}(\cosh\xi) = \frac{\sqrt{\pi}(-k)^m e^{-k\xi}}{\sqrt{(2k-1)\sinh\xi}} \tag{7.53}$$

while c^{-m}_{kn} and s^{-m}_{kn} can be shown to grow slower than k^{2n+1}; polynomial growth in k. The series coefficients then decay geometrically as $e^{-k\xi}$, and $\xi > 0$ everywhere except the z-axis and $r = \infty$, so the series converge everywhere, although slowly near the z axis and for large r. In these cases the series terms grow significantly in magnitude before converging, which sacrifices accuracy because the series can only be accurate to the last digit of the largest term in the series. This causes problems in dealing with extremely tight tori.

7.4 T-matrix on a spherical harmonic basis

7.4.1 Derivation

For any bounded scatterer, the scattered field is expandable on a basis of outgoing spherical harmonics that converge outside the circumscribing sphere, and by linearity of Laplace's equation, the expansion coefficients are linearly related to the coefficients of the incident field. Therefore the T-matrix for any bounded scatterer should exist on a basis of spherical harmonics. In fact for a torus, the incident and scattered fields may both be expanded on interior or exterior spherical harmonics (see sec. 7.4.2). First we look at the standard case where the external field is expanded on regular spherical harmonics and the scattered field will be expanded on irregular harmonics. So the potentials are assumed to have the following expansions:

$$V_{\mathrm{e}} = \sum_{m=-\infty}^{\infty} \sum_{n=|m|}^{\infty} A^m_n \hat{S}^m_n, \tag{7.54}$$

$$V_{\mathrm{s}} = \sum_{m=-\infty}^{\infty} \sum_{n=|m|}^{\infty} C^m_n S^m_n, \tag{7.55}$$

equivalently the sum over n can be written in matrix notation:

$$V_{\mathrm{e}} = \sum_m \mathbf{A}^T \hat{\mathbf{S}}, \tag{7.56}$$

$$V_{\mathrm{s}} = \sum_m \mathbf{C}^T \mathbf{S}, \qquad \mathbf{C} = \mathbf{T}\mathbf{A}. \tag{7.57}$$

where for example $\mathbf{A}$, $\hat{\mathbf{S}}$ are $1 \times N$ (N being the numerical truncation order) column vectors containing the elements A^m_n or $\hat{S}^m_n$ for all $n \geq 0$, for a fixed m, and $\mathbf{T}$ is the T-matrix. The vectors and matrices start their index from $n = 0$ even though the spherical harmonics are zero for $n < m$; this is to match the dimensionality of the toroidal matrices which start from $n = 0$.

It is not possible to expand the internal potential V_{i} as a series of spherical harmonics, following the discussion in Section 7.3. We know V_{i} may be represented as a series of toroidal harmonics ψ^m_n which are singular on the z-axis, so it is a fair assumption that the analytic continuation of V_{i} is singular on at least the z-axis (although technically it may be possible that a series of functions that are singular in some region could cancel exactly resulting in a smooth function, but this seems unlikely). This singularity would prohibit expansions in terms of both external or internal spherical harmonics since *every* spherical annulus would contain singular points. This means that the P and Q matrices have no representation on a spherical basis, and therefore it would be impossible to compute the T-matrix directly via the extended boundary method on a spherical basis. However, since the problem can be solved using toroidal harmonics, we can use this and apply the spherical-toroidal transformations of Section 7.3 without considering V_{i}.

It will be useful to express the relationships between spherical and toroidal harmonics in matrix notation:

$$\hat{\mathbf{S}} = \mathbf{M}_r^c \psi^c + \mathbf{M}_r^s \psi^s, \tag{7.58}$$

$$\boldsymbol{\Psi}^c = \mathbf{N}_i^c \mathbf{S}, \tag{7.59}$$

$$\boldsymbol{\Psi}^s = \mathbf{N}_i^s \mathbf{S}, \tag{7.60}$$

where the elements of matrices **M** and **N** can be determined from (7.44,7.45,7.46) to be

$$\begin{aligned}
[M_r^c]_{nk}^m &= \frac{\varepsilon_k}{2\pi} P_n^m(0) c_{kn}^{-m}, \\
[M_r^s]_{nk}^m &= \frac{-1}{\pi} P_{n+1}^m(0) s_{kn}^{-m}, \\
[N_i^c]_{nk}^m &= P_k^{-m}(0) c_{nk}^m, \\
[N_i^s]_{nk}^m &= -P_{k+1}^{-m}(0) s_{nk}^m.
\end{aligned} \tag{7.61}$$

The subscripts r, i stand for regular or irregular (referring to the type of spherical harmonic), and the superscripts c, s refer to cosine or sine of η.
First the excitation potential in (7.56) must be expressed on a basis of toroidal harmonics by applying (7.58):

$$V_\mathrm{e} = \sum_m \mathbf{A}^T [\mathbf{M}_r^c \psi^c + \mathbf{M}_r^s \psi^s] \tag{7.62}$$

then V_s is found via the toroidal-basis T-matrix solution (7.30):

$$V_\mathrm{s} = \sum_m \mathbf{A}^T [\mathbf{M}_r^c (\bar{\mathbf{T}}^c)^T \boldsymbol{\Psi}^c + \mathbf{M}_r^s (\bar{\mathbf{T}}^s)^T \boldsymbol{\Psi}^s]. \tag{7.63}$$

Expanding the toroidal functions back into spherical harmonics with (7.60):

$$V_\mathrm{s} = \sum_m \mathbf{A}^T [\mathbf{M}_r^c (\bar{\mathbf{T}}^c)^T \mathbf{N}_i^c + \mathbf{M}_r^s (\bar{\mathbf{T}}^s)^T \mathbf{N}_i^s] \mathbf{S}. \tag{7.64}$$

Comparing this to (7.57), and noting that $\mathbf{C}^T = \mathbf{A}^T \mathbf{T}^T$, the T-matrix is found to be

$$\mathbf{T} = (\mathbf{N}_i^c)^T \bar{\mathbf{T}}^c (\mathbf{M}_r^c)^T + (\mathbf{N}_i^s)^T \bar{\mathbf{T}}^s (\mathbf{M}_r^s)^T. \tag{7.65}$$

The $v = c$ term $(\mathbf{N}_i^c)^T \bar{\mathbf{T}}^c (\mathbf{M}_r^c)^T$ contributes to the entries of **T** with only n and k both even, while $(\mathbf{N}_i^s)^T \bar{\mathbf{T}}^s (\mathbf{M}_r^s)^T$ contributes only to entries with n and k both odd. Hence $T_{nk}^m = 0$ for $n + k$ odd as expected for particles with reflection symmetry about z.

Here we have not used normalized spherical basis functions, and as a consequence **T** is not symmetric for $m > 0$. The quasi-static limit of the conventional symmetric electromagnetic T-matrix in [8] can be obtained from:

$$\lim_{k_1 \to 0} T_{nk}^{22,m} = \frac{-i(k_1 a)^{n+k+1}}{(2n-1)!!(2k-1)!!} \sqrt{\frac{(n+1)(k+1)}{nk(2n+1)(2k+1)} \frac{(n+m)!(k-m)!}{(n-m)!(k+m)!}} T_{nk}^m \tag{7.66}$$

where k_1 is the wavenumber in the surrounding medium.

7.4.2 Interior/exterior T-matrices

In the above derivation we assumed that the external potential was created by a source that could be expanded as a series of *regular* spherical harmonics, but because the torus excludes the origin, the external field may come from near the origin (for example a point source at the origin) and *irregular* harmonics must be used instead. Similarly, to compute the scattered field near the origin, a regular basis must be used. The T-matrix derived above applies only if V_e is expanded on $\hat{S}_m^m$ and V_s is expanded on S_n^m, and we denote this matrix $\mathbf{T}(r \to i)$.

Following similar derivations, expressions for the other matrices can be found, and all four variations of these T-matrices are

$$\begin{aligned}\mathbf{T}(r\to i) &= (\mathbf{N}_i^c)^T\bar{\mathbf{T}}^c(\mathbf{M}_r^c)^T + (\mathbf{N}_i^s)^T\bar{\mathbf{T}}^s(\mathbf{M}_r^s)^T\\ \mathbf{T}(r\to r) &= (\mathbf{N}_r^c)^T\bar{\mathbf{T}}^c(\mathbf{M}_r^c)^T + (\mathbf{N}_r^s)^T\bar{\mathbf{T}}^s(\mathbf{M}_r^s)^T\\ \mathbf{T}(i\to r) &= (\mathbf{N}_r^c)^T\bar{\mathbf{T}}^c(\mathbf{M}_i^c)^T + (\mathbf{N}_r^s)^T\bar{\mathbf{T}}^s(\mathbf{M}_i^s)^T\\ \mathbf{T}(i\to i) &= (\mathbf{N}_i^c)^T\bar{\mathbf{T}}^c(\mathbf{M}_i^c)^T + (\mathbf{N}_i^s)^T\bar{\mathbf{T}}^s(\mathbf{M}_i^s)^T\end{aligned} \tag{7.67}$$

The transformation matrices not already defined in (7.61) are

$$\begin{aligned}{[M_i^c]}^m_{nk} &= \frac{\varepsilon_k(-)^k}{2\pi}P_n^m(0)c_{kn}^{-m},\\ {[M_i^s]}^m_{nk} &= \frac{(-)^k}{\pi}P_{n+1}^m(0)s_{kn}^{-m},\\ {[N_r^c]}^m_{nk} &= (-)^n P_k^{-m}(0)c_{nk}^m,\\ {[N_r^s]}^m_{nk} &= (-)^n P_{k+1}^{-m}(0)s_{nk}^m.\end{aligned} \tag{7.68}$$

For example, $\mathbf{T}(r\to r)$ applies if the source is outside the torus' circumscribing sphere, and if the scattered field is to be evaluated near the hole. For a conducting torus two pairs of these T-matrices in (7.67) are identical. Mathematically it is straightforward to show that $\mathbf{T}(i\to r)=\mathbf{T}(r\to i)$. Physically this is due to the fact that the problem for a conductor does not distinguish the scattered and external/incident fields - the problem of determining the incident field from the scattered is the same as determining the scattered from the incident. And $\mathbf{T}(r\to r)=\mathbf{T}(i\to i)$, which can be shown by applying radial inversion about the sphere of radius a centred at the origin. The geometry transforms as $r\to a^2/r$ which preserves the torus, while potentials transform as $V\to(a/r)V(r\to a^2/r)$, so $\hat{S}_n^m \leftrightarrow S_n^m$. This argument only applies to the conducting torus since the permittivity also transforms as $\varepsilon\to(a^2/r^2)\varepsilon$.

From the static T-matrix we can make deductions of the applicability of the full-wave T-matrix. Since the high order limit of the spherical wave functions tends towards the solid spherical harmonics, the boundaries of convergence of the full wave solution are identical to that for the quasistatic solution. We note that even with the option of interior and exterior spherical harmonics to express the scattered field, it is not possible to compute the scattered field in an intermediate spherical annulus around the mid section of the torus $r\sim a$, due to the singularity of the scattered field. For example in the simple case of a conducting torus held at constant potential, it can be shown that both the interior and exterior spherical harmonic solutions diverge in the annulus $a<r<R_0$. This is analogous to spheroids with high aspect ratio - there is a region near the spheroid where the fields cannot be expressed using spherical basis functions.

7.5 Derived physical quantities

The T-matrix is amenable to calculate spatial fields, capacitance, polarizability, resonance conditions and cross sections. The following results also validate the T-matrix expressions.

7.5.1 Spatial fields

To verify the boundary conditions we plot the potential induced by a point dipole for the extreme cases of a conducting ($\varepsilon\to-\infty$) and non-conducting torus ($\varepsilon=0$) in Figure 7.6. In both cases the equi-potential lines visually satisfy the boundary conditions in (7.23). For a conducting torus the results for $\varepsilon=-10^7$ coincide with conducting solution (7.31).

Since gold nanoparticles are often used for their field enhancements, the electric field is plotted for a gold nano-torus in water excited by a uniform field, showing a strong field enhancement in the gap. The plots in Figure 7.6 have also been calculated using the spherical T-matrix and spherical harmonics, to verify that both approaches converge to the same result (at least where the spherical solution converges).

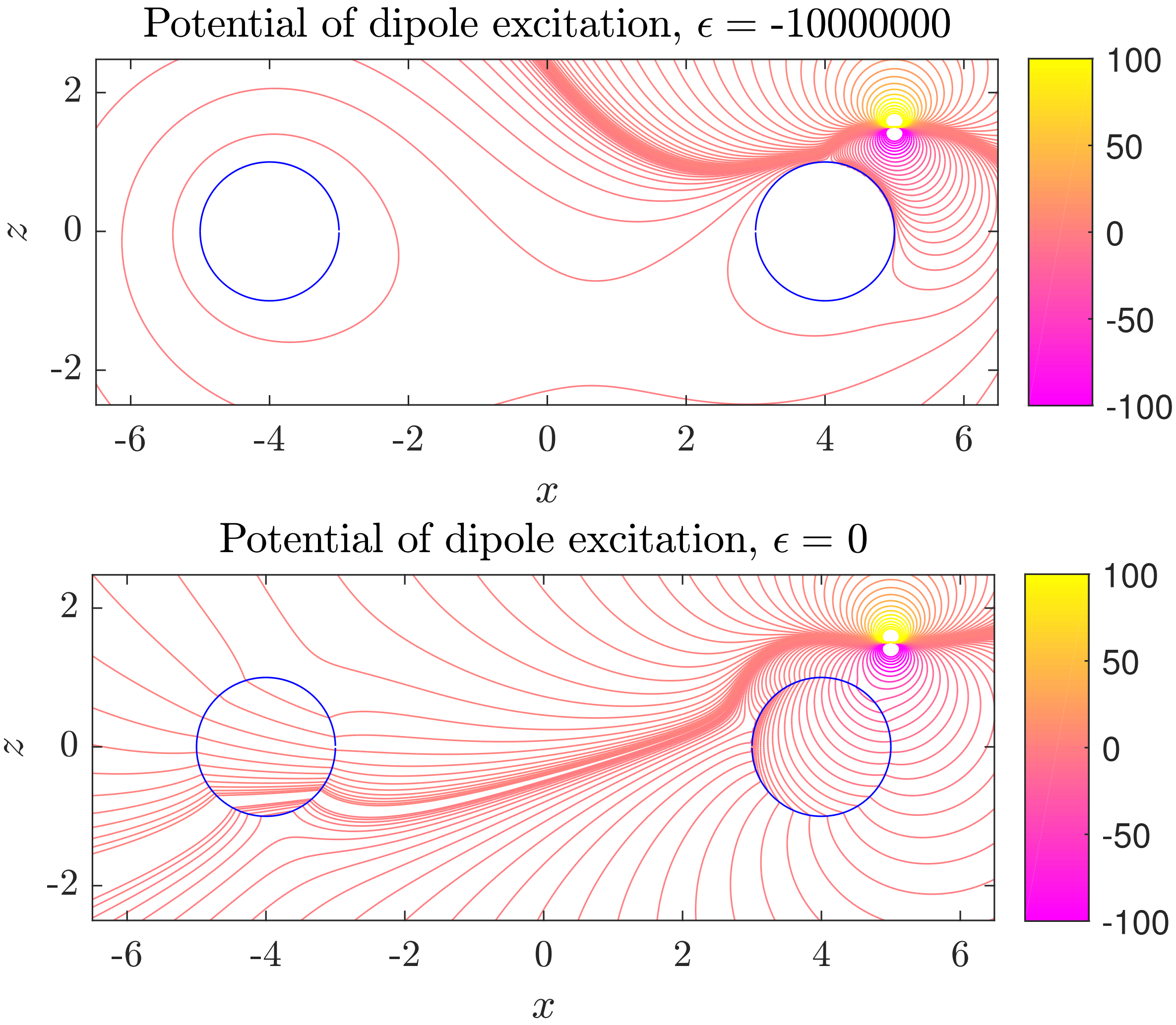

Figure 7.6: Cross section of the equi-potential lines for a dipole located at $x = 5, z = 1.5$ for a torus with $R_0 = 4, r_0 = 1$, $\varepsilon = 0$ or $\varepsilon = -10^7$. The contour lines are more densely spaced around small values of V for better visualization of the interaction with the torus (although this results in a dense accumulation around $V = 0$). The potential was computed using toroidal T-matrices and toroidal harmonics. Matrices were truncated at $n, m < N = 30$ for $\varepsilon = -10^7$ and $N = 50$ (approximately 15 s computation time) for $\varepsilon = 0$.

7.5.2 Capacitance and dipolar response

The capacity C of a conducting torus held at a uniform potential V_0 is related to T^0_{00}:

$$C = 4\pi\varepsilon_0 a T^0_{00}, \tag{7.69}$$

$$T^0_{00} = -\frac{2}{\pi}\sum_{q=0}^{\infty} \varepsilon_q \frac{Q_{q-1/2}(\beta_0)}{P_{q-1/2}(\beta_0)}. \tag{7.70}$$

And for the dipole polarizability α we consider a uniform field along a Cartesian axis, exciting dipole moment $\mathbf{p}$ in a conducting torus. The polarizability is related to T^0_{11}, T^1_{11}:

$$p_w = \alpha_{ww} E_w, \qquad w = x, y, z, \tag{7.71}$$

$$\alpha_{zz} = 4\pi\varepsilon_0 a^3 T^0_{11}, \tag{7.72}$$

$$\alpha_{xx} = \alpha_{yy} = 4\pi\varepsilon_0 a^3 T^1_{11}, \tag{7.73}$$

where

$$T^0_{11} = -\frac{16}{\pi}\sum_{q=1}^{\infty} q^2 \frac{Q_{q-1/2}(\beta_0)}{P_{q-1/2}(\beta_0)}, \tag{7.74}$$

$$T^1_{11} = \frac{1}{\pi}\sum_{q=0}^{\infty} \varepsilon_q (4q^2-1)\frac{Q^1_{q-1/2}(\beta_0)}{P^1_{q-1/2}(\beta_0)}. \tag{7.75}$$

These results agree with [37].

7.5.3 Plasmon resonances

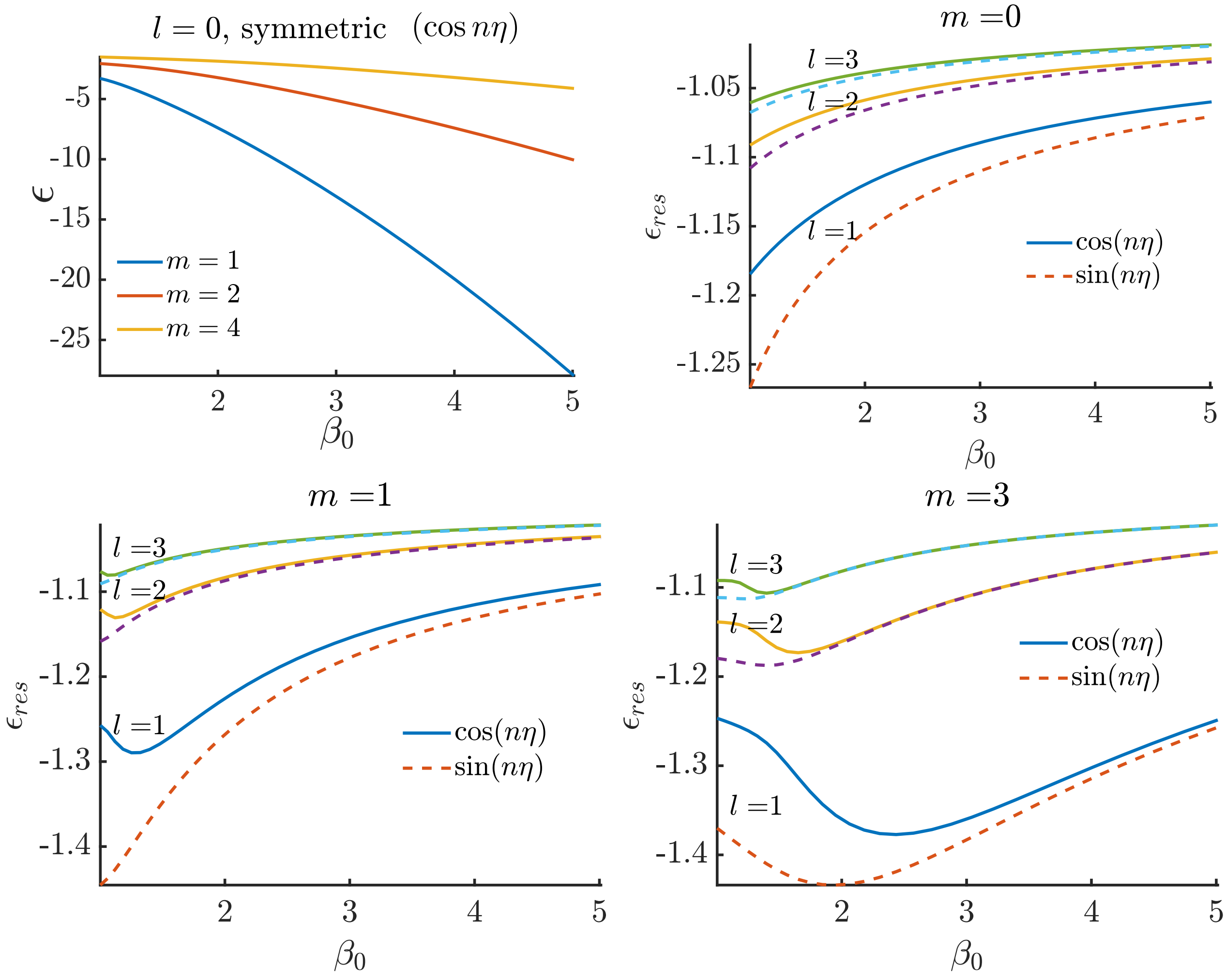

Figure 7.7: Relative resonant permittivities of tori of aspect ratio $\beta_0 = R_0/r_0$. The dashed (solid) curves correspond to the resonances of $\bar{\mathbf{T}}^c$ ($\bar{\mathbf{T}}^s$), which are symmetric (antisymmetric) about z. Resonances are labeled with mode number l in order of increasing ε. By convention the antisymmetric s modes start at $l = 1$ to match the symmetric modes. The top left plot shows the strong resonances that only occur for $\bar{\mathbf{T}}^c$. The other plots show the next three strongest resonances for both $v = c, s$; these resonances tend towards $\varepsilon = -1$, for all values of m, v, β_0. The matrix size used in calculations ranged from $N = 250$ for $\beta_0 = 1.01$ to $N = 12$ for $\beta_0 = 5$.

From the explicit expressions for the toroidal matrices in (7.35,7.36), we can calculate the plasmon resonances; the values of ε that produce $V = \infty$. These are labeled ε_l^{mv} for $l = 0, 1, 2...$, $m = 0, 1, 2...$, $v = c, s$. We have replaced the index n with l because each resonant mode consists of *all* toroidal harmonics for $n \geq 0$. A natural choice is to let l order these in terms of magnitude $|\varepsilon_l^{mv}|$ (ε_l^{mv} are all real and negative), which appears to also order the resonances in terms of resonance magnitude. ε_l^{mv} can be found from the condition $\det(\bar{\mathbf{Q}}) = 0$, through

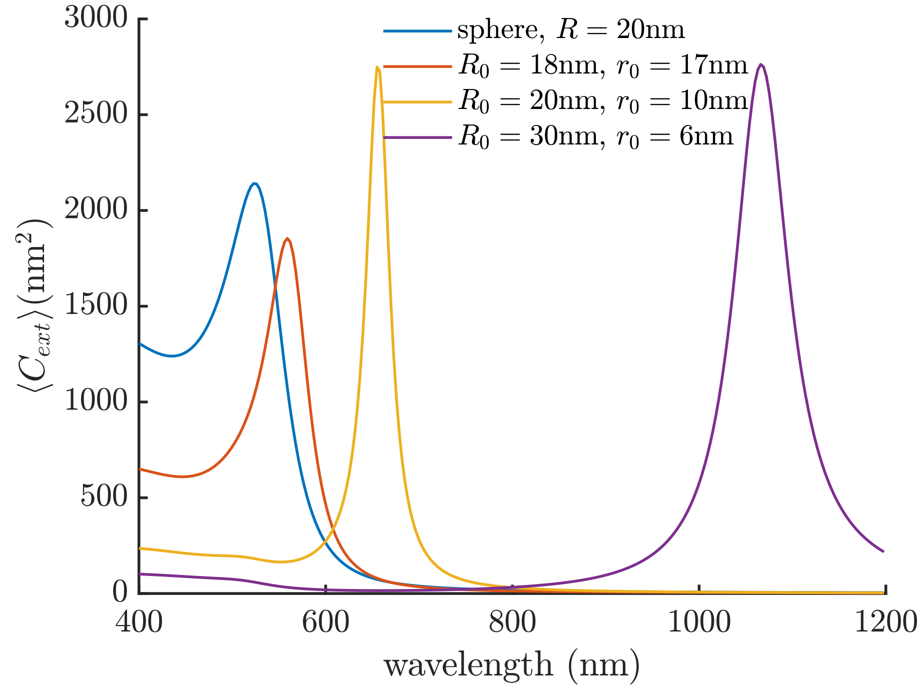

Figure 7.8: Extinction cross sections for a sphere and gold nano-tori in water. The dielectric function of gold was taken from Eq. (E.2) of [57], and $\varepsilon_{\text{water}} = 1.77$. The radiative correction $T_{11}^{22,1} \to 1/(1 - T_{11}^{22,1})$ has been applied [114, 27] which makes a small change to the data.

$\varepsilon_l^{mv} = 1 - 1/\lambda_l^{mv}$ where λ_l^{mv} are the eigenvalues of $\hat{\mathbf{Q}}^{mv}$ and $\bar{\mathbf{Q}}^{mv} = \mathbf{I} - (\varepsilon - 1)\hat{\mathbf{Q}}^{mv}$. This does not involve an implicit solution because $\hat{\mathbf{Q}}$ is independent of ε.

In Figure 7.7 the conditions for resonances are plotted as a function of aspect ratio β_0, and agree with the continued fraction approach [103, 111, 112]. Also, these results confirm the discussion of [113] claiming that $m = 0$ resonances exist, even though they were not obtained in [112, 111].

7.5.4 Extinction cross section

The extinction cross section is the effective area of an object in terms of how much electromagnetic radiation is removed, either absorbed or scattered, from an incident plane wave. It may be obtained from the elements of the full-wave T-matrix [8]. In the small particle limit, only the dominant terms $T_{11}^{22,m}$ for $m = 0, 1$ contribute. The orientation averaged extinction cross-section is relevant to suspensions of particles in solution or the atmosphere, since these particles are often assumed to be randomly oriented. It is calculated as the sum of the extinction in all Cartesian directions, which in terms of the T-matrix reads

$$\lim_{k_1 \to 0} \langle C_{ext} \rangle = -\frac{2\pi}{k_1^2} \mathrm{Re}\{T_{11}^{22,0} + 2T_{11}^{22,1}\}, \tag{7.76}$$

and we can simplify the formulas (7.65) and (7.66) for multipole order 1 to express these spherical T-matrix elements in terms of the toroidal T-matrix elements:

$$\lim_{k_1 \to 0} T_{11}^{22,0} = -i(k_1 a)^3 \frac{32}{3\pi} \sum_{n=0}^{\infty} \sum_{k=0}^{\infty} nk\, \bar{T}_{nk}^{m=0,s}, \tag{7.77}$$

$$\lim_{k_1 \to 0} T_{11}^{22,1} = i(k_1 a)^3 \frac{2}{3\pi} \sum_{n=0}^{\infty} \sum_{k=0}^{\infty} \varepsilon_k (4n^2 - 1) \bar{T}_{nk}^{m=1,c}. \tag{7.78}$$

The extinction cross-section is plotted in Figure 7.8 for various nano-tori and is consistent with results from [102, 115, 116]. The dominant response comes from $T_{11}^{22,1}$ in the spherical basis, exciting the planar dipole moment. In the toroidal basis, the largest matrix element is $\bar{T}_{11}^{1c}$, exciting the mode Ψ_1^{1c} among others which are less pronounced. The mode [2] Ψ_1^{1c} is visualized in figure 7.3 (second column, center row) and corresponds to excitation along the width of the torus, which is the $l = 0, m = 1$ plasmon resonance in Figure 7.7. We cannot see the resonances for $l \geq 1$ due to the considerable imaginary part of the dielectric function (another name for the permittivity ε, which is a function of the wavelength) of gold. In Figure 7.8, $T_{11}^{22,0}$ is almost negligible and has no resonance, because the torus has a more restrictive dimension along the z direction. The tighter torus (red curve) shows a resonance in the visible range, surprisingly similar to that of a sphere, perhaps because the surface plasmons accumulate towards the edges of the torus where the torus appears locally spherical. This resonance shifts in to the infrared as the torus becomes thinner.

7.6 Thin ring limit

We can find analytic results for the T-matrix elements in the thin ring limit, $\beta_0 \to \infty$. The limits of the Legendre functions are [62]

$$P^m_{-1/2}(\beta_0) \to \frac{\sqrt{2/(\pi\beta_0)}}{\Gamma(-m+\frac{1}{2})}\left[\log(8\beta_0) - 2\sum_{p=1}^{m}\frac{1}{2n-1}\right] \qquad m \geq 0 \tag{7.79}$$

$$P^m_{n-1/2}(\beta_0) \to \frac{(n-1)!(2\beta_0)^{n-1/2}}{\sqrt{\pi}\Gamma(n-m+\frac{1}{2})} \qquad n > 0 \tag{7.80}$$

$$Q^m_{n-1/2}(\beta_0) \to \frac{(-)^m\sqrt{\pi}\Gamma(n+m+\frac{1}{2})}{n!(2\beta_0)^{n+1/2}}. \tag{7.81}$$

(7.79) agrees with [108] but includes the sum for more accuracy. And we will need $Q^m_{-1/2}(\beta_0)$ to second order:

$$Q^m_{-1/2}(\beta_0) \to \frac{\pi(-)^m(2m-1)!!}{2^m\sqrt{2\beta_0}}\left[1+\frac{4m^2+3}{16\beta_0^2}\right] \tag{7.82}$$

which can be obtained from its hypergeometric function. It can be shown that the toroidal Q-matrices in this limit are lower triangular - $\bar{Q}^{mc}_{nk} = \bar{Q}^{ms}_{nk} = 0$ for $n < k$, with

$$\begin{aligned}
&\bar{Q}^{m\substack{c\\s}}_{nk} \to \delta_{nk}\frac{\varepsilon+1}{2} + (1-\delta_{nk})(1\pm\delta_{k0})\frac{\varepsilon-1}{4}\frac{\Gamma(k+m+\frac{1}{2})}{\Gamma(n+m+\frac{1}{2})}\frac{(n-1)!}{k!} \qquad n \geq k, n \neq 0\\
&\bar{Q}^{mc}_{00} \to 1 + \frac{\varepsilon-1}{\beta_0^2}\frac{4m^2+1}{8}\left[\log(8\beta) - 2\sum_{p=1}^{|m|}\frac{1}{2p-1}\right]\\
&\bar{Q}^{ms}_{00} = 1 \quad \forall\beta_0.
\end{aligned} \tag{7.83}$$

Now we use the R-matrix $\bar{\mathbf{R}} = \bar{\mathbf{Q}}^{-1}$, which has the following limit:

$$\bar{R}^{m,\substack{c\\s}}_{nk} \to \frac{2\delta_{nk}}{\varepsilon+1} + (1-\delta_{nk})\begin{pmatrix}1+\varepsilon\delta_{k0}\\1-\delta_{k0}\end{pmatrix}\frac{\varepsilon-1}{(\varepsilon+1)^{n-k+1}}\frac{\Gamma(k+m+\frac{1}{2})}{\Gamma(n+m+\frac{1}{2})}\prod_{p=k+1}^{n-1}\left(\frac{\varepsilon-1}{2}+p(\varepsilon+1)\right) \qquad n \geq k, n \neq 0. \tag{7.84}$$

This expression for $\bar{\mathbf{R}}$ is the inverse of $\bar{\mathbf{Q}}$ in (7.83), i.e. $\sum_{p=0}^{\infty}\bar{Q}_{np}\bar{R}_{pk} = \delta_{nk}$, which can be verified in Mathematica. To obtain a result for the T-matrix entry T^m_{00}, it is also necessary to include the second order for the element R^{mc}_{00}:

$$\begin{aligned}
&\bar{R}^{mc}_{00} \to 1 - \frac{\varepsilon-1}{\varepsilon+1}\frac{2m^2(\varepsilon+1)+1}{4\beta_0^2}\left[\log(8\beta) - 2\sum_{p=1}^{|m|}\frac{1}{2n-1}\right]\\
&\bar{R}^{ms}_{00} = 1 \quad \forall\beta_0.
\end{aligned} \tag{7.85}$$

---

[2] In the context of quasistatic scattering, a harmonic function corresponds to an oscillating current or charge distribution when multiplied by the factor $e^{-i\omega t}$, which is a mode of vibration.

The second order for $\bar{R}^{mc}_{00}$ is obtained by including the 2nd order element Q^{mc}_{01} (above the diagonal) and inverting the matrix consisting of just the top left 2×2 block of $\bar{\mathbf{Q}}^{mc}$. Then the T-matrix (7.86) is obtained through (7.37):

$$\begin{aligned}
\bar{T}^{mv}_{nk} &\to (-)^m \frac{\pi\Gamma(n+m+\frac{1}{2})\Gamma(n-m+\frac{1}{2})}{n!(n-1)!(2\beta_0)^{2n}}(\bar{R}^{mv}_{nk}-\delta_{nk}) \qquad n\geq k, n\neq 0\\
\bar{T}^{mc}_{00} &\to -\frac{\pi^2}{8}\frac{\varepsilon-1}{\varepsilon+1}\frac{2m^2(\varepsilon+1)+1}{\beta_0^2}\\
\bar{T}^{ms}_{n0} &= \bar{T}^{ms}_{0k} = 0.
\end{aligned} \tag{7.86}$$

The upper diagonal entries of $\bar{\mathbf{T}}^{mv}$ with $n\leq k$ can be obtained from the symmetry property (7.38). In this limit there is just one resonance at $\varepsilon=-1$, consistent with the trends seen in Figure 7.7 for large β_0, and the resonance for a cylinder. All elements have been checked numerically against the exact matrix elements in Section 7.2.
An important feature is that the top left 2×2 square of $\bar{\mathbf{T}}^{mc}$ are all order β_0^{-2}, while all other entries decay more quickly as β_0^{-4} or less, meaning that both modes $n=0,1$ dominate both the excitation V_e and response V_s for each m. For $\bar{\mathbf{T}}^{ms}$ then only T^{ms}_{11} are significant.

We can now determine limits for the static dipolar polarizabilities per unit volume, to $\mathcal{O}(\beta_0^{-2})$, using (7.77,7.78) with (7.86):

$$\alpha^{\mathrm{ring}}_{zz} \to 2\frac{\varepsilon-1}{\varepsilon+1}, \tag{7.87}$$

$$\alpha^{\mathrm{ring}}_{xx} \to \frac{\varepsilon+3}{2}\frac{\varepsilon-1}{\varepsilon+1}. \tag{7.88}$$

These produce reasonable accuracy ($\lesssim 10\%$) for aspect ratios $\beta_0 \gtrsim 5$, but fail when $|\varepsilon| >> \beta_0$. I couldn't find a reference to check the polarizabilities, but an interesting comparison can be made to the polarizabilities of a thin prolate spheroid, or needle:

$$\alpha^{\mathrm{needle}}_{zz} \to \varepsilon-1, \tag{7.89}$$

$$\alpha^{\mathrm{needle}}_{xx} \to 2\frac{\varepsilon-1}{\varepsilon+1}. \tag{7.90}$$

$\alpha^{\mathrm{ring}}_{zz}$, $\alpha^{\mathrm{needle}}_{xx}$ apply when the long dimension of the wire is perpendicular to the applied electric field, and both are of the form $\alpha_\perp = 2(\varepsilon-1)/(\varepsilon+1)$. On the other hand $\alpha^{\mathrm{ring}}_{xx}$ and $\alpha^{\mathrm{needle}}_{zz}$ both diverge as $\varepsilon\to\infty$, where the long dimension of the wire is aligned with the electric field. $\alpha^{\mathrm{needle}}_{zz}$ is of the form $\alpha_{||}=\varepsilon-1$. Intuitively, for $\alpha^{\mathrm{ring}}_{xx}$ the ring is half aligned perpendicular and half parallel to the incident field, so that $\alpha^{\mathrm{ring}}_{xx} = (\alpha_\perp+\alpha_{||})/2$.

Numerical tests show that for very large $|\varepsilon|$ and very thin rings, the approximate expressions for $\bar{\mathbf{R}}^{m,c}$ break down, particularly for $m=0$. For analysis of the thin ring limit for conducting tori, see [108].

7.7 Conclusion

The problem of a dielectric torus in an arbitrary electrostatic field has been solved semi-analytically using the T-matrix, and expressions are found for the matrix elements on bases of both toroidal and spherical harmonics, using series relationships between the harmonics. Resonant permittivities are calculated from matrix eigenvalues and agree with results from solving a continued fraction equation. Fully analytic asymptotic expressions are given in both the conducting and thin ring limits. The T-matrix has been linked the time-harmonic T-matrix governing electric multipole interactions, $\mathbf{T}^{22}$. These results demonstrate the existence of the T-matrix for such a complex shape, at least in the small size limit. It is also found that similar T-matrices can be defined depending on whether the source is near or far from the torus hole and whether the scattered field is to be evaluated near or far from the origin.

One could numerically obtain the T-matrix for other ring like particles by applying the basis transformations between spherical and toroidal harmonics and evaluating the surface integrals using toroidal harmonics.

To extend these results to the Helmholtz equation, one would need a basis suited to the toroidal geometry but unfortunately the Helmholtz equation is not separable in toroidal coordinates. A basis of toroidal wavefunctions were presented in [117], although these are not orthogonal.

In the next chapter we will apply a similar analysis to the bispherical system. Bispherical and toroidal coordinates essentially differ by a real/imaginary interchange of the focal distance, and the corresponding harmonics differ by a shift of the separation constant by $\pm 1/2$, so there are some interesting similarities in their relationships to spherical harmonics and in the T-matrices of each geometry.

Chapter 8

Electrostatic T-matrices for the Two Sphere System

There are several methods for calculating the electrostatic interactions of two spheres. The ”re-expansion method” relies on spherical harmonic expansions and uses the translation relations for the spherical harmonics to find a matrix relation between the coefficients of the incident and scattered fields [118, 119]. This method is equivalent to the multi-particle T-matrix method where each sphere has its own T-matrix and the fields produced by each sphere are expanded on offset spherical bases [15, 120]. The problem can also be approached using a radial inversion transformation to make the spheres concentric, then solve the problem using spherical harmonics [121]. The problem is also naturally formulated using bispherical harmonics which are partially separable solutions to Laplace's equation, based on the bispherical geometry. For perfectly conducting spheres there is a simple analytic solution involving a series of bispherical harmonics [122]. However for dielectric spheres, analytic solutions are complicated as the series coefficients are computed by a three-term recurrence, with initial values computed as continued fractions [123, 124, 125, 126]. Bispherical harmonics can also be used to solve problems with sphere-plane geometry [127, 128, 129, 130]. For conducting spheres in a time-harmonic field, the bispherical solution can be extended to calculate the lowest few orders in a low frequency expansion [131].

In this chapter we look at bispherical harmonics and their relationships to spherical harmonics, in terms of radial inversion, finite sums and infinite series. Then as done for the torus, we apply the null field surface integral equations to solve Laplace's equation for two spheres in terms of a T-matrix with a basis of bispherical harmonics, and find simple analytic expressions for the surface integrals in the matrix elements. The matrix approach is used to derive a new expression for the resonance conditions of identical spheres. We then compare the bispherical harmonic series to the offset spherical harmonic series for a point charge between two spheres. The spherical series converges faster in the far field while the bispherical series converges faster near the surface.

8.1 Spherical and bispherical harmonics

Here we compare the spherical and bispherical coordinate systems, and their corresponding solutions to Laplace's equation.

8.1.1 Spherical harmonics

We define the exterior and interior spherical harmonics as:

$$S_n^m = \left(\frac{a}{r}\right)^{n+1} P_n^m(u) e^{im\phi}, \tag{8.1}$$

$$\hat{S}_n^m = \left(\frac{r}{a}\right)^{n} P_n^m(u) e^{im\phi}, \tag{8.2}$$

we have included the factor a which will be set equal to the half focal length of the bispherical coordinate system.

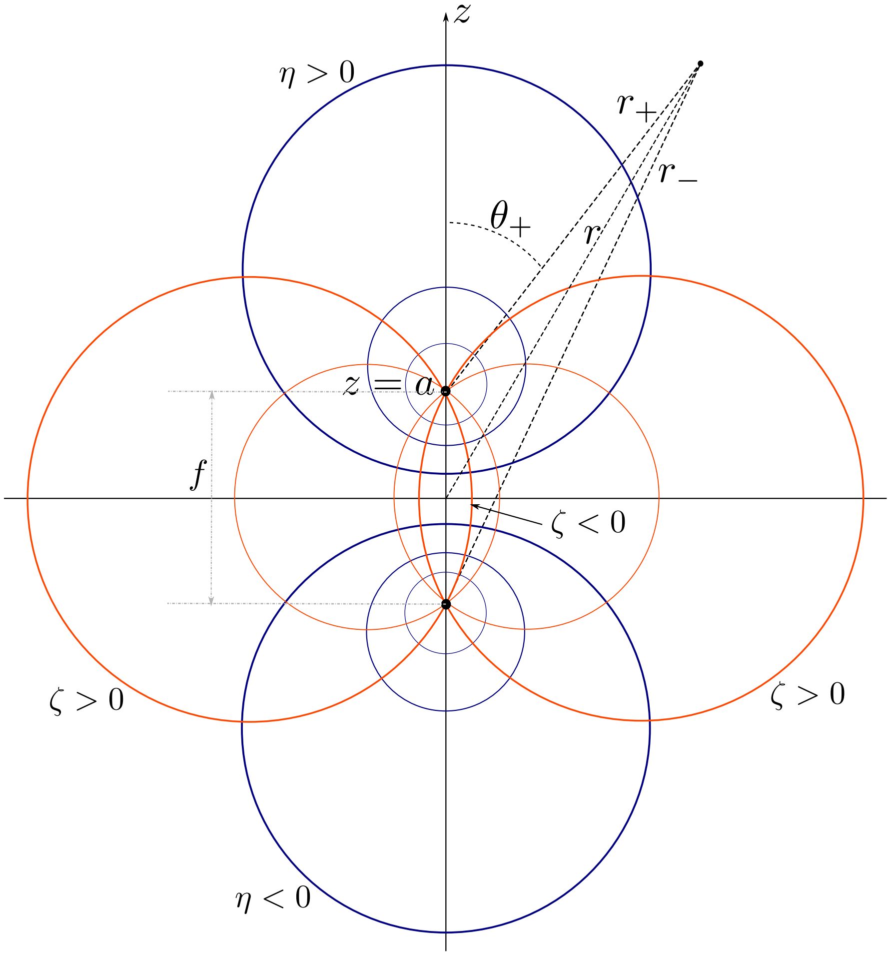

Figure 8.1: Bispherical coordinate system.

8.1.2 Bispherical harmonics

We use bispherical coordinates $\eta, \zeta, \phi \in [-\infty, \infty], [-1, 1], [0, 2\pi)$ with focal length $f = 2a$:

$$\eta = \operatorname{arcsinh} \frac{2az}{\sqrt{(r^2 + a^2)^2 - (2az)^2}}, \tag{8.3}$$

$$\zeta = \frac{r^2 - a^2}{\sqrt{(r^2 + a^2)^2 - (2az)^2}}. \tag{8.4}$$

For convenience we also define

$$\beta = \cosh \eta = \frac{r^2 + a^2}{\sqrt{(r^2 + a^2)^2 - (2az)^2}}. \tag{8.5}$$

The bispherical coordinate system is defined along with two foci on the z-axis at $z = \pm a$, illustrated in Figure 8.1. η =constant defines a sphere with radius $a \sinh \eta$ and center $z = a \coth \eta$ on the z-axis. $\eta = 0$ corresponds to the xy-plane and $\eta = \pm\infty$ at the foci. ζ defines the latitude on each sphere, in particular on the z-axis, we have $\zeta = 1$ for $|z| > a$ and $\zeta = -1$ for $|z| < a$.
Laplace's equation is partially separable in bispherical coordinates where the harmonics must be multiplied by a prefactor $\Delta = \sqrt{2(\beta - \zeta)}$. The relevant solutions are:

$$B^m_{n\pm} = \Delta e^{\pm(n+1/2)\eta} P^m_n(\zeta) e^{im\phi}. \tag{8.6}$$

We see that bispherical harmonics are similar in form to spherical harmonics, containing a radial part $e^{\pm(n+1/2)\eta}$ and an angular part $P^m_n(\zeta)$. B^m_{n+} and B^m_{n-} are singular at the positive and negative foci respectively.

Solutions containing $Q^m_n(\zeta)$ are ignored since they are singular on the entire z axis, cutting through the surfaces of the spheres. This is unlike the case of the torus where the axial toroidal harmonics, which are also singular on the z-axis, are still useful for fields inside the torus.

8.1.3 Radial inversion and relationships between the harmonics

Radial inversion or the Kelvin transformation is a conformal transformation in 3 dimensions where the radius from a given center, r, is reciprocated about a given reference sphere radius, R, through $x \to R^2/x$. This transformation is useful because it also preserves harmonicity of solutions to Laplace's equation by including the prefactor R/r. It is a common technique for solving problems in complicated geometries that are related to simpler geometries through inversion, for example it was used in Ref. [121] to solve the electrostatics problem of two spheres illuminated by a point dipole. The geometry was inverted about one of the foci of the corresponding bispherical coordinate system; this transformation complicates the boundary conditions, but makes the spheres concentric, allowing for the problem to be solved using spherical harmonics. We will see that this transformation also interchanges between the spherical and bispherical harmonics themselves.

Consider two offset spherical coordinate systems $(r_\pm, u_\pm, \phi)$ centred at $z = \pm a$. We will apply radial inversion about one of the foci, for example on the coordinate r_+, about the radius $f \equiv 2a$, while u_+ remains constant. This transforms spherical to bispherical coordinates:

$$e^{\pm\eta} = \frac{r_\mp}{r_\pm} = \frac{1}{f} r_\mp \left(r_\pm \to \frac{f^2}{r_\pm} \right), \tag{8.7}$$

$$\zeta = \pm u_\mp \left(r_\pm \to \frac{f^2}{r_\pm} \right). \tag{8.8}$$

Now we may consider the inversion of the corresponding harmonics. For the translated spherical harmonics we will use the notation $S^m_{n\pm} \equiv S^m_n(r \to r_+, u \to u_+)$. Considering the coordinate inversions in (8.8), a bispherical harmonic is actually the inversion of an offset exterior spherical harmonic about the other focus. For example B^m_{n+} is the inversion of $\hat{S}^m_{n+}$ about the lower focus at $z = a$.

$$B^m_{n\pm} = (\mp)^{n+m}\, 2^{n+1} \frac{f}{r_\mp} S^m_{n\pm} \left(r_\mp \to \frac{f^2}{r_\mp} \right). \tag{8.9}$$

The 2^{n+1} arises from $f^{n+1} = (2a)^{n+1}$, and the alternating signs arise from the symmetry of the Legendre functions $P^m_n(u) = (-)^{n+m} P^m_n(-u)$. A similar transformation can be realized for *interior* spherical harmonics, where a bispherical harmonic that is singular at one focus is the inversion of an interior spherical harmonic centered at the *other* focus:

$$B^m_{n\pm} = \frac{(\pm)^{n+m}}{2^n} \frac{f}{r_\pm} \hat{S}^m_{n\pm} \left(r_\pm \to \frac{f^2}{r_\pm} \right). \tag{8.10}$$

The similarity of (8.9) and (8.10) is related to the fact that the bispherical harmonics treat one focus as the origin and the other as infinity, evaluating to zero at one and diverging at the other, just as the spherical harmonics behave near the origin and at infinity.

Using Eq. (8.10), we can translate the spherical harmonics to the other focus, and use the fact that spherical harmonics simply transform from interior to exterior types when inverted about their own center, to obtain an expression for the bispherical harmonics simply in terms of offset spherical harmonics. The translation relation for the regular spherical harmonics may be found for example in Ref. [132]:

$$\hat{S}^m_{n\pm} = \sum_{k=m}^{n} \binom{n+m}{k+m} (\mp)^{n+k} 2^{n-k} \hat{S}^m_{k\pm}. \tag{8.11}$$

Taking (8.10), translating the spherical harmonics with (8.11), then evaluating the inversion gives

$$2^{n+1} S^m_{n\pm} = \sum_{k=m}^{n} \binom{n+m}{k+m} (\mp)^{n} (-)^{k} B^m_{k\pm}, \tag{8.12}$$

And the inverse relation can be found by first inverting the translation (8.11), then noting relation (8.10):

$$B^m_{n\pm} = \sum_{k=m}^{n} \binom{n+m}{k+m} (\pm)^{k} 2^{k+1} S^m_{k\pm}. \tag{8.13}$$

So bispherical harmonics are just simple linear combinations of offset spherical harmonics. Eq. (8.12) was given in [122] for $m = 0$, who noted that a bispherical harmonic of order $n = 0$ is actually just an offset point charge: $B^0_{0\pm} = f/r_\pm$.

We may also relate bispherical harmonics to spherical harmonics centered at the origin, by taking the relationships (8.12), (8.13) and translating the spherical harmonics using a similar translation relation:

$$S^m_{n\pm} = \sum_{k=n}^{\infty} (\mp)^{n+k} \binom{k-m}{n-m} S^m_k. \tag{8.14}$$

then by rearranging, we have the following series expansion for bispherical harmonics for $r > a$:

$$B^m_{n+} = \sum_{k=m}^{\infty} 2\, D^m_{nk} S^m_k, \tag{8.15}$$

where we define

$$D^m_{nk} = \sum_{p=0}^{\min(n,k)} \binom{n+m}{p+m} \binom{k-m}{p-m} 2^p. \tag{8.16}$$

For $m = 0$, the series coefficients are the Delannoy numbers encountered in combinatorics [133], OEIS A008288, which count (among other things) the number of paths on a n by k grid from $(0,0)$ to (n,k) where the allowed moves are either $(0,1)$, $(1,0)$ or $(1,1)$. Intuitively each binomial coefficient comes from a translation of the spherical harmonics - looking at the z-axis, this corresponds to a simple binomial expansion. The 2^p arises due to the translation of the interior spherical harmonics by *twice* the focal length. The series can be used to derive new properties of the Delannoy numbers [134]. For $m > 0$, these coefficients do not appear to be documented, and could be seen as a generalization of the Delannoy numbers.

The inverse relationship expressing spherical harmonics as a series of bispherical harmonics can be found by geometric transformations. Taking the expansion Eq. (8.15) and multiplying both sides by $\sqrt{r/2a}$, we notice a similarity in the forms of the left and right hand sides: both have something to the power of $n + 1/2$, times a Legendre function. So we can interchange between the functions simply by interchanging $e^{\pm\eta} \leftrightarrow r/a$ and $\zeta \leftrightarrow u$. In fact, for example taking the upper sign in Eq. (8.15), this transformation is equivalent to a translation $z \to z + a$ followed by an inversion $r_+ \to a/r_+$ as depicted in Figure 8.2:

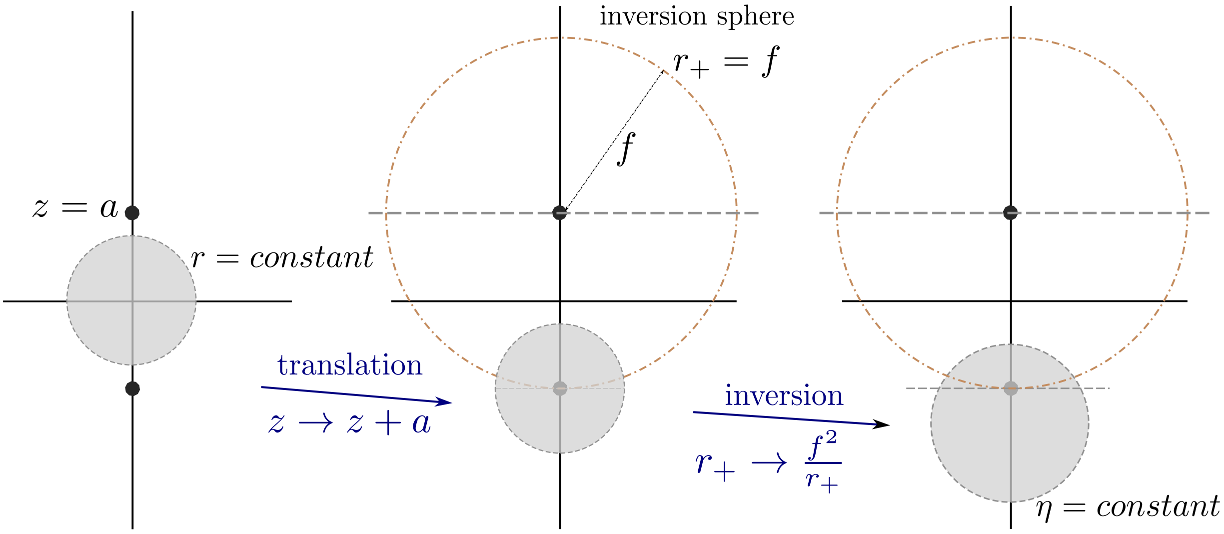

Figure 8.2: geometric transformation of $r/a \to e^\eta$.

And the extra prefactor $\Delta\sqrt{r/2a}$ on the left hand side actually transforms to its own reciprocal (which can be shown with some algebra), so the expansion can be rearranged to give:

$$S^m_n = \sum_{k=m}^{\infty} (-)^{n+k} D^m_{nk} B^m_{k+}. \qquad z < 0 \tag{8.17}$$

So the relationships between spherical and bispherical harmonics are symmetrical. And by applying similar translations to we can also find the relationship between the bispherical harmonics and *interior* spherical harmonics:

$$B^m_{n\pm} = \sum_{k=m}^{\infty} 2(-)^{n+m}(\pm)^{k+m} D^m_{nk} \hat{S}^m_k. \qquad r < a \tag{8.18}$$

8.1.4 Comparison to toroidal-spherical expansions

We should compare these to the relationships between spherical and toroidal harmonics (7.44-7.47).

We can obtain a recurrence relation for D^m_{nk} by applying the partial differential operator $r\partial_r$ which preserves harmonicity of solutions to Laplace's equation. The effect on spherical harmonics is simple:

$$r\frac{\partial}{\partial r} S^m_k = -(k+1)S^m_k, \tag{8.19}$$

while for bispherical harmonics, the effect is

$$2r\frac{\partial}{\partial r} B^m_{n\pm} = (n+m)B^m_{n-1,\pm} - (n-m+1)B^m_{n+1,\pm} - B^m_{n\pm}, \tag{8.20}$$

which can be derived using the recurrence for the associated Legendre functions: $(n-m+1)P^m_{n+1}(\zeta) = (2n+1)\zeta P^m_n(\zeta) - (n+m)P^m_{n-1}(\zeta)$.
Applying $2r\partial_r + 1$ to the expansion (8.15), rearranging, and equating coefficients of spherical harmonics, we get

$$(n-m+1)D^m_{n+1,k} = (2k+1)D^m_{n,k} + (n+m)D^m_{n-1,k}. \tag{8.21}$$

which resembles the recurrence relation for the toroidal-spherical expansion coefficients c^m_{nk}, s^m_{nk}, with $n \to n-1/2$.

A useful tool is the univariate generating function of D^m_{nk} which can be found by evaluating (8.15) on the z axis for $m = 0$. For $m > 0$ the functions go to zero on the z-axis so we divide both sides by $(1-u^2)^{m/2}$ and take limits. The generating function is

$$\sum_{k\geq m} D^m_{kn} z^k = 2^m z^m \frac{(1+z)^{n-m}}{(1-z)^{n+m+1}}. \tag{8.22}$$

By expanding the generating function (8.22) via the binomial series for the numerator and denominator separately, and multiplying these, it is possible to find the following alternate expression for D^m_{nk}:

$$D^m_{nk} = 2^{-m} \sum_{p=0}^{k+m} \binom{n+m}{p} \binom{n+k-p}{n-m}. \tag{8.23}$$

Inspection reveals the bispherical-spherical and toroidal-spherical coefficients are related by a shift $n \to n-1/2$ and multiplied by i^k (due to the change of focal length $a \to -ia$), which matches the transformation between bispherical and toroidal harmonics. This means that toroidal harmonics also have a type of symmetric relationship with spherical harmonics; this is derived in [25].

8.2 Two dielectric spheres in an arbitrary electrostatic excitation

Having presented the properties of bispherical harmonics, we now look at physical problems for the interaction of two spheres under electrostatic excitation.

8.2.1 T-matrix/EBCM for a single sphere using bispherical harmonics

We start with the T-matrix for a single dielectric sphere, which will subsequently be used in constructing the T-matrix solution for two spheres in Section 8.3. Consider a sphere offset above the xy-plane at $\eta = \eta_0$, with permittivity ε_i in a medium with permittivity ε_o. We write the total potential outside as a sum of the excitation potential V_e and scattered potential V_s: $V_\mathrm{o} = V_\mathrm{s} + V_\mathrm{e}$. We assume that V_e can be expressed as a series of bispherical harmonics that are regular inside the sphere (B^m_{n-}) and similarly for the internal potential V_i. The scattered potential V_s should be expanded on B^m_{n+} since it must solve Laplace's equation everywhere outside the sphere:

$$V_\mathrm{e} = \sum_{n=0}^{\infty} \sum_{m=-n}^{n} a^m_n B^m_{n-} \tag{8.24}$$

$$V_\mathrm{i} = \sum_{n=0}^{\infty} \sum_{m=-n}^{n} b^m_n B^m_{n-} \tag{8.25}$$

$$V_\mathrm{s} = \sum_{n=0}^{\infty} \sum_{m=-n}^{n} c^m_n B^m_{n+}. \tag{8.26}$$

The boundary conditions at the surface $\eta = \eta_0$ are

$$V_\mathrm{i} = V_\mathrm{o}, \tag{8.27}$$

$$\varepsilon \frac{\partial V_\mathrm{i}}{\partial \eta} = \frac{\partial V_\mathrm{o}}{\partial \eta}, \tag{8.28}$$

where $\varepsilon = \varepsilon_\mathrm{i}/\varepsilon_\mathrm{o}$. Within the EBCM, the problem is instead solved using the equivalent integral equations:

$$\int_s \frac{\partial V_\mathrm{i}(\mathbf{r}')}{\partial n'_\perp} G(\mathbf{r},\mathbf{r}')\mathrm{d}s' = \begin{cases} V_\mathrm{e}(\mathbf{r}) - V_\mathrm{i}(\mathbf{r}) & \mathbf{r} \text{ inside} \\ -V_\mathrm{s}(\mathbf{r}) & \mathbf{r} \text{ outside} \end{cases} \tag{8.29}$$

where s is the surface of the sphere and $n'_\perp$ is the outward unit normal. The Green function has the following expansion in bispherical coordinates [53] sec. 10.3:

$$G(\mathbf{r},\mathbf{r}') = \frac{1}{8\pi a} \sum_{n=0}^{\infty} \sum_{m=-n}^{n} (-)^m \begin{cases} B^m_{n+}(\mathbf{r}) B^{-m}_{n-}(\mathbf{r}') & \eta < \eta' \\ B^m_{n-}(\mathbf{r}) B^{-m}_{n+}(\mathbf{r}') & \eta > \eta' \end{cases} \tag{8.30}$$

(In the notation for B^{-m}_{n-}, the negative in the subscript represents $e^{-\eta}$ dependence, while the $-m$ is a negative integer). We then insert the expansions of the potentials and Green functions into the integral equations, and equate the prefactors of $B^m_{n+}(\mathbf{r})$ on both sides. This leads to (dropping integration primes):

$$\frac{\varepsilon - 1}{8\pi a} (-)^m \sum_{k=m}^{\infty} b^m_k \int_s \mathrm{d}s \frac{\partial B^m_{k-}}{\partial n_\perp} \begin{cases} B^{-m}_{n+} & = a^m_n - b^m_n \\ B^{-m}_{n-} & = -c^m_n. \end{cases} \tag{8.31}$$

The relations are conveniently written in matrix form, defining the Q and P matrices as

$$Q^m_{nk} = \frac{\varepsilon - 1}{8\pi a} (-)^m \int_s \frac{\partial B^m_{k-}}{\partial n_\perp} B^{-m}_{n+} \mathrm{d}s + \delta_{nk} \tag{8.32}$$

$$P^m_{nk} = -\frac{\varepsilon - 1}{8\pi a} (-)^m \int_s \frac{\partial B^m_{k-}}{\partial n_\perp} B^{-m}_{n-} \mathrm{d}s. \tag{8.33}$$

Then the series coefficients are related by

$$\mathbf{a} = \mathbf{Q}\mathbf{b}, \quad \mathbf{c} = \mathbf{P}\mathbf{b}, \quad \mathbf{c} = \mathbf{T}\mathbf{a}, \text{ with } \mathbf{T} = \mathbf{P}\mathbf{Q}^{-1}. \tag{8.34}$$

The problem can be solved independently for each m, so that $\mathbf{a},\mathbf{b},\mathbf{c}$ are infinitely long vectors running over n for a fixed m, and similarly $\mathbf{Q},\mathbf{P},\mathbf{T}$ are 2 dimensional matrices running over n and k, with a separate matrix for each m.
In the case of a conducting sphere where $|\varepsilon| \to \infty$, $\mathbf{Q}$ and $\mathbf{P}$ both become infinite, while $\mathbf{T} \to \mathbf{T}^\infty$, with

$$[\mathbf{T}^\infty]^m_{nk} = -e^{-(2n+1)|\eta_0|}\delta_{nk}, \tag{8.35}$$

which agrees with [124].

8.2.2 Analytic forms for integrals

We now evaluate the surface integral (8.32). Explicitly the surface normal and infinitesimal element are

$$\mathrm{d}s = \frac{-a^2\mathrm{d}\zeta\mathrm{d}\phi}{(\beta-\zeta)^2}, \qquad \frac{\partial}{\partial n_\perp} = \frac{\zeta-\beta}{a}\frac{\partial}{\partial\eta}, \tag{8.36}$$

so that Eq. 8.32 becomes

$$Q^m_{nk} = -\frac{\varepsilon-1}{2}\frac{(n-m)!}{(n+m)!}e^{(n-k)\eta_0}\left[\frac{\sinh\eta_0}{2}\int_{-1}^{1}\frac{P^m_n(\zeta)P^m_k(\zeta)}{\beta_0-\zeta}\mathrm{d}\zeta - \left(k+\frac{1}{2}\right)\int_{-1}^{1}P^m_n(\zeta)P^m_k(\zeta)\mathrm{d}\zeta\right] + \delta_{nk}, \tag{8.37}$$

with a similar result for $\mathbf{P}$. The integral on the left can be evaluated as (see Ref. [135] - note their $P^m_n(z>1)$ differ by $(-)^m$)

$$\frac{1}{2}\int_{-1}^{1}\frac{P^m_n(\zeta)P^m_k(\zeta)}{\beta-\zeta}\mathrm{d}\zeta = (-)^m P^m_{\min(n,k)}(\beta)Q^m_{\max(n,k)}(\beta). \tag{8.38}$$

The recurrence relation on n for $Q^m_n(\beta)$ is unstable in the direction of increasing n, so backward recursion should be used instead where the initial values can be found with the modified Lentz algorithm [136]. This is a common implementation for calculating spheroidal harmonics which contain the same functions Q^m_n.

The second integral in (8.37) is simply $2\delta_{nk}(n+m)!/(n-m)!/(2n+1)$. We then have analytic expressions for the matrix elements of $\mathbf{P}$ and $\mathbf{Q}$ for a sphere above the xy plane ($\eta_0 > 0$). For $\eta_0 < 0$, the potentials are expanded on the opposite basis functions, and the normal to the sphere changes sign. The matrices are actually independent of the sign of η_0, so we can incorporate the results for spheres above or below the xy-plane:

$$Q^m_{nk} = \delta_{nk} - \frac{\varepsilon-1}{2}e^{(n-k)|\eta_0|}\left[(-)^m\frac{(n-m)!}{(n+m)!}\sinh|\eta_0|P^m_{\min(n,k)}(\beta_0)Q^m_{\max(n,k)}(\beta_0) - \delta_{nk}\right], \tag{8.39}$$

$$P^m_{nk} = \frac{\varepsilon-1}{2}e^{-(n+k+1)|\eta_0|}\left[(-)^m\frac{(n-m)!}{(n+m)!}\sinh|\eta_0|P^m_{\min(n,k)}(\beta_0)Q^m_{\max(n,k)}(\beta_0) - \delta_{nk}\right]. \tag{8.40}$$

Like for the torus, the matrices are related by $\mathbf{P} = \mathbf{T}^\infty(\mathbf{Q}-\mathbf{I})$, and hence

$$\mathbf{T} = \mathbf{T}^\infty(\mathbf{I}-\mathbf{Q}^{-1}). \tag{8.41}$$

Numerically (8.41) and (8.34) give the same result.

8.2.3 Plane (half space)

For a plane ($\eta_0 = 0$), the limiting forms of the Legendre functions are [62]:

$$\lim_{\beta\to1+} P^m_n(\beta) = \frac{(n+m)!}{(n-m)!}\frac{1}{m!}\left(\frac{\beta-1}{2}\right)^{m/2}, \tag{8.42}$$

$$\lim_{\beta\to1+} Q^m_n(\beta) = \frac{(-)^m(m-1)!}{2}\left(\frac{\beta-1}{2}\right)^{-m/2}, \quad m>0 \tag{8.43}$$

$$\lim_{\beta\to1+} Q^0_n(\beta) = \frac{1}{2}\ln\frac{2}{\beta-1}, \tag{8.44}$$

so the product $\sinh|\eta_0|P^m_{\min(n,k)}(\beta_0)Q^m_{\max(n,k)}(\beta_0)$ goes to zero for all n,k,m. Then we have

$$\mathbf{Q}_{\text{plane}} = \frac{\varepsilon+1}{2}\mathbf{I}, \qquad \mathbf{P}_{\text{plane}} = -\frac{\varepsilon-1}{2}\mathbf{I}, \qquad \mathbf{T}_{\text{plane}} = -\frac{\varepsilon-1}{\varepsilon+1}\mathbf{I}, \tag{8.45}$$

which agrees with [124]. These matrices are again independent of whether the half space occupies $z<0$ or $z>0$. This result allows for a fully analytical treatment for a conducting sphere in a dielectric half-space.

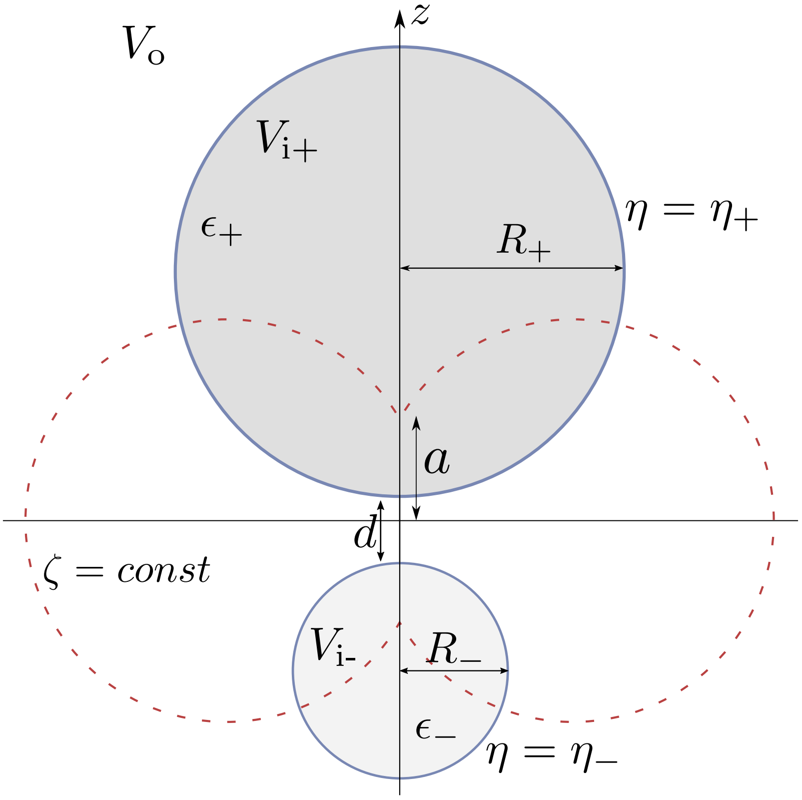

Figure 8.3: Schematic of the problem of two spheres under electrostatic excitation. The red dotted line is not physical; it represents some arbitrary curve of constant ζ.

8.3 T-matrix for two spheres

We now use the results of the previous section to derive the T-matrix for a two sphere or sphere-plane system. We do not consider the case of one sphere inside the other (both above or below the xy plane), as in [137], but this can be treated with minor modifications. Also, bispherical coordinates cannot be used to treat touching spheres; tangent sphere coordinates may be used instead [138, 139], or equivalently transformation optics (radial inversion about the contact point) [140]. The approach we will follow is comparable to the re-expansion method for treating multiple spheres in spherical coordinates, where the (diagonal) T-matrix on a spherical harmonic basis for each sphere is translated to obtain the interaction matrix of the entire system. Here with bispherical harmonics, the T-matrix for an individual sphere is not diagonal but the basis functions are better suited to geometry and do not need to be translated.

8.3.1 Coordinate system

Consider two spheres (or a sphere and a plane) of possibly different radii and permittivities, with centers on the z-axis above and below the xy-plane. We must set up the appropriate bispherical coordinate system, depicted in Figure 8.3. Depending on the sphere sizes and separation, we must place the two foci $z=\pm a$ such that it is possible that the sphere surfaces then lie at $\eta=\eta_+$ for the upper sphere and $\eta=\eta_-$ for the lower. The plane $z=0$ may not lie directly in the center of the gap.

Given the diameters of the spheres $D_\pm = 2R_\pm$, and the separation between their surfaces d, the focal length of the bispherical coordinates should be set to

$$a = \frac{\sqrt{d(D_+ + d)(D_- + d)(D_+ + D_- + d)}}{D_+ + D_- + 2d}, \tag{8.46}$$

and the sphere surfaces $\eta = \eta_\pm$ are then given by

$$\sinh \eta_\pm = \pm \frac{a}{R_\pm}. \tag{8.47}$$

We may also divide the gap into $d = d_+ + d_-$ where $d_\pm$ is the distance from the origin to each sphere surface:

$$d_\pm = \frac{R_\pm}{\cosh \eta_\pm - 1}. \tag{8.48}$$

8.3.2 General solution

Denote the potential inside each sphere by $V_{\mathrm{i}+}$ and $V_{\mathrm{i}\text{-}}$, and the scattered potentials by $V_{\mathrm{s}+}$ and $V_{\mathrm{s}-}$, so that $V_\mathrm{o} = V_\mathrm{e} + V_{\mathrm{s}+} + V_{\mathrm{s}-}$. Here V_e must be expanded on different basis functions depending on which surface we apply the boundary integral equations to. Following the same rationale as for the single sphere in the previous section, the potentials are expanded as

$$V_\mathrm{e} = \sum_{n,m} \begin{cases} a^m_{n-} B^m_{n-} & \eta = \eta_+ \\ a^m_{n+} B^m_{n+} & \eta = \eta_- \end{cases}, \tag{8.49}$$

$$V_{\mathrm{i}\pm} = \sum_{n,m} b^m_{n\mp} B^m_{n\mp}, \tag{8.50}$$

$$V_{\mathrm{s}\pm} = \sum_{n,m} c^m_{n\pm} B^m_{n\pm}. \tag{8.51}$$

Since the scattered field from one sphere adds to the incident field for the other, the matrix relations between the coefficients are now

$$\begin{aligned} \mathbf{b}_\pm &= \mathbf{Q}_\pm^{-1}(\mathbf{a}_\mp + \mathbf{c}_\mp), \\ \mathbf{c}_\pm &= \mathbf{T}_\pm(\mathbf{a}_\mp + \mathbf{c}_\mp), \end{aligned} \tag{8.52}$$

where for example $\mathbf{Q}_+$ is the Q-matrix for the sphere $\eta = \eta_+$, computed from (8.39). Rearranging these we get the scattered coefficients in terms of the known incident coefficients:

$$\mathbf{c}_\pm = (\mathbf{I} - \mathbf{T}_\pm \mathbf{T}_\mp)^{-1} \mathbf{T}_\pm (\mathbf{a}_\mp + \mathbf{T}_\mp \mathbf{a}_\pm), \tag{8.53}$$

and the internal coefficients are obtained by applying (8.41) to (8.52):

$$\mathbf{b}_\pm = \mathbf{a}_\mp + \mathbf{c}_\mp - [\mathbf{T}_\pm^\infty]^{-1} \mathbf{c}_\pm. \tag{8.54}$$

These expressions provide the solution for an arbitrary external field, but one must first determine the expansion coefficients $\mathbf{a}_\pm$ for the excitation potential in bispherical coordinates - see Section 8.5 for typical fields.

In Ref. [25], where a T-matrix was derived for a torus in terms of toroidal harmonics, a main goal was to present the T-matrix on a basis of spherical harmonics through the linear expansions between the two basis sets. But in this case the solution in terms of spherical harmonics can be obtained directly using the re-expansion method.

8.3.3 Identical spheres

The full solution (8.53) requires up to three matrix inversions, but this number can be reduced in cases of symmetry. For two identical spheres on opposite sides of the *xy*-plane, we have $\mathbf{P}_+ = \mathbf{P}_- = \mathbf{P}$, and similarly for the other matrices. For incident fields symmetric about *z*, we can make further simplifications:

$$\mathbf{a}_+ = \mathbf{a}_- \tag{8.55}$$

$$\mathbf{c}_+ = \mathbf{c}_- = \mathbf{T}(\mathbf{I}-\mathbf{T})^{-1}\mathbf{a}_+ \tag{8.56}$$

$$= \mathbf{P}(\mathbf{Q}-\mathbf{P})^{-1}\mathbf{a}_+ \tag{8.57}$$

$$\mathbf{b}_+ = \mathbf{b}_- = \mathbf{a}_+ + (\mathbf{I} - [\mathbf{T}^\infty]^{-1})\mathbf{c}_+, \tag{8.58}$$

we present (8.57) as it involves only one matrix inversion. Similarly for antisymmetric fields:

$$\mathbf{a}_+ = -\mathbf{a}_- \tag{8.59}$$

$$\mathbf{c}_+ = -\mathbf{c}_- = -\mathbf{T}(\mathbf{I}+\mathbf{T})^{-1}\mathbf{a}_+ \tag{8.60}$$

$$= -\mathbf{P}(\mathbf{Q}+\mathbf{P})^{-1}\mathbf{a}_+ \tag{8.61}$$

$$\mathbf{b}_+ = -\mathbf{b}_- = -\mathbf{a}_+ - (\mathbf{I} + [\mathbf{T}^\infty]^{-1})\mathbf{c}_+. \tag{8.62}$$

8.4 Plasmon resonances

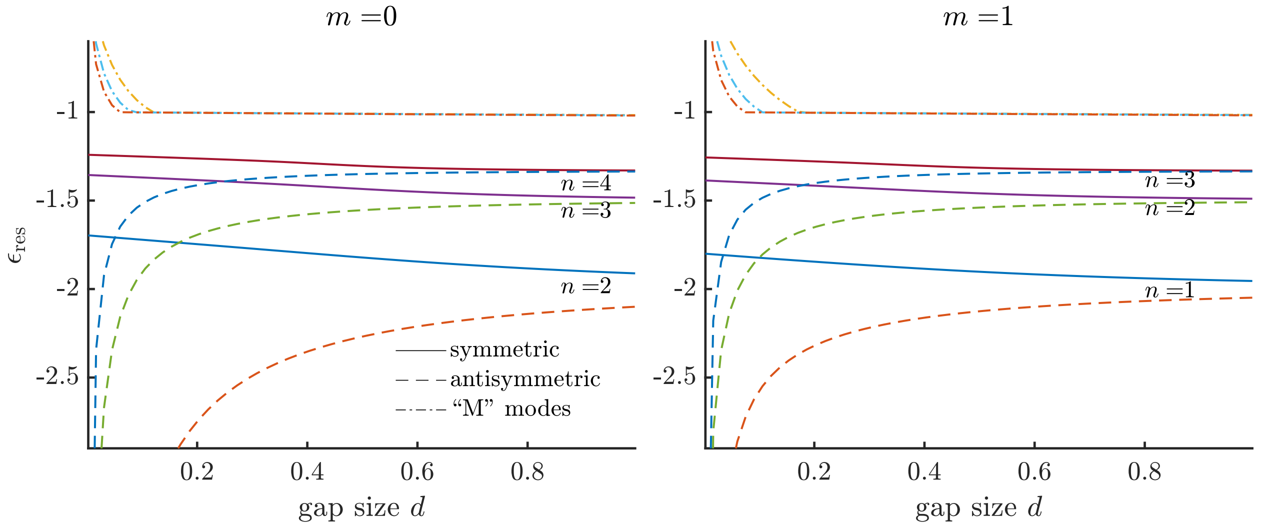

Figure 8.4: Values of the permittivity corresponding to plasmon resonances of two identical spheres with diameter $D = 1$, separated by a gap d. The first three resonances for each type are plotted, while higher resonances tend towards $\varepsilon_{\text{res}} = -1$. As the spheres become further apart, and the resonance conditions tend towards the values for a single sphere, $\varepsilon_{\text{res}} = -1 - 1/n$. The resonant permittivities of the "M" modes are only greater than -1 for $d \lesssim 1.2$. The eigenvalues were computed with matrix sizes ranging from 40 for $d \approx 1$ to 800 as $d \to 0$, and convergence was checked by changing the matrix size.

One advantage of this formulation is that the plasmon resonance conditions $\varepsilon = \varepsilon_{\text{res}}$ can be obtained from matrix eigenvalues. For a single sphere the plasmon resonances are simply $\varepsilon_{\text{res},n} = -1 - 1/n$, lying between -2 and -1. Alternatively, these resonant permittivities can also be calculated from the bispherical matrix formulation by noting that resonance occurs when $\mathbf{Q}$ is singular. If we write the Q-matrix as $\mathbf{Q} = \mathbf{I} - (\varepsilon - 1)\hat{\mathbf{Q}}$, then the resonances occur when $\det(\mathbf{I} - (\varepsilon - 1)\hat{\mathbf{Q}}) = 0$, where $\hat{\mathbf{Q}}$ is independent of ε. The resonances are then given by $\varepsilon_{\text{res},n} = 1 + 1/\lambda_n$ where λ_n are the eigenvalues of $\hat{\mathbf{Q}}$. It has been checked that these eigenvalues do in fact approach $-1 - 1/n$ as the matrix size increases. It would be interesting to prove that the infinite matrix $\hat{\mathbf{Q}}$ has these simple eigenvalues despite containing fairly complex Legendre functions. And perhaps a simple expression for the torus resonances in Section 7.5.3 could also be found since the torus T-matrices are mathematically similar to the bispherical T-matrices.

For two identical spheres, equations (8.57) and (8.61) show that resonances occur when $\mathbf{Q}+\mathbf{P}$ is singular for symmetric (s) modes (about z), and when $\mathbf{Q}-\mathbf{P}$ singular for antisymmetric (a) modes. If we define $\bar{\mathbf{Q}}^{s/a} = (\mathbf{I}\mp\mathbf{T}^{\infty})\hat{\mathbf{Q}}$, then resonances occur at $\varepsilon^{s/a}_{\mathrm{res},n} = 1+1/\lambda^{s/a}_n$ where $\lambda^{s/a}_n$ are the eigenvalues of $\bar{\mathbf{Q}}^{s/a}$. The size of the shifts due to the sphere-sphere coupling is directly related to the absolute value of the elements in $\mathbf{T}^{\infty}$, which grow as $\beta_0 \to 1$. Some low order resonance conditions are plotted in Figure 8.4. As the spheres approach each other, the conditions for the antisymmetric modes $\varepsilon^{a}_{\mathrm{res},n}$ tend towards $-\infty$. For symmetric modes, $\varepsilon^{s}_{\mathrm{res},n}$ generally tend towards -1 for all n, except for very close spheres with $d \lesssim 0.27R$ (for $m=0$), where "M" modes with $\varepsilon_{\mathrm{res}} > -1$ start to appear [141]. These modes have very strong electric field in the gap and can only be excited by a localized source, for example a molecule in the gap. For non-identical spheres, the resonance condition is $\det(\mathbf{I}-\mathbf{T}_{\pm}\mathbf{T}_{\mp}) = 0$. However, for this case it does not seem to be possible to express ε explicitly in terms of the eigenvalues; the eigenvalue problem becomes non-linear. In Ref. [126], a different matrix was used involving a non-linear eigenvalue problem for the resonances of nonidentical spheres.

8.5 Expansions of incident fields

For convenience we provide the expansions of some basic incident fields in terms of bispherical harmonics.

8.5.1 Constant potential

A constant can be expanded onto bispherical harmonics as [53]

$$1 = \Delta \sum_{n=0}^{\infty} e^{-(n+1/2)|\eta|} P_n(\zeta). \tag{8.63}$$

8.5.2 Uniform field

A uniform field in any direction can be split into x, y and z components [53]:

$$\frac{z}{a} = \mathrm{sign}(\eta)\Delta \sum_{n=0}^{\infty} (2n+1) e^{-(n+1/2)|\eta|} P_n(\zeta), \tag{8.64}$$

$$\frac{x+iy}{a} = 2\Delta \sum_{n=0}^{\infty} e^{-(n+1/2)|\eta|} P^1_n(\zeta) e^{im\phi}. \tag{8.65}$$

8.5.3 Point charge

The expansion of a point charge is given in Eq. (8.30). In particular for a point charge at the origin, we have

$$\frac{a}{r} = \Delta \sum_{n=0}^{\infty} (-)^n e^{-(n+1/2)|\eta|} P_n(\zeta). \tag{8.66}$$

8.5.4 Dipole

Expansions for the dipole potential in bispherical harmonics, can be derived by differentiating the expansion of a point charge in the z and x directions. A dipole at $\mathbf{r}' = (x_0, y_0, z_0)$ can be separated into its Cartesian components. For $w = x,\ y$ or z we have

$$2a\frac{w-w_0}{|\mathbf{r}-\mathbf{r}_0|^3} = -\sum_{n=0}^{\infty}\sum_{m=-n}^{n} (-)^m \begin{cases} \dfrac{\partial B^m_{n-}(\mathbf{r}_0)}{\partial w_0} B^{-m}_{n+}(\mathbf{r}) & \eta < \eta' \\ \dfrac{\partial B^m_{n+}(\mathbf{r}_0)}{\partial w_0} B^{-m}_{n-}(\mathbf{r}) & \eta > \eta'. \end{cases} \tag{8.67}$$

Explicit forms of the derivatives are

$$\frac{\partial B^m_{n\pm}}{\partial z} = \frac{\pm}{2a}[(2n+1)B^m_{n,\pm} - (n+m)B^m_{n-1,\pm} - (n-m+1)B^m_{n+1,\pm}], \tag{8.68}$$

$$\begin{aligned}\frac{\partial B^m_{n\pm}}{\partial x} &= \frac{1}{4a}[(n+m)(n+m-1)B^{m-1}_{n-1,\pm} - B^{m+1}_{n-1,\pm} \\ &- 2(n+m)(n-m+1)B^{m-1}_{n\pm} + 2B^{m+1}_{n\pm} + (n-m+1)(n-m+2)B^{m-1}_{n+1,\pm} - B^{m+1}_{n+1,\pm}],\end{aligned} \tag{8.69}$$

$$\begin{aligned}\frac{\partial B^m_{n\pm}}{\partial y} &= \frac{i}{4a}[-(n+m)(n+m-1)B^{m-1\,*}_{n-1,\pm} - B^{m+1\,*}_{n-1,\pm} + 2(n+m)(n-m+1)B^{m-1\,*}_{n\pm} + 2B^{m+1\,*}_{n\pm} \\ &- (n-m+1)(n-m+2)B^{m-1\,*}_{n+1,\pm} - B^{m+1\,*}_{n+1,\pm}].\end{aligned} \tag{8.70}$$

where * denotes complex conjugate.

8.6 Comparison to re-expansion method

Here we compare the rate of convergence of the bispherical expansion to the re-expansion method based on spherical harmonics. The re-expansion method involves expanding the potentials on two basis of offset spherical harmonics and translating them on to the other basis using a translation matrix. This results in a linear system similar in form to (8.52).

Firstly for two identical spheres in a uniform field, the offset spherical series converge faster than the bispherical series in both near and far fields, especially for close spheres.

However, for a point source incident field where the spherical series tend to converge slower, the bispherical series converge faster near the the surface. Briefly, we cover the re-expansion method for identical spheres with a point charge midway between them [119]. Similar to Section 8.3.2, the potential outside is written as $V_\mathrm{o} = V_\mathrm{e} + V_{\mathrm{s}+} + V_{\mathrm{s}-}$, where

$$V_\mathrm{e} = \frac{R}{r}, \qquad V_{\mathrm{s}\pm} = \sum_{n=0}^{\infty} C_{n\pm}\left(\frac{R}{r_\pm}\right)^{n+1} P_n(u_\pm). \tag{8.71}$$

The coefficients C_{n+} and C_{n-} are given by a matrix inversion:

$$\mathbf{C}_\pm = (\mathbf{I}+\mathbf{M})^{-1}\mathbf{W}, \qquad C_{n-} = (-)^n C_{n+}, \tag{8.72}$$

where the elements of matrices **M** and **W** are

$$\begin{aligned}M_{nk} =& \frac{n(\varepsilon-1)}{n(\varepsilon+1)+1}\binom{n+k}{k}(-)^{n+k}\left(\frac{R}{2R+d}\right)^{n+k+1}, \\ W_{nk} =& \frac{n(\varepsilon-1)}{n(\varepsilon+1)+1}(-)^{n+1}\left(\frac{2R}{2R+d}\right)^{n}.\end{aligned} \tag{8.73}$$

The spatial potential in one quadrant is plotted in Figure 8.5, along with the relative error for this solution and the bispherical solution (8.57). The bispherical solution is more accurate near the surface but not in the far field. Figure 8.6 compares the rates of convergence of the partial series for the potential at the position of the point charge. The bispherical series converges faster at the point charge itself for a wide range of the separation distance. Similar results are found for dipoles, where such calculations can be used for example to calculate the decay rate modification of an emitter in the gap in the quasi-static approximation [142].

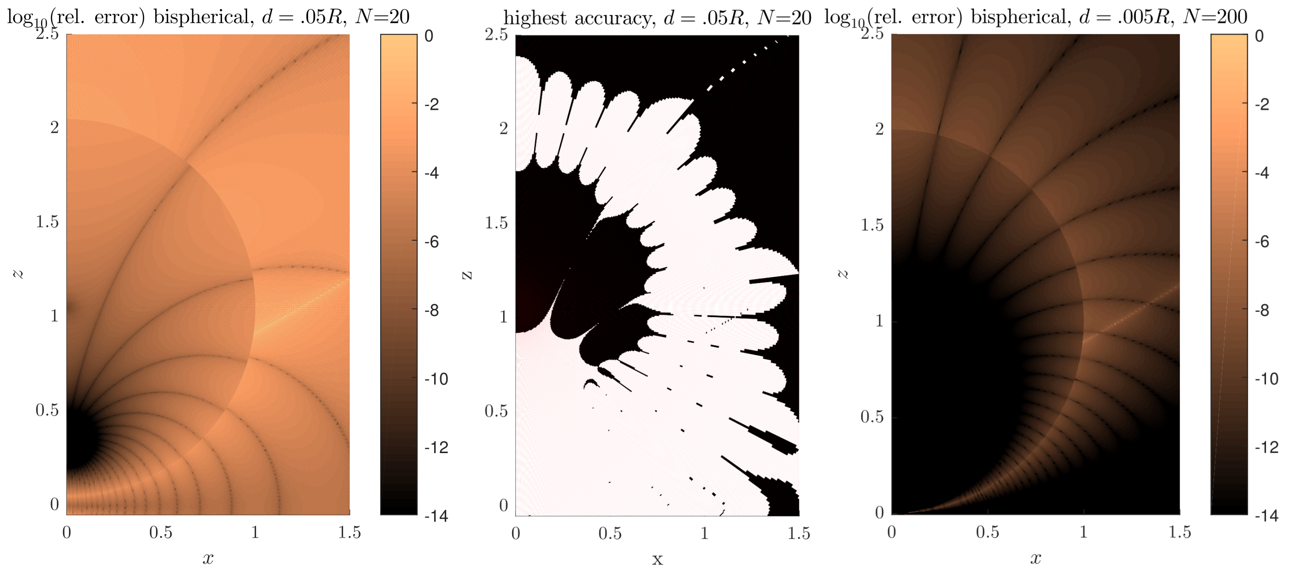

Figure 8.5: Left: relative error in bispherical solution for a point charge located at the center of two identical spheres with $\varepsilon = 1.5$ separated by a gap of $2d = 0.1R$, computed with $N = 20$ terms. The error is compared to the bispherical expansion with enough terms to converge in all space to an accuracy of 10^{-14}. The radial dark lines are from the oscillations of the Legendre functions and the bright diagonal line is where the potential passes through zero. The arcsinh is taken (similar to a log scale) for visual purposes. Center: black/white regions are where the spherical/bispherical solution is more accurate when truncated at $N = 20$. Right: same as the left plot but for a smaller gap, computed with $N = 200$ terms.

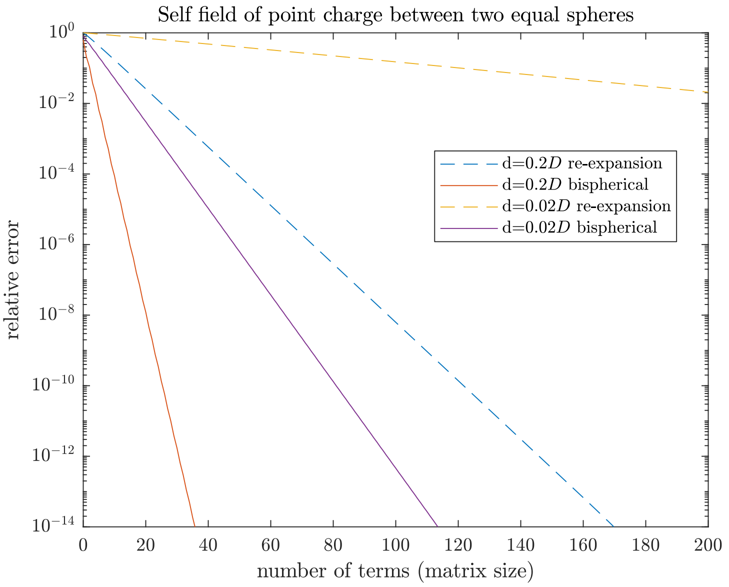

Figure 8.6: Potential at the position of the point charge between two identical spheres, comparing the rate of convergence of the bispherical and re-expansion solutions. $\varepsilon = 1.5$, d is the gap size and D the sphere diameters

Comparing the results of these different but equivalent approaches could yield more analytic results. The bispherical harmonics solution for two conducting spheres is analytic in terms of a series – the T-matrix is diagonal, while the spherical harmonic solution requires a matrix inversion. It is possible to transform between the two bases using the expansions in Section 8.1.3 to convert the analytic bispherical solution into the spherical solution where the spherical harmonics are centered at the center of each sphere. This gives analytic expressions for the T-matrix elements on a spherical basis centred at the foci $z = \pm a$ in terms of a series of a product of binomial coefficients (Eq. (8.13)) and the diagonal bispherical T-matrix (Eq. (8.35) combined with (8.53)). The spherical harmonics can then be translated to the center of each sphere. However, the series coefficients can be numerically unstable to compute when alternating signs are involved.

Similarly for the single offset dielectric sphere, the T-matrix is diagonal for a basis of offset spherical harmonics, so by converting the spherical harmonics into bispherical harmonics, this can be used to obtain a direct series expression for the bispherical T-matrix. Again the series is unstable, and not of much practical help since the T-matrix for a *two* sphere problem requires another matrix inversion anyway as per Eq. (8.53).

8.7 Conclusion

In this chapter we have investigated the many connections between spherical and bispherical harmonics in terms of Kelvin inversion, finite sums and infinite series. Following this, analytic expressions for the electrostatic T-matrix for two arbitrary spheres on a basis of bispherical harmonics were derived, demonstrating the versatility of the T-matrix method for electrostatics problems. We have also derived the plasmon resonance conditions using this formalism, which finds all types of modes including M-modes which can be excited by molecules in the gap, and have a very strong localized field which is ideal for surface enhanced Raman spectroscopy [143]. We have also demonstrated that the bispherical T-matrix is an ideal method of computation for these situations where molecules are located in the gap.

Chapter 9

Conclusion

The focus of this thesis has been to derive new analytic results for image theory and the T-matrix method. For image theory our approach has been to find the singularities of the analytic continuation of the potential and their corresponding charge distribution, which we defined as reduced images. We found the reduced image of a point charge in an infinite cylinder, and on the axis or inside a prolate spheroid. For the dielectric sphere, we have modified the existing image solution to apply for all values of the permittivity, and for an oscillating acoustic source near a sphere, found evidence that the image lies on a radial line segment. In all these cases the exact image itself is too complex to be practical but studying these images highlights issues of convergence and they may be used to create simpler approximate image solutions.

The image of a point source depends radically on the geometry of the boundary, in some cases like the sphere and plane being simple, but in others like the spheroid or cylinder being extremely complex. There is no guarantee of a simple or numerically stable expression for the image density even for analytic boundaries, and this may be the case for the spheroid or for the spherical wave near the sphere. More progress could be in finding just the *locations* of the image singularities, for example finding conditions for the image to be points, lines or surfaces, and finding approximations or inequalities for the extent of these singularities depending on the curvature of the boundary. A numerical method of analytic continuation would be of great use, to find even approximate locations of the singularities of a potential function. Using this information one should be able to solve the problem approximately by placing simple image charges on the singularity, or use the numerical data as an initial guess for an iterated image charge algorithm.

In part two we derived analytic expressions for the T-matrix elements of a spheroid in the small size limit, for the lowest non-zero order of all elements for electric and magnetic multipole responses. These expressions contain what we call generalized depolarization factors which tell us the resonance conditions of each multipole in the small size limit. For the torus we derived the T-matrices on their corresponding basis of toroidal harmonics, and used this to calculate the plasmon resonance conditions and find simple formulae for the limit of a thin ring. We then converted the T-matrix to a spherical basis to obtain new expressions for the quasi-static limit of the time harmonic T-matrix. A similar analysis was made for the sphere dimer, finding the electrostatic T-matrix on a basis of bispherical harmonics, and using this formalism to calculate the resonance conditions. We did not have to convert the T-matrix to a spherical basis since this is best done directly via the re-expansion method using spherical harmonics, but the bispherical harmonic T-matrix has different convergence properties which are ideal for calculating fields near the sphere gap, a region of interest for nano-photonics and surface enhanced Raman spectroscopy. Overall these results indicate that analytic analysis of the quasistatic T-matrix can provide simple approximations and reveal much about the plasmon resonances of small particles. The T-matrix method applies differently depending on the shape and topology of the particle(s). For the spheroid the approach is relatively straightforward due to the similar nature of the spherical and spheroidal harmonics. For the torus, while the problem is completely expressible on a toroidal harmonic basis, we have only managed to express the *reflected* field on a basis of spherical harmonics; the internal field is likely singular near the origin and at infinity and therefore cannot be expressed with spherical harmonics. So the **P** and **Q** matrices do not exist on a spherical basis and the null field method cannot be used. The bispherical system also excludes the origin and the internal field may well be singular between the spheres again making the null field method intractable using a basis of spherical harmonics centered at the origin. Ultimately the convergence and existence of the T-matrix approach is governed by the locations of the singularities of the internal and scattered fields. Extending these results to higher order in frequency would be practical, since nano-particles used in photonics are often too large for the full electrostatic approximation to be very accurate.

These results are of universal interest since the Laplace operator appears in many important partial differential equations, including the heat equation, the Navier-Stokes equation, the Schrödinger equation and the Helmholtz equation, which are much more difficult numerically and analytically. The same concepts of analytic continuation, image singularities and orthogonal basis expansions apply to these equations also. It would be beneficial to extend the results of this thesis to these other differential equations, at least asymptotically, for example in a low frequency expansion where these equations may be reduced to Laplace's equation with more complex boundary conditions.

Bibliography

[1] E. Le Ru and P. Etchegoin. *Principles of Surface-Enhanced Raman Spectroscopy: and related plasmonic effects*. Elsevier, 2008.

[2] E. C. Le Ru and P. G. Etchegoin. “Quantifying SERS enhancements”. *MRS bulletin* 38.8 (2013), p. 631.

[3] B. Auguié, B. L. Darby, and E. C. Le Ru. “Electromagnetic interactions of dye molecules surrounding a nanosphere”. *Nanoscale* 11.25 (2019), pp. 12177–12187.

[4] W. Thomson. *Reprint of papers on electrostatics and magnetism*. Cambridge University Press, 2011.

[5] M. Majic, B. Auguié, and E. C. Le Ru. “Spheroidal harmonic expansions for the solution of Laplace's equation for a point source near a sphere”. *Phys. Rev. E* 95.3 (2017). ISSN: 24700053.

[6] M. Majic and E. C. Le Ru. “New class of solutions to Laplace equation: Regularized multipoles of negative orders”. *Phys. Rev. Res.* 1 (2019), p. 033213.

[7] P. Waterman. “Matrix formulation of electromagnetic scattering”. *Proceedings of the IEEE* 53.8 (1965), pp. 805–812.

[8] M. I. Mishchenko, L. D. Travis, and A. A. Lacis. *Scattering, absorption, and emission of light by small particles*. Cambridge university press, 2002.

[9] W. R. Smythe. *Static and dynamic electricity*. 1988.

[10] M. Zahn. “Point charge between two parallel grounded planes”. *American Journal of Physics* 44.11 (1976), pp. 1132–1134.

[11] R. Terras and R. A. Swanson. “Electrostatic image problems with plane boundaries”. *American Journal of Physics* 48.7 (1980), pp. 526–531.

[12] J. Jackson and K. Wijk. “Classical Electrodynamics-Solutions”. *American Journal of Physics* 67 (1999), p. 841. URL: `http://link.aip.org/link/?AJPIAS/67/841/27)Z7`.

[13] D. J. Griffiths and C. Inglefield. *Introduction to Electrodynamics*. 2005. DOI: `10.1119/1.4766311`. arXiv: `0712.0689`.

[14] L. Davis and J. Reitz. “Solution of potential problems near the corner of a conductor”. *Journal of Mathematical Physics* 16.6 (1975), pp. 1219–1226.

[15] L Poladian. “General theory of electrical images in sphere pairs”. *The Quarterly Journal of Mechanics and Applied Mathematics* 41.3 (1988), pp. 395–417.

[16] I. V. Lindell. “Electrostatic image theory for the dielectric sphere”. *Radio Science* 27.1 (1992), pp. 1–8.

[17] I Lindell and E. Alanen. “Exact image theory for the Sommerfeld half-space problem, Part I: Vertical magnetic dipole”. *IEEE Transactions on Antennas and Propagation* 32.2 (1984), pp. 126–133.

[18] I Lindell and E. Alanen. “Exact image theory for the Sommerfeld half-space problem, part II: Vertical electrical dipole”. *IEEE transactions on antennas and propagation* 32.8 (1984), pp. 841–847.

[19] I Lindell and E. Alanen. “Exact image theory for the Sommerfeld half-space problem, Part III: General formulation”. *IEEE Transactions on Antennas and Propagation* 32.10 (1984), pp. 1027–1032.

[20] K. Nikoskinen and I. Lindell. “Image solution for Poisson's equation in wedge geometry”. *IEEE transactions on antennas and propagation* 43.2 (1995), pp. 179–187.

[21] W. Somerville, B Auguié, and E. Le Ru. “Severe loss of precision in calculations of T-matrix integrals”. *Journal of Quantitative Spectroscopy and Radiative Transfer* 113.7 (2012), pp. 524–535.

[22] T. Rother and M. Kahnert. *Electromagnetic wave scattering on nonspherical particles*. Springer, 2009.

[23] M. Majic. "Image theory for a sphere with negative permittivity". *Journal of Mathematical Physics* 60.6 (2019), p. 062902.

[24] M. Majic and E. C. Le Ru. "Quasistatic limit of the electric-magnetic coupling blocks of the T-matrix for spheroids". *Journal of Quantitative Spectroscopy and Radiative Transfer* 225 (2019), pp. 16–24.

[25] M Majic. ""Electrostatic T-matrix for a torus on bases of toroidal and spherical harmonics"". *Journal of Quantitative Spectroscopy and Radiative Transfer* 235 (2019), pp. 287 –299. ISSN: 0022-4073. DOI: `https://doi.org/10.1016/j.jqsrt.2019.07.010`. URL: `http://www.sciencedirect.com/science/article/pii/S0022407319303322`.

[26] M. Majic, B. Auguié, and E. C. Le Ru. "Laplace's equation for a point source near a sphere: improved internal solution using spheroidal harmonics". *IMA Journal of Applied Mathematics* 83.6 (2018), pp. 895–907.

[27] M. Majic et al. "Approximate T-matrix and optical properties of spheroidal particles to third order with respect to size parameter". *Physical Review A* 99.1 (2019), p. 013853.

[28] M. Majic and E. C. Le Ru. "Numerically stable formulation of Mie theory for an emitter close to a sphere". *Applied Optics* 59.5 (2020), pp. 1293–1300.

[29] M. Majic. "A surface integral approach to Poisson's equation and analytic expressions for the gravitational field of toroidal mass distributions". *Applied Numerical Mathematics* 148 (2020), pp. 98–108.

[30] J. Dougall. "The determination of Green's Function by means of cylindrical or spherical harmonics". *Proceedings of the Edinburgh Mathematical Society* 18 (1900), pp. 33–83.

[31] C. Bouwkamp and N. De Bruijn. "The electrostatic field of a point charge inside a cylinder, in connection with wave guide theory". *Journal of Applied Physics* 18.6 (1947), pp. 562–577.

[32] J. Pumplin. "Application of Sommerfeld-Watson transformation to an electrostatics problem". *American Journal of Physics* 37.7 (1969), pp. 737–739.

[33] A Dillmann and G Grabitz. "On a method to evaluate Fourier-Bessel series with poor convergence properties and its application to linearized supersonic free jet flow". *Quarterly of applied mathematics* 53.2 (1995), pp. 335–352.

[34] D. C. Wood. "The computation of polylogarithms" (1992).

[35] J. Greenwood. "A simple method of summing Bessel series". *Mathematical Proceedings of the Cambridge Philosophical Society*. Vol. 64. 3. Cambridge University Press. 1968, pp. 705–710.

[36] P. Rančić. "A point ground electrode in the presence of spherical ground inhomogenity: analysis of two approximate closed form solutions for electrical scalar potential". *Proc. International PhD Seminar Computational Electromagnetics and Technical Applications*. 2006, pp. 213–223.

[37] V Belevitch and J Boersma. "Some electrical problems for a torus". *Philips Journal of Research* 38.3 (1983), pp. 79–137.

[38] M. Majic and E. C. L. Ru. "Relationships between solid spherical and toroidal harmonics". *arXiv preprint arXiv:1802.03484* (2018).

[39] A Peskoff. "Green's function for Laplace's equation in an infinite cylindrical cell". *Journal of mathematical physics* 15.12 (1974), pp. 2112–2120.

[40] J.-E. Sten and I. Lindell. "An electrostatic image solution for the conducting prolate spheroid". *Journal of electromagnetic waves and applications* 9.4 (1995), pp. 599–609.

[41] J.-E. Sten. "Focal image charge singularities for the dielectric elliptic cylinderLadunsspiegelung am dielektrischen elliptischen Zylinder". *Electrical Engineering* 79.1 (1996), pp. 9–15.

[42] I. Lindell, G Dassios, and K. Nikoskinen. "Electrostatic image theory for the conducting prolate spheroid". *Journal of Physics D: Applied Physics* 34.15 (2001), p. 2302.

[43] I. Lindell and K. Nikoskinen. "Electrostatic Image Theory for the Dielectric Prolate Spheroid". *Journal of Electromagnetic Waves and Applications* 15.8 (2001), pp. 1075–1096. ISSN: 0920-5071.

[44] G. Dassios and J. C.-E. Sten. “The image system and Green’s function for the ellipsoid” (2009).

[45] C. Xue and S. Deng. “Green’s function and image system for the Laplace operator in the prolate spheroidal geometry”. *AIP Advances* 7.1 (2017), p. 015024. ISSN: 2158-3226. DOI: `10.1063/1.4974156`. URL: `http://aip.scitation.org/doi/10.1063/1.4974156`.

[46] G. Dassios and J. C.-E. Sten. “On the Neumann function and the method of images in spherical and ellipsoidal geometry”. *Mathematical Methods in the Applied Sciences* 35.4 (2012), pp. 482–496.

[47] C. Xue, R. Edmiston, and S. Deng. “Image Theory for Neumann Functions in the Prolate Spheroidal Geometry”. *Advances in Mathematical Physics* 2018 (2018).

[48] G. Nemes and A. B. Olde Daalhuis. “Large-parameter asymptotic expansions for the Legendre and allied functions”. *SIAM Journal on Mathematical Analysis* 52.1 (2020), pp. 437–470.

[49] G. N. Watson. “The diffraction of electric waves by the earth”. *Proceedings of the Royal Society of London. Series A, Containing Papers of a Mathematical and Physical Character* 95.666 (1918), pp. 83–99.

[50] L Felsen. “Alternative field representations in regions bounded by spheres, cones, and planes”. *IRE Transactions on Antennas and Propagation* 5.1 (1957), pp. 109–121.

[51] M. Majic. “The image of a point charge in an infinite conducting cylinder”. *arXiv preprint arXiv:2001.10651* (2020).

[52] G. B. Jeffery. “The relations between spherical, cylindrical, and spheroidal harmonics”. *Proceedings of the London Mathematical Society* s2-16.1 (1916), pp. 133–139. ISSN: 1460244X. DOI: `10.1112/plms/s2-16.1.133`.

[53] P. M. Morse and H. Feshbach. *Methods of theoretical physics*. New York: McGraw-Hill, 1953.

[54] H Alshal, T Curtright, and S Subedi. “Image Charges Re-Imagined”. *arXiv preprint arXiv:1808.08300* (2018).

[55] W. Norris. “Charge images in a dielectric sphere”. *IEE Proceedings-Science, Measurement and Technology* 142.2 (1995), pp. 142–150.

[56] A. Moroz. “Superconvergent representation of the Gersten–Nitzan and Ford–Weber nonradiative rates”. *The Journal of Physical Chemistry C* 115.40 (2011), pp. 19546–19556.

[57] E. Le Ru and P. Etchegoin. *Principles of Surface-Enhanced Raman Spectroscopy: and related plasmonic effects*. Elsevier, 2009.

[58] E. A. Galapon. “The problem of missing terms in term by term integration involving divergent integrals”. *Proc. R. Soc. A* 473.2197 (2017), p. 20160567.

[59] K. Bhattacharya. “Analogy of the grounded conducting sphere image problem with mirror optics”. *European journal of physics* 32.5 (2011), p. 1163.

[60] I. Lindell, J.-E. Sten, and R. Kleinman. “Low-frequency image theory for the dielectric sphere”. *Journal of Electromagnetic Waves and Applications* 8.3 (1994), pp. 295–313. ISSN: 0920-5071. DOI: `10.1163/156939394X00885`. URL: `http://www.tandfonline.com/doi/abs/10.1163/156939394X00885`.

[61] I. Lindell and K. Nikoskinen. “Electrostatic Image Theory for the Dielectric Prolate Spheroid”. *Journal of Electromagnetic Waves and Applications* 15.8 (2001), pp. 1075–1096. ISSN: 0920-5071. DOI: `10.1163/156939301X00436`. URL: `http://www.tandfonline.com/doi/abs/10.1163/156939301X00436`.

[62] *NIST Digital Library of Mathematical Functions*. http://dlmf.nist.gov/, Release 1.0.16 of 2017-09-18. F. W. J. Olver, A. B. Olde Daalhuis, D. W. Lozier, B. I. Schneider, R. F. Boisvert, C. W. Clark, B. R. Miller and B. V. Saunders, eds. URL: `http://dlmf.nist.gov/`.

[63] I. S. Gradshteyn and I. M. Ryzhik. *Table of integrals, series, and products*. Academic press, 2014.

[64] J. B. Keller, S. Rubinow, and M. Goldstein. “Zeros of Hankel functions and poles of scattering amplitudes”. *Journal of Mathematical Physics* 4.6 (1963), pp. 829–832.

[65] S.-E. Sandström and C. Ackrén. “Note on the complex zeros of Hν’(x)+ iζHν (x)= 0”. *Journal of Computational and Applied Mathematics* 201.1 (2007), pp. 3–7.

[66] E. M. Ferreira and J. Sesma. “Zeros of the Macdonald function of complex order”. *Journal of computational and applied mathematics* 211.2 (2008), pp. 223–231.

[67] D. Veberic. “Having fun with Lambert W (x) function”. *arXiv preprint arXiv:1003.1628* (2010).

[68] P. C. Waterman. “Symmetry, unitarity, and geometry in electromagnetic scattering”. *Physical review D* 3.4 (1971), p. 825.

[69] P. Barber and C. Yeh. “Scattering of electromagnetic waves by arbitrarily shaped dielectric bodies”. *Appl. Optics* 14.12 (1975), pp. 2864–2872.

[70] P. W. Barber and S. C. Hill. *Light scattering by particles: computational methods*. Singapore: World Scientific, 1990.

[71] A. Doicu and T. Wriedt. “Calculation of the T-matrix in the null-field method with discrete sources”. *J. Opt. Soc. Am. A* 16.10 (1999), pp. 2539–2544.

[72] M. I. Mishchenko. “Comprehensive thematic T-matrix reference database: A 2017-2019 update”. *J. Quant. Spectrosc. Radiat. Transfer* 242 (2020), p. 106692. DOI: 10.1016/j.jqsrt.2019.106692.

[73] A. Quirantes. “A T-matrix method and computer code for randomly oriented, axially symmetric coated scatterers”. *Journal of Quantitative Spectroscopy and Radiative Transfer* 92.3 (2005), pp. 373–381.

[74] J. Markkanen and A. J. Yuffa. “Fast superposition T-matrix solution for clusters with arbitrarily-shaped constituent particles”. *Journal of Quantitative Spectroscopy and Radiative Transfer* 189 (2017), pp. 181–188.

[75] F. M. Schulz, K. Stamnes, and J. J. Stamnes. “Scattering of electromagnetic waves by spheroidal particles: a novel approach exploiting the T-matrix computed in spheroidal coordinates”. *Applied Optics* 37.33 (1998), pp. 7875–7896.

[76] V. Farafonov. “The Rayleigh hypothesis and the region of applicability of the extended boundary condition method in electrostatic problems for nonspherical particles”. *Optics and Spectroscopy* 117.6 (2014), pp. 923–935.

[77] V. Farafonov et al. “On the analysis of Waterman’s approach in the electrostatic case”. *Journal of Quantitative Spectroscopy and Radiative Transfer* 178 (2016), pp. 176–191.

[78] M. Majic et al. “Electrostatic limit of the T-matrix for electromagnetic scattering: Exact results for spheroidal particles”. *Journal of Quantitative Spectroscopy and Radiative Transfer* 200 (2017), pp. 50–58.

[79] A. Stevenson. “Electromagnetic scattering by an ellipsoid in the third approximation”. *Journal of Applied Physics* 24.9 (1953), pp. 1143–1151.

[80] M. R. Majić et al. “Electrostatic limit of the T-matrix for electromagnetic scattering: Exact results for spheroidal particles”. *Journal of Quantitative Spectroscopy and Radiative Transfer* 200 (2017), pp. 50–58.

[81] G. Jansen. “Transformation properties of spheroidal multipole moments and potentials”. *Journal of Physics A: Mathematical and General* 33.7 (2000), p. 1375.

[82] V. A. Antonov and A. S. Baranov. “Relation between the expansions of an external potential in spherical functions and spheroidal harmonics”. *Technical Physics* 47.3 (2002), pp. 361–363. ISSN: 1063-7842.

[83] M. I. Mishchenko, L. D. Travis, and A. A. Lacis. *Scattering, absorption, and emission of light by small particles*. 3rd electronic release. Cambridge: Cambridge University Press, 2002.

[84] J. R. Allardice and E. C. Le Ru. “Convergence of Mie theory series: criteria for far-field and near-field properties”. *Applied Optics* 53.31 (2014), pp. 7224–7229.

[85] W. R. C. Somerville, B. Auguié, and E. C. Le Ru. “Severe loss of precision in calculations of T-matrix integrals”. *J. Quant. Spectrosc. Rad. Transfer* 113.7 (2012), pp. 524 –535.

[86] W. R. C. Somerville, B. Auguié, and E. C. Le Ru. “A new numerically stable implementation of the T-matrix method for electromagnetic scattering by spheroidal particles”. *J. Quant. Spectrosc. Rad. Transfer* 123 (2013), pp. 153–168.

[87] W. R. Somerville, B. Auguié, and E. C. Le Ru. “Simplified expressions of the T-matrix integrals for electromagnetic scattering”. *Optics letters* 36.17 (2011), pp. 3482–3484.

[88] N. A. Gumerov and R. Duraiswami. “A scalar potential formulation and translation theory for the time-harmonic Maxwell equations”. *Journal of Computational Physics* 225.1 (2007), pp. 206–236.

[89] W. R. C. Somerville, B. Auguié, and E. C. Le Ru. “Accurate and convergent T-matrix calculations of light scattering by spheroids”. *J. Quant. Spectrosc. Rad. Transfer* 160 (2015), pp. 29–35.

[90] W. R. C. Somerville, B. Auguié, and E. C. Le Ru. “SMARTIES: User-friendly codes for fast and accurate calculations of light scattering by spheroids”. *J. Quant. Spectrosc. Rad. Transfer* 174 (2016), pp. 39 –55.

[91] E. C. Le Ru, W. R. C. Somerville, and B. Auguié. “Radiative correction in approximate treatments of electromagnetic scattering by point and body scatterers”. *Phys. Rev. A* 87.1 (2013), p. 012504.

[92] V. Il’in and V. Farafonov. “Rayleigh approximation for axisymmetric scatterers”. *Optics letters* 36.20 (2011), pp. 4080–4082.

[93] E. C. Le Ru and P. G. Etchegoin. *Principles of Surface Enhanced Raman Spectroscopy and Related Plasmonic Effects*. Amsterdam: Elsevier, 2009.

[94] P. Knipp and T. Reinecke. “Classical interface modes of quantum dots”. *Physical Review B* 46.16 (1992), p. 10310.

[95] B. Auguié et al. “Numerical investigation of the Rayleigh hypothesis for electromagnetic scattering by a particle”. *J. Opt.* 18 (2016), p. 075007.

[96] D Schebarchov et al. “Mind the gap: testing the Rayleigh hypothesis in T-matrix calculations with adjacent spheroids”. *Optics Express* 27.24 (2019), pp. 35750–35760.

[97] A. G. Kyurkchan, B. Y. Sternin, and V. E. Shatalov. “Singularities of continuation of wave fields”. *Physics-Uspekhi* 39.12 (1996), p. 1221.

[98] L. Bi and P. Yang. “Modeling of light scattering by biconcave and deformed red blood cells with the invariant imbedding T-matrix method”. *Journal of biomedical optics* 18.5 (2013), p. 055001.

[99] J. Love. “The dielectric ring in a uniform, axial, electrostatic field”. *Journal of Mathematical Physics* 13.9 (1972), pp. 1297–1304.

[100] G. Venkov. “Low-frequency acoustic scattering of a plane wave from a soft and hard torus”. *Journal of Computational Acoustics* 15.02 (2007), pp. 181–197.

[101] C. M. Dutta et al. “Plasmonic properties of a metallic torus”. *The Journal of chemical physics* 129.8 (2008), p. 084706.

[102] M. Salhi, A. Passian, and G. Siopsis. “Toroidal nanotraps for cold polar molecules”. *Physical Review A* 92.3 (2015), p. 033416.

[103] K. V. Garapati et al. “Poloidal and toroidal plasmons and fields of multilayer nanorings”. *Physical Review B* 95.16 (2017), p. 165422.

[104] P. Vafeas. “Low-frequency electromagnetic scattering by a metal torus in a lossless medium with magnetic dipolar illumination”. *Mathematical Methods in the Applied Sciences* 39.14 (2016), pp. 4268–4292.

[105] V. T. Erofeenko. “Addition theorems connected with toroidal, cylindrical and spherical harmonic functions”. *Differentsial’nye Uravneniya* 19.8 (1983), pp. 1416–1427.

[106] G. C. Shushkevich. “Electrostatic field of a thin, unclosed spherical shell and a torus”. *Technical Physics* 43.7 (1998), pp. 743–748.

[107] M. Andrews. “Alternative separation of Laplace’s equation in toroidal coordinates and its application to electrostatics”. *Journal of Electrostatics* 64.10 (2006), pp. 664–672. ISSN: 03043886. DOI: `10.1016/j.elstat.2005.11.005`.

[108] R. W. Scharstein and H. B. Wilson. "Electrostatic excitation of a conducting toroid: exact solution and thin-wire approximation". *Electromagnetics* 25.1 (2005), pp. 1–19.

[109] V. G. Farafonov and V. I. Ustimov. "Properties of the T-matrix in the Rayleigh approximation". *Optics and Spectroscopy* 119.6 (2015), pp. 1022–1033. ISSN: 0030-400X. DOI: `10.1134/S0030400X15120103`. URL: `http://link.springer.com/10.1134/S0030400X15120103`.

[110] S. Kuyucak, M. Hoyles, and S.-H. Chung. "Analytical solutions of Poisson's equation for realistic geometrical shapes of membrane ion channels". *Biophysical journal* 74.1 (1998), pp. 22–36.

[111] K Avramov, T Ivanov, and I Zhelyazkov. "High-frequency surface waves on a toroidal isotropic plasma". *Plasma physics and controlled fusion* 35.12 (1993), p. 1787.

[112] J. D. Love. "Quasi-static modes of oscillation of a cold toroidal plasma". *Journal of Plasma Physics* 14.1 (1975), pp. 25–37.

[113] M. Salhi. "Surface Plasmon Modes in Toroidal Nanostructures and Applications". *PhD thesis, University of Tennessee* (2016).

[114] A Wokaun, J. Gordon, and P. Liao. "Radiation damping in surface-enhanced Raman scattering". *Physical Review Letters* 48.14 (1982), p. 957.

[115] M. El-Shenawee et al. "Torus nano-antenna: Enhanced field and radiation pattern". *Antennas and Propagation Society International Symposium, 2009. APSURSI'09. IEEE*. IEEE. 2009, pp. 1–4.

[116] A. Mary et al. "Optical absorption of torus-shaped metal nanoparticles in the visible range". *Physical Review B* 76.24 (2007), p. 245422.

[117] V. Weston. "On toroidal wave functions". *Journal of Mathematics and Physics* (1960).

[118] M. Washizu and T. B. Jones. "Dielectrophoretic interaction of two spherical particles calculated by equivalent multipole-moment method". *IEEE Transactions on Industry Applications* 32.2 (1996), pp. 233–242.

[119] F. Lindén, H. Cederquist, and H. Zettergren. "Interaction and charge transfer between dielectric spheres: Exact and approximate analytical solutions". *The Journal of chemical physics* 145.19 (2016), p. 194307.

[120] I. V. Lindell, J. C.-E. Sten, and K. I. Nikoskinen. "Electrostatic image method for the interaction of two dielectric spheres". *Radio science* 28.03 (1993), pp. 319–329.

[121] J. R. Zurita-Sánchez and A. I. Tec-Chim. "Quasi-static potential created by an oscillating dipole in the vicinity of two nanospheres (dimer): inversion transformation method". *Journal of Optics* 16.6 (2014), p. 065002.

[122] G. B. Jeffery. "On a Form of the Solution of Laplace's Equation Suitable for Problems Relating to Two Spheres". *Proceedings of the Royal Society A: Mathematical, Physical and Engineering Sciences* 87.593 (1912), pp. 109–120. ISSN: 1364-5021. DOI: `10.1098/rspa.1912.0063`. URL: `http://www.jstor.org/stable/93249{\%}5Cnhttp://rspa.royalsocietypublishing.org/cgi/doi/10.1098/rspa.1912.0063`.

[123] R. D. Stoy. "Solution procedure for the Laplace equation in bispherical coordinates for two spheres in a uniform external field: Perpendicular orientation". *Journal of Applied Physics* 66.10 (1989), pp. 5093–5095. ISSN: 00218979. DOI: `10.1063/1.343737`.

[124] J. D. Love. "Dielectric sphere-sphere and sphere-plane problems in electrostatics". *The Quarterly Journal of Mechanics and Applied Mathematics* 28.4 (1975), pp. 449–471.

[125] P. Chaumet and J. Dufour. "Electric potential and field between two different spheres". *Journal of Electrostatics* 43.2 (1998), pp. 145–159. ISSN: 03043886. DOI: `10.1016/S0304-3886(97)00170-8`.

[126] R. Klinkla, U. Pinsook, and S. Boonchui. "Role of symmetry in coupled localized surface plasmon resonance of a nanosphere pair". *Plasmonics* 10.3 (2015), pp. 643–653.

[127] D. B. Large. "Electric potential near a spherical body in a conducting half-space". *Geophysics* 36.4 (1971), pp. 763–767.

[128] J. Berry. "Electrostatic forces on a conducting sphere due to a charge on a dielectric half-space". *Journal of Physics A: Mathematical and General* 9.11 (1976), p. 1939.

[129] A. Khachatourian et al. “Electrostatic force between a charged sphere and a planar surface: A general solution for dielectric materials”. *Journal of Chemical Physics* 140.7 (2014), pp. 1–10. ISSN: 00219606. DOI: `10.1063/1.4862897`.

[130] A. Starkov, O. Pakhomov, and I. Starkov. “Electroelastic field of a sphere located in the vicinity of a plane piezoelectric surface”. *Technical Physics* 61.1 (2016), pp. 23–27.

[131] P. Vafeas, D. Lesselier, and F. Kariotou. “Estimates for the low-frequency electromagnetic fields scattered by two adjacent metal spheres in a lossless medium”. *Mathematical Methods in the Applied Sciences* 38.17 (2015), pp. 4210–4237.

[132] M. V. Gelderen. “The shift operators and translations of spherical harmonics”. *DEOS Progress Lett.* 1 (1998), pp. 57–67.

[133] C. Banderier and S. Schwer. “Why Delannoy numbers?” *Journal of statistical planning and inference* 135.1 (2005), pp. 40–54.

[134] M. Majic. “Relationships between spherical and bispherical harmonics, and an electrostatic T-matrix for dimers” (2019).

[135] T. Macrobert. “On Neumann’s Formula for the Legendre Functions”. *Glasgow Mathematical Journal* 1.1 (1952), pp. 10–12.

[136] B. I. Schneider et al. “A new Fortran 90 program to compute regular and irregular associated Legendre functions”. *Computer Physics Communications* 181.12 (2010), pp. 2091–2097. ISSN: 00104655. DOI: `10.1016/j.cpc.2010.08.038`. URL: `http://dx.doi.org/10.1016/j.cpc.2010.08.038`.

[137] J.-T. Chen, J.-W. Lee, and H.-C. Shieh. “A Green’s Function for the Domain Bounded by Nonconcentric Spheres”. *Journal of Applied Mechanics* 80.1 (2012), p. 014503. ISSN: 0021-8936. DOI: `10.1115/1.4007071`. URL: `http://appliedmechanics.asmedigitalcollection.asme.org/article.aspx?doi=10.1115/1.4007071`.

[138] G. S. Smith and R. Barakat. “Electrostatics of two conducting spheres in contact”. *Applied Scientific Research* 30.6 (1975), pp. 418–432. ISSN: 00036994. DOI: `10.1007/BF00455966`.

[139] M. Pitkonen. “Polarizability of a pair of touching dielectric spheres”. *Journal of Applied Physics* 103.10 (2008), p. 104910.

[140] A. Fernández-Domínguez, S. Maier, and J. Pendry. “Collection and concentration of light by touching spheres: a transformation optics approach”. *Physical review letters* 105.26 (2010), p. 266807.

[141] V. Klimov and D. Guzatov. “Strongly localized plasmon oscillations in a cluster of two metallic nanospheres and their influence on spontaneous emission of an atom”. *Physical Review B* 75.2 (2007), p. 024303.

[142] D. V. Guzatov and V. V. Klimov. “Properties of spontaneous radiation of an atom located near a cluster of two spherical nanoparticles”. *Quantum Electronics* 35.10 (2005), p. 891.

[143] P. G. Etchegoin and E. C. Le Ru. “Basic electromagnetic theory of SERS”. *Surface Enhanced Raman Spectroscopy* (2011), pp. 1–37.